Interface Design and Characterization for Stable Inorganic Perovskite Solar Cells.

Dissertation

zur Erlangung des akademischen Grades
"doctor rerum naturalium"
(Dr. rer. nat.)
in der Wissenschaftsdisziplin “physikalische Chemie”

eingereicht an der
Mathematisch-Naturwissenschaftlichen Fakultät
Institut für Chemie
der Universität Potsdam
und
Helmholtz-Zentrum Berlin für Materialien und Energie

Von

Zafar Iqbal

Berlin, July 2023

Printed and/or published with the support of the German Academic Exchange Service.

Date of Defense

November 15, 2023

Ph.D. Supervisors

Prof. Dr. Antonio Abate
Prof. Dr. Andreas Taubert

Reviewers

Prof. Dr. Antonio Abate
Prof. Dr. Andreas Taubert
Dr.Philip Schulz

Published online on the
Publication Server of the University of Potsdam:
https://doi.org/10.25932/publishup-61831
https://nbn-resolving.org/urn:nbn:de:kobv:517-opus4-618315

List of Contents

Abstract iv
Zusammenfassung vi
Chapter 1 Introduction and Fundamentals 1
1.1 Climate change - a Collective Challenge. 1
1.2 Perovskite Solar Cells 3
1.3 $CsPbI_3$: An introduction, Challenges, Progress and Prospects 6
1.4 Working Principle of Perovskite Solar Cell 10
1.5 Relevant Interface Energetics 12
1.6 Surface Band Bending 14
1.7 Energy Level Alignment 17
1.8 Open Circuit Voltage Loss 18
1.9 Energy Level Alignments in $CsPbI_3$ 19
1.10 Interfaces Limit SQ-limit 23
1.11 Motivation 26
Outlines 27
References 27
Chapter 2 Methods 34
2.1. Samples preparations 34
2.2 Ultraviolet-Visible spectroscopy (UV-Vis) 36
2.3. Photoluminescence spectroscopy (PL) 37
2.4. X-ray Diffraction (XRD) 39
2.5. Scanning Electron Microscopy (SEM) 40
2.6. Kelvin Probe Measurements (KP) 40
2.7. Transient Surface Voltage (trSPV) 42
2.7.1 Simulations of Charge Extraction and Recombination 42
2.8. Photoemission Spectroscopies 43
2.8.1.X-Ray Photoelectron Spectroscopy (XPS) 45
2.8.2. Hard X-Ray Photoemission Spectroscopy (HAXPES) 46
2.8.3. Ultraviolet Photoemission Spectroscopy (UPS) 46
2.9. Device Performance (*JV,* EQE) 47
2.10 Stability Testing 48
References 49

Chapter 3 52
The Potential Effect of Dry and Ambient Air Annealing Environment on the $CsPbI_3$ Surface Chemistry and its Subsequent Interfacial Dynamics. 52
3.1 The Highlight of the Work 52
3.2 Introduction 52
3.3 Experimental section 53
3.4 Film Characterization 53
3.5. Surface Chemistry and Electronic Structure Profile Investigation by HAXPES 55
3.6 Investigation of Interfacial Dynamics 62
3.7 Device Performance 64
3.8 Conclusion 67
References 68
Chapter 4 71
Interface Design for Better Charge Extraction and Energy Levels Alignment at the Interface 71
4.1 Highlights of the work 71
4.2 Statement of the Challenges 71
4.3 Introduction 71
4.4 Result and Discussion 74
4.4.1 $CsPbI_3$ film characterizations 74
4.4.2 Surface Passivation 75
4.4.3 XPS study 76
4.4.4 Interfacial Energy Level Alignment 78
4.4.5 Charge Extraction Dynamics 81
4.4.6 Device Performance 84
4.4.7 Device Stability 85
4.5 Conclusion 88
References 88
Chapter 5 92
Interface Design for P3HT Hole Transport Layer 92
5.1 Statement of the Challenge 92
5.2 Introduction 92
5.3 Methods 93
5.4 Results and Discussion 94
4.5 Conclusion 96

References 96
Chapter 6 98
Summary and Outlook 98
Outlook 102
Appendix 103
Appendix A3 108
Appendix A 4 120
Declaration of Originality 131
Acknowledgment 132

Abstract

We live in an era driven by fossil fuels. The prevailing climate change suggests that we have to significantly reduce greenhouse gas emissions. The only way forward is to use renewable energy sources. Among those, solar energy is a clean, affordable, and sustainable source of energy. It has the potential to satisfy the world's energy demand in the future. However, there is a need to develop new materials that can make solar energy usable. Photovoltaics (PV) are devices that convert photon energy into electrical energy. The most commonly used solar cells are based on crystalline silicon. However, the fabrication process for silicon solar cells is technologically difficult and costly. Solar cells based on lead halide perovskites (PSCs) have emerged as a new candidate for PV applications since 2009. To date, PSCs have achieved 26% power-conversion-efficiency (PCE) for its single junction, and 33.7% PCE for tandem junction devices. However, there is still room for improvement in overall performance. The main challenge for the commercialization of this technology is the stability of the solar cells under operational conditions. Inorganic perovskite $CsPbI_3$ has attracted researchers' interest due to its stability at elevated temperatures, however, inorganic perovskites also have associated challenges, *e.g.* phase stability, larger voltage loss compared to their organic-inorganic hybrid counterparts, and interface energy misalignment. The most efficient inorganic perovskite solar cell is stable for up to a few hundred hours while the most stable device in the field of inorganic PSCs reported so far is at 17% PCE. This suggests the need for improvement of the interfaces for enhanced open circuit voltage (V_{OC}), and optimization of the energy alignment at the interfaces. This dissertation presents the study on interfaces between the perovskite layer and hole transport layer (HTL) for stable $CsPbI_3$ solar cells.

The first part of the thesis presents an investigation of the $CsPbI_3$ film annealing environment and its subsequent effects on the perovskite/HTL interface dynamics. Thin films annealed in dry air were compared with thin films annealed in ambient air. Synchrotron-based hard X-ray spectroscopy (HAXPES) measurements reveal that annealing in ambient air does not have an adverse effect; instead, those samples undergo surface band bending. This surface band modification induces changes in interface charge dynamics and, consequently, an improvement in charge extraction at the interfaces. Further, transient surface photovoltage (tr-SPV) simulations show that air-annealed samples exhibit fewer trap states compared to samples annealed in dry air. Finally, by annealing the $CsPbI_3$ films in ambient air, a PCE of 19.8% and V_{oc} of 1.23 V were achieved for an *n-i-p* structured device.

Interface engineering has emerged as a strategy to extract the charge and optimize the energy alignment in perovskite solar cells (PSCs). An interface with fewer trap states and energy band levels closer to the selective contact helps to attain improved efficiencies in PSCs. The second part of the thesis presents a design for the $CsPbI_3$/HTM interface. In this work, an interface between $CsPbI_3$ perovskite and its hole selective contact $N^2,N^2,N^{2'},N^{2'},N^7,N^7,N^{7'},N^{7'}$-octakis(4-methoxyphenyl)-9,9′-spirobi[9H-fluorene]-2,2′,7,7′-tetramine(Spiro-OMeTAD), realized by trioctylphosphine oxide (TOPO), a dipole molecule is introduced. On top of a perovskite film well-passivated by *n*-octyl ammonium Iodide (OAI), it created an upward surface band-bending at the interface byTOPO that optimizes energy level alignment and enhances the extraction of holes from the perovskite layer to the hole transport material. Consequently, a V_{oc} of 1.2 V and high-power conversion efficiency (PCE) of over 19% were achieved for inorganic $CsPbI_3$ perovskite solar cells. In addition, the work also sheds light on the interfacial charge-selectivity and the long-term stability of $CsPbI_3$ perovskite solar cells.

The third part of the thesis extends the previous studies to polymeric poly(3-hexylthiophene-2,5-diyl) (P3HT) as HTL. The $CsPbI_3$/P3HT interface is critical due to high non-radiative recombination. This work presents a $CsPbI_3$/P3HT interface modified with a long-chain alkyl halide molecule, *n*-hexyl trimethyl ammonium bromide (HTAB). This molecule largely passivates the $CsPbI_3$ perovskite surface and improves the charge extraction across the interface. Consequently, a V_{oc} of over 1.00 V and 14.2% PCE were achieved for $CsPbI_3$ with P3HT as HTM.

Overall the results presented in this dissertation introduce and discuss methods to design and study the interfaces in $CsPbI_3$-based solar cells. This study can pave the way for novel interface designs between $CsPbI_3$ and HTM for charge extraction, efficiency and stability.

Zusammenfassung

Wir leben in einem Zeitalter, das von fossilen Brennstoffen geprägt ist. Der fortschreitende Klimawandel erfordert eine merkliche Reduktion der Treibhausgasemissionen. Der einzige Weg hin zu einer nachhaltigen Energiewirtschaft ist die Implementierung erneuerbarer Energiequellen. Solarenergie hat das Potential, den Energiebedarf der Welt langfristig auf saubere und kostengünstige Weise zu decken. Es müssen jedoch neue Materialien zur Marktreife entwickelt werden, die die Solarenergie nutzbar machen können. In der Photovoltaik (PV) wird Lichtenergie in elektrische Energie umwandelt, wobei die gängisten Solarzellen aus kristallinem Silizium bestehen. Die Herstellung von Silizium-Solarzellen ist jedoch technisch aufwending und kostspielig. Deshalb haben sich Solarzellen auf Basis von Bleihalogenid-Perowskiten (engl. *perovskite solar cells*, PSCs) seit 2009 als mögliche Alternative zur Siliziumtechnologie entwickelt. Bisweilen konnten Wirkungsgrade (engl. *power conversion efficiency*, PCE) von 26% in einem einzelnen Halbleiterübergang und von 33.7% in einem Tandemübergang erzielt werden. Diese Werte sind jedoch steigerbar und werden regelmäßig übertroffen. Die größte Herausfoderung für die Entwicklung dieser Technologie ist die Stabilität der Solarzellen unter Betriebsbedingungen. Der anorganische Perowskit $CsPbI_3$ ist aufgrund seiner Stabilität bei hohen Temperaturen deshalb besonders interessant für die Forschung, obwohl das Material seine eigenen Herausforderungen birgt, wie zum Beispiel seine Phaseninstabilität, größere Leerlaufspannungsverluste im Vergleich zu seinen organisch-anorganisch-hybriden Analoga und Fehlaurichtung der Energiebänder an der Grenzfläche. Die Stabilität der effizientesten Solarzelle auf $CsPbI_3$-Basis liegt bei einigen hundert Stunden, während die stabilste Solarzelle einen Wirkungsgrad von nunmehr 17% erzielt. Dies deutet auf die Notwendigkeit hin, die Grenzflächen zu den angrenzenden ladungsselektiven Kontakten zu verbessern – mit dem Ziel, die Leerlaufspannung (engl. *open-circuit voltage*, V_{OC}) zu erhöhen und die Ausrichtung der Energiebänder an den Grenzflächen zu optimieren. Diese Dissertation befasst sich mit der Untersuchung der Grenzflächen zwischen der Perowskitschicht und der Lochtransportschicht (engl. *hole transport layer*, HTL) für stabile $CsPbI_3$-Solarzellen.

Im ersten Teil der Arbeit werden die Temperbedingungen für $CsPbI_3$-Dünnfilme und ihre Auswirkungen auf die Ladungsträgerdynamik an der Perowskit/HTL-Grenzfläche untersucht. Dünnfilme, die in trockener Atmosphäre getempert wurden, wurden mit Dünnfilmen verglichen, die in Standardatmosphäre getempert wurden. Synchrotrongestützte Messungen der Photoelektronenspektroskopie mit harter Röntgenstrahlung (engl. *hard X-ray*

photoelectron spectrpscopy, HAXPES) zeigen, dass das Tempern in Umgebungsluft keine nachteiligen Auswirkungen hat; stattdessen erfahren jene Proben eine Verbiegung der Energiebänder an der Oberfläche. Diese Modifikation der Oberflächenbänder führt zu Veränderungen in der Grenzflächenladungsdynamik und in der Folge zu einer Verbesserung der Ladungsträgerextraktion über die Grenzfläche. Darüber hinaus zeigen Simulationen der transienten Oberflächenphotospannung (engl. *transient surface photovoltage*, trSPV), dass luftgetemperte Proben im Vergleich zu trockengetemperten Proben weniger Fallenzustände aufweisen. Letztlich wurde durch das Tempern der $CsPbI_3$-Filme in Umgebungsluft eine PCE von 19,8% und ein V_{OC} von 1,23 V für eine Solarzelle in n-*i*-p-Architektur erreicht.

Die Manipulation der Grenzflächen ist eine Strategie, um die Extraktion von Ladungsträgern und die Ausrichtung der Energiebänder in PSCs zu kontrollieren. Eine Grenzfläche mit geringerer Dichte an Fallenzuständen sowie der Fähigkeit, das Energiebandniveau näher an das des selektiven Kontakts zu verschieben, trägt zur Verbesserung des Wirkungsgrads von PSCs bei. Im zweiten Teil der Arbeit wird ein Design für die $CsPbI_3$/HTM-Grenzfläche vorgeschlagen. Dabei wird das Dipolmolekül Trioctylphosphinoxid (TOPO) an der Grenzfläche zwischen $CsPbI_3$-Perowskit und dem lochselektiven Kontakt N^2, N^2, $N^{2'}$, $N^{2'}$, N^7, N^7, $N^{7'}$, $N^{7'}$-octakis(4-Methoxyphenyl) -9,9′-Spirobi[9H-Fluoren] -2,2′,7,7′-Tetramin (spiro-OMeTAD) eingeführt. Auf einem mit n-Octylammoniumiodid (OAI) passivierten Perowskitfilm erzeugt TOPO eine nach oben gerichtete Oberflächenbandverkrümmung, die die Ausrichtung der Energieniveaus optimiert und die Extraktion von Löchern aus $CsPbI_3$ in den HTL verbessert. Infolgedessen wurden in den hergestellten Solarzellen ein V_{OC} von 1,2 V und eine PCE von über 19% erzielt. Darüber hinaus nimmt die Arbeit auch die Ladungsträgerselektivität an der Grenzfläche und die Langzeitstabilität von $CsPbI_3$-Perowskit-Solarzellen in den Fokus.

Der dritte Teil der Arbeit erweitert die bisherigen Untersuchungen auf das Polymer Poly-(3-hexylthiophen-2,5-diyl) (P3HT) als HTL. Die $CsPbI_3$/P3HT-Grenzfläche ist aufgrund der hohen nicht-radiativen Rekombination kritisch. In dieser Arbeit wird eine $CsPbI_3$/P3HT-Grenzfläche vorgestellt, die mit einem langkettigen Alkylhalogenidmolekül, n-Hexyltrimethylammoniumbromid (HTAB), modifiziert wurde. Dieses Molekül passiviert die $CsPbI_3$-Perowskit-Oberfläche weitgehend und verbessert die Ladungsträgerextraktion an der Grenzfläche. Für $CsPbI_3$ mit P3HT als HTM konnte ein V_{OC} von über 1,00 V und 14,2% PCE erreicht werden.

Insgesamt werden in dieser Dissertation Methoden zur Entwicklung und Untersuchung von Grenzflächen für Solarzellen auf $CsPbI_3$-Basis vorgestellt und diskutiert. Diese Studie kann Wege für neuartiges Grenzflächendesign zwischen $CsPbI_3$ und HTM im Hinblick auf Ladungsträgerextraktion, Effizienz und Stabilität eröffnen.

List of Abbreviations

B. E	Binding Energy
CBM	Conduction band minimum
CPD	Contact Potential difference
EA	Electron Affinity
EDC	(photo)electron distribution curve
E_f	Fermi Level
EQE	External Quantum Efficiency
ETM	Electron transport material
E_{vac}	Vacuum Level
FA	Formamidinium
FF	Fill Factor
FTO	Fluorine-doped tin oxide
HAXPES	Hard X-ray photoelectron spectroscopy
HOMO	Highest occupied molecular orbitals
HTAB	*n*-hexyl trimethylammonium bromide
HTM	Hole transport material
IE	Ionization Energy
IMFP	Inelastic mean free path
IPES	inverse photoemission spectroscopy
J_{sc}	Short Circuit Current
JV	Current density-voltage
K_{eETM}	Electron extraction rate constant
K_h	Hole extraction rate constant
KP	Kelvin probe
LUMO	Lowest occupied molecular orbitals
MA	Methylammonium
MPPT	Maximum Power Point Trackings
OAI	*n*- octyl ammonium iodide
P3HT	poly(3-hexylthiophene)
PES	X-ray photoemission spectroscopy
St-PL	Steady State Photoluminescence
PLQY	Photoluminescence quantum yield
PSC	Perovskite Solar cell
PV	Photovoltaic
QFLS	Quasi-fermi level splitting
RH	Relative humidity
SEM	Scanning Electron Microscope
Sipro-OMeTAD	2,2',7,7'-Tetrakis[N,N-di(4 methoxyphenyl)amino]-9,9'-spirobifluorene
SRH	Shockley-Read-Hall
TOPO	Trioctylphosphine oxide
TRPL	Time-resolved photoluminescence
Tr-SPV	Transient surface photovoltage
UPS	Ultraviolet photoelectron
UV-Vis	Ultraviolet and visible absorption spectroscopy
VB	Valence band
VBM	Valence band maximum
V_{OC}	Open Circuit Voltage
WF	Work function
XPS	X-ray photoelectron spectroscopy
XRD	X-Ray Diffraction

Chapter 1

Introduction and Fundamentals

1.1 Climate change - a Collective Challenge.

Last year, a devastating flood struck Pakistan. A third of the country was under water, with 15% population being affected directly by the flood and an estimated 15-billion-dollar economic loss. However, according to the European Union data index, Pakistan is responsible for less than 1% of the world's warming gases, yet it is the eighth most vulnerable nation in the world. [(1)] This incident is just an example, but many disastrous events have happened recently, affecting oceans, glaciers, and the atmosphere. Climate change is not confined but a collective challenge of humankind and the earth's natural habitat. Other than humans, all living species are susceptible to this problem. Climate change is such a severe issue that the 17 sustainable goals set by the United Nations are directly or indirectly linked to climate change. [(2)]

Recent studies show that human activities pollute the air, oceans, and lands. It also caused to rise in the temperature of the earth's surface. The human-caused global surface temperature increases from 1850-1900 to 2010-2019 is 0.8°C to 1.3°C. [(3)] This increase is likely due to greenhouse gases, including the infrared (IR) radiation-absorbing molecules CH_4, N_2O, CO_2, and water vapours. [(4).] Today, over 80% of energy is produced by greenhouse gas-producing fossil fuels, melting the planet. It is like discharging a non-rechargeable battery. The only way forward is to use renewable energy sources and make carbon-free energy production in the coming years. Renewable energies include hydro, wind, biomass, and photovoltaics.

The energy needed for a supportable life on earth is around 21TW. Above all mentioned renewable energy sources, only solar energy can augment the clean supply in the future. In recent times photovoltaics (PV) has emerged as a competing candidate for electricity production [(5)] and now, it exceeds by 1TeraWatt the global installed capacity. [(6)] **Figure 1.1** illustrates the installed global renewable energy technologies. The report was published by Nancy. M. Heaegal *et al.* suggest increasing the PV installation growth by 25% annually to meet the target of 75TW by 2050. [(6)]

However, the mainly used PV technology is based on the crystalline-based solar cell. It has better efficiency and long-term stability, but the laborious fabrication and high cost are the

main hurdles to increasing production. Contrarily, modern technologies are based on thin films, which are comparatively low-cost and easy to synthesize.

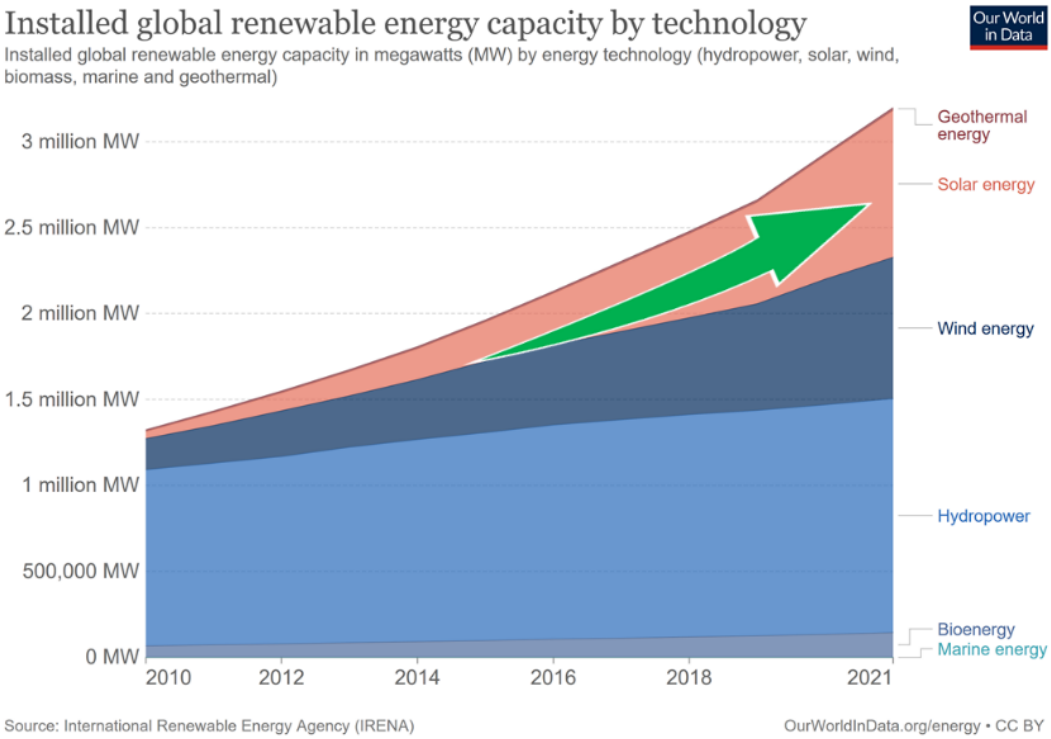

Figure1.1 Installed global renewable energy capacity by technology. Source [5]

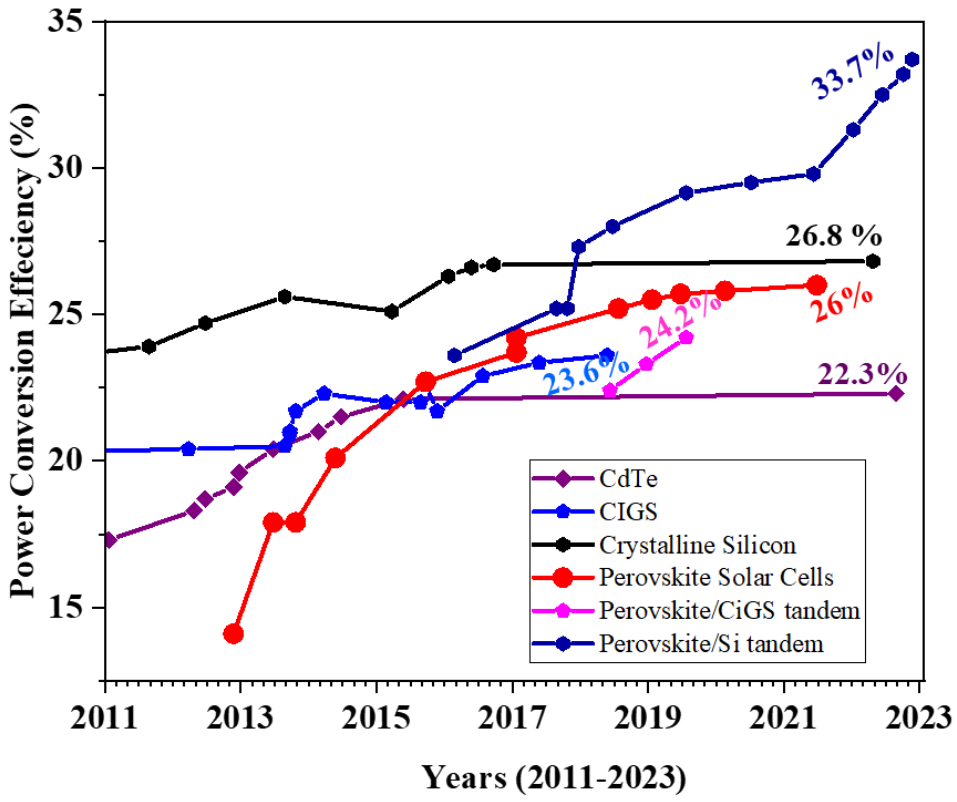

Figure 1.2 Best solar cell efficiencies reported over twenty years (2003-2023). The data was collected by the NREL webpage. [7]

Figure 1.2 shows the state-of-the-art PV technologies with their efficiency compared with crystalline silicon-based solar cells over the past ten years of research. The data shows that, among the modern technologies, halide perovskite solar cells (PSC) have emerged as a new candidate in the optoelectrical industry, surpassing the record power conversion efficiency (PCE) set by contemporary photovoltaic technologies with excellent power conversion efficiencies of 26 % for single-junction and 33.7 % for tandem solar cell designs as shown in **Figure 1.2**. It also indicates that other technologies have achieved a plateau, and there has yet to be much progress over one decade. However, perovskite solar cells have shown an exponential increase in efficiency since 2013.

1.2 Perovskite Solar Cells

Perovskites halide (HaP) are a class of materials having a composition of ABX_3, where A is a monovalent cation, B is a divalent metal and X is a monovalent halide. The right choice of A, B, and X is important for the material's structure and follows the Goldschmidt tolerance factor. [8] A is often methylammonium (MA^+), formamidinium (FA^+) or Cs^+, B is mainly Pb^{2+} or Sn^{2+}, and X is a halide, I^-, Br^-, or Cl^-. The electronic profile of the perovskite halide is determined by the choice of ions forming the ABX_3 structure. These materials have unique opto-physical properties, *e.g.*, tunable band gap [9-11], long charge carrier diffusion length [12,13], high tolerance of defects [14,15], and high absorption coefficient [16,17].

Perovskite solar cell (PSC) device structure has three architect designs in which the absorber layer (perovskite film) is sandwiched between *n*-type and *p*-type materials and it makes *n*-*i*-*p* and *p*-*i*-*n* (inverted) configurations. In contrast, *n*-*i*-*p* can be mesoporous or planar. These *n*-type and *p*-type materials are employed as charge extraction layers or selective contact (*These layers' details are added in the solar cell working principle section 1.4*). **Figure 1.3** shows the structures of perovskite solar cell devices. In PSC devices, *n*-*i*-*p* configurations have shown better performances than inverted designs. [18,19] However, the inverted design is easy to fabricate and these find applications in tandem applications [20,21].

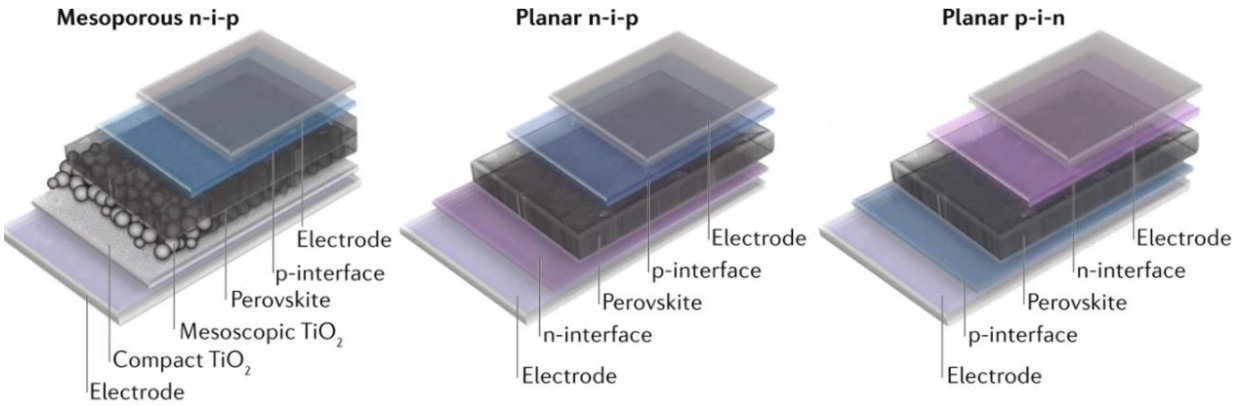

Fig.1.3 Perovskite solar cell configurations: Illustration of an *n- i-p* perovskite solar cell (PSC) with a mesoscopic layer, of a regular *n-i-p* planar heterojunction PSC and of a *p-i-n* planar heterojunction PSC (also known as inverted planar PSC). Reproduced with permission. By Deying Luo *et al*., *Nature Reviews Materials*, 2020, 5(1), 44-60. [(22)] Copyright © 2020 Springer Nature.

The device's performance depends on the perovskite properties and the charge extraction layers. A variety of hole transport layers and electron transport layers have been employed. The band gap and the electronic properties of these materials play a significant role in the device's operation. **Figure 1.4** shows the generally used perovskite compositions, hole and electron transport layers, and the best efficiencies reported until now. Generally, the perovskites are classified as broad, narrow, and mid-band gaps.

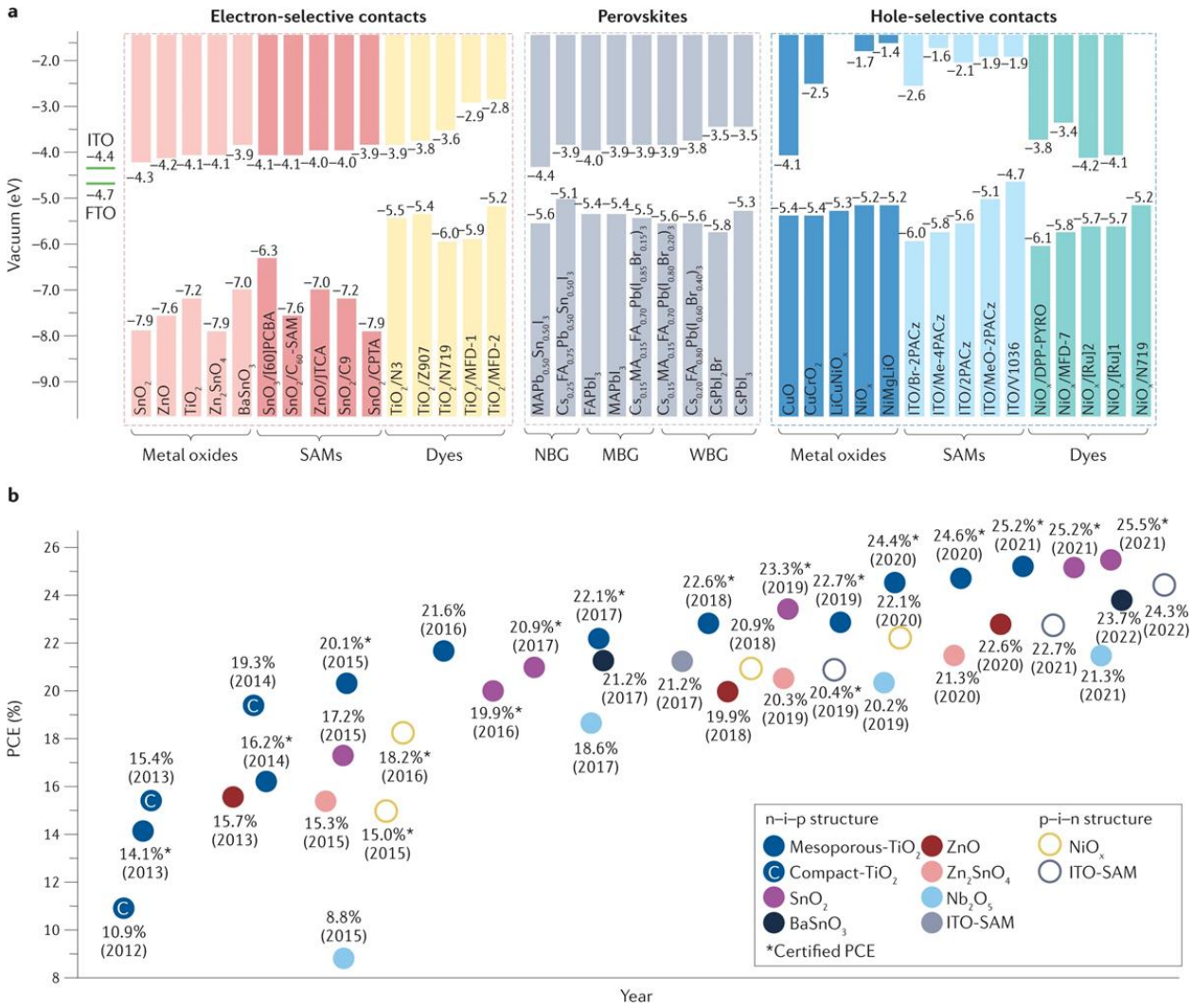

Figure1.4. Properties and performance of various metal-oxide charge transport layers. a) Band alignment of electron-selective and hole-selective metal oxides, self-assembled monolayers (SAMs), and dye contacts concerning commonly used metal-halide perovskite absorbers. b) Main advancements in perovskite solar cells' power conversion efficiency (PCE) using various metal-oxide electron-selective and hole-selective contacts. FTO, fluorine-doped tin oxide; ITO, indium tin oxide; MBG, mid-bandgap; NBG, narrow bandgap; WBG, wide bandgap. Reproduced with permission. By F.H. Isikgor *et al. Nature Reviews Materials*,2023,**8**(2),89-108. [(23)] Copyright © 2023 Springer Nature.

1.3 $CsPbI_3$: An introduction, Challenges, Progress, and Prospects

$CsPbI_3$, an inorganic halide perovskite, is a promising candidate for light absorbers in solar cells. [24] It has an excellent optical property with a suitable band gap (~1.70eV). [25] It shows outstanding thermal and chemical stability [25,26] as compared to other members of perovskite halide materials (e.g., $MAPbI_3$, $FAPbI_3$, $FASnI_3$, etc.) as these are susceptible to degradation under the extreme environmental condition of humidity, heat, and light soaking [27-29]. Due to its ideal band gap, it has the potential for perovskite/Si tandem solar cell applications. [30] To date, the most efficient device for $CsPbI_3$-based solar cells reported over 21% efficiency, which is 75% of the SQ-limit [31], while the SQ-limit for $CsPbI_3$-based solar cells is ~29%. Historically, $CsPbI_3$ was used as a photoconductive material for the first time back in 1958, and with the advancement of perovskite halides solar cells in 2019 [32], it was believed as a valuable material for photovoltaic applications (PV) in 2015. [33-36]

$CsPbI_3$ has four geometric phases in its perovskite structure. These polymorphs include cubic (α-phase), tetragonal(β-phase) and orthorhombic (γ-phase and δ-phase). [37,38] The first challenge is the phase stability of the desirable absorbing phases at the operational temperature.

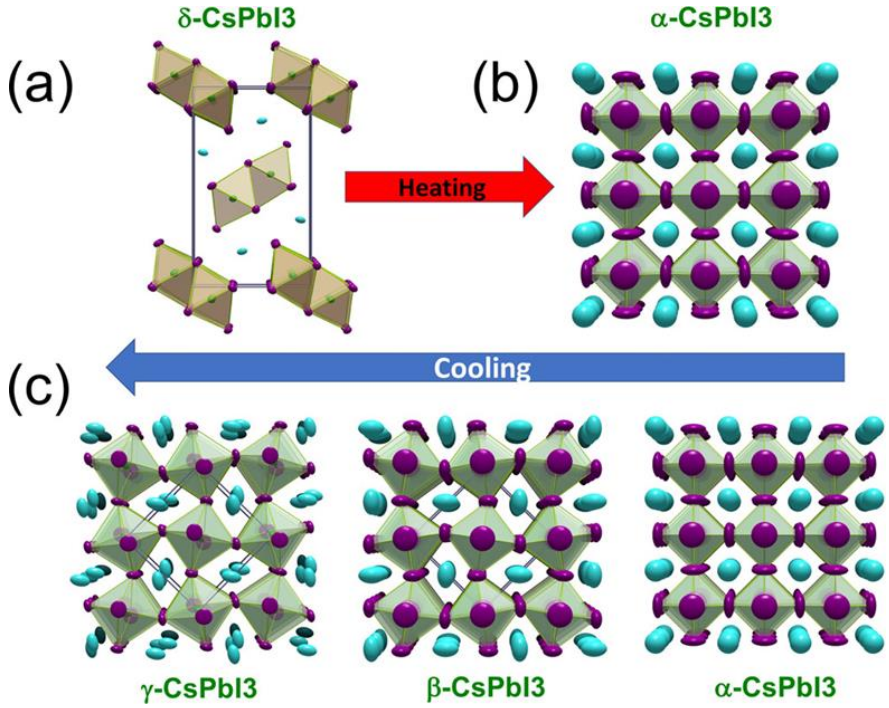

Figure 1.5. **Structural phase transitions in $CsPbI_3$ *versus* temperature.** a) The initial yellow perovskite phase (δ-$CsPbI_3$, NH_4CdCl_3-type) converts to b) black perovskite phase (α-$CsPbI_3$, $CaTiO_3$-type) as the temperature exceeds the transition temperature. c) Upon cooling, the black perovskite phase is retained. It can be undercooled below the transition temperature, where the typical perovskite distortions (tetragonal β-$CsPbI_3$, orthorhombic γ-$CsPbI_3$) can be observed to

room temperature. These metastable phases transform to the thermodynamic δ- CsPbI3 upon standing. It is reproduced with permission. By Arthur Marronnier *et al*. [39], ACS Nano 2018, 12, 3477−3486. Copyright © 2018 American Chemical Society.

Figure 1.5 shows the phase variation with temperature. It shows that *α*, *β* and *γ*-phase exist are higher temperature ranges while the non-perovskite δ-phase exists around the room temperature ranges. Among all phases, *α*-$CsPbI_3$ has the most suitable band gap (~1.68eV), while *δ*-phase is unwanted (~2.8eV) for PV applications. One adapted approach to this challenge is changing the Gibbs's free energy (ΔG) landscape for the $CsPbI_3$ perovskite. [40] The methods used to stabilise are based on alloying [41-43] and grain size control [40,44], as shown in **Figure1.6**

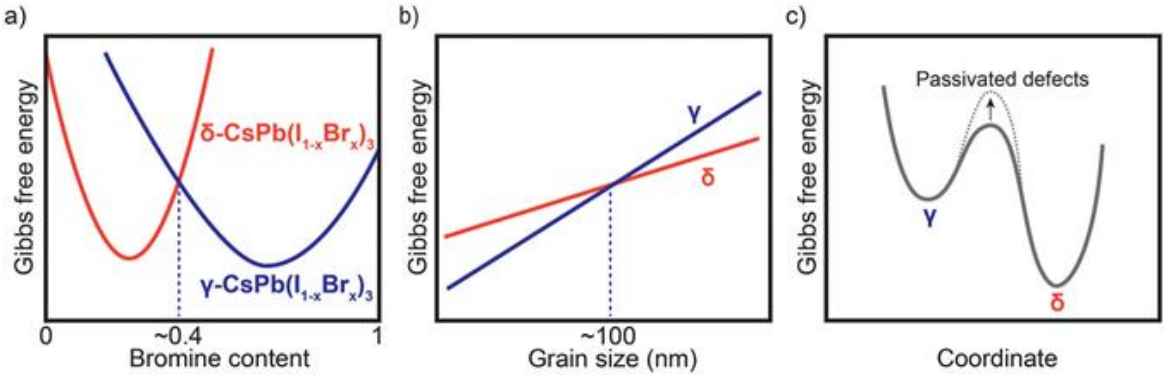

Figure 1.6. **Approaches for achieving stability at working conditions** a) Simplified representation of Gibbs free energy vs bromine content of *γ*- and *δ*-$CsPb(I_{1-x}Br_x)_3$. Free energy curves may include additional local minima, resulting in spontaneous phase segregation. b) Scheme of Gibbs free energy as a function of grain size for *γ*- and *δ*-CsPbI3. c) Scheme illustrating an increase in the energy barrier for *γ*- to *δ*-phase transition due to defect passivation. Reproduced with permission. By Alan B. Kaplan *et al*., [45] APL Energy. 2023,**1**(1). Copyright © 2023, AIP Publishing.

However, these approaches have their limitations as they tend to change the material's intrinsic properties. For example, by alloying bromine contents, the band gap of the materials is raised to 2eV, by which the absorption pattern of light significantly changes and consequently, the upper limit (SQ-limit) also decreases compared to pure $CsPbI_3$. Similarly, grain size reduction also compromises the performance of the device.

The other approach to stabilise the photoactive phase at the operating temperature is to play with the kinetic pathway that leads the black phase (*α*-$CsPbI_3$) to the yellow phase (*δ*-$CsPbI_3$) [46], as shown in **Figure 1.6c**. This method is very appealing in decreasing the density of states in $CsPbI_3$.In this method, the crystallisation process is managed by some additives, and then

the film is treated with some molecules (passivation). Here are a few representative examples from recent literature.

1. Jingbi You *et al.* used a solvent growth approach to stabilise α-$CsPbI_3$ films. In this method, the wet film stands in the solvent for a few minutes, which helps crystal growth. They have reported 15% PCE with 500 hours of stability. [47]
2. Yixin Zhao *et al.* used organic additives to manipulate the crystallization process; they used DMAI as an additive to make pinhole-free films and further by surface treatment with choline Iodide (CHI) and phenyltrimethylammonium chloride (PTACl), they achieved 18.4% and 19.03% PCE respectively. [48,49]
3. Controlling the intermediate phases for the crystal growth proved to be another effective technique. Soek *et al.* used MACl dripping to control the intermediate phase. It achieved 20.37% efficiency by passivating the film with *n*-OAI. [50] Qingbo Meng *et al.* have used molten salts to control crystal growth and have reported over 21% PCE. [31]

Another challenge is that the open-circuit voltage deficit is far more significant than hybrid organic-inorganic halide perovskite solar cells. [51] The origin of this higher deficit is due to interfacial mismatching (energy alignment). (*The efforts to improve the energy alignment at the interfaces have been described in the energy alignment* ***section 1.9***)

The device stability of $CsPbI_3$-based solar cells needs specific improvements. The most efficient device, with a record efficiency of over 21%, is only stable for up to 500 hours at room temperature. In contrast, the most durable device, which holds a record stability of t_{80} lifetime of around 51k hours, has 17% efficiency. [52]

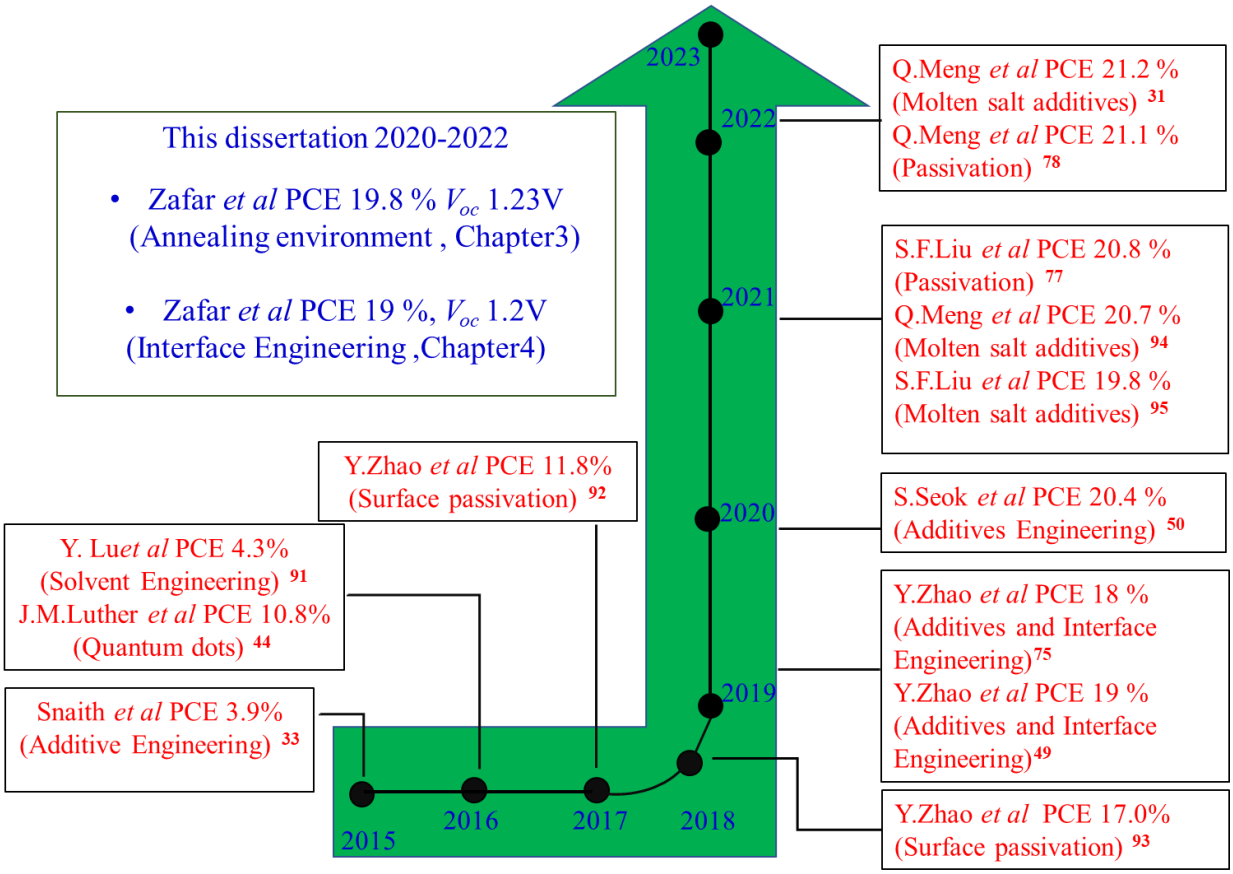

Figure 1.7. Efficiency evolution of $CsPbI_3$ (2015-2023), strategies, methods, and progress. (some paradigmatic work)

Inorganic halide solar cells have shown tremendous progress since 2015 when the first work on $CsPbI_3$ was published. **Figure 1.7** summarizes some of the representative work, strategies, and methods adopted to increase efficiency. In the future, it is anticipated that $CsPbI_3$ will play an essential role in PV technology advancement. There are a few points enlisted as a prospect for $CsPbI_3$.

- Most of the work on $CsPbI_3$ has been based on the *n-i-p* structure of the device. It has Spiro-OMETAD as hole transport material (HTM) which has its limitations. It is susceptible to high temperatures, compromising its stability at high temperatures. There is a need to look for new hole transport materials for $CsPbI_3$ devices for stability at high temperatures.
- Bromine incorporation can widen the band gap. However, it can be used in perovskite/Si tandem solar cells.
- Due to higher thermal and chemical stability, it can be considered a candidate for accelerating ageing testing and applications. Besides, it has the capability of recycling and restoration of the initial PCE after re-annealing. [53]

- CuSCN hole transport material has been used in the most stable device. There is a need to modify the interfaces for CuSCN to improve efficiency. This combination can be an excellent baseline and a game-changer for PV.
- There is still room to improve the crystallisation process to increase the film's thickness and quality.

1.4 Working Principle of Perovskite Solar Cell

The working principle of perovskite solar cells is illustrated schematically in **Figure 1.8**. It involves four steps absorption, diffusion, extraction, and collection of charges. In the solar cell, light is absorbed by the perovskite layer, and the absorbed photons generate the excitons. Then the produced excitons are dissociated into the electrons and the holes at the operational conditions. These electrons and holes are known are charge carriers due to their point charges. The Fermi levels of electrons and holes are represented by E_{fn} and $E_{fp,}$ respectively. The quantitative difference between these two levels is given quasi-Fermi level splitting (QFLS) and describes the total available free energy that can be transformed into work done. To extract this potential, each level must connect energetically with the charge-extracting layers, while these layers extract the charges due to energy offset. The more energy alignment, the more charge extraction will be on the electrodes. These materials make interfaces with the perovskite layer. These are the perovskite/electron transport layer (ETL) interface and the perovskite/hole transport layer (HTL). The charge carriers move towards ETL and HTL due to the electric field and their concentration gradient at the interface, and the selective contacts extract the charges. Finally, the charges are collected on the respective electrodes, generating the current. [54,55]

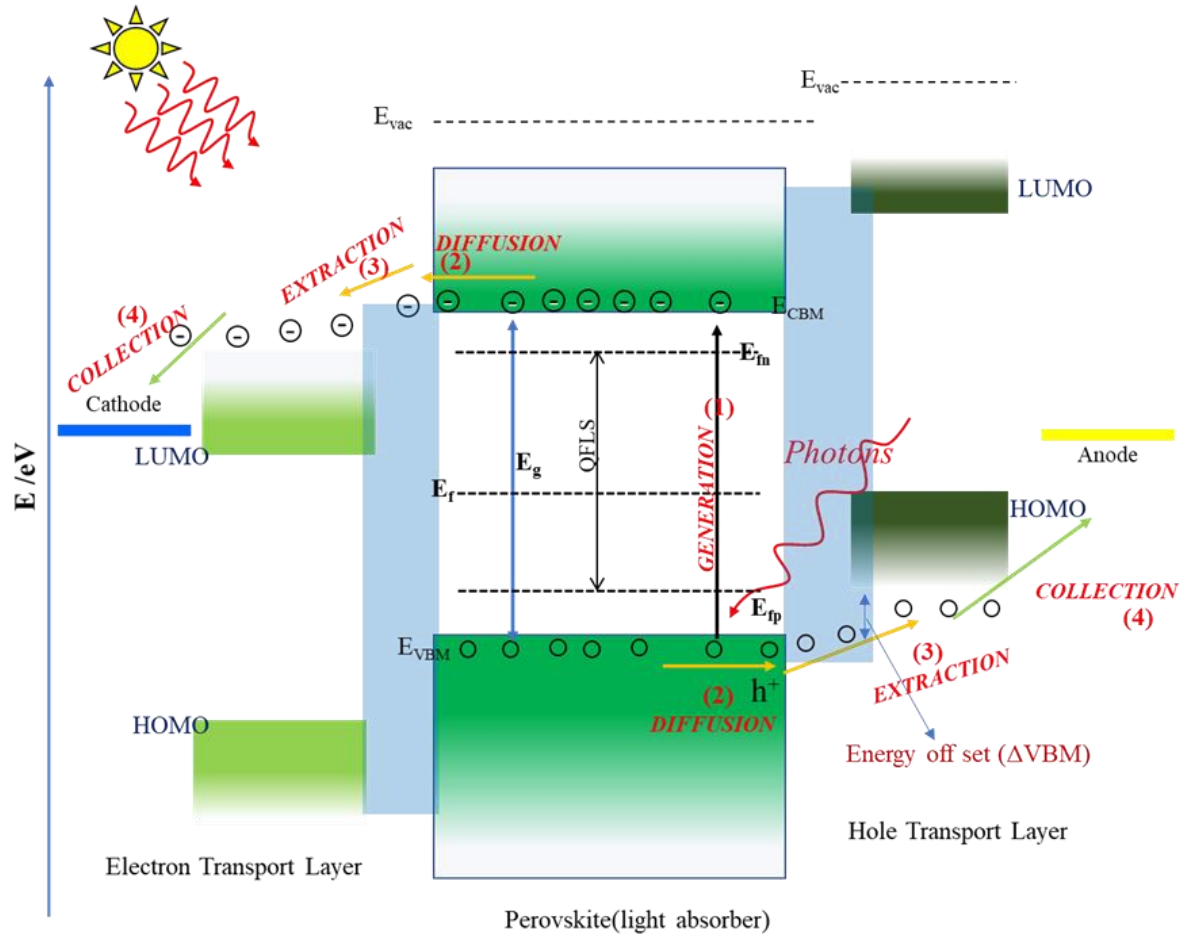

Figure 1.8. Description of working of the solar cell. The different coloured arrows show the various physical processes during the operation.

The working principle suggests that each falling photon will generate a pair of holes and electrons and then external quantum efficiency (EQE) will be 100% (*as discussed in **Method section 2.9***). However, the EQE and, ultimately, the efficiency is limited by the non-radiative recombination happening in the bulk of the materials and the interfaces. **Figure 1.9** shows the non-radiative pathway for the charge carriers to reach the selective contact and the electrodes. These are categorised mainly into four types. Type I and II are bulk recombinations in the perovskite layer due to defects. It can be decreased by defect passivation, controlling the crystallisation process and passivation. Type III and type IV recombination arise in the interfaces due to trap states at the charge extraction layer or the misalignment of energy level at the interface. The better choice of selective contacts and interface engineering and the formation of graded *pn*-junction are the possible solutions to minimise the non-recombination at the interfaces. [22,56-58]

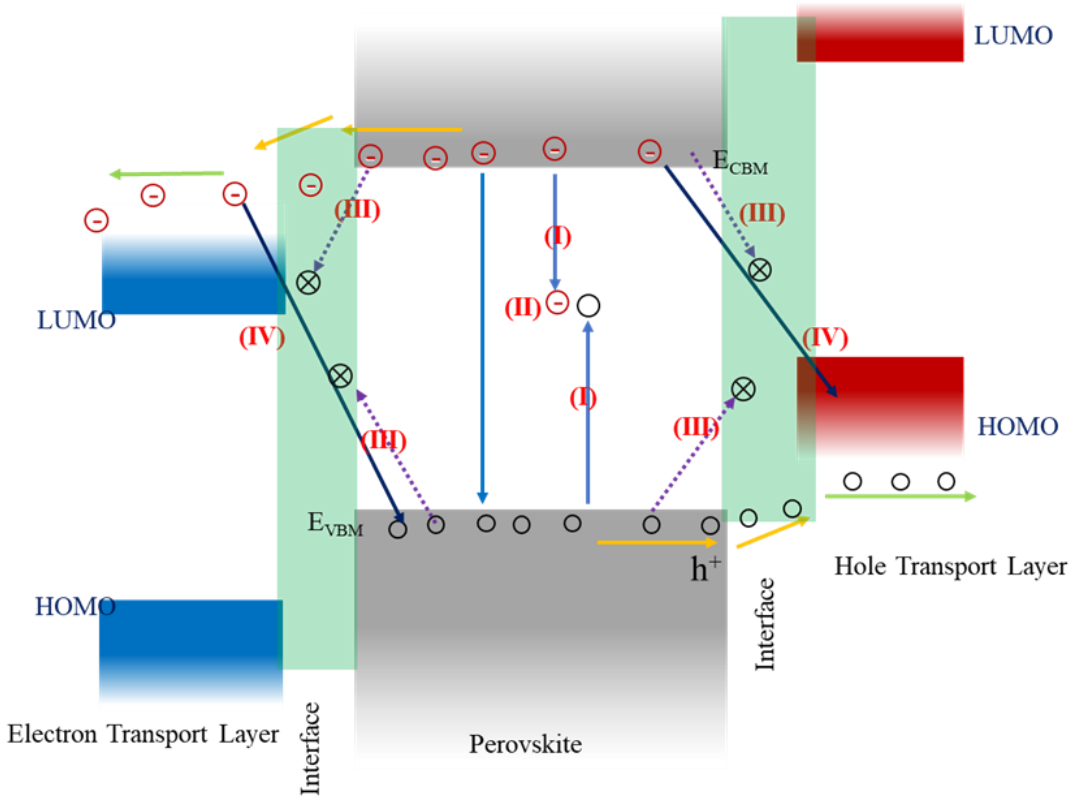

Figure 1.9: Diagram to illustrate the bulk and interface-induced recombination in perovskite solar cell (PSC).

1.5 Relevant Interface Energetics

Figure 1.10 illustrates the band formation in a material. The valence electrons of the atoms combined to make the hybridized orbitals. These hybridized orbitals (sp^3, sp^3d, sp^3d^2, *etc*.) overlap with the hybridized orbitals of the other atom. The overlapping gives rise to bonding and antibonding orbitals due to different orientations and energy. These anti-banding and bonding orbitals create an energy band with the electrons' occupied and unoccupied allowed energy states. These two levels are classified as the highest occupied molecular orbitals (HOMO) and the lowest unoccupied molecular orbitals (LUMO). The HOMO levels correspond to the valence band (VB), the highest band occupied by the electrons and their energy position is VBM. In contrast, the LUMO levels correspond to the conduction band, the lowest empty band with allowed energy levels, and its energy position is CBM.

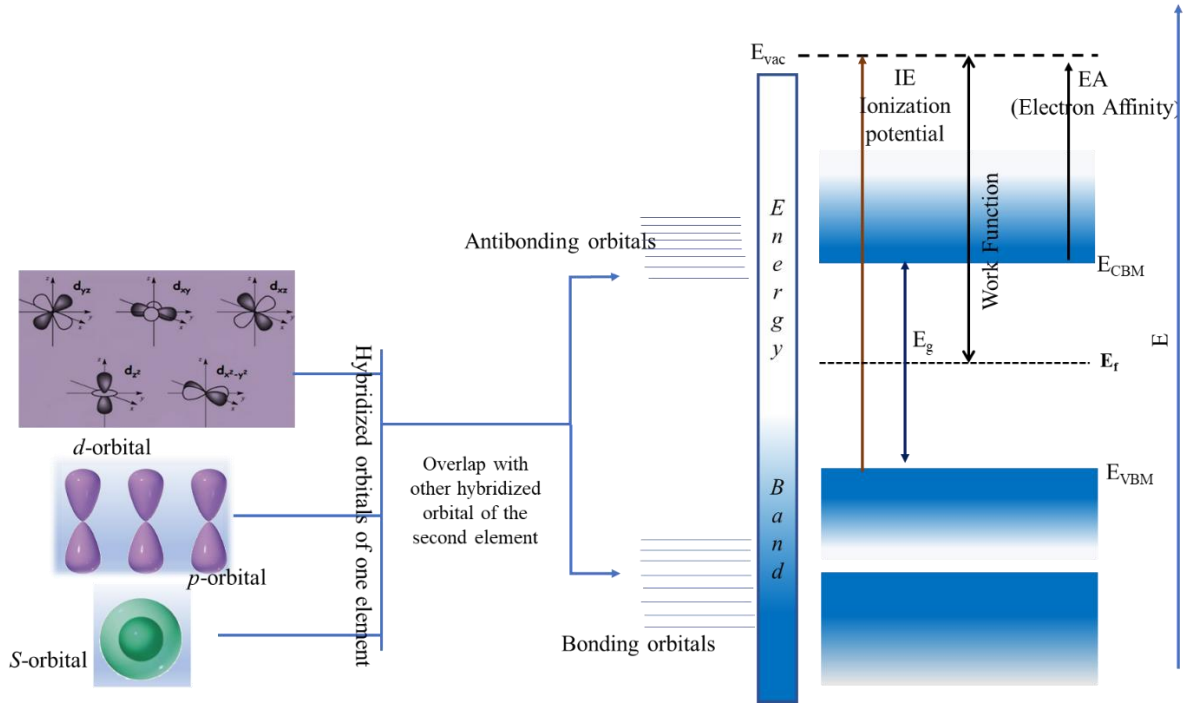

Figure1.10. Schematic illustration of the band formation and relevant energetic quantities. The figure is drawn by the author by developing the understanding of the topic by reading the book "Chemical Structure and Reactivity" by James Keeler.

The energy difference between VBM and CBM is known as the band gap (E_g). It can be defined as the energy required by an electron in VBM to reach CBM. Generally, the energy values are in electron volts ($1eV=1.6\times10^{-19}J$). The metals have no band gap and their CBM and VBM are closer together, while insulators have a considerable band gap, *i.e.*, >5eV. The semiconductor materials have a band gap of 0.5-4eV. It is an important optical property and it can be a direct band gap or an indirect band gap, depending on the momentum of VBM and CBM. Silicon has a 1.1 eV (indirect), while perovskite halides have a direct band gap ranging from 1.5-2.5eV.

Fermi level is a hypothetical energy level at which the probability of finding an electron is 50%. It is positioned within the band gap. The position of the Fermi level helps to differentiate between *n*-type and *p*-type semiconductors. In *n*-type semiconductors, the Fermi level is set close to the VBM, while in *p*-type semiconductors, it is closer to the CBM levels.

E_{vac} is the energy an electron requires to move outside the bulk of the material. It is an essential parameter in interface properties and the energy landscape changes it at the surface.

Work function is the energy difference between E_{vac} and the Fermi-level. The value of the work function helps to envisage the charge carrier transfer way and the energy level alignment. (*The*

detail of the work function is discussed in Chapter 2 of the Method chapter with PES techniques in ***Section 2.8***).

Ionization energy (IE) and electron affinity (EA) are crucial semiconductor material properties. IE is the energy required for an electron to move from VBM to the vacuum level under equilibrium conditions. At the same time, EA is the energy released by an electron moving from the vacuum level to the CBM level. The position of CBM and VBM can be accessed by IE and EA values.

1.6 Surface Band Bending

Surface band bending is the change in the surface energy states activated by a difference in the Fermi level of the two materials at the interface. The built-in potential on the interfaces induces this phenomenon. [59] Surface band bending is an essential feature of the semiconductor materials, and it tends to change the interface charge dynamins [60-62] and the surface charge recombination for the device operation. [63]

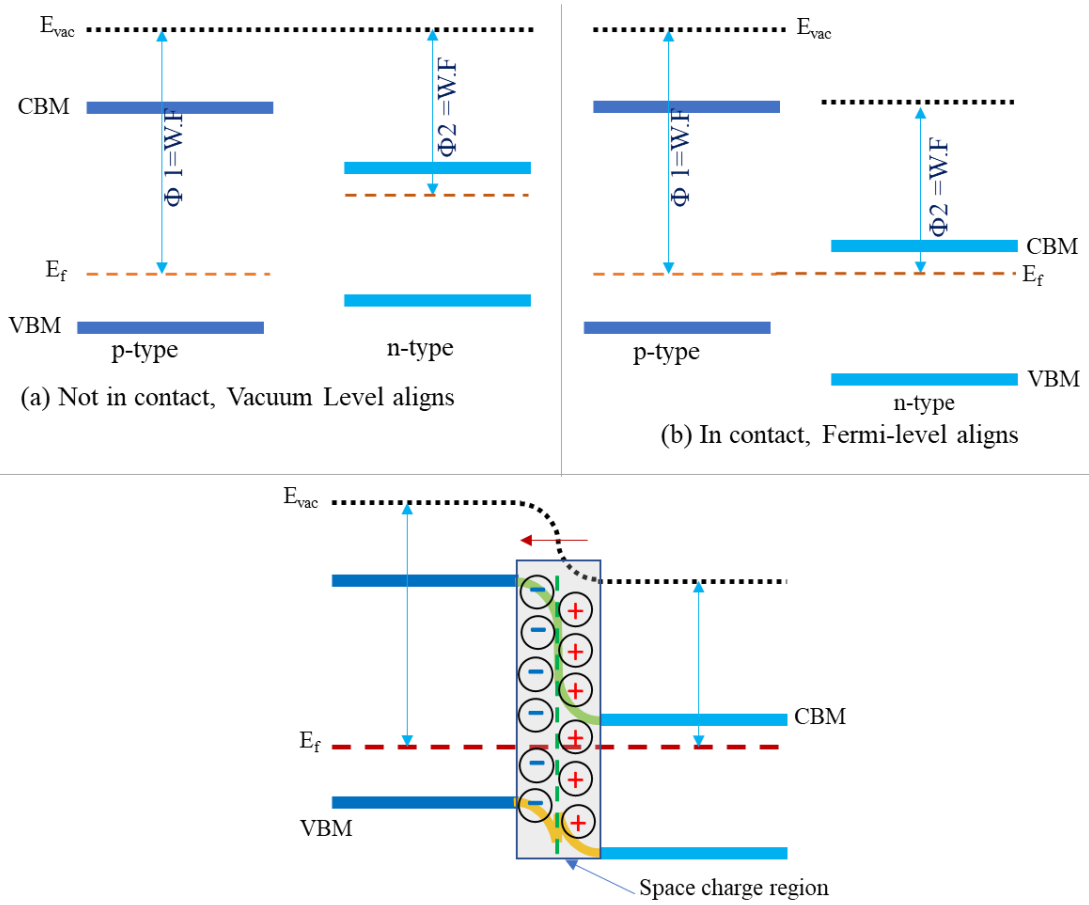

(a) Not in contact, Vacuum Level aligns

(b) In contact, Fermi-level aligns

(c) Band bending in space charge region

Figure 1.11. Surface Band bending demonstration with energy diagrams of a *p*-type and *n*-type semiconductor. E_{vac} is vacuum level energy, CBM is energy (position) of the conduction band minimum, and VBM corresponds to the energy of the valence band maximum level. At the same time, Φ1 and Φ2 are the work functions of *p*-type and *n*-type semiconductors, respectively. The figure is drawn by the author by developing an understanding of the topic.

Figure 1.11 illustrates the band-bending phenomena in *p*-type and *n*-type semiconductors. When the materials are not in contact, their vacuum levels are aligned, and their Fermi levels are positioned near VBM in *n*-type and to CBM in *p*-type material. When these materials are connected, their Fermi levels are aligned so that the energetics are preserved, and the band follows the change in vacuum level, as shown in **Figure 1.11 b**. Due to diffusion current flow at the interface, a Helmholtz layer is formed on the interface of two materials, and a space charge region is obtained. When the electron is depleted in this region, the Helmholtz layer is known as the depletion layer, and the energy levels bend upward. In contrast, when electrons accumulate in the Helmholtz layer region, it is known as the accumulation region and experiences downward band bending at the interface. [59,64,65]. The presence of an electric field in the space charge region is a driving force to create the surface band bending at the interface, as shown in **Fig1.11c**.

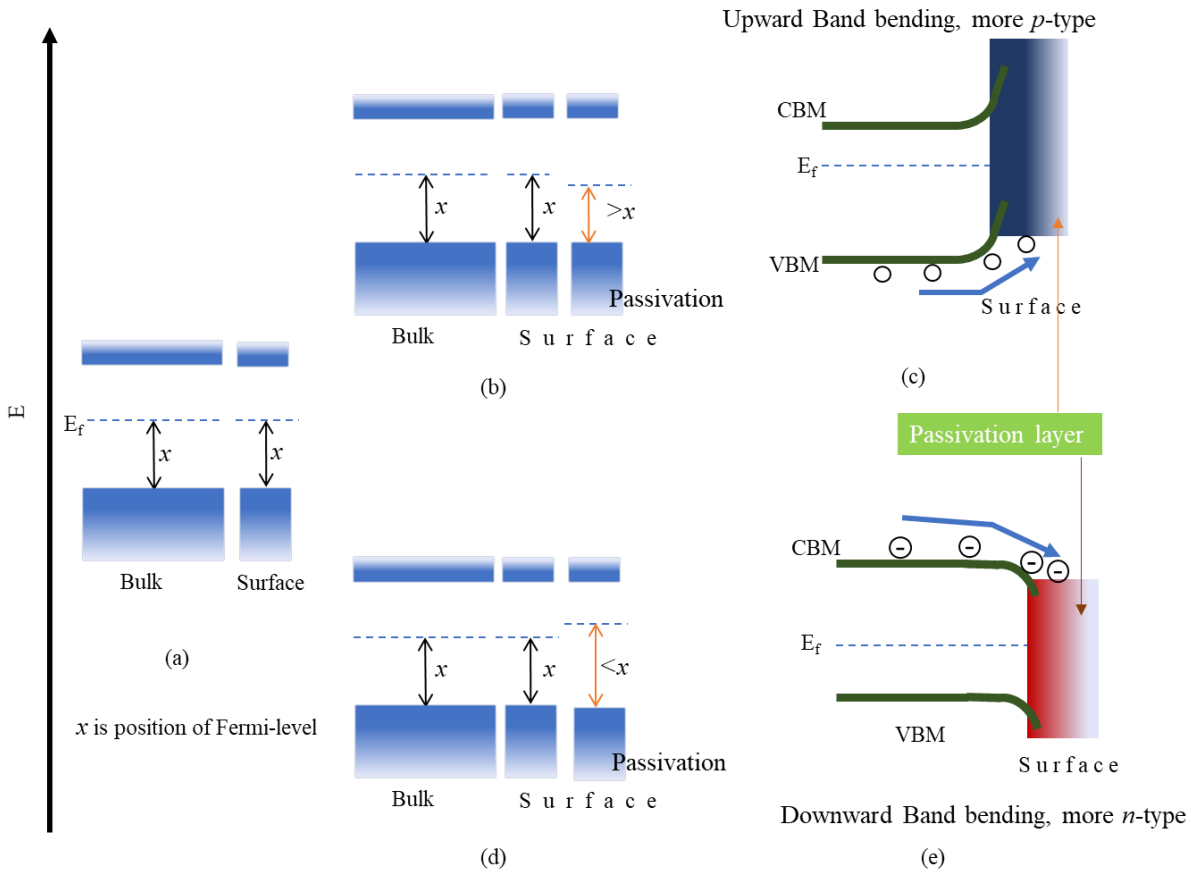

Figure 1.12 Surface band bending in perovskite halide materials induced by the passivating layer. The figure is drawn by the author by developing the understanding of the topic by reading the articles reference 66,67.

Figure 1.12 illustrates the surface band bending of the intrinsic perovskite halide material. **Figure 1.12** shows no surface band bending on the perovskite, *i.e.,* the bulk and the surface have the same energy levels. "*x*" represents the position of Fermi-level concerning valence band maxima. However, the Fermi-level position changes under the influence of the passivation layer, as shown in **Figures 1.12 b** and **d**. The passivation layer causes to bend the surface energy levels upward or downward. **Figure 1.12 c** describes the upward band bending, making the perovskite more *p*-type material. This surface band bending on the perovskite surface helps to create a cascade route for the hole movement and ultimately achieves better energy alignment. However, **Figure 1.12 e** shows downward band bending by the passivation layer, making it more n-type material.

Nazeer Ud Din *et al.* reported the surface band bending in triple cation perovskite. [(66)] They treated the perovskite film with an inorganic molecule perhydropoly(silazane). They found that the Fermi levels of the surface states are changed, and the valence band shows upward surface band bending. This surface band bending boosted the charge extraction on the hole transport layer, V_{OC}, the efficiency of the devices, and the stability of the perovskite solar cell.

S.Wang *et al.* introduced the strategy to make the *n*-type surface band bending for $CsPbI_3$ inverted devices. [(67)] In this work, they did the post-treatment on $CsPbI_3$ film with propylamine hydrochloride to induce an *n*-type transition which resulted in better charge extraction due to low energy offset at the interface and achieved 20.1% state-of-the-art efficiency for $CsPbI_3$ based solar cell and an improved V_{OC} of over 1.2V as compared to the control device.

Besides the passivation or surface treatment methods with suitable molecules, the annealing step can also cause surface band bending on the intrinsic and bare perovskite film. [(68)] L. S. Mende *et al.* annealed $MAPbI_3$ samples in three different conditions and reported that the annealing condition highly influenced the surface band bending, which caused the increase in V_{OC} for the perovskite solar cell.

Considering surface band bending as a promising technique to play around the interface of the perovskite material, the question arises of how to choose the molecules to shift the surface states upward or downward. To address this query, L. Canil *et al.*, [(69)] provided a tool kit to

select the molecules for the surface treatment to bend it accordingly. They have categorized the molecules into two classes.

I. These are Lewis bases with electron-donating properties. Upon treatment with the surface, they tend to induce upward band bending (*p*-type) by decreasing the work function (Φ), and they are known as “negative dipoles”.
II. These are Lewis acids with electron-withdrawing properties. Upon treatment with the surface of the semiconductor, they tend to induce downward band bending (more *n*-type) by increasing the work function (Φ), and they are known as “positive dipoles”.

The concept of electron withdrawing and electron donating functional group involves undergrad chemistry, which provides the required surface state bending information. However, the deposition methods needed to be developed for better interactions with the surface.

In the above discussion, it can be concluded that surface band bending induced by molecular treatment or annealing is a critical technique to decrease the energy offset between the absorber layer and the selective contact. It improves the interface's charge extraction, energy alignment, and charge separation at the interfaces. Consequently, there is an increase in open circuit voltage, the devices' efficiency, and the solar cells' stability. In this work, all these strategies (passivation, molecular treatment, and annealing environment) have been applied for surface band bending at the interface. That will be described in detail in the following chapters.

1.7 Energy Level Alignment

In PSC, the energy band alignment between the absorber material and the selective contacts is a determining factor for better efficiency. The non-ideal alignment between these components leads to poor performance in the solar cells. [70,71]

To understand how the perovskite absorber and organic layer interfaces are energetically aligned. Currently, Z. H Lu *et al.* presented a universal band alignment rule. [72] They have used bare perovskite samples and surface-modified perovskite samples with different organic molecules and ionization energies as selective contacts. **Figure 1.13** shows that the interface energy alignment follows the three energy regions; the region 1 is a flat region with no slope, and in this region, the lowest unoccupied molecular orbitals (LUMO) are pinned to the Fermi-level (E_f) of the perovskite (bare/passivated). In the second region, there is a vacuum alignment, and the perovskite work function mediates the band-off sets of both perovskite and the selective

organic contact. In the third region, the occupied molecular levels of the organic molecule are pinned to the Fermi-level (E_f) of the perovskite (bare/passivated).

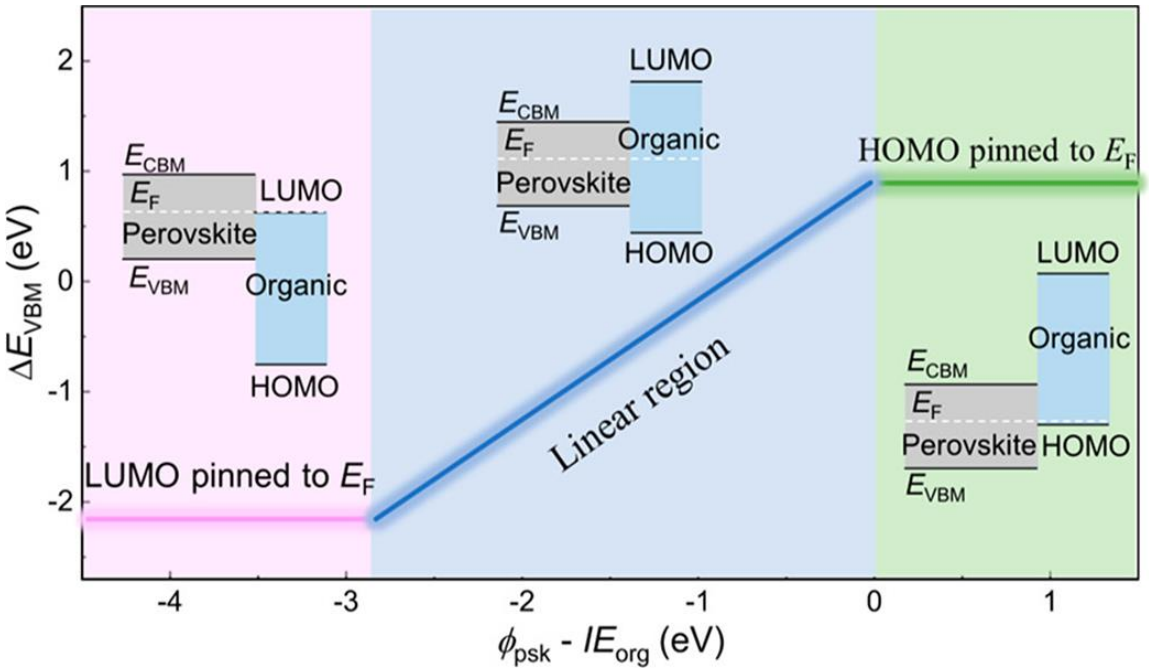

Figure 1.13 Band alignments at the interface of SP-perovskite and organics, where the SP-perovskite includes $CsFAPbI_3$ (E_g = 1.65 eV) and $CsFAPbIBr_3$ (E_g = 1.77 eV). The interface valence band offset (ΔE_{VBM}) is plotted against the difference between the work function (ϕ_{psk}) of the underlying perovskite and ionization energies (IE_{org}) of the organic molecules deposited on perovskite. The inset shows the respective energy-level diagrams in each scenario beside each region. Note that these inset schematics are not drawn to scale and reproduced with permission. By Z. H, Lu *et al*., *ACS Energy Lett*. 2023, 8. [72]. Copyright © 2023 American Chemical Society.

Martin Stolterfoht *et al.* conducted a detailed study about the V_{OC} loss at the interfaces employing different charge transport layers. [73] This work suggests that the energy alignment can be inferred from the solar cell devices' external V_{OC} and internal quasi-Fermi-level splitting (QFLS). Generally, QFLS values are higher than external V_{OC} due to charge recombination at the surface. However, the V_{OC} values equal to QFLS values propose better energy band alignment at the interfaces and, consequently, higher efficiency. Their work was investigated by photoluminescence spectroscopy and ultraviolet photoemission spectroscopy (UPS) measurements.

1.8 Open Circuit Voltage Loss

It is described by the following equation given by

$$V_{loss} = E_g - eV_{oc} \qquad 1.1$$

Whereas E_g is the optical band gap of the perovskite composition, the elementary charge, and V_{oc} is the measured open circuit voltage of the device. Max *et al.* studied the voltage loss of inorganic perovskites [51], as shown in Figure **1.14**. Using photoluminescence spectroscopy, the authors have conducted layer-by-layer V_{OC} loss for the stack of $CsPbI_2Br$ for both *n-i-p* and *p-i-n* structures. This study revealed a high QFLS and V_{OC} mismatch compared to organic-inorganic perovskite solar cells. The UPS measurements have verified that the energy level mismatch at the interface causes voltage loss for inorganic solar cells.

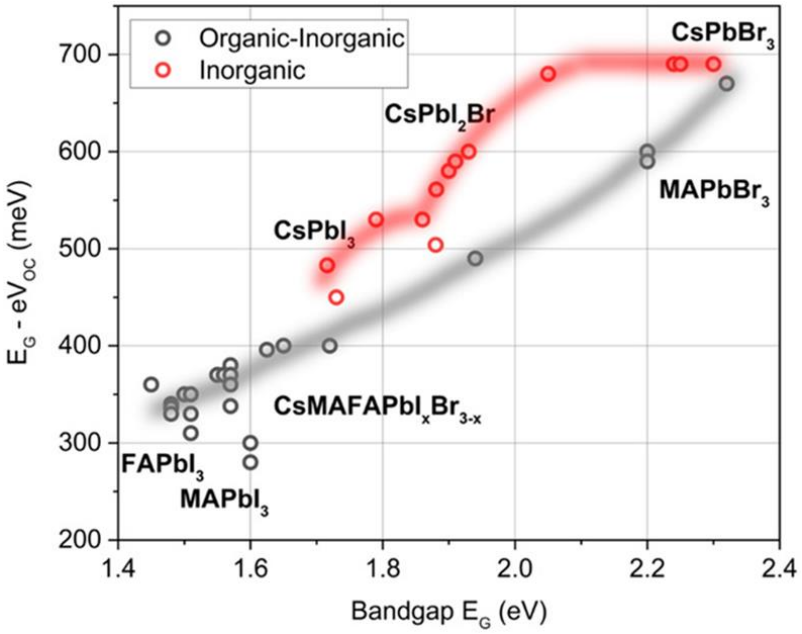

Figure1.14. Selected voltage loss (E_g – e·V_{oc}) values for various organic–inorganic and inorganic perovskite solar cells based on record V_{oc} for different bandgaps. Reproduced with permission. By Max Grischek *et al*., Sol. RRL 2022, 6, 2200690, [51], Copyright © 2022 The Authors. *Solar RRL* published by Wiley-VCH.GmbH.

1.9 Energy Level Alignments in $CsPbI_3$

In $CsPbI_3$, the energy alignment has been achieved by using the passivation of the perovskite layer with different molecules.

I. Walina Ma *et al.* used polymeric materials on the $CsPbI_3$ and hole transport interface for the band alignment at the interface. [74] **Figure 1.15** shows that quantum dots $CsPbI_3$ exhibit a deep VBM of 5.71eV, which has a long offset with the hole transport layer (Spiro-OMeTAD). UPS has measured the HOMO levels (VBM). These polymeric materials provide a stair for charge transport. Among these molecules, poly[4,8-bis[(2-ethylhexyl)oxy]benzo[1,2-b:4,5-b']dithiophene-2,6-diyl-alt-3-fluoro-2-[(2-ethylhexyl) carbonyl]thieno[3,4-b]thiophene-4,6-diyl] (PTB7) provides the best efficiency and

increases in V_{oc} as compared to control (without interlayer) devices due to better energy level alignment at the interface between the absorber layer and Spiro-OMeTAD.

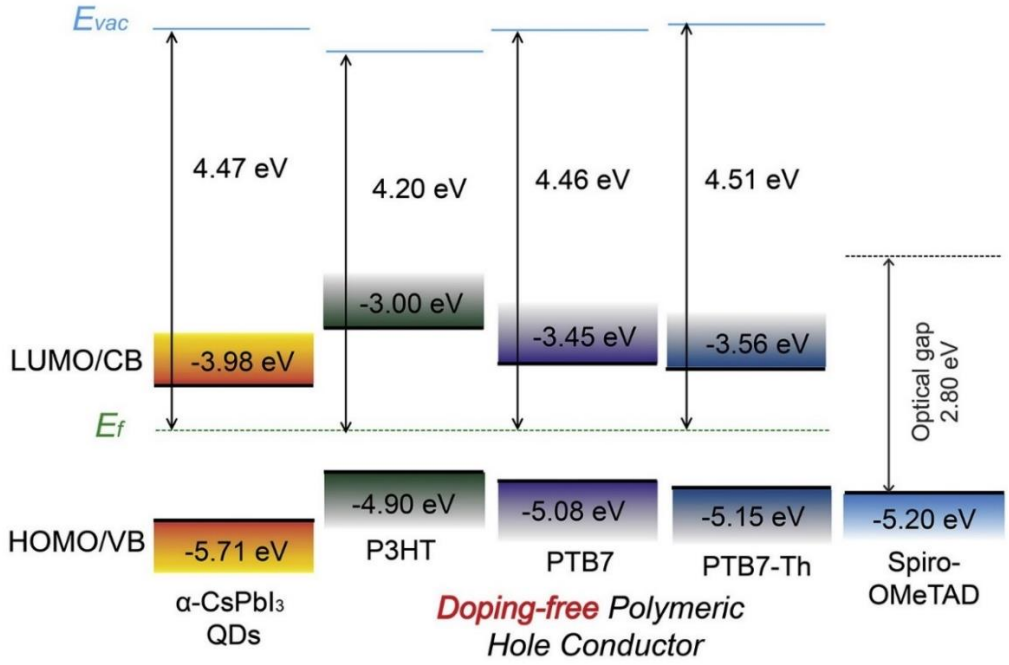

Figure1.15. Energy levels of MeOAc-treated $CsPbI_3$ QDs, conjugated polymers, and Spiro-OMeTAD. Reproduced with permission. By Wanli Ma *et al.*, *Joule*, 2018,**2**(11), [74], Copyright © 2018 Elsevier Inc.

II. Yixin Zhao *et al.* stabilized *β*-$CsPbI_3$ for the first time, and they applied Choline Iodide (CHI) for surface treatment. [48] This treatment fills the cracks and pin-holes in the $CsPbI_3$ film by passivation and improves the energy alignment between the absorber and HTM at the interface. The CHI treatment changes the perovskite CBM to 120meV and improves the energy alignment at both interfaces. The interface modification and band energy alignment improve the V_{OC} of the champion device up to 18.4% (versus 15.1 % for the control device), an increase in V_{OC} from 1.05 to 1.11V, and a 10% increase in *FF*.

III. Wei Lan *et al.* did interface engineering for $CsPbI_3$-based solar cells for energy alignment. [75] In this work, the ETM/perovskite interface was modified by using [6,6]-phenyl-C61-butyric acid methyl ester (PCBM) while the hole transport layer (HTL)/perovskite layer interface was modified by using 2-fluoro-1,4-phenylenediammonium iodide (2FPPD). These two molecules changed the interface energetics, as shown in **Figure 1.16,** for an *n-i-p* device structure. The stack's valence band maxima (VBM) and conduction band maxima (CBM) have been calculated from

the UPS and UV-Vis measurements. The graph shows an energy level alignment due to this interface modification. This energy level alignment further decreases the energy offset between the absorber $CsPbI_3$ and the selective contact and provides a stairway for carrier mobility and charge diffusion. Consequently, this energy level alignment increases the V_{OC}, *FF*, PCE, and stability for the modified interfaces solar cells.

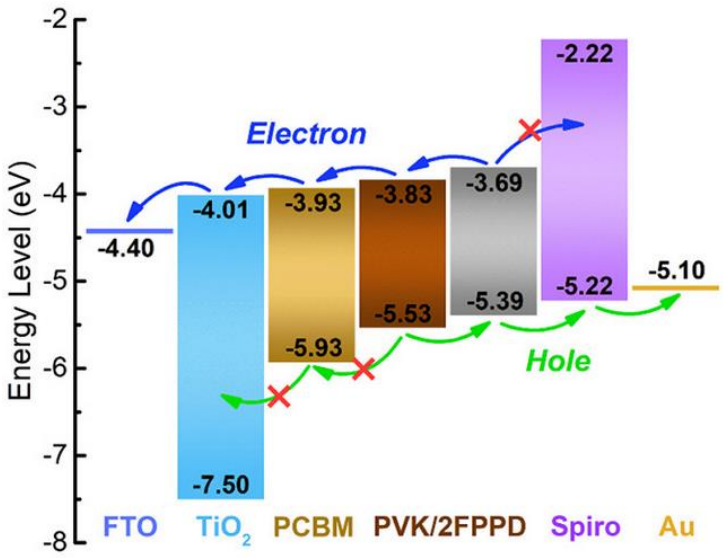

Figure 1.16. schematic energy level diagram of PSCs based on PCBM/PVK/2FPPD. Reproduced with permission. By Wei Lan *et al.*, *ACS Appl. Energy Mater*. 2022, 5, 13419−13428. [(76)], Copyright © 2022 American Chemical Society.

IV. Xiaojing Gu *et al.* have used histamine (HA) molecules on the $CsPbI_3$ surface and achieved over 20% PCE. [(76)] **Figure 1.17a** shows that the passivation of HA does not change the band gap of the perovskite material. **Figure 1.17 b** shows the UPS data for the raw and HA-treated inorganic perovskite materials. It shows a significant change (decrease) in the work function of the treated sample and VB levels. **Figure 1.17 c** demonstrates the energy band diagram, which shows that due to HA molecule treatment, there is an upward shift in the VB level from -5.45eV to -5.40eV which leads to improving the charge extraction at the interface, and ultimately, they have achieved the PCE over 20% for $CsPbI_3$ solar cell with an increase in V_{OC} of 38meV.

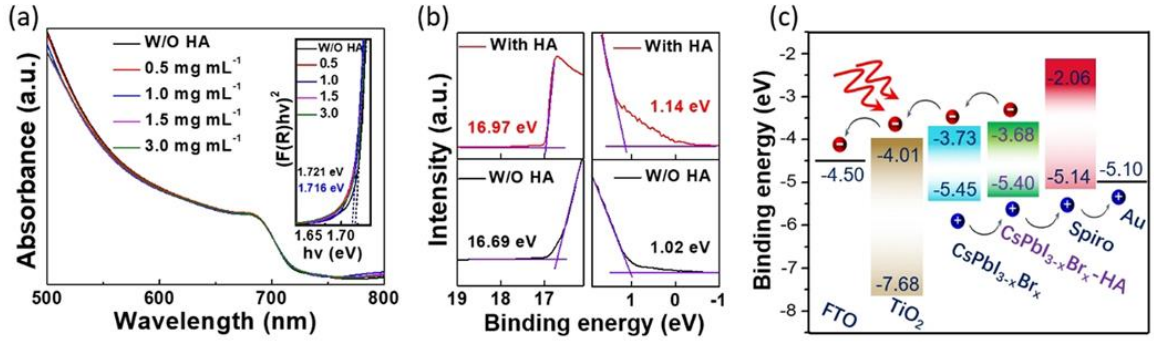

Figure 1.17. Optical properties of inorganic perovskite thin films with HA passivation. a) UV/Vis spectra, insert: Tauc plots. b) UPS spectra. c) Energy diagram of a complete PSC passivated by HA. Reproduced with permission. By Frank Liu *et al*., Angew. Chem. 2021, 133, 23348 –23354. [77], Copyright © 2021 Wiley-VCH GmbH.

V. J.wang *et al.* treated γ-$CsPbI_3$ with acyloin ligand **(**1,2-di(thiophene-2-yl)ethane-1,2-dione (DED)) and 2,2-di thienyl ketone (DTK) molecules individually. [77] **Figure 1.18** shows the device stack. **Figure 1.18 b** shows the energy levels diagram. To reveal the effect of these molecules, they have used UPS and UV-Vis to calculate VBM, Fermi levels, and a change in CBM. The diagram shows an upward shift in the VB levels of the γ-$CsPbI_3$ from -5.68eV to -5.54eV, making the hole extraction flow easier. By treating these molecules, PCE over 21% with a V_{OC} of 1.244V was achieved.

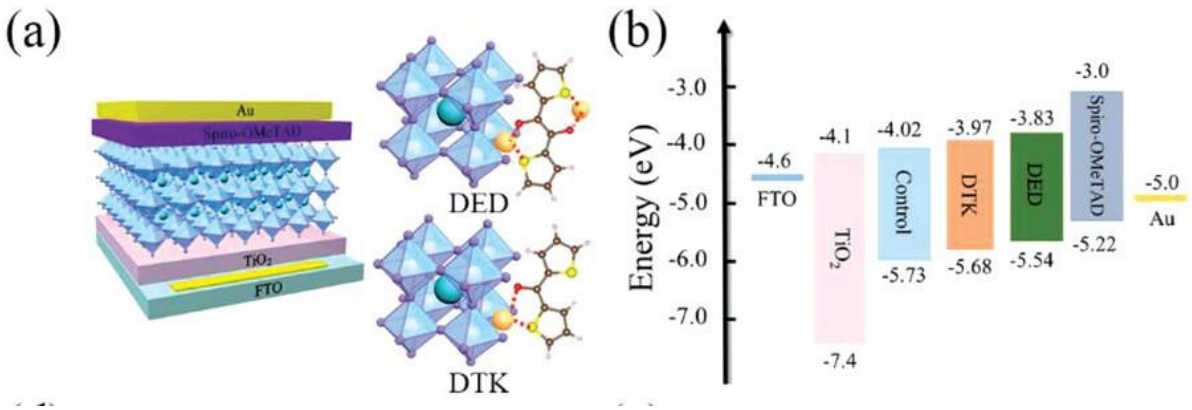

Figure 1.18. a) The device structure and the passivation models; b) schematic energy-level alignment of the control, DTK-$CsPbI_3$, and DED-$CsPbI_3$ films, respectively. Reproduced with permission. By J. Wang *et al*., Advanced Materials, 2023, 35, 2210223. [77], Copyright © 2023 Wiley-VCH GmbH.

It is concluded from the examples mentioned above that energy alignment is a crucial factor in achieving high efficiency and stability in the devices. At the same time, the surface treatment with suitable molecules with functionality plays a role in defect passivation and energy alignment at the interface. This method has been proven an effective one for fabricating state-of-the-art $CsPbI_3$-based devices.

1.10 Interfaces Limit SQ-limit

William Shockley and Hans J. Queisser calculated the maximum theoretical limit of the efficiency of a single *p-n* junction-based solar cell in ideal conditions, known as the Shockley–Queisser efficiency limitation (SQ limit) or detail balance limit of the *p-n* junction. [78] In SQ-limit, it is assumed that:

i. All the light is absorbed even above the band gap of the semiconductor.
ii. All the photo-generated carriers (holes, electrons) are collected at the respective electrodes.
iii. There is only radiative recombination in the *p-n* junction.

However, the real-world conditions for a solar cell differ from those assumed for the SQ model cell calculations. [79] These include;

i. Radiative recombination (Auger, defect, interface, surface recombination, etc.)
ii. Thermalization (cell heats up while measuring)
iii. Incomplete charge collection
iv. Reflection loss, transparency, and no absorption below the band gap.
v. Poor selectivity leads to resistive losses.

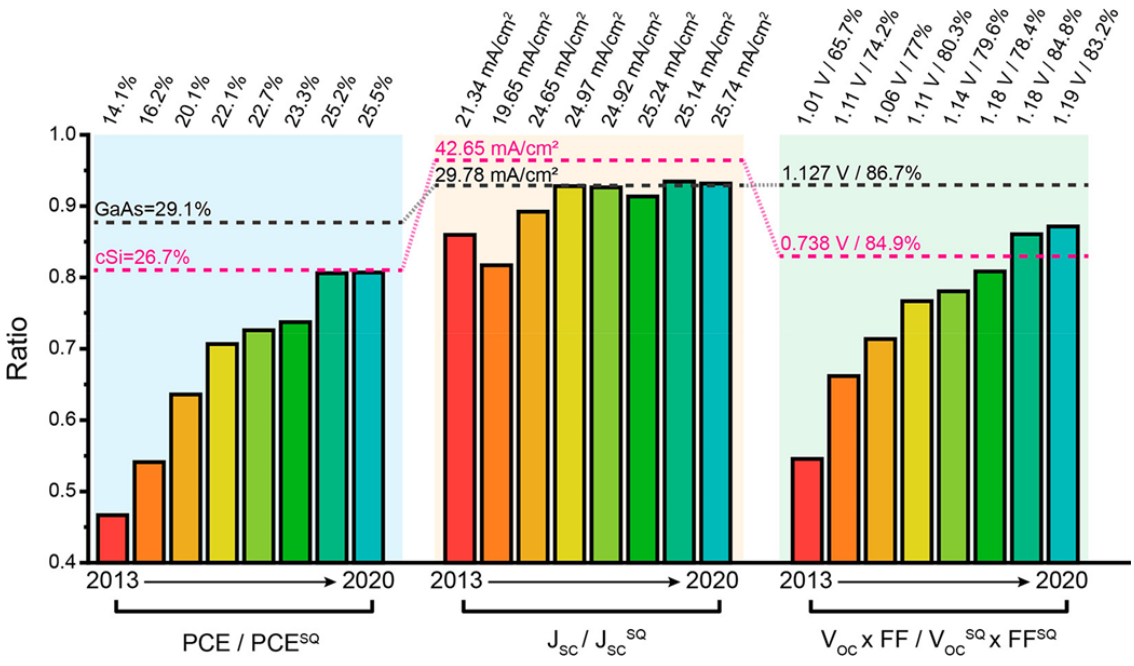

Figure 1.19. Bar graphs show the progress of perovskite solar cells' device performance as each device parameter's ratio approaches its SQ limit. The dotted lines show values for c-Si (in pink) and GaAs (in black). RepIt has reproduced permission. By J. Seo *et al.*, ACS Energy Letters,2022, 7 (6), [80], Copyright © 2022 American Chemical Society.

Figure 1.19 illustrates the chronicle progress in the efficiency of the single junction perovskite solar cells over time. The device performance paraments, *i.e.*, PCE, J_{SC}, $V_{OC,}$ and *FF* values, are given on the top, and the ratio of these values to the SQ-limit of the perovskite solar cell is provided on the *x*-axis of the plot. Additionally, the highest efficiency recorded for crystalline silicon solar cells and GaAs, to date, are also shown in the graph. However, it is to mention that the theoretical efficiency cap for these three established technologies differs in values, *i.e.* perovskite has an SQ-limit of ~31%, c-Si has ~33%, and GaAs has ~33%. [81] The difference in the values is due to the difference in the band gap of these materials.

The left plot shows the ratio of *c*-Si, GaAs, and perovskite solar cells (PSC) individual power conversion efficiency (PCE) to their theoretical limit values. In the start, the perovskite PCE ratio was even 0.5 but over the past few years; it approached 0.8 of the SQ limit. The graph shows that GaAs leads with 29.1% PCE and a ratio of 0.9. The middle bar graph shows a ratio of the J_{SC} (of c-Si, GaAs, PSC) to the Shockley–Queisser limit values for J_{SC}. The data indicate that J_{SC} has attained a 0.9 ratio of the theoretical limit by achieving the maximum J_{SC} of 25.74 mA/cm^2 for the best reported PSC. The right bar graph shows the ratio of the product of V_{oc} and *FF* to the product of V_{oc} and *FF* SQ limit. The values have the same trend as observed in PCE values. However, the product leads to the *c*-Si values. The V_{oc} and *FF* absolute maximum values, *i.e.* 1.19 V and 83.2% far leg behind V_{oc}(SQ)1.135V and *FF*(SQ) 91% values. [82]

It is concluded from the above discussion that the solar cell parameters, low $V_{oc,}$ and *FF* are the main roadblocks to attaining SQ-limit values for perovskite solar cells.

The V_{OC} of the perovskite solar cell in terms of the diode equation is given by the following relation as [83]

$$J_R = J_0 . e^{\left(\frac{qV_{oc}}{nK_BT}\right)} \quad 1.2$$

It transforms into

$$V_{oc} = \frac{nK_BT}{q} . ln\left(\frac{J_{sc}}{J_0} + 1\right) \quad 1.3$$

$$J_{sc} = J_0 . \left(e^{\left(\frac{qV_{oc}}{nK_BT}\right)} - 1\right) \quad 1.4$$

The above equations state that V_{OC} depends on the dark saturation current (J_0) and the current under light illumination (J_{SC}). J_0 is directly related to the non-radiative recombination in solar

cells. [84] It has been reported that non-radiative recombination decreases QFLS and V_{OC} [73]. In **equation 1.4**, K_B is the Boltzmann constant, T is temperature, and q is the elementary charge.

The V_{oc} of the solar cell for the different band gap (E_g) absorber can be written by the following relation as [85]

$$qV_{oc} = E_g - nK_BTln\frac{I_0}{I} \quad 1.5$$

The above equation involves constant factors and the ideality factor "*n*" can be used to determine the recombination mechanism in the device. [85] The value *n*=1 for the ideality factor corresponds to radiative recombination, *n*=2 for Shockley-Read Hall recombination (SRH), whereas the value of *n* is even less than 1 corresponds to the surface recombination. [86]
Ronald Österbacka *et al.* introduced the two equations to relate V_{oc} with the charge transport properties, contact properties, and surface recombination in perovskite solar cells. [87]

$$qV_{oc} = E_g - \varphi_{b-}\frac{K_BT}{2}ln\left(\frac{N_pN_v{}^2}{\mu_nG}\right) \quad 1.6$$

$$qV_{oc} = E_g - \varphi_{b-}\frac{2K_BT}{3}ln\left(K\frac{S_pN_v{}^{3/2}}{G}\right) \quad 1.7$$

The equations represent the contact barrier on the interfaces, μ_p and μ_n are the hole and electron mobilities across the surface, β is the radiative recombination constant, S_p is the surface recombination velocity of the holes, and *K* is the parameters for perovskite. The above equations describe the recombination at the interfaces limited by the charge carrier diffusion in the selective contacts, and surface recombination is the cathode. [87] The following equation gives the charge carrier diffusion and mobility of the holes and the electrons. [86]

$$\mu = {qD}/{K_BT} \quad 1.8$$

Where D is the diffusion coefficient and μ is the carrier mobility. The following relation gives the solar cell's fill factor (FF) in terms of V_{oc} and ideality factor (*n*). [88]

$$FF = \frac{\frac{qV_{oc}}{nK_BT} - \ln\left(\frac{qV_{oc}}{nK_BT} + 0.72\right)}{\frac{qV_{oc}}{nK_BT} + 1} \quad 1.9$$

This equation suggests that determining the ideality factor(*n*) in the solar cells can help us disentangle the *FF* limits into non-radiative recombination and charge transport losses in a device. [89]A solar cell with less value of ideality factor will have a higher FF and *vice versa*.

It is inferred from the above mathematical equations that V_{OC} and *FF* depend on the surface and interface physical properties, *e.g.*, carrier mobilities, QFLS, all types of non-radiative recombination, and charge transport properties at the interfaces of the solar cell. It also suggests that it is imperative to design the interface to enhance solar cell efficiency.

1.11 Motivation

German physicist and Nobel laureate Herbert Kroemer coined the famous phrase "*the interface is the device*." [90]. He was awarded the Nobel Prize in Physics in 2000 for developing semiconductor heterostructures.

The motivation of this work is based on specific questions and problems related to the $CsPbI_3$-based solar cell, which is believed to be the game changer in the future for its stability at elevated temperatures. The recent literature and discussion above conclude that the interfaces limit the device's performance. It further suggests a need for interfacial study and a new interface design for this perovskite.

The dissertation is based on the following points that the scientific community must address.

- The $CsPbI_3$ film is annealed in a dry or ambient air box environment. To my knowledge, no reports have conclusive evidence about surface chemistry and buried interfaces of $CsPbI_3$ films and solar cells. This work presents synchrotron-based HAXPES measurements for surface chemistry and buried interface with a better penetration depth at the interface.
- The rate of charge extraction at the interface is an essential factor in the device's operation. Here a very detailed layer-by-layer trSPV study was conducted to study the charge extraction kinetics at the interface with the help of simulations.
- The only approach to optimize energy alignment is based on passivating the perovskite surface with some molecule. Here, it suggests that a new interface design is needed on a well-passivated film for better energy alignment at the interface and device performance.

- This dissertation also reports two interface designs for stable devices for Spiro-OMeTAD and P3HT.

Outlines

This dissertation describes the interfaces for $CsPbI_3$-based solar cells. The outlines of the thesis are as follows.

- The first chapter describes the general introduction to the main challenge that humanity is facing- "climate change". As a solution to this challenge, it suggests renewable energy sources *e.g.* solar energy. Further, it describes solar energy, an introduction to solar cells, its different technologies, perovskite solar cells, Inorganic perovskite solar cells, motivation for this work, fundamentals of semiconductors, interfaces, and solar cells. At the end of the chapter, about the Schockly-Quiesser Limit (SQ limit).
- **Chapter 2** describes the methods and characterization tools that have been used in this work. The basic principle of each technique, its theory, and the key information that can be collected by applying these techniques have been summarized in this chapter.
- The potential influence of the annealing environment on the $CsPbI_3$ surface and then its interface with the hole transport layer is investigated in **Chapter 3**. Synchrotron-based HAXPES has been used to investigate the buried interfaces. This chapter concludes that there is no harm in annealing the films in the air.
- **Chapter 4** presents an interface design for $CsPbI_3$ and Spiro-OMeTAD interfaces. In this work diploe molecule, TOPO is used that modify that interface and increases the stability. Here cyclic MPP tracking has been introduced as a method to calculate the overall energy production. It also offers a detailed interfacial study by using PL, trPL, tr-SPV, KP, XPS, and UPS.
- **Chapter 5** illustrates an interface design for $CsPbI_3$ and P3HT interfaces. This chapter includes only primarily results for $CsPbI_3$/P3HT that need further research to improve the efficiency.
- **Chapter 6** includes a summary of the overall work, key points, key findings, and an outlook for future work.

References

1. https://edition.cnn.com/2022/09/02/asia/pakistan-floods-climate-explainer-intl-hnk/index.html. (accessed on May12, 2023)

2. https://sdgs.un.org/goals (accessed on May12, 2023)
3. V. Masson-Delmotte, P. Zhai, A. Pirani, C. Péan, S. Berger, *et al*., "Climate change 2021: the physical science basis."Contribution of working group I to the sixth assessment report of the intergovernmental panel on climate change, 2021, Vol. **2**
4. https://www.bloomberg.com/graphics/2015-whats-warming-the-world/ (accessed on May17, 2023)
5. https://ourworldindata.org/renewable-energy (accessed on May18, 2023)
6. N. M. Haegel, R. Margolis, T. Buonassisi, D. Feldman, A. Froitzheim, R. Garabedian, *et al*., "Terawatt-scale photovoltaics: Trajectories and challenges." *Science*,2017, **356**,6334,141-143.
7. https://www.nrel.gov/pv/interactive-cell-efficiency.html (accessed on May18, 2023)
8. C. J. Bartel, B. R. Goldsmith, L. M. Ghiringhelli, *et al*., "New tolerance factor to predict the stability of perovskite oxides and halides.", *Science Advances*, 2019, **5**(2),693.
9. V. D. Innocenzo, A. R. S. Kandada, M . D. Bastiani, M. Gandini, A . Petrozza, "Tuning the Light Emission Properties by Band Gap Engineering in Hybrid Lead Halide Perovskite", *Journal of American Chemical Society*, 2014, **136**(51), 17730–17733.
10. S .A. Kulkarni, T. Baikie, P. P. Boix, N. Yantara, N. Mathews, S. Mhaisalkar, "Band-gap tuning of lead halide perovskites using a sequential deposition process", *Journal of Material Chemistry A*, 20 14, **2**, 9221-9225.
11. E. L. Unger, L. Kegelmann, K. Suchan, D. Sörell, L. Korte, S. Albrecht, "Roadmap and roadblocks for the band gap tunability of metal halide perovskites", *Journal of Material Chemistry A*, 2017, **5**, 11401-11409.
12. W. Rehman, R. L. Milot, G. E. Eperon, C. Wehrenfennig, J .L. Boland, H. J. Snaith, M. B. Johnston, L. M. Herz, "Charge-Carrier Dynamics and Mobilities in Formamidinium Lead Mixed-Halide Perovskites", *Advanced Materials*., 2015, **27**, 7938–7944.
13. J. Lim, M. T. Hörantner, N. Sakai, J. M. Ball, S. Mahesh, N. K. Noel, Y. H. Lin, J. B. Patel, D. P. McMeekin, M. B. Johnston, B. Wenger, H. J. Snaith, "Elucidating the long-range charge carrier mobility in metal halide perovskite thin films", *Energy & Environmental Sciences*, 2019, **12**, 169-176.
14. H. Huang, M. I. Bodnarchuk, S. V. Kershaw, M. V. Kovalenko, A.L. Rogach " Lead Halide Perovskite Nanocrystals in the Research Spotlight: Stability and Defect Tolerance.", *ACS Energy Letter*, 2017, **2**(9), 2071–2083.
15. J. B. C. Baena , M. Saliba ,T. Buonassisi, M . Grätzel, A.Abate ,W.Tress, A.Hagfeldt "Promises and challenges of perovskite solar cells", *Science*, 2017, **358**, 739–744.
16. W. Zhang, G. Eperon, H. Snaith, "Metal halide perovskites for energy applications", *Nature Energy*, 2016, **1**, 16048.
17. S. D. Wolf, J. Holovsky , S. J. Moon, P. Löper, B. Niesen, M. Ledinsky, F. J. Haug, J. H. Yum, C. Ballif . "Organometallic Halide Perovskites: Sharp Optical Absorption Edge and Its Relation to Photovoltaic Performance", *Journal of Physical Chemistry Letter*, 2014, **5**, 6.
18. T. Zhang, F. Wang, H.-B. Kim, I.-W. Choi, C. Wang, E. Cho, *et al*.," Ion-modulated radical doping of spiro-OMeTAD for more efficient and stable perovskite solar cells.", *Science*, 2022, **377** (6605), 495-501

19. M. Jeong,. Cho, M. Kim, B. Lee, *et al*., "Stable perovskite solar cells with efficiency exceeding 24.8% and 0.3-V voltage loss.", *Science*, 2020, **369** (6511), 1615-1620
20. W. Chen, Y. Wu, Y. Yue, J. Liu, W. Zhang, X. Yang, et al. "Efficient and stable large-area perovskite solar cells with inorganic charge extraction layers" *Science*, 2015, **350** (6263), 944-948.
21. D. Luo, L. Zhao, J. Wu, Q. Hu, Y. Zhang, Z. Xu, *et al*., "Dual-source precursor approach for highly efficient inverted planar heterojunction perovskite solar cells.", *Advanced Materials*, 2017, **29**(19), 1604758.
22. D. Luo, R. Su, W. Zhang, Q. Gong and R. Zhu., "Minimizing non-radiative recombination losses in perovskite solar cells.", *Nature Reviews Materials*, 2020, **5**(1),44-60.
23. F. H. Isikgor, S. Zhumagali, L. V. T. Merino, M. De Bastiani, I. McCulloch and S. De Wolf., "Molecular engineering of contact interfaces for high-performance perovskite solar cells.", *Nature Reviews Materials*, 2023, **8**(2),89-108.
24. W. Xiang, S. (F.) Liu, Wolfgang Tress. "A review on the stability of inorganic metal halide perovskites: challenges and opportunities for stable solar cells", *Energy & Environmental Sciences*, 2021, **14**, 2090-2113
25. H.Yao, J.Zhao, Z.Li, Z.Ci, and Z.Jin., "Research and progress of black metastable phase $CsPbI_3$ solar cells" , *Materials Chemistry Frontiers*, 2021, **5**, 1221-1235.
26. H. Meng, Z. Shao, L. Wang, Z. Li, R. Liu, Y. Fan, G. Cui, S. Pang., "Chemical Composition and Phase Evolution in DMAI-Derived Inorganic Perovskite Solar Cells" *ACS Energy Letter*, 2020, **5**(1), 263–270.
27. J.A. Christians, P.A. M.Herrera, P .V. Kamat., "Transformation of the Excited State and Photovoltaic Efficiency of CH3NH3PbI3 Perovskite upon Controlled Exposure to Humidified Air." , *Jornal Of Americal Chemical Society*, 2015, **137**, 4.
28. Y, B, Lu , W. Y. Cong , C. B. Guan , H. Sun , Y. Xin , K. Wang ,S. Song., "Light enhanced moisture degradation of perovskite solar cell material $CH_3NH_3PbI_3$.", *Journal of Material Chemistry A*, 2019, **7**, 27469-27474.
29. B. Philippe, B.W. Park, R. Lindblad, J. Oscarsson, S. Ahmadi, E.M. J. Johansson ,H. Rensmo., "Chemical and Electronic Structure Characterization of Lead Halide Perovskites and Stability Behavior under Different Exposures—A Photoelectron Spectroscopy Investigation." *Chemistry of Materials*, 2015, 27, **5**, 1720–1731.
30. W. Ahmad, J. Khan, G.Niu, J.Tang., "Inorganic $CsPbI_3$ Perovskite-Based Solar Cells: A Choice for a Tandem Device" *Solar. RRL*, 2017, **1**, 1700048.
31. Y. Cui, J. Shi, F. Meng, B. Yu, S. Tan, S. He, *et al*., "A Versatile Molten-Salt Induction Strategy to Achieve Efficient $CsPbI_3$ Perovskite Solar Cells with a High Open-Circuit Voltage >1.2 V.", *Advanced Materials*, 2022, **34** (45),2205028.
32. C. K. MØLler., "Crystal Structure and Photoconductivity of Caesium Plumbohalides." *Nature*,1958, **182** (4647), 436-1436.
33. G. E. Eperon, G. M. Paternò, R. J. Sutton, A. Zampetti, A. A. Haghighirad, F. Cacialli, *et al*., "Inorganic cesium lead iodide perovskite solar cells." *Journal of Materials Chemistry A*, 2015, **3** (39),19688-19695
34. T. S. Ripolles, K. Nishinaka, Y. Ogomi, Y. Miyata and S. Hayase., "Efficiency enhancement by changing perovskite crystal phase and adding a charge extraction

interlayer in organic amine free-perovskite solar cells based on cesium.", *Solar Energy Materials and Solar Cells*, 2016, **144**, 532-536
35. L. Protesescu, C. H. Hendon, *et al*., "Nanocrystals of cesium lead halide perovskites ($CsPbX_3$, X= Cl, Br, and I): novel optoelectronic materials showing bright emission with wide color gamut.", *Nano Letters*, 2015, **15**(6), 3692-3696
36. J. Song, J. Li, X. Li, L. Xu, Y. Dong and H. Zeng., "Quantum Dot Light-Emitting Diodes Based on Inorganic Perovskite Cesium Lead Halides ($CsPbX_3$).", *Advanced Materials*, 2015, **27**(44),7162-7167.
37. B. Wang and A. Navrotsky., "Thermodynamic studies of bromide incorporation into cesium lead iodide ($CsPbI_3$).", *The Journal of Physical Chemistry C*, 2020, **124**(16), 8639-8642
38. J. A. Steele, H. Jin, I. Dovgaliuk, R. F. Berger, T. Braeckevelt, H. Yuan, *et al.*, "Thermal unequilibrium of strained black CsPbI3 thin films." *Science*,2019, **365**(6454),679-684.
39. A. Marronnier, G. Roma, S. Boyer-Richard, L. Pedesseau, J.-M. Jancu, Y. Bonnassieux, *et al.*, "Anharmonicity and disorder in the black phases of cesium lead iodide used for stable inorganic perovskite solar cells.", *ACS Nano*,2018,**12** (4), 3477-3486.
40. B. Zhao, S.-F. Jin, S. Huang, N. Liu, J.-Y. Ma, D. J. Xue, *et al*., "Thermodynamically Stable Orthorhombic γ-CsPbI3 Thin Films for High-Performance Photovoltaics.", *Journal of the American Chemical Society*, 2018, **140** (37),11716-11725.
41. J. Liang, P. Zhao, C. Wang, Y. Wang, Y. Hu, G. Zhu, *et al*., "$CsPb_{0.9}Sn_{0.1}IBr_2$ Based All-Inorganic Perovskite Solar Cells with Exceptional Efficiency and Stability.", *Journal of the American Chemical Society*, 2017, **139**(40),14009-14012
42. J. Liang, X. Han, J.-H. Yang, B. Zhang, Q. Fang, J. Zhang, *et al*., "Defect Engineering-Enabled High-Efficiency All-Inorganic Perovskite Solar Cells.", *Advanced Materials*, 2019, **31**, (51),1903448.
43. F. Meng, B. Yu, Q. Zhang, Y. Cui, S. Tan, J. Shi, *et al*., "Ge Incorporation to Stabilize Efficient Inorganic CsPbI3 Perovskite Solar Cells.", *Advanced Energy Materials*, 2022 **12**, (10),2103690
44. A. Swarnkar, A. R. Marshall, E. M. Sanehira, B. D. Chernomordik, D. T. Moore, J. A. Christians, *et al*., "Quantum dot–induced phase stabilization of α-CsPbI3 perovskite for high-efficiency photovoltaics.", *Science*, 2016, **354**(6308), 92-95.
45. A. B. Kaplan, Q. C. Burlingame, R. Holley, Y.-L. Loo., "Prospects for inorganic $CsPbI_3$ perovskite solar cells with commercially viable lifetimes." *APL Energy*, 2023,**1**(1).
46. C.C. Lin, S.-K. Huang, C.-E. Hsu, Y.-C. Huang, C.-Y. Wei, C.-Y. Wen, *et al*., "Exploring the Origin of Phase-Transformation Kinetics of $CsPbI_3$ Perovskite Nanocrystals Based on Activation Energy Measurements." *The Journal of Physical Chemistry Letters*,2020, **11**(9), 3287-3293.
47. P. Wang, X. Zhang, Y. Zhou, Q. Jiang, Q. Ye, Z. Chu, *et al*., "Solvent-controlled growth of inorganic perovskite films in dry environment for efficient and stable solar cells.", *Nature Communications*, 2018, **9** (1), 2225.
48. Y. Wang, M. I. Dar, L. K. Ono, T. Zhang, M. Kan, Y. Li, *et al*.," Thermodynamically stabilized β-CsPbI3–based perovskite solar cells with efficiencies> 18%.", *Science* 2019, **365**(6453), 591-595.

49. Y. Wang, X. Liu, T. Zhang, X. Wang, M. Kan, J. Shi, *et al*.," The Role of Dimethylammonium Iodide in CsPbI3 Perovskite Fabrication: Additive or Dopant?", *Angewandte Chemie International Edition*, 2019, **58**(46),16691-16696
50. S. M. Yoon, H. Min, J. B. Kim, G. Kim, K. S. Lee, S. I. Seok., "Surface Engineering of Ambient-Air-Processed Cesium Lead Triiodide Layers for Efficient Solar Cells.", *Joule* 2021, **5**(1),183-196
51. M. Grischek, P. Caprioglio, J. Zhang, F. Pena-Camargo, K. Sveinbjörnsson, F. Zu, *et al*., "Efficiency Potential and Voltage Loss of Inorganic CsPbI2Br Perovskite Solar Cells.", *Solar RRL*, 2022, **6**(11), 2200690
52. X. Zhao, T. Liu, Q. C. Burlingame, T. Liu, R. Holley, G. Cheng, *et al*., "Accelerated aging of all-inorganic, interface-stabilized perovskite solar cells.", *Science*, 2022, **377** (6603), 307-310
53. C. Liu, Y. Yang, X. Xia, Y. Ding, Z. Arain, S. An, *et al*., "Soft Template-Controlled Growth of High-Quality CsPbI3 Films for Efficient and Stable Solar Cells.", *Advanced Energy Materials*, 2020, **10**(9),1903751.
54. I. Mora-Sera., "How Do Perovskite Solar Cells Work?", *Joule*,2018, **2**(4),585-587.
55. H. S. Jung and N.-G. Park., "Perovskite Solar Cells: From Materials to Devices.", *Small*, 2015,**11**(1) ,10-25
56. K. K. Wong, A. Fakharuddin, P. Ehrenreich, T. Deckert, M. Abdi-Jalebi, R. H. Friend, *et al*., "Interface-Dependent Radiative and Nonradiative Recombination in Perovskite Solar Cells.", *The Journal of Physical Chemistry C*,2018, **122** (20), 10691-10698.
57. C. M. Wolff, P. Caprioglio, M. Stolterfoht ,D. Neher., "Nonradiative Recombination in Perovskite Solar Cells: The Role of Interfaces." *Advanced Materials*, 2019,**31** (52),1902762.
58. S. Cacovich, G. Vidon, M. Degani, M. Legrand, L. Gouda, J.-B. Puel, *et al*., "Imaging and quantifying non-radiative losses at 23% efficient inverted perovskite solar cells interfaces.", *Nature Communications*, 2022,**13**(1),2868.
59. Z. Zhang and J. T. Yates Jr, "Band bending in semiconductors: chemical and physical consequences at surfaces and interfaces.", *Chemical Reviews*, 2012,**112**(10), 5520-5551.
60. M. Mews, M. Liebhaber, B. Rech ,L. Korte, "Valence band alignment and hole transport in amorphous/crystalline silicon heterojunction solar cells." *Applied Physics Letters*, 2015,**107**, 013902-1.
61. M. Çopuroğlu, H. Sezen, R. L. Opila and S. Suzer," Band-bending at buried SiO2/Si interface as probed by XPS.", *ACS applied materials & interfaces*, 2013, **5**(12),5875-5881.
62. R. Varache, J. Kleider, W. Favre, L. Korte., "Band bending and determination of band offsets in amorphous/crystalline silicon heterostructures from planar conductance measurements.", *Journal of Applied Physics*, 2012, **112**(12),123717.
63. R. S. Bonilla, P. R. Wilshaw., "On the c-Si/SiO2 interface recombination parameters from photo-conductance decay measurements.", *Journal of Applied Physics*, 2017, **121**, (13), 135301.
64. T. Dittrich., Materials Concept for Solar Cells., 2013, Imperial College Press.
65. J.A. Spies, R. Schafer, J.F. Wager, P. Hersh, H.A.S. Platt, D.A. Keszler, G. Schneider, R. Kykyneshi, J. Tate, X. Liu, A.D. Compaan, W.N. Shafarman., "pin double-

heterojunction thin-film solar cell p-layer assessment.", *Solar Energy Materials and Solar Cells*, 2009, **93**, (8), 1296-1308.
66. H. Kanda, N. Shibayama, A. J. Huckaba, Y. Lee, S. Paek, N. Klipfel, *et al*., "Band-bending induced passivation: high performance and stable perovskite solar cells using a perhydropoly (silazane) precursor.", *Energy & environmental science*, 2020, **13**(4), 1222-1230.
67. S. Wang, M.-H. Li, Y. Zhang, Y. Jiang, L. Xu, F. Wang, *et al*., "Surface *n*-type Band Bending for Stable Inverted CsPbI3 Perovskite Solar Cells with over 20% Efficiency.", *Energy & Environmental Science*, 2023,**16**, 2572-2578
68. H. Hu, S. Birkhold, M. Sultan, A. Fakharuddin, S. Koch and L. Schmidt-Mende., "Surface band bending influences the open-circuit voltage of perovskite solar cells.", *ACS Applied Energy Materials*, 2019, **2**(6), 4045-4052.
69. L. Canil, T. Cramer, B. Fraboni, D. Ricciarelli, D. Meggiolaro, A. Singh, *et al.*, "Tuning halide perovskite energy levels." *Energy & Environmental Science*, 2021, **14**(3),1429-1438.
70. S. Tan, T. Huang, I. Yavuz, R. Wang, T. W. Yoon, M. Xu, *et al*., "Stability-limiting heterointerfaces of perovskite photovoltaics." *Nature*, 2022, **605**, (7909), 268-273.
71. J. Haddad, B. Krogmeier, B. Klingebiel, L. Krückemeier, S. Melhem, Z. Liu, *et al*., "Analyzing Interface Recombination in Lead-Halide Perovskite Solar Cells with Organic and Inorganic Hole-Transport Layers.", *Advanced Materials Interfaces*, 2020 ,**7**(16), 2000366.
72. N. Chen, D. Luo, P. Chen, S. Li, J. Hu, D. Wang, *et al*., "Universal Band Alignment Rule for Perovskite/Organic Heterojunction Interfaces.", *ACS Energy Letters*, 2023, **8**, (3),1313-1321
73. M. Stolterfoht, D. Neher, *et al*., "The impact of energy alignment and interfacial recombination on the internal and external open-circuit voltage of perovskite solar cells.", *Energy Environ. Sci*., 2019, **12**, 2778.
74. J. Yuan, X. Ling, D. Yang, F. Li, S. Zhou, J. Shi, *et al*., "Band-Aligned Polymeric Hole Transport Materials for Extremely Low Energy Loss α-CsPbI3 Perovskite Nanocrystal Solar Cells.", *Joule*, 2018, **2**(11), 2450-2463.
75. H. Guan, Y. Lei, Q. Wu, X. Zhou, H. Wang, G. Wang, *et al*., "An Interface Co-modification Strategy for Improving the Efficiency and Stability of CsPbI3 Perovskite Solar Cells.", *ACS Applied Energy Materials*, 2022, **5**(11),13419-13428.
76. X. Gu, W. Xiang, Q. Tian, S. Liu., "Rational Surface-Defect Control via Designed Passivation for High-Efficiency Inorganic Perovskite Solar Cells." *Angewandte Chemie International Edition*, 2021, **60**(43), 23164-23170.
77. J. Wang, Y. Che, Y. Duan, Z. Liu, S. Yang, D. Xu, *et al*.,"21.15%-Efficiency and Stable γ-$CsPbI_3$ Perovskite Solar Cells Enabled by an Acyloin Ligand." *Advanced Materials*, 2023, **35**, 2210223.
78. W. Shockley and H. J. Queisser., "Detailed balance limit of efficiency of p-n junction solar cells.", *Journal of applied physics*, 1961, **32** (3), 510-519.
79. T. Markvart., "Shockley-Queisser detailed balance limit after 60 years.", *Wiley Interdisciplinary Reviews: Energy and Environment*, 2022, **11**(4),430.

80. J. J. Yoo, S. S. Shin and J. Seo., "Toward Efficient Perovskite Solar Cells: Progress, Strategies, and Perspectives.", *ACS Energy Letters*, 2022, **7** (6), 2084-2091.
81. https://www.lmpv.nl/db/ (accessed on May 23, 2023)
82. W. E.I. Sha, X. Ren, L. Chen, W. C. H. Choy., "The efficiency limit of $CH_3NH_3PbI_3$ perovskite solar cells." *Applied Physics Letters*, 2015, **106**(22).
83. P.Caprioglio, M. Stolterfoht, C. M. Wolff, T. Unold, B. Rech,S. Albrecht, D. Neher., " On the Relation between the Open-Circuit Voltage and Quasi-Fermi Level Splitting in Efficient Perovskite Solar Cells.", *Advanced Energy Materials*., 2019, **9**, 1901631.
84. J. Yao, T. Kirchartz, M.S. Vezie, M. A. Faist, W. Gong, Z. He, H. Wu, J. Troughton, T. Watson, D. Bryant, J. Nelson., "Quantifying Losses in Open-Circuit Voltage in Solution-Processable Solar Cells.", *Physical review Applied*, 2015, **4,** 014020.
85. W. Tress, M. Yavari, K. Domanski, P. Yadav, B. Niesen, J. P. Correa Baena, *et al*., "Interpretation and evolution of open-circuit voltage, recombination, ideality factor and subgap defect states during reversible light-soaking and irreversible degradation of perovskite solar cells.", *Energy & Environmental Science*, 2018, **11**(1),151-165.
86. H. Pan, H. Shao, X. L. Zhang, Y. Shen, M. Wang., "Interface engineering for high-efficiency perovskite solar cells.", *Journal of Applied Physics*, 2021, **129**(13),130904.
87. O. J. Sandberg, A. Sundqvist, M. Nyman and R. Österbacka., "Relating Charge Transport, Contact Properties, and Recombination to Open-Circuit Voltage in Sandwich-Type Thin-Film Solar Cells.", *Physical Review Applied*, 2016, **5** (4), 044005.
88. Z. Guo, A. K. Jena, G. M. Kim, T. Miyasaka.," The high open-circuit voltage of perovskite solar cells: a review.", *Energy & Environmental Science*, 2022, **15**, 3171.
89. M. Stolterfoht, C. M. Wolff, Y. Amir, L. Perdigón-Toro, P. Caprioglio, *et al*.," Approaching the fill factor Shockley–Queisser limit in stable, dopant-free triple cation perovskite solar cells.", *Energy & Environmental Science*, 2017, **10**(6),1530-1539.
90. The editor "The interface is still the device". *Nature Materials*, 2012, **11**(2), 91-91.
91. P. Luo, W. Xia, S. Zhou, L. Sun, J. Cheng, C. Xu, *et al*., "Solvent engineering for ambient-air-processed, phase-stable CsPbI3 in perovskite solar cells." *The Journal of physical chemistry letters*, 2016,**7**(18), 3603-3608.
92. T. Zhang, M. I. Dar, G. Li, F. Xu, N. Guo, M. Grätzel, *et al*., "Bication lead iodide 2D perovskite component to stabilize inorganic *α*-CsPbI3 perovskite phase for high-efficiency solar cells." *Science advances*, 2017, **3**(9),1700841
93. Y. Wang, T. Zhang, M. Kan, Y. Zhao., "Bifunctional Stabilization of All-Inorganic α-CsPbI3 Perovskite for 17% Efficiency Photovoltaics." *Journal of the American Chemical Society*, 2018, **140**(39),12345-12348
94. B. Yu, J. Shi, S. Tan, Y. Cui, W. Zhao, H. Wu, *et al*., "Efficient (> 20%) and stable all-inorganic cesium lead triiodide solar cell enabled by thiocyanate molten salts." *Angewandte Chemie International Edition* , 2021, **60**(24), 13436-13443
95. J. Zhang, Y. Fang, W. Zhao, R. Han, J. Wen, S. Liu., "Molten-Salt-Assisted CsPbI3 Perovskite Crystallization for Nearly 20%-Efficiency Solar Cells." *Advanced Materials*, 2021, **33**(45), 2103770.

Chapter 2

Methods

This chapter comprises the basic working principle and a brief introduction to the methods, characterization tools, and sample preparation used in this thesis. All the parameters and the physical quantities that have been studied with these techniques are discussed here. This chapter will briefly overview the methods to support reading the results rather than a detailed description of the instrumentation. The details of the measurements, procedures, and equipment have been added in the **Appendix**.

These techniques include,

I. Optical characterization *i.e.* UV-Vis spectroscopy, photoluminescence spectroscopy (PL), transient photoluminescence (trPL), transient photovoltage (tr-SPV), and external quantum efficiency (EQE)
II. Structure and microscopic analysis *i.e.* XRD and SEM
III. Energetic levels measurements *i.e.* Kelvin Probe Method (KP), X-ray photoelectron spectroscopy (XPS), hard X-ray photoemission spectroscopy (HAXPES), and ultraviolet photoemission spectroscopy (UPS).
IV. Device performance *i.e.* EQE measurements, *J-V* measurements, constant light illuminations MPP tracking, Cyclic MPP tracking.

2.1. Samples preparations

This section presents the preparation method used to make state-of-the-art devices and sample preparation for characterization. However, the details of solution preparation and spin coating techniques (program, annealing, time, etc.) have been added in **Appendix 4.1**. Depending on the measurements, the samples were prepared on glass, patterned Fluorine-doped tin oxide (FTO), or quartz substrates. The layout of the solar cell devices architect is the *n-i-p* structure in which compact TiO_2 is used as an electron transport layer while spiro-OMeTAD and P3HT were used as a hole transport layer (HTM).

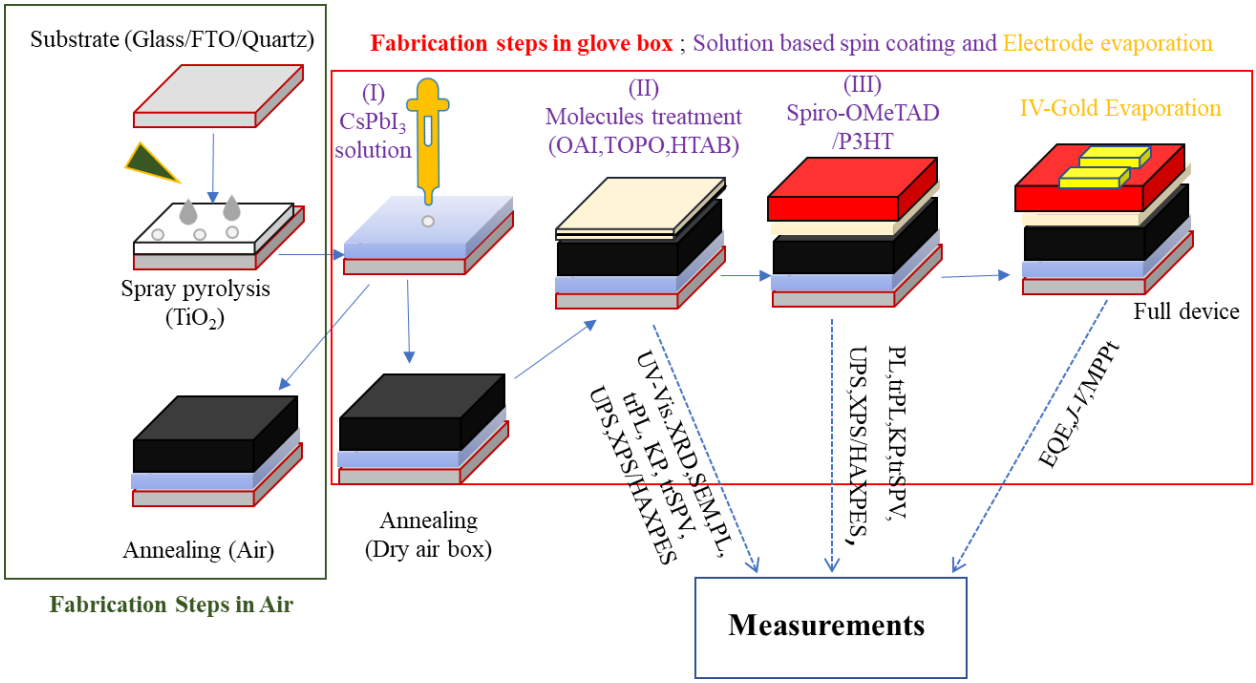

Figure 2.1 Sample preparations and device fabrication steps in air and glove box. The dash-line arrows represent the characterizations conducted at different stages.

Figure 2.1 illustrates a step-by-step preparation method, the medium of preparation, and the measurements conducted at every step. The substrates were cleaned, and compact TiO_2 (TiO_2-c) film was deposited by the spray pyrolysis method. Then the samples were shifted to a nitrogen-filled glove box where the humidity and oxygen levels were strictly controlled below 0.1ppm level. The $CsPbI_3$ solution was spin-coated on the TiO_2-c with an intermediate MACl solution dripping during the spin-coating process. The wet films were either shifted to a dry air box glove box with humidity control around 1% (RH~ 1%) or annealed in ambient air (RH~ 35-50%). After the perovskite film formation, the samples were again shifted to the glove box, and then the molecules (long chain /dipole molecules) were deposited by spin coating method while the films were annealed in the glove box. On the well-passivated perovskite film, *i.e.* treated with molecules, the next layer of the HTM was also deposited in the glove box. The samples were soaked with oxygen in a dry air box, the step needed for the spiro-OMeTAD layer only, and then finally, the gold layer was evaporated in the glove box under a high vacuum.

Besides device fabrication, the most critical step is to do spin-coating on two molecules on the perovskite surface as a passivating and interlayer between perovskite film and HTM simultaneously. Either they tend to make phobic contact with the beneath layer or tend to dissolve the beneath layer. The best choice of solvent helped to resolve this issue. The perovskite surface was capped with two different molecules (OAI, TOPO) simultaneously.

Here the first molecule (*n*-OAI) was dissolved in a polar solvent *i.e.* Isopropyl alcohol. In contrast, the TOPO solution was prepared in Toluene, a non-polar solvent.

2.2 Ultraviolet-Visible spectroscopy (UV-Vis)

The basic principle of Ultraviolet-Visible spectroscopy (UV-Vis) is the absorption of the specific (wavelength of) light by the molecules in their ground state and their transition to the excited state. The absorption of the light holds the Beer-Lambert Law, which is given by, [(1)]

$$A = -log\frac{I_0}{I} = \varepsilon bc \qquad 2.1$$

Whereas,

A = Absorbance of the material (optical density).

I_0 = Incident intensity of the light.

I = Transmitted intensity of the light.

ε = absorptivity (the extinction coefficient).

b = Path length of the absorbing medium.

c = concentration.

Inversely the Transmittance is given by

$$T\ (\%) = 100\ \frac{I}{I_0} \qquad 2.2$$

$$A = -log_{10}T \qquad 2.3$$

The absorbance (A) of the light in a material has a logarithmic relationship to the transmittance (T). When there is no absorbance, then it is 100% transmittance. However, when absorbance is 1, then transmittance is 10%. While reflectance (R) is given by

$$R = 1 - (A + T) \qquad 2.4$$

Besides absorption properties, UV-Vis spectroscopy helps calculate the material's band gap and optical depth. $CsPbI_3$ has a critical band gap that changes with the temperature and varies for different polymorphs. [(2)] For an ideal semiconductor (*i.e.*defect-free) with a direct band gap the absorption coefficient is given by,

$$\alpha \propto \frac{\sqrt{h\nu - E_g}}{h\nu} \quad (2.5)$$

$$\alpha h\nu \propto \sqrt{h\nu - E_g} \quad (2.6)$$

That can be written as,

$$(\alpha h\nu)^2 \propto h\nu - E_g \quad (2.7)$$

The absorption coefficient (α) can be calculated using the following relation;

$$\alpha = \frac{2.303A}{d} \quad (2.8)$$

In the experiment, absorbance (A) was calculated by transmittance measurements of the thin films while thickness (*d*) of the film was measured by cross-sectional SEM of the perovskite film. **Equation 2.7**. defines the Tauc. plot method, in which, $(\alpha h\nu)^2$ is plotted against energy $(h\nu)$ and the linear segment is fitted to calculate the band gap (E_g)at the *x*-axis. [3,4]

2.3. Photoluminescence spectroscopy (PL)

When a material absorbs light higher than its band gap, the photoexcited carriers are generated in the lowest unoccupied molecular orbitals (LUMO). *i.e*. conduction band (CBM) leaving holes behind in the highest occupied molecular orbitals (HOMO levels) *i.e*. valence band (VBM) of the material. If these carriers are not extracted away (as in laser) these carriers recombine through the radiative process with the emission of photons (PL spectrum), this is known as the Photoluminescence phenomenon. However, non-radiative recombination leads to the emission of phonons. The following relation gives PL quantum yield (PLQY). [5]

$$PLQY = \frac{\phi_E}{\phi_A} = \frac{J_{rad}}{J_G} = \frac{J_{rad}}{J_R} = \frac{J_{rad}}{J_{rad} + J_{non-rad}} \quad (2.9)$$

Whereas ϕ_A is absorbed photon (s) flux and ϕ_E is emitted photon(s) flux. This relation shows that the higher the PL quantum yield values, the lesser the non-radiative recombination in a material will occur. The high PLQY values also indicate the excellent quality of the material with a lower density of traps. At open circuit conditions (V_{oc}), no current flows then generated current (J_G) and the recombination current (J_R) are equal. While J_R contains radiative (J_{rad}) and non-radiative ($J_{non\text{-}rad}$) components. The Shockley equation gives the radiative recombination.

$$J_{rad} = J_{0,rad} e^{\mu/K_B T} \quad 2.10$$

Where $J_{0,\ rad}$ is the current density in the dark (radiative recombination) [6] and K_B is the Boltzmann constant with values 1.380649×10^{-23} joule per kelvin (K). **Equation 2.9** is used to calculate the Qausi Fermi-levels splitting (QFLS) which is given by the following equation, [5]

$$QFLS = K_B T . \ln\left(\frac{J_{rad}}{J_{0,rad}}\right) = K_B T . \ln\left(PLQY \frac{J_{rad}}{J_{0,rad}}\right) \quad 2.11$$

Quasi-Fermi level splitting (QFLS) is the difference between the electrons and holes quasi-Fermi levels in the absorber layer under non-equilibrium conditions. QFLS tells about the energy level alignment at the interfaces as given by, [7]

QFLS = V_{oc} (Aligned energy levels)

QFLS> V_{oc} (Mis-aligned energy levels)

The PL spectrum for a semiconductor layer can be defined as, [8]

$$Y_{PL} \propto B(np - n_i^2) \quad 2.12$$

Whereas B is the radiative recombination coefficient, *n*, and *p* represent the densities of the holes and electrons respectively and n_i^2 is given by

$$n_i^2 = N_c N_v e^{\left(-E_g/kT\right)} \quad 2.13$$

Equation 2.12 can be modified as

$$Y_{PL} \propto B(\Delta n(t)^2 + \Delta n(t) p_0) \quad 2.14$$

While "Δn" which is carrier density in a semiconductor can be related to main recombination processes as

$$\frac{d}{dt}\Delta n(t) = -B\Delta n(t)^2 - A\Delta n(t)^3 - \frac{\Delta n(t)}{\tau} + G(t) \quad 2.15$$

Whereas, $B\Delta n(t)^2$defines radiative recombinations, $A\Delta n(t)^3$ is Auger recombinations, $\frac{\Delta n(t)}{\tau}$ represents Shockley-Read Hall recombination (SRH) and G(t) are surface recombination. Würfel related Y_{PL} with QFLS for the non-thermal conditions, Given that absorptivity as $a(E) = (1 - R)\ (1\ - e^{-ad})$

$$Y_{PL}(E) = \frac{1}{\frac{h^3}{2\pi}\frac{c^2}{n^2}} \frac{a(E)E^2}{\exp\left(\frac{E-\Delta E_{fn}}{kT}\right)-1} \quad 2.16$$

Here, h is Planck's constant, c is the speed of light, E is the energy of the photon, ΔE_{fn}defines QFLS, $a(E)$is the spectral absorptivity of the absorber, and *k* is the Boltzmann constant. This is known as Würfel's generalized Plank's law. [9]

Another mode of PL is known as transient Photoluminescence spectroscopy (TRPL). In TRPL we have a light pulse that generates carriers in the CBM and VBM of the materials. While in steady-state photoluminescence (stPL) we have constant illumination of the light. [10] It is a powerful technique used to study charge carrier recombination kinetics of a photoluminescent material and carrier lifetime.

$$I_{PL}(t) = A\exp\left(-\frac{t}{\tau_{fast}}\right) + B\exp\left(-\frac{t}{\tau_{slow}}\right) \quad 2.17$$

In the equation, the coefficients A and B define the relative amplitudes for the fast and slow lifetimes,τ_{fast} and τ_{slow}. An effective photoluminescence lifetime τ_{eff} can be given by the following relation [11]

$$\tau_{eff} = \frac{A\tau_{fast} + B\tau_{slow}}{A+B} \quad 2.18$$

2.4. X-ray Diffraction (XRD)

In a crystal such as a perovskite, the atoms are arranged in a periodic order. The periodic interatomic distance "*d* " can be obtained from Bragg's law due to constructive interference of the incident X-ray beam with wavelength λ.

$$n\lambda = 2dSin\theta \quad 2.19$$

In this technique, the incident X-rays at angle θ are scattered at the atoms of the crystal. The detector continuously scans the angle 2θ *via* a goniometer and detects a signal whenever the X-rays reflected in the periodic arrangement interfere constructively. The incident beam can be at a fixed angle (grazing incidence geometry) or vary symmetrically to the goniometer (Bragg-Brentano geometry). This way, a diffractogram is obtained. From the diffraction pattern, the space group can be derived. The individual peak positions and integral breadths contain information about the sample's microstructure (crystallite size and microstrain).

As $CsPbI_3$ assumes different phases within different temperature regimes, XRD can be used to confirm its crystal structure. [12]

2.5. Scanning Electron Microscopy (SEM)

The beam of electrons that is accelerated with high voltage, upon interaction with the material for analysis, causes various photons and electron emissions *i.e.* secondary electrons, backscattered electrons (BSE), auger electrons, electron-hole pairs, elastically scattered electrons and inelastically scattered electrons, *etc.*, which leads to making practical analytical techniques. These include wavelength and energy-dispersive X-ray spectroscopy (EDX, WDX), Electron backscatter diffraction (EBSD), Electron beam induced current (EBIC), Cathodoluminescence (CL) and Scanning electron microscopy (SEM), *etc.* [13,14]

The SEM technique combines secondary electrons (SE) and backscattered electrons (BSE). The emission of secondary electrons tells about topography, potential contrast, and doping contrast in the specimen (film) [15], while BSE(s) are used for composition and crystallographic study by SEM. [16]

This work used the SEM technique to analyze the grain size and morphology of the bare and passivated perovskite film. It also comprises devices with cross-sectional images for layer analyses and thickness measurements.

2.6. Kelvin Probe Measurements (KP)

The Kelvin Probe method is used for the work function "Φ" (WF) measurements. This method makes the material (sample) and the reference probe a parallel plate capacitor. The working principle has been demonstrated in **Fig.2.2**. **Figure 2.2a** shows that when the two materials (reference probe and sample) are separate and have different electronic energy levels and energy diagram *i.e.* Fermi-levels and Φ but their vacuum level is the same. However, when a wire connects these materials the current flows until the equilibrium is attained and their Fermi-levels (E_f) are aligned. The current flow in the circuit from the lower work function to the higher work function *i.e.* from material (sample) to the reference probe.

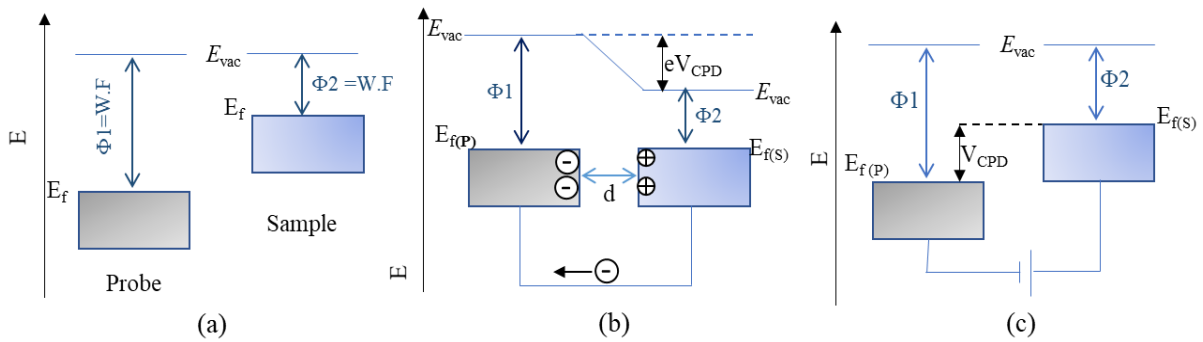

Figure 2.2 The working principle of the Kelvin probe method. (a)The Fermi levels of the probe and sample, are aligned to the vacuum levels. (b)The reference probe and the sample after connection, their Fermi-levels align (c) An applied external voltage equal (but opposite in direction) to the V_{CPD} is induced until the vacuum level is aligned and no current flows. $E_{f(P)}$ and $E_{f(s)}$ are the Fermi levels of the probe and the material (sample). Φ1 and Φ2 are the probe and sample work functions, respectively. E_{vac} is the vacuum level, and *d* is the distance between the sample and probe (parallel plate capacitor).

Figure 2.2b shows that the drop in vacuum level is referred to as a potential difference (contact potential difference V_{CPD}) related to the change in WF.

$$\Delta WF = \Phi 1 - \Phi 2 = eV_{CPD} \qquad 2.20$$

Figure 2.2b shows a parallel plate capacitor in which the relation can calculate the potential difference (VCPD) $Q = C.V$. Where 'Q' is the stored charge and 'C' is the capacitance. In this relation, Q cannot be measured precisely for this experiment. Lord Kelvin devised the method by applying external voltage (V_b) which is equal but opposite to $V_{CPD,}$ which causes the discharge in the capacitor and E_{vac} to get aligned again as shown in **Figure 2.2c**. [17] The following relation can calculate the WF of the samples

$$V_{CPD} = -V_b \qquad 2.21$$

$$V_{CPD} = \frac{WF_s - WF_P}{e} \qquad 2.22$$

To ensure that the WF of the probe remains constant inert materials like gold metal are used as a reference probe. Due to the inert nature of the reference probe, this method can be used to measure the change in KP of the semiconductor's work function with light. The light-induced change in electrostatic potential between the sample and reference material leads to another technique that is known as surface photovoltage (SPV). [18]

2.7. Transient Surface Voltage (trSPV)

Charge extraction at the interfaces is measured using transient surface photovoltage spectroscopy (tr-SPV). The tr-SPV amplitude is given.

$$\mathrm{SPV(t)} \propto (n(\mathrm{t}) - p(\mathrm{t})) \times 0.5\mathrm{L}) \qquad 2.23$$

The signal amplitude is directly proportional to the charge-separated charges at a device's interfaces (buried) (L is the thickness of the light absorber layer, *i.e.* $CsPbI_3$ film in our work). Transient SPV provides essential insights into the dynamics of charge extraction and recombination. [19,20] It also helps us to distinguish the different processes at the interfaces [21] This technique was employed to study the self-assembled monolayer-composed hole transport materials for the efficiency of hole extraction. [20]

2.7.1 Simulations of Charge Extraction and Recombination

Equation 2.24 describes the simulation model for charge separation, trapping, and recombination where *n* and *p* are the concentration of photo-induced electrons and holes. K_e and K_h constants correspond to electron and hole injection rates from perovskite to HTM. The constant K_{eTiO} corresponds to electron injection rates from perovskite to the electron transport layer (TiO_2). Similarly, K_{eb} and K_{hb} are reinjection rates of electron and hole to perovskite from the hole transport layer (HTM) *i.e.* Spiro-OMeTAD, which effectively include back tunneling /thermionic emission, and diffusion of the free carriers, as well as the drift of the free carriers due to the presence of the space charge. C_b is radiative recombination constant. N_t and σ are concentration and capture a cross-section of defects responsible for SRH non-radiative recombination. τ_{HTM} and τ_{ETM} characterizes the carriers' lifetime in HTM and ETM. The system of the equations cannot be solved analytically; therefore, the Adams backward differentiation formula (BDF) is used for solving algorithm. The Levenberg-Marquardt method has been used to fit constants with minimal deviation from experimental SPV results. SPV data were extrapolated logarithmically for better fitting results. [22]

$$\frac{dp}{dt} = -K_h p + K_{hb} p_{HTM} - C_b(pn) - p\sigma_{ht} v_h n_t \qquad 2.24$$

$$\frac{dn}{dt} = -K_e n + K_{eb} n_{HTM} - C_b(np) - n\sigma_{et} v_e (N_t - n_t) - K_{eTiO} n \qquad 2.25$$

$$\frac{dp_{HTM}}{dt} = K_h p - K_{hb} p_{HTM} - \frac{p_{HTM}}{\tau_{HTM}} \qquad 2.26$$

$$\frac{dn_{HTM}}{dt} = K_e n - K_{eb} n_{HTM} - \frac{n_{HTM}}{\tau_{HTM}} \qquad 2.27$$

$$\frac{dn_{ETM}}{dt} = K_{eTiO}n - \frac{n_{ETM}}{\tau_{ETM}} \quad 2.28$$

$$\frac{dn_t}{dt} = n\sigma_{et}v_e(N_t - n_t) - p\sigma_{ht}v_h n_t \quad 2.29$$

More significant $d_{PER} \gg d_{HTM}$, $d_{PER} \gg d_{ETM}$**,** and assuming a uniform distribution of charges in perovskite, ETM, and HTM layers; so SPV signal can be simplified in the form

$$SPV = \frac{L}{2}\frac{n_{ETM}}{\varepsilon_{TiO}\varepsilon_0} + \frac{L}{2}\frac{n_{HTM} - dp_{HTM}}{\varepsilon_{HTM}\varepsilon_0} + \frac{L}{2}\frac{n - p - nt}{\varepsilon_{pero}\varepsilon_0} \quad 2.30$$

Where $L = d_{PER}/2$ -charge separation distance

2.8. Photoemission Spectroscopies

X-ray photoemission spectroscopy (PES) based techniques are widely used to study surface chemistry, energetics, and electronic profile of the interfaces in perovskite halides solar cells (PSC). [23,24] These are considered non-destructive techniques and include X-ray photoelectron spectroscopy (XPS), hard X-ray photoemission spectroscopy (HAXPES), ultraviolet photoemission spectroscopy (UPS), and inverse photoemission spectroscopy (IPES), *etc*.

PES is based on the law of photoelectric-effect which was explained by Albert Einstein in 1905 and given as

$$K_{max} = hv - \Phi \quad 2.31$$

These techniques are generally measured under high vacuum conditions (UHV) [25] as this method minimizes the surface contamination of the sample and offers the measurements in a more realistic environment. Nevertheless, these techniques are very surface sensitive and their probing depth in a PES measurement is linked to their inelastic mean free path (IMFP). The IMFP is defined as the mean distance that an injected electron, with definite kinetic energy, can cover through the lattice until it scatters (inelastically), and loses its energy to the surroundings. **Figure 2.3** shows the "universal curve" that relates IMFP with wavelength and yields the approximate attenuation length for different PES techniques.

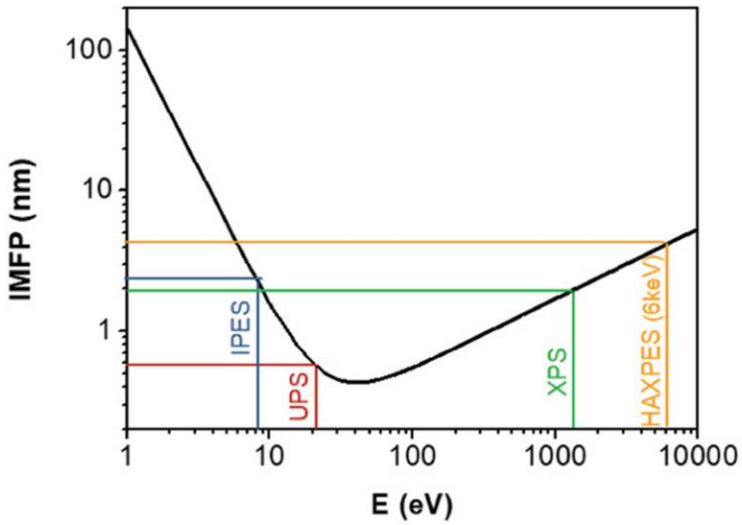

Fig.2.3. The plot of the Inelastic mean free path (IMFP) of the electrons versus the electron kinetic energy for different techniques. Adapted with permission, [26] *John Wiley and Sons*.

Figure 2.4(a) explains different energetics quantities that can be measured by using PES techniques. As per Molecular theory (MOT) the orbitals of the atoms overlap to make the molecular orbitals and make HOMO and LUMO energy levels. While band theory describes the position of the electron (energy levels) which states that these HOMO levels make the band known as the valence band and its energy position is defined as the valence band maxima (VBM), while the LUMO levels make the conduction band and its energy level corresponds to conduction band minima (CBM). While the following relations give work function and Ionization energy

$$\Phi = E_{Vac} - E_f \qquad 2.32$$

$$\text{IE} = E_{Vac} - E_{VBM} \qquad 2.33$$

Photoemission spectroscopy has three operational steps.

1. The sample is irradiated by the high-energy photons These are generated by an X-ray tube, a gas discharge lamp, or by synchrotron beams, or by laser excitation) then the electrons are injected following the photoelectric effect as shown in **Figure 2.4**.
2. These excited electrons travel to the vacuum level(surface). While on their way to the surface, these experience many scatterings and hence lose a part of their initial kinetic energy.
3. The electrons that do not lose their kinetic energy, escape the surface and are detected by the spectrophotometer. The kinetic energy of these electrons can be related to their binding energies.

We can write these step mathematically as follow

$$E_k = h\nu - E_B - \Phi \qquad 2.34$$

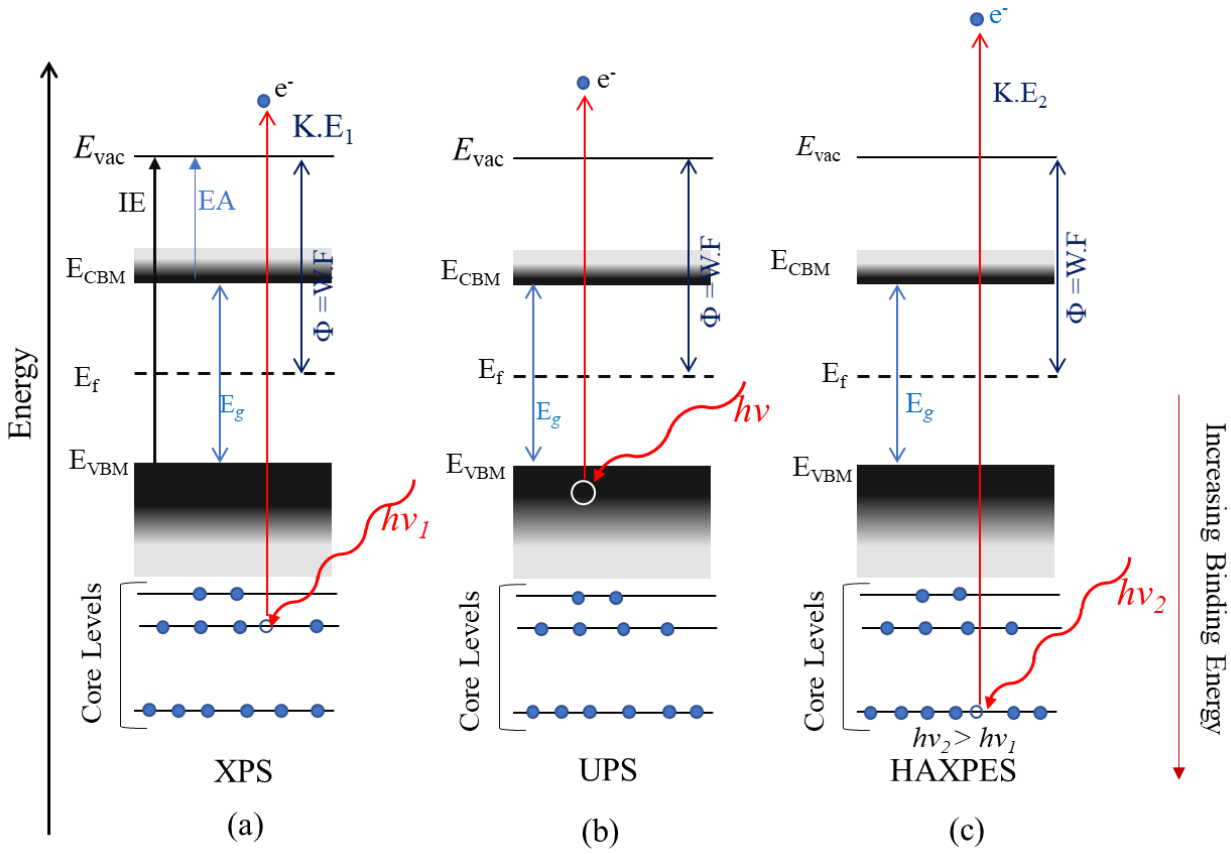

Figure 2.4 Schematic energy diagram of PES, illustrating (a) XPS (b)UPS (c) HAXPES. The abbreviations are already discussed in the text.

2.8.1.X-Ray Photoelectron Spectroscopy (XPS)

XPS measurements give information about the surface-confined elements and their chemical environment (chemical shift). In this technique, photons are excited by energies between 150eV and 2000eV, considered in the soft X-ray range. The typical sources available for laboratory-based XPS measurements are Al kα(1486.6eV) and Mg kα(1256.6eV) based radiations.

In a sample under analysis, all the elements (on the surface) show specific peaks in the spectrum. These peaks are related to the energy levels of the elements in that composition. The peak analysis can determine the material's composition and the chemical environment. Compared to literature values, the chemical shift in the binding energy of the orbital (s) tells about the chemical environment and composition. [27,28]

XPS peaks notation is based on term symbols (quantum numbers) and is commonly used in the literature. [28] For example, in "I $3d_{5/2}$", 3 represents the principle quantum number (n) that is given by,

n =1, 2, 3, 4……,

Then "d" is orbital angular momentum quantum number (l) *i.e.* whereas the values of orbital angular momentum quantum number correspond as

l =0,1,2,3,4……(n-1),

l= 0 is for S orbital,

l= 1 is for p orbital

l=3 is for f orbital

s represents the spin angular momentum quantum number *i.e.* +½, -½. The total angular momentum is given by,

$$J = l + s \qquad 2.35$$

For *l=0, s* orbital is singlet, so there is no splitting. For *l>0 i.e. p, d, f.*The "*j*" levels give rise to doublets. The binding energy between two *j*-values *i.e.* $3d_{5/2}$ and $3d_{7/2}$ is known as spin-orbit splitting. The binding energy (B.E) of the level with lower "*j*" values in doublet has higher binding energy for example B.E of $3d_{5/2}$ > B.E $3d_{7/2.}$The values of the spin-orbit splitting decrease with distance from the nucleus due to the increased shielding effect.

2.8.2. Hard X-Ray Photoemission Spectroscopy (HAXPES)

The working principle of HAXPES is similar to XPS. In HAXPES, higher excitation energies are used compared to XPS [29] as shown in **Fig 2.4c**. These can be generated by synchrotron by using Ag Lα(3984.2eV) anode for laboratory-based measurements. Due to higher energy excitations, the penetration depth is increased. This is considered a reliable technique for studying buried interfaces. [30]

2.8.3. Ultraviolet Photoemission Spectroscopy (UPS)

In UV photoelectron spectroscopy measurements, lower energies are used than XPS and HAXPES. In **Figure 2.3,** the universal curve shows UPS has less penetration depth. It can

probe the electrons in the top surface atoms' outermost valence levels, which gives information about the material's work function and valence band edge (VBM).

In measurements, the samples are exposed to UV photons generated by either He(I) or He(II) discharge lamps with emissions at 21.2eV and 40.8eV respectively.

In PES techniques, when the excited electrons travel through the solid (bulk), experience collisions. These tend to lose their initial kinetic energy on their way to the vacuum levels and these make a background contribution to the (photo)electron distribution curve (EDC). In UPS data, the spectrometer collects the excited electrons to recover the curve and density of the states, which gives information about VBM. [31]

2.9. Device Performance (*JV*, EQE)

The performance of a device can be described in terms of power conversion efficiency (PCE) current-voltage characteristics (*J-V* measurements), External Quantum Efficiency (EQE), and long-term stability under operation.

Figure 2.5 describes *J-V* measurements under dark and illuminations. The following relation defines the PCE of the device

$$PCE = FF.\frac{V_{oc}I_{sc}}{P_{in}} \tag{2.36}$$

The following relation gives the Fill Factor (FF)

$$FF = \frac{V_{mp}I_{mp}}{V_{oc}I_{sc}} \tag{2.37}$$

Whereas I_{mp} and V_{mp} are the current and voltage at the maximum power point. It is described in **Figure 2.5.**

$$Maximum\ Power\ Point\ (mpp) = FF \times V_{oc} \times I_{sc} \tag{2.38}$$

External Quantum Efficiency is defined as a function of the wavelength of the photons. It is defined as the ratio of the conversion of an incident photon (incoming) to an electron by the solar cell. EQE is also used to measure the J_{sc} of the device under the light.

$$J_{sc,EQE} = \int_{\lambda=300}^{\lambda=800} qEQE(\lambda)S(\lambda)d\lambda \tag{2.39}$$

Figure 2.6 illustrates the EQE diagram. Ideally, one incoming photon should produce one electron-hole which corresponds to 100%EQE. However, EQE is reduced due to several factors that include reflection and transmission of the photons from the surface. Other than these factors EQE is also reduced due to surface recombination and low diffusion length.

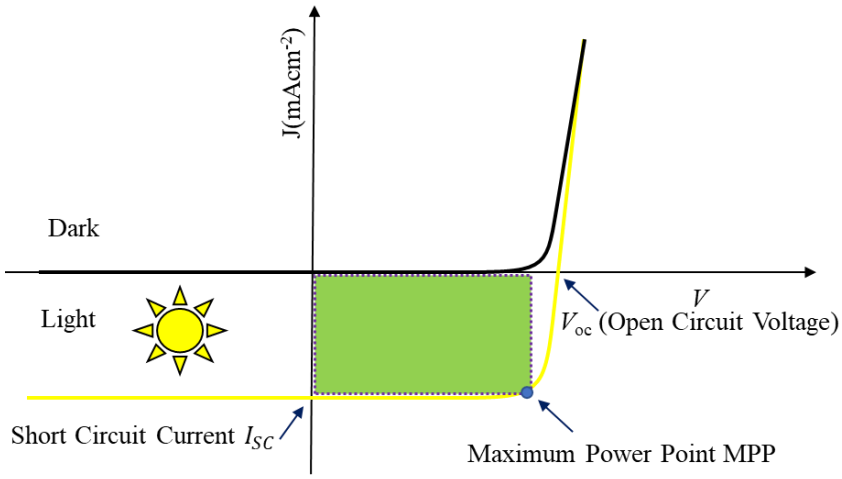

Fig 2.5. *J-V* characteristic of a solar cell device under dark and under illumination.

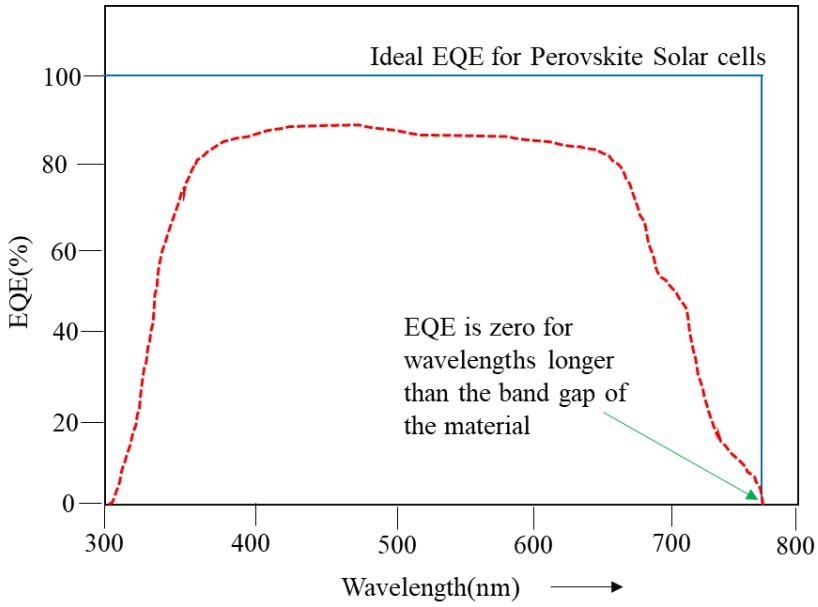

Fig 2.6. EQE of the perovskite solar cell device was measured under 1 sun illumination.

2.10 Stability Testing

It measures the evolution (change in) of PCE with time. Generally, the efficiency is measured with time on maximum power point known as MPP tracking up to a hundred hours. It gives the information about the stability of the devices. The figures of merit for stability are T_{80} and

T_{s80}. T_{80} is when 20% of the initial PCE drops to 80% and is considered the optimal stability testing time. Whereas T_{s80} is "stabilized T_{80} time". During the aging test, the device drops its PCE rapidly known as "burn-in" and stabilizes. T_{s80} is when there is a 20% drop in the PCE of the device after burn-in. [32,33]

Recommended books

1. "Optical Processes in Semiconductors" by Jacques I. Pankove, Prentice-Hall, 1971.
2. "Advanced Characterization Techniques for Thin Film Solar Cells" by Abou-Ras *et al*, Wiley-VCH, (2011), p299-341.
3. "Physics of Solar Cells-From Basic Principles to Advanced Concepts" by Peter Würfel, WILEY-VCH, EUR 57,99
4. "The Physics of Solar Cells" By Jenny Nelson. Imperial College Press.
5. "Materials Concepts for Solar Cells" By Thomas Dittrich Imperial College Press, 2014.
6. "Surface Photovoltage Analysis of Photoactive Materials", By Thomas. Dittrich and Steffen. Fengler, World Scientific (Europe) 2020.

References

1. Swinehart, Donald F. "The beer-lambert law.", *Journal of Chemical Education*, 1962, 39,**7**,333-335.
2. L. A. Frolova, D. V. Anokhin, A. A. Piryazev, S. Yu. Luchkin, N.N. Dremova, K. J. Stevenson, and P.l A. Troshin., " Highly Efficient All-Inorganic Planar Heterojunction Perovskite Solar Cells Produced by Thermal Co-evaporation of CsI and PbI2.", *Journal of Physical Chemistry Letter*, 2017, **8**, 67−72
3. J. Tauc, "Amorphous and Liquid Semiconductors.", *Springer*, Boston, MA, 1974,159.
4. J. Tauc., "Optical properties and electronic structure of amorphous Ge and Si.", *Materials Research Bulletin*, 1968, **3**,37-46.
5. P.Caprioglio, M. Stolterfoht, C. M. Wolff, T.Unold, B.Rech,S. Albrecht, D. Neher., " On the Relation between the Open-Circuit Voltage and Quasi-Fermi Level Splitting in Efficient Perovskite Solar Cells.", *Advanced Energy Materials*, 2019, **9**, 1901631.
6. J.Yao, T. Kirchartz, M.S. Vezie, M. A. Faist, W.Gong, Z. He, H. Wu, J. Troughton, T. Watson, D.Bryant, J.Nelson., "Quantifying Losses in Open-Circuit Voltage in Solution-Processable Solar Cells.", *Physical Review Applied*, 2015, ***4,*** 014020.
7. M.Stolterfoht, D. Neher, *et al.*, "The impact of energy alignment and interfacial recombination on the internal and external open-circuit voltage of perovskite solar cells.", *Energy & Environmental Science*, 2019, **12**, 2778.

8. T. Kirchartz, J. A.Märquez, M. Stolterfoht,T.Unold., " Photoluminescence-Based Characterization of Halide Perovskites for Photovoltaics.", *Advanced Energy Materials*, 2020, **10**, 1904134.
9. P. Würfel, "The chemical potential of radiation", *Journal of Physics C: Solid State Physics*,1982, **15**, 3967-3985.
10. H. Cho, S. H Jeong, M.H.Park *et al*, "Overcoming the electroluminescence efficiency limitations of perovskite light-emitting diodes.", *Science.* 2015, **350**, 1222-5.
11. T. Unold and L. Gütay, Advanced Characterization Techniques for Thin Film Solar Cells, Edited by D. Abou-Ras, T. Kirchartz and U. Rau, Wiley-VCH, 2011, 151–175.
12. A. Marronnier, J. Even *et al*., "Anharmonicity and Disorder in the Black Phases of Cesium Lead Iodide Used for Stable Inorganic Perovskite Solar Cells.", *ACS Nano* 2018, **12**, 3477−3486.
13. H. Seiler., "Electron Spectroscopy in the Scanning Electron Microscope.", *Ultramicroscopy*,1985,**17**,1-8.
14. Abou-Ras *et al*, "Advanced Characterization Techniques for Thin Film Solar Cells" Wiley-VCH, (2011), 299-341.
15. S. L. Elliott, R. F. Broom, C. J. Humphreys., "Dopant profiling with the scanning electron microscope—A study of Si.", *Journal of Applied Physics*, 2002, **91**(11), 9116–9122.
16. T. Zaefferer, N. N. Elhami, "Theory and application of electron channeling contrast imaging under controlled diffraction conditions.", *Acta Materialia*,2014,**75**,20-50.
17. L.Kelvin. "Contact Electricity of Metals.", *Philosophical Magazine Series*,1898, **5**(46), 82–120.
18. L. Kronik and Y. Shapira, "Surface photovoltage phenomena: theory, experiment, and applications.", *Surface Science Reports*,1999, **37**(1).
19. T. Dittrich and S. Fengler, "Surface Photovoltage Analysis of Photoactive Materials", World Scientific (Europe), 2020.
20. I.Levine, A. Al Ashouri, A. Musiienko, *et al*., "Charge transfer rates and electron trapping at buried interfaces of perovskite solar cell", *Joule*, 2021, **5**, 2915–2933.
21. S. Fengler, H. Kriegel, M. Schieda, *et al*., "Charge Transfer in c-Si(n++)/TiO2 (ALD) at the Amorphous/Anatase Transition: A Transient Surface Photovoltage Spectroscopy Study.", *ACS Applied Materials & Interfaces*, 2020, **12**, 3140−3149.
22. K. Prashanthan, I. Levine, A. Musiienko, E. Gutierrez-Partida, H. Hempel, K. Lips, *et al*., " Internal electric fields control triplet formation in halide perovskite-sensitized photon upconverters.", *iScience*, 2023, **26**(4)
23. G. Sadoughi, D. E. Starr, E. Handick, S. D. Stranks, M. Gorgoi, R. G. Wilks, M. Bär, H. J. Snaith., "Observation and Mediation of the Presence of Metallic Lead in Organic–Inorganic Perovskite Films.", *ACS Applied Materials & Interfaces*,2015, **7**, 24.
24. D. E. Starr, G. Sadoughi, E. Handick, R. G. Wilks, J.H. Alsmeier, L. Köhler, M. Gorgoi, H.J.Snaith,M. Bär., "Direct observation of an inhomogeneous chlorine distribution in $CH_3NH_3PbI_{3-x}Cl_x$ layers: surface depletion and interface enrichment.", *Energy & Environmental Science*, 2015, **8**, 1609-1615.
25. J. F. Watts, J. Wolstenholme, "An Introduction to Surface Analysis by XPS and AES.", *John Wiley & Sons, Ltd, Chichester, UK* 2003.

26. S. Bochu, M.Ralaiarisoa, A.Etcheberry, P. Schulz., “Photoemission Spectroscopy Characterization of Halide Perovskites.” *Advanced Energy Materials*, 2020, **10**, 1904007
27. P. van der Heide, “X-Ray Photoelectron Spectroscopy: An Introduction to Principles and Practices.”, Wiley, Hoboken, NJ 2011.
28. J. F. Moulder, W. F. Stickle, P. E. Sobol, K. D. Bomben, “Handbook of X-Ray Photoelectron Spectroscopy.”, Perkin-Elmer Corporation, Eden Prairie, MN 1992.
29. C. S. Fadley, in Hard X-Ray Photoelectron Spectroscopy (Ed: J. Woicik), Springer International Publishing, Cham 2016.
30. J. Zillner, H.-G. Boyen,.P. Schulz, J. Hanisch, N. Gauquelin,J. Verbeeck, J. Küffner, D. Desta, L. Eisele, E. Ahlswede,M. Powalla.,“ The role of SnF_2 additive on interface Formation in All-Lead-free $FASnI_3$ Perovskite Solar Cells.” *Advanced Functional Materials.* 2022, **32**, 2109649.
31. S. Morton, Handbook Spectroscopy, Wiley-VCH Verlag GmbH & Co. KGaA, Weinheim, Germany, 2014,779–820.
32. M.V. Khenkin, E.A. Katz, A. Abate, *et al.* “Consensus statement for stability assessment and reporting for perovskite photovoltaics based on ISOS procedures”, *Nature Energy*, 2020, **5**, 35–49.
33. L. Rakocevic, F. Ernst, N. T. Yimga, *et al.* “Reliable Performance Comparison of Perovskite Solar Cells Using Optimized Maximum Power Point Tracking”, *Solar RRL*, 2019, **3**, 1800287.

Chapter 3

The Potential Effect of Dry and Ambient Air Annealing Environment on the $CsPbI_3$ Surface Chemistry and its Subsequent Interfacial Dynamics.

This chapter is based on the peer review article submitted "**Unveiling the Potential of Ambient Air Annealing for Highly-Efficient Inorganic $CsPbI_3$ Perovskite Solar Cells**." This manuscript is under review by the time of writing this chapter,

3.1 The Highlight of the Work

The annealing step plays a significant impact on the crystallization, growth kinetics, and thus overall quality of the perovskite film. Generally, inorganic perovskite halide films are annealed in dry air or ambient air. However, the influence of the annealing environment on the surface chemistry, on the following interfaces, and the interface dynamics have not been investigated so far. $CsPbI_3$-based solar cells have been reported as the most stable perovskite solar cells with 17% efficiency and stability up to 33 years of outdoor operation. To increase its efficiency further, and to find the marketplace, it is imperative to study the surface and its consequent interfaces thoroughly. This chapter includes the key findings that will bridge the knowledge gap for $CsPbI_3$ surface and interface dynamics.

3.2 Introduction

Inorganic halide perovskites promise to outperform their organic-inorganic hybrid counterparts in terms of their long-term stability at operating temperatures (reaching up to 65 °C). [(1)] Among the $CsPbX_3$ compositions, $CsPbI_3$ has the lowest bandgap, E_g (~ 1.7 eV) [(2)], making it an excellent candidate for applications in a tandem structure. [(3)] Owing to the better chemical and thermal stability, $CsPbI_3$ has received great attention in the perovskite photovoltaic community. [(4)] $CsPbI_3$ undergoes crystal phase transitions, transforming from a cubic (α) phase to a tetragonal (β) phase, to an orthorhombic (γ) phase as its temperature decreases from above 300 °C to room temperature. [(5)] Due to the low tolerance factor in $CsPbI_3$, maintaining phase stability at room temperature requires considerations. [(6)] (The strategies for phase stability have been summarized in **Chapter Section 1.3**).In addressing the cited challenge, Y.Wang *et al.* introduced dimethylammonium iodide (DMAI) in the precursors of $CsPbI_3$, which resulted in a stabilized β-phase with a band gap of 1.68 eV. [(7,8)] While the critical role of this organic moiety DMAI has been investigated largely. It is concluded that it takes part in crystallization but it does not retain in the crystal structure whereas it sublimizes in dry air annealing [(8-11)] It

is also been found that annealing in the presence of oxygen removes the organic cations added in the precursor solution and passivates halide vacancies. [12,13]

As mentioned, the annealing step in all-inorganic perovskites is very important for its film growth and crystallization. Generally, the samples are annealed in a dry air box or ambient air. To compare the annealing process in two different environments and then their potential impact on the properties of $CsPbI_3$ is investigated here. One annealing process was performed in a dry air box in which the relative humidity (RH) was strictly controlled by ~1% by dry airflow (hereafter, mentioned to as "dry air") and the other annealing process was performed in ambient air with RH between ~45-50 % (hereafter, mentioned to as "ambient air"). The as-prepared $CsPbI_3$ films were afterward treated with *n*-OAI making a 10-20 *nm* layer with a 2D structure, thereby improving their stability. [14,15] As a reference sample, the dry air box annealed $CsPbI_3$ without *n*-OAI (hereafter, referred to as "OAI-free"). In this work, a detailed analysis of the interface between $CsPbI_3$ and the hole transport material (HTM) is reported. Further, it investigated how its properties are affected by annealing in ambient air and a dry air box. The transient surface photovoltage (tr-SPV) technique was applied to measure the charge extraction and trap state density on the $CsPbI_3$/HTM interface. A very detailed Hard X-ray photoelectron spectroscopy (HAXPES) measurements reveal that annealing in air results in a modification of the $CsPbI_3$ surface/interface region that can be explained by band bending enhancement. Finally, $CsPbI_3$-based devices were fabricated. Using ambient air-annealed absorbers, PCE values of up to 19.80% are reached with an average 50meV increase in the V_{OC} of the devices. This work, thus paves the way for new fabrication strategies involving air annealing processing

3.3 Experimental section

The detailed method is described in **Appendix section A3.1 - 3.2**. However, the annealing step is added here. The wet films were annealed in a dry air box with relative humidity (RH) of ~ 1% for 1 min at 210 °C and other films were annealed in the air in a fume hood at 210°C (RH~45-50%) until a black perovskite film was obtained.

3.4 Film Characterization

Initially, the films were characterized with Ultraviolet-Visible (UV-Vis) absorption spectroscopy and steady-state photoluminescence emission spectroscopy (st-PL) as shown in **Figure 3.1a**. The left coordinate of **Figure 3.1a** shows that both $CsPbI_3$ films have absorption edges around ~735 nm with a band gap of around ~1.69 eV as shown in **Figure 3.1b** which is

consistent with the available literature values. [7,8] The st-PL was performed through an excitation wavelength of 445 nm on the top side of the film (perovskite side). The excitation wavelength and the direction of illumination are important in PL analysis to know the penetrations and surface passivation. [16] The dry air annealed film shows peak emission at 764.31 nm while the ambient air annealed film exhibits stronger PL intensity with a blue-shift peak emission at 762.54 nm. The higher PL intensity and blue shift in the excitation peak indicate a decrease in traps on the surface of $CsPbI_3$ film [13,16]

In **Figure 3.1a**, it can be seen that emission peaks of both dry air annealed and ambient air annealed $CsPbI_3$ films are centered at around 1.62 eV (~762-764nm), which is around 80 meV smaller than the optical bandgap. The red shift in PL emission spectra is known as the " Stokes shift " and it has been reported in organic-inorganic hybrid perovskite thin films. [17] A bit higher Stokes shift in inorganic perovskite halides can be attributed to the higher Urbach energy of $CsPbI_3$ perovskite films **(Appendix A4.2)** nearly five times higher than organic-inorganic hybrid perovskite thin films as $MAPbI_3$ films have Urbach energy around 4meV.[18]

Furthermore, the morphology of both films was analyzed by scanning electron microscopy (SEM) **Figure 3.1c-d** shows cross-sectional SEM images for the dry air and ambient air annealed $CsPbI_3$, from which it is inferred that both films have epitaxial growth, almost the same thickness. These films have a similar grain size as confirmed by top-view SEM images (**Figure A3.1**). XRD analysis also confirms that there is no yellow phase while both control and target film exist in orthorhombic (γ) and tetragonal phase (β) as shown in **Figure A3.2.**

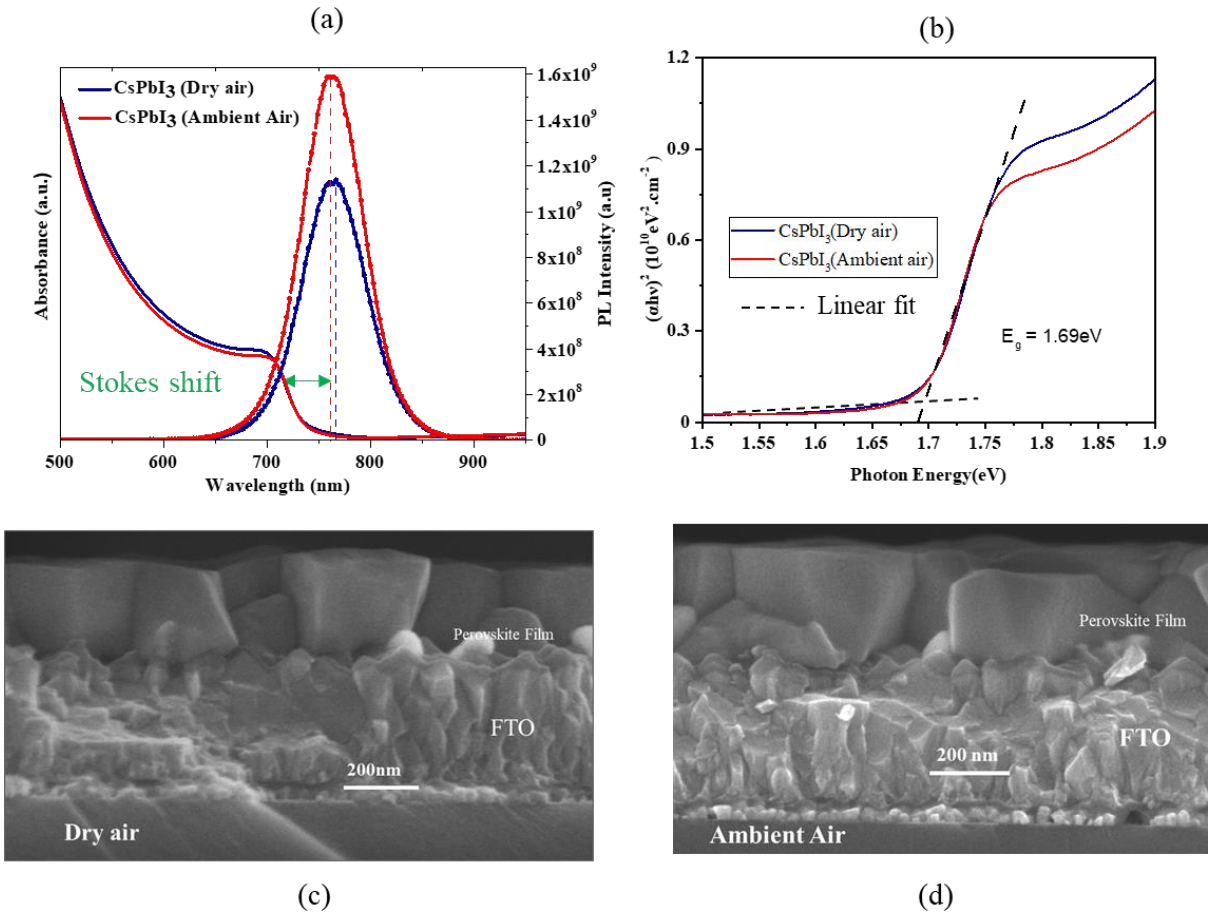

Figure 3.1 Films characterization. a) Absorbance and emission spectra of dry and ambient air annealed films measured by UV-Vis spectroscopy (left coordinates) and steady-state photoluminescence emission spectroscopy (right coordinates). b) Tauc plots of dry air annealed and ambient air annealed $CsPbI_3$ film calculated from UV/Vis absorption spectra. Cross-sectional SEM images of both, c) dry air and d) ambient air at high magnification (scale bar = 200nm). These films were deposited on FTO/compact TiO_2 substrates.

3.5. Surface Chemistry and Electronic Structure Profile Investigation by HAXPES

HAXPES was employed to characterize the chemical structure of $CsPbI_3$ and its interface to the HTM and how it is changed by the different annealing processes *i.e.* annealing in a dry air box and annealing in ambient air. To study this, the $CsPbI_3$ samples were deposited on Fluorine-doped tin oxide (FTO) coated glass substrates, which is a transparent conducting oxide material used in solar cell devices. These samples include $CsPbI_3$ films annealed in dry and ambient air, both covered with *n*-OAI while a dry air annealed sample without *n*-OAI (as mentioned, OAI-free). These three samples are designated as bare samples as they do not have an HTM layer. (*i.e.* spiro-OMeTAD). To study the $CsPbI_3$ interface, a series of additional samples with HTM layers are prepared. The spiro-OMeTAD layers of 5nm,20 nm, and 200 nm

were deposited on the dry air annealed and ambient air annealed samples. The purpose of making various thickness layers of HTM is to probe the interface by HAXPES. Normally, in a device ~200nm spiro-OMeTAD layer is deposited. However, the $CsPbI_3$/HTM interface cannot be probed through this layer. The relationship between the penetration depth and the excitation energy is illustrated in **Section 2.8** in **Chapter 2** in detail. **Figure 3.2a** shows the HAXPES survey spectra of the bare samples that show Cs, Pb, and I-related photoemission signals in all samples while C and N-related photoemission signals only in the OAI-treated samples.

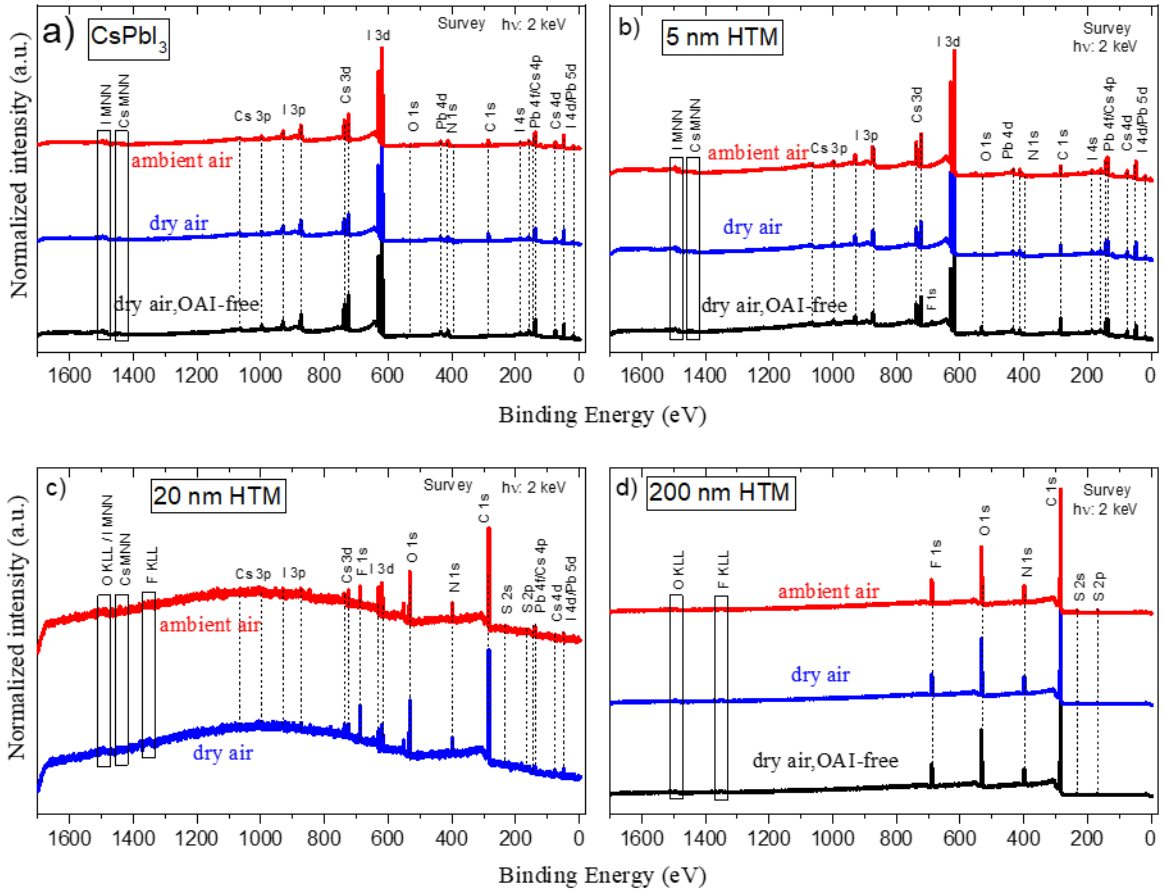

Figure 3.2 Hard X-ray photoelectron spectroscopy (HAXPES) survey spectra of $CsPbI_3$ films (*i.e.*, dry air annealed OAI-free, dry air annealed (covered with *n*-OAI) and ambient air annealed (covered with *n*-OAI) a) with no HTM layer. These samples were covered with b) 5 nm, c) 20 nm, and d) 200 nm films of Spiro-OMeTAD. The spectra were measured using 2 keV excitations and normalized to background intensity, with vertical offsets added for clarity.

Contrarily to previous reports that terminal ions make bonds with oxygen at the surface,[13] no bonded oxygen is seen to result from the annealing treatments in different RH, and close investigation of the most prominent halide perovskite-related HAXPES peaks, Cs 3d, I 3d, and Pb 4f **Figures 3.3** and **A3.3** and the corresponding shallow core level peaks, Cs 4d, I 4d, and

Pb 5d **Figures 3.4 and A3.4** show no significant change in line shape between the measurements of the dry air and ambient air annealed (and *n*-OAI passivated) $CsPbI_3$ absorbers. These measurements were performed in both 2keV and 6keV excitations owing to differences in their penetration depth. However, *n*-OAI-modified $CsPbI_3$ shows relatively broader emission lines as compared to OAI-free samples. This can be attributed to the formation of an *n*-OAI-modified thin surface layer. Furthermore, the OAI-free $CsPbI_3$ absorber also exhibits a small signal from metallic Pb, which is absent in the *n*-OAI treated samples, as shown in **Figures A3.3c** and **A3.4c** The survey spectra of the HTM thickness series in **Figures 3.2 b-d** are consistent with the growth of a spiro-OMeTAD-based HTM (that is showing F and S related peaks from Li-TSFI and FK 209 that are used as dopants in spiro-OMeTAD, detail in **Appendix discussion**) which increasingly attenuates the photoemission signal from the underlying $CsPbI_3$ as it becomes thicker, with only HTM-related signal appearing for the sample with a 200 nm thick HTM. There is little or no difference in the growth and composition of the HTM layer on the differently-prepared $CsPbI_3$ films, except for the 5 nm data set, where a clear F 1s signal is present only in the spectrum measured on the sample prepared with an OAI-free $CsPbI_3$.

Quantification of the Cs:Pb: I stoichiometry for the 0 nm, 5 nm, and 20 nm (shown in **Figure 3.5 a,b** based on the measurements of perovskite-related shallow core levels using 2 keV and 6 keV, respectively confirms that the elemental composition is unchanged as a result of either the different annealing processes or by the deposition of the HTM, with the largest differences being the slightly elevated I and decreased Pb photoemission line intensities associated with the presence of the OAI-modified surface layer. This stability of the $CsPbI_3$ composition and its good agreement with the nominal composition strongly suggests that no extensive chemical reactions have occurred, in any of the cases, at the surface of the bare $CsPbI_3$ absorbers or the corresponding interfaces to the HTM. With the largest differences being the slightly elevated I and decreased Pb photoemission line intensities associated with the presence of the OAI-modified surface layer. This stability of the $CsPbI_3$ composition and its good agreement with the nominal composition strongly suggests that no extensive chemical reactions have occurred, in any of the cases, at the surface of the bare $CsPbI_3$ absorbers or the corresponding interfaces to the HTM.

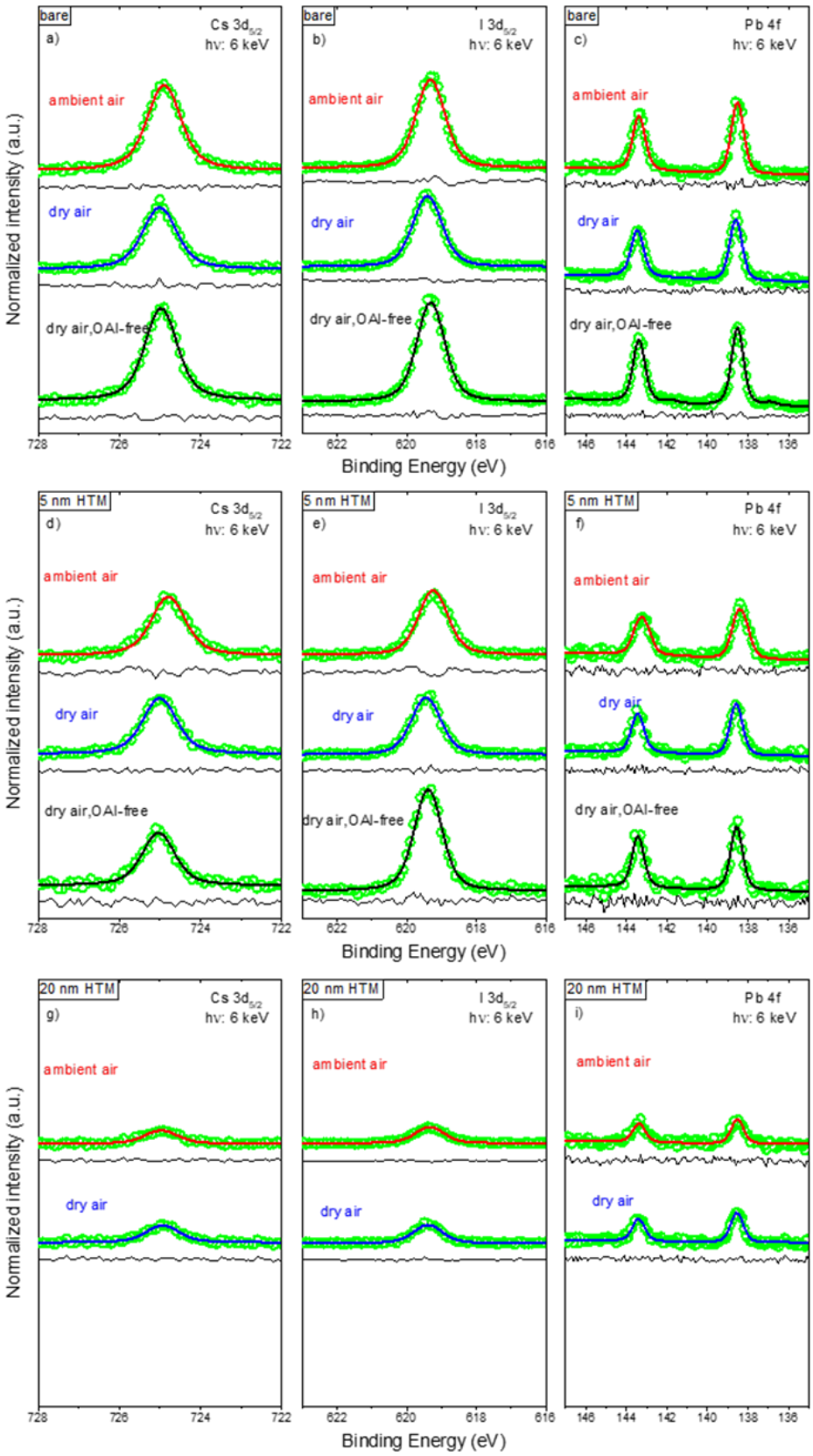

Figure 3.3 HAXPES detail spectra of the Cs $3d_{5/2}$ (a, d, g), I $3d_{5/2}$ (b, e, h), and Pb 4f (c, f, i) photoemission lines for the variously treated $CsPbI_3$ films (*i.e.*, OAI-free, dry air annealed and ambient air annealed) with 0 nm (i.e., bare), 5 nm and 20 nm films of spiro-OMeTAD,

respectively. The spectra were measured using 6 keV excitation and normalized to background intensity, with vertical offsets added for clarity. Curve fit results are included.

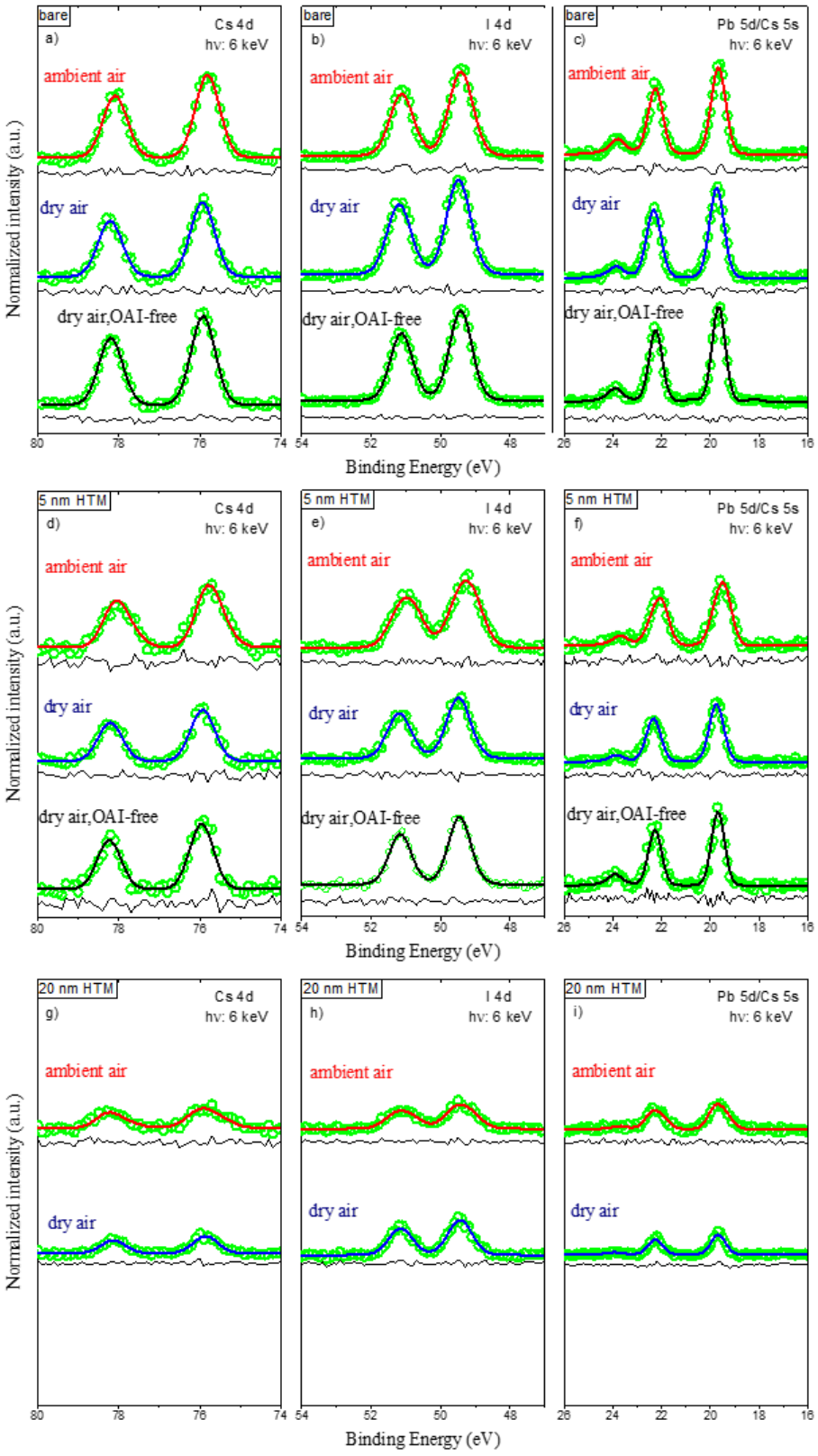

Figure 3.4. HAXPES detail spectra of the Cs 4d (a, d, g), I 4d (b, e, h), and overlapping Pb 5d/Cs 5s (c, f, i) photoemission lines for the variously treated $CsPbI_3$ films (*i.e.*, OAI-free, dry

air and ambient air annealed) with 0 nm *(i.e.*, bare - a, b, c), 5 nm (d, e, f), and 20 nm (g, h, i) films of spiro-OMeTAD, respectively. The spectra were measured using 6 keV excitation and normalized to background intensity, with vertical offsets added for clarity. Curve fit results are included.

Despite this apparent chemical stability, close inspection of the collected HAXPES HTM/$CsPbI_3$ data reveals that there is a slight change in the linewidths of the perovskite-derived core level spectra between the dry air and ambient air annealed $CsPbI_3$ absorbers – the photoemission lines collected for the samples based on $CsPbI_3$ absorbers annealed in ambient air are slightly broader in all cases, as presented in **Figure 3.6a, b**. Such a broadening can arise from changes in chemical structure (*i.e.*, formation of new species beneath the HTM) or electronic structure profiles. Due to the relatively high information depth of HAXPES measurements, probing a sample volume in which band bending occurs will result in a line broadening [19-23] rather than in a shift in peak position**.** As discussed above, there are no indications for pronounced chemical changes in the $CsPbI_3$ films, although because of the same high HAXPES information depth-induced integration effect, the formation of a thin interlayer (similar to the differences that was observe as a result of OAI-induced surface modification) cannot be ruled out. In the case that one would attribute the observed line broadening to be due to a band bending enhancement, one could speculate that the ambient air annealing alters the defect distribution and/or concentration in the $CsPbI_3$ absorber allowing for a more pronounced upward band bending in the absorber upon interface formation with the HTM. An interface-formation-induced upward band bending in the absorber, *i.e.* a binding energy (BE) shift of the absorber-related photoemission lines towards the Fermi-level (reducing the binding energy) can indeed be observed when comparing the halide perovskite related photoemission lines for the HTM/$CsPbI_3$ samples based on absorbers annealed in ambient and dry air. The BE of the Cs 3d, I 3d, and Pb 4f (**Figure 3.3** and **A3.3**) lines and of the corresponding shallow core level peaks Cs 4d, I 4d, and Pb 5d (**Figures 3.4 and A3.4**) of the HTM/$CsPbI_3$ samples based on the absorber annealed in ambient air are systematically lower than those made from absorbers annealed in dry air. (Shifts in BE of the peaks Cs $4d_{5/2}$, I $4d_{5/2}$, and Pb $5d_{5/2}$ peaks of the investigated samples compared to BE values of the bare, OAI-free $CsPbI_3$ sample are presented in **Figure A3.5 c, d.**) This effect is most pronounced for the samples with a nominal 5 nm thick HTM layer, while it seems to almost disappear for the HTM/$CsPbI_3$ samples with a nominal 20 nm spiro-OMeTAD film.

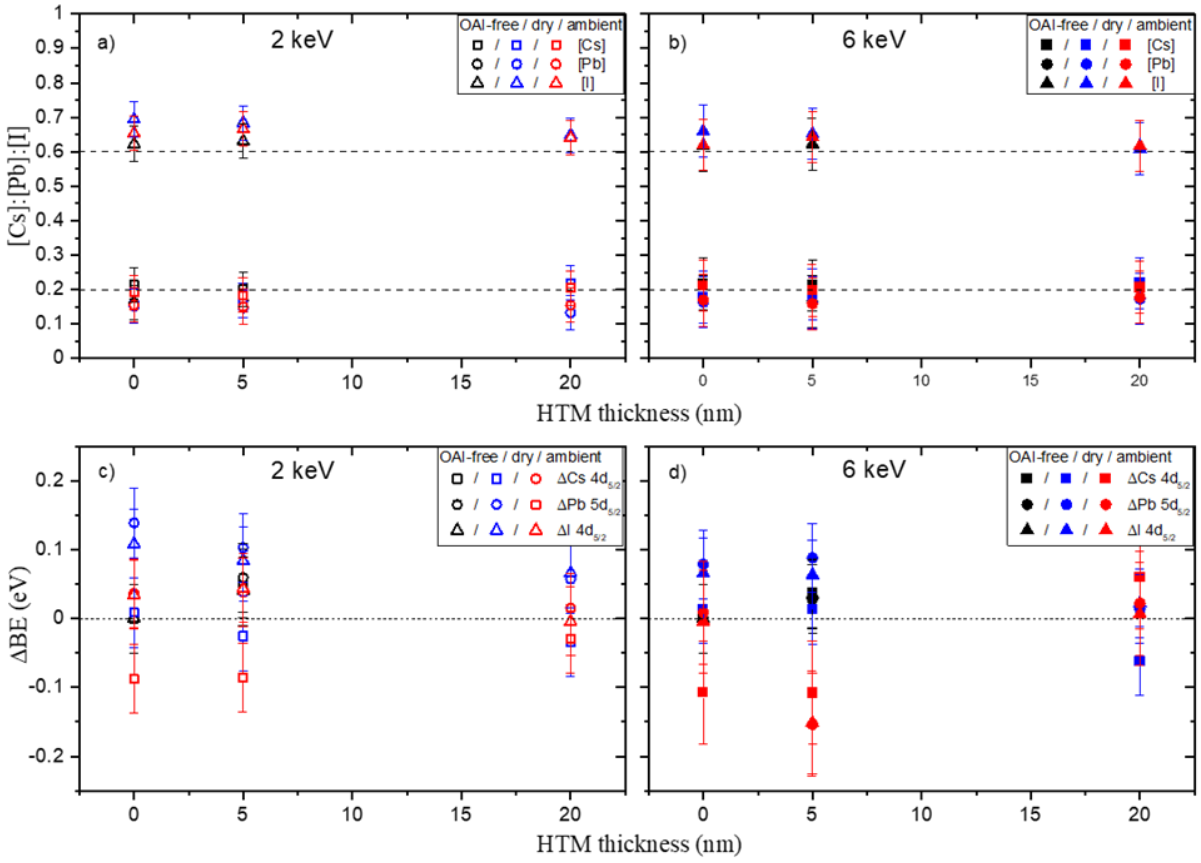

Figure 3.5. [Cs]: [Pb]: [I] surface composition of variously treated $CsPbI_3$ films (*i.e.*, OAI-free, dry air and ambient air annealed) with 0 nm (i.e., bare), 5 nm and 20 nm films of HTM, determined by HAXPES measurements employing a) 2 keV and b) 6 keV excitations. Horizontal dashed lines are added to show a [Cs]: [Pb]: [I] composition ratio of 1:1:3 ratio, the nominal stoichiometry of the $CsPbI_3$ samples. Changes in binding energy (BE) values of the HAXPES Cs $4d_{5/2}$, I $4d_{5/2}$, and Pb $5d_{5/2}$ peaks, measured with excitation energies of c) 2 keV and d) 6 keV (derived from the spectra shown in **Figs. A3.4 and Fig 3.4**), compared to the corresponding peak BE values of the bare, OAI-free $CsPbI_3$ sample.

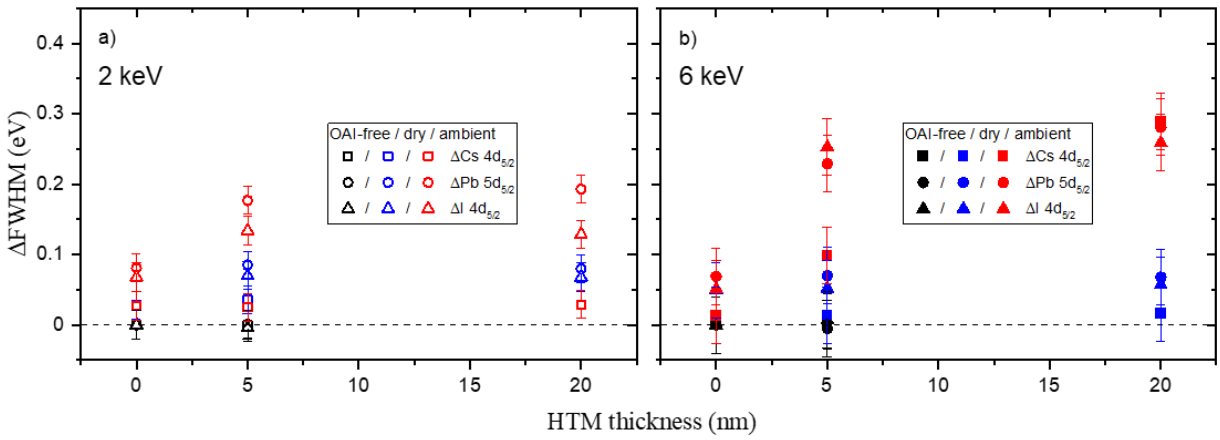

Figure 3.6 Changes in full-width-half-maximum (FHWM) values of the HAXPES Cs $4d_{5/2}$, Pb $5d_{5/2}$, I $4d_{5/2}$ peaks of $CsPbI_3$ absorbers annealed in dry or ambient air with 0 nm (*i.e.*, bare), 5 nm and 20 nm films of HTM, measured with excitation energies of a) 2 keV and b) 6 keV

(derived from the spectra shown in **Figs. A3.4 and 3.4**), compared to the corresponding peak FHWM values of the bare, OAI-free $CsPbI_3$ sample

3.6 Investigation of Interfacial Dynamics

The above discussion concludes that a surface band bending is exhibited by the ambient air annealed $CsPbI_3$ samples which induces a change in the interface dynamics. To further study the effect on the interface a series of measurements were applied that include PL spectroscopy (st-PL), transient photoluminescence spectroscopy (TRPL), transient surface photovoltage (tr-SPV), and kelvin probe measurements.

Figure 3.7a presents Quasi Fermi level splitting (QFLS), for both dry air and ambient air annealed perovskite films (*n*-OAI covered) deposited over ETL (TiO_2) and capped with HTL (spiro-OMeTAD) (*i.e.* similar to device stack), measured by st-PL. It shows that the ambient air annealed sample has higher QFLS as compared to the dry air annealed sample. It further shows the difference between the best achieved V_{OC} of the devices (V_{OC} detail in next section) and QFLS of the samples. The ambient air annealed sample has less difference between QFLS and V_{OC} compared to dry air samples, which is consistent with the decreased energy level offset and surface band bending [24,25] Further, time-resolved PL (TRPL) spectroscopy was applied to know the carrier charge dynamics of the air annealed and dry air box annealed samples. TrPL measurements show that the air annealed sample has less initial decay as shown in **Figure 3.7 b**. By fitting the biexponential equation (**Eq.2.17**) on the curves t_2 for both samples has been measured which increases from 250 ns to 270 ns for dry air and ambient air samples respectively, indicating the reduction in nonradiative recombination by annealing in the air that can be attributed to surface band banding change during annealing in ambient air. (TRPL of the samples without HTL is included in **Appendix Figure A3.6)**. The fitted parameter values are given in **Table A3.1**.

Charge carrier extraction by HTL or ETL is an essential part of PSC. The hole extraction rate coefficient (K_h) determines how fast holes can be extracted from the active perovskite absorber to the selective HTL layer. The knowledge of K_h for different HTL interfaces allows them to cross-compare their hole extraction capabilities. [26] The fast extraction $-1/K_h <$ carrier lifetime– ensures the collection of the carriers before their recombination in the active material or surface. [27,28] Transient surface photovoltage (tr-SPV) measurements were conducted to study charge carrier extraction dynamics for two devices (FTO/TiO_2/Perovskite: OAI/Spiro-OMeTAD) annealed at different conditions (*i.e.* dry air and ambient air). To generate charge

carriers, a 5 ns light pulse with photon energy 1.8 eV and fluence equal to 1 sun was employed (more details in **Appendix.**) The tr-SPV measurements revealed a significant boost in the amplitude and rise speed of the ambient air-annealed sample signal compared to the dry air-annealed sample, as shown in **Figure 3.74c.** Such an increase in trSPV signal can be caused by more efficient charge extraction - larger K_h or suppressed trap concentration. [26,27] Another evidence of more favorable band bending at the surface of the ambient air facilitating hole extraction comes from Kelvin probe measurements as shown in **Figure 3.7d**. It is found that the work function increases from 3.88 eV to 4.30 eV for the dry air and ambient air annealed samples, respectively. The ambient air sample has a work function that is much closer to that of the HTM layer. The change in WF can be attributed to the surface band bending.

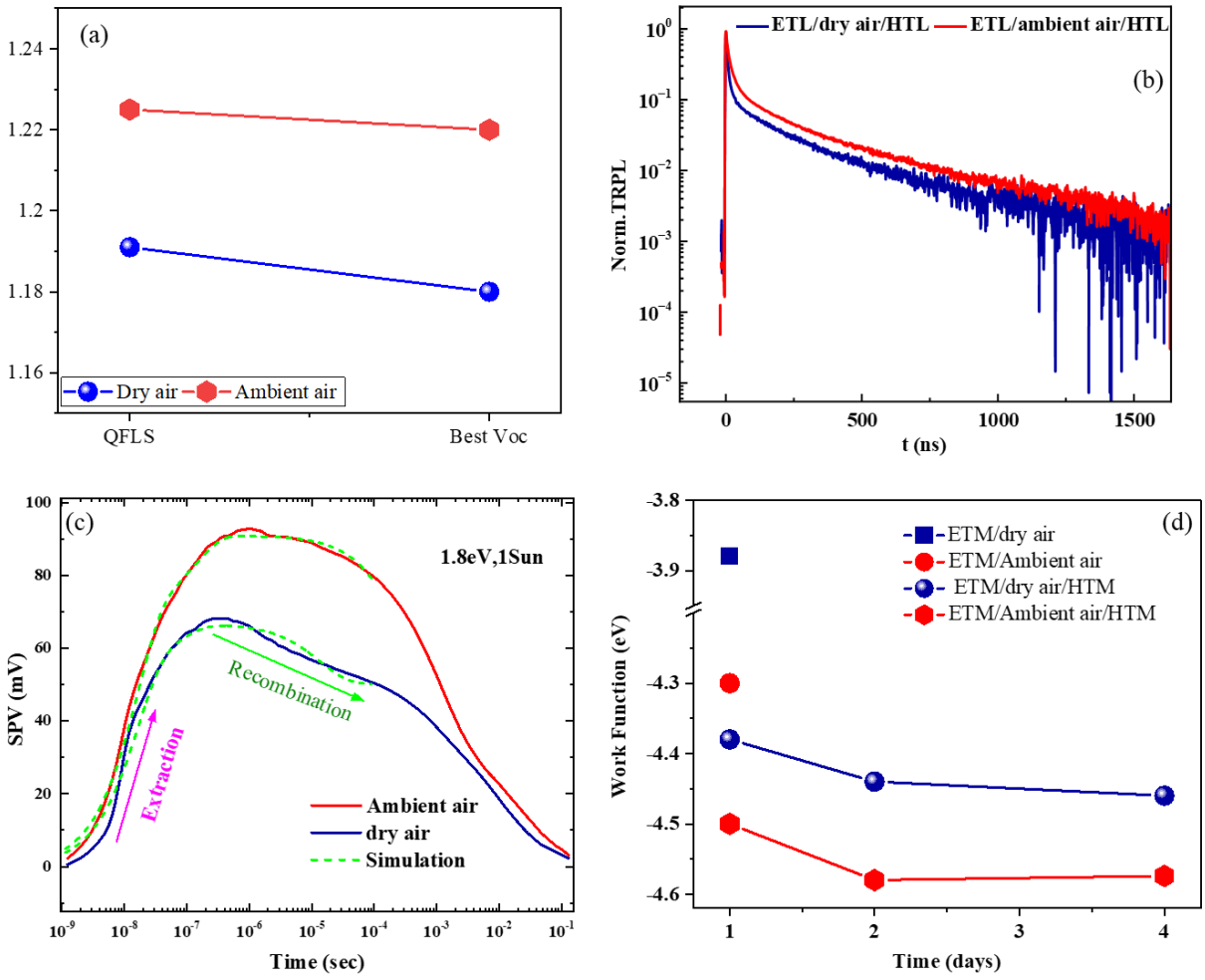

Figure 3.7. Interfacial dynamics study for perovskite/HTL interface. All the perovskite films were deposited on ETL (TiO_2) and capped with HTL (Spiro-OMeTAD). a) Quasi Fermi levels splitting calculated for perovskite film annealed in dry air and ambient air and the champion V_{OC} device. b) trPL measurements for dry air annealed and ambient air annealed samples. c)Transient surface photovoltage (tr-SPV) measurements for dry and ambient air-

annealed perovskite samples measured under 1 sun illumination and 1.8eV laser beam. d) Work function measurements with the Kelvin Probe method for dry air annealed and ambient air annealed samples.

Figure 3.7 d shows a work function change for spiro-OMeTAD capped dry and ambient air annealed samples for up to four days. The time tracking shows that more accelerated increase in WF in the ambient air-annealed samples. The consequences of this WF change will be discussed in the next section. Both trap passivation and favorable band bending can enhance the charge extraction at the HTL interface. The simulations, based on the kinetic equation to calculate the charge extraction rate constant and the concentration of traps at the perovskite surface, were carried out. (Details of simulations are added in **Appendix 2.7.1** and **Table A3.2**) After fitting experimental results, it was found that the ambient air annealed sample has a 3 times faster extraction rate, which resulted in the faster rise of the tr-SPV signal, as shown in **Figure 3.7c**. The air-annealed sample also demonstrated a much lower concentration of defects (5.6×10^{11} compared to 3.7×10^{14} cm^{-3} in control) at the perovskite surface, which acts as a charge recombination center. The results suggest that annealing enhances hole extraction and, at the same time, passivates defects, thereby enhancing charge collection at the HTL interface

3.7 Device Performance

The dry and ambient air-annealed films were used to fabricate *n-i-p* devices with the structure FTO/TiO_2-$_C$/$CsPbI_3$: OAI/Spiro-OMeTAD/Au. To know, the thickness of the layers, the cross-sectional SEM images of the devices are shown in Appendix (**Figure A3.7**). The device fabrication involves the HTM layer oxygen soaking step. This O_2 soaking causes a change in LUMO levels of spiro-OMeTAD, making it more p-type. [29,] However, the soaking time for both types of devices varies. The devices were soaked for 6 days with an HTM layer and subsequently to measure the work function (Kelvin probe measurements) and to see the change in device performance. The *J-V* curve of the two kinds of devices *i.e.* dry and ambient air annealed has been shown in **Figure 3.8 a**, which shows that ambient air annealed devices achieve efficiency plateau in less time soaking as compared to dry air annealed film-based devices. It shows that ambient air-annealed film-based devices needed less time for oxygen soaking (**Figure A3.8**). Although this requires further investigation, a possible reason behind this could be the band bending on the air-annealed film surface which causes a decrease in offset and hence better energy alignment. **Figure 3.8 b**, shows the *JV*-curve for the champion devices. The ambient air annealed-based device exhibited an improved 19.8 % PCE with a V_{OC} of 1.22 Volts, a J_{SC} of 20.4 $mA/cm^{2,}$ and a fill factor of 78.9% which is higher than dry air

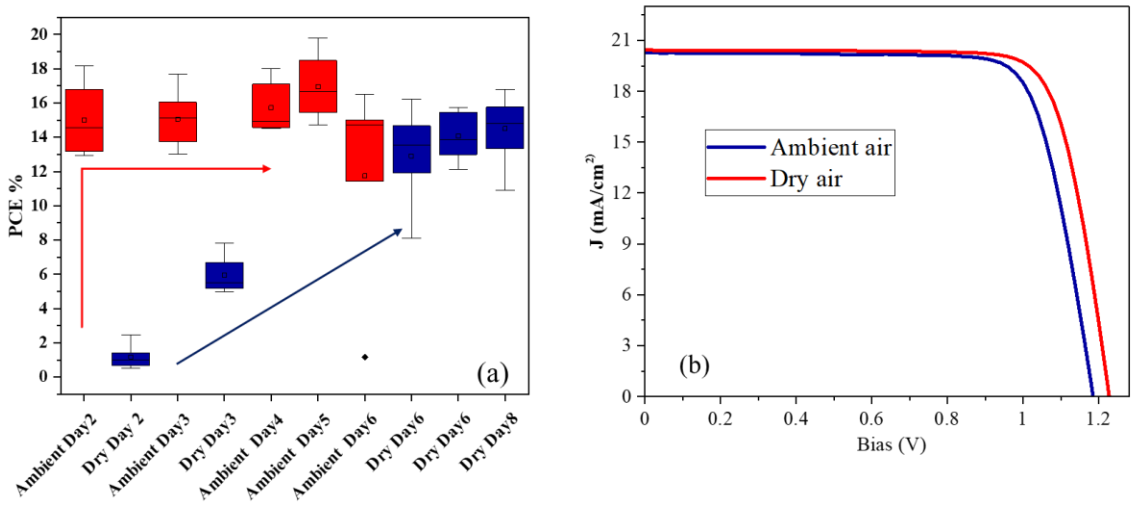

(c)

Device	J_{SC} (mA/cm²)	V_{oc} (Volts)	FF (%)	PCE(%)
Dry air	20.27	1.18	77.7	18.6
Ambient air	20.42	1.22	78.9	19.8

Figure 3.8. Device performance (a)PCE measured for dry air and ambient air annealed $CsPbI_3$ film-based devices soaked at different days (b) *J-V* curve for champion dry air and ambient air annealed $CsPbI_3$ film-based devices c) Table with champion device performance parameters.

annealed film-based device in which the champion device has reported 18.6% PCE, with V_{OC} of 1.18 Volts, a J_{SC} of 20.2 mA/cm^{2,} and a fill factor of 77.7%.

Statistically, a total of 36 solar cells (18 dry air and 18 ambient air) were made and each device contains 6 pixels (individual solar cells). The overall summarized 90 pixels results in the box chart in **Figure 3.9** while very few pixels were shunted *i.e.* 17,18 pixels for each condition. The statistics show that there is a clear difference between the averages for example there is almost a 50meV increase in V_{OC} in ambient air-treated samples. Moreover, it also shows that this work is very reproducible. It can be seen that there is no significant difference between J_{sc} and FF for both types of devices.

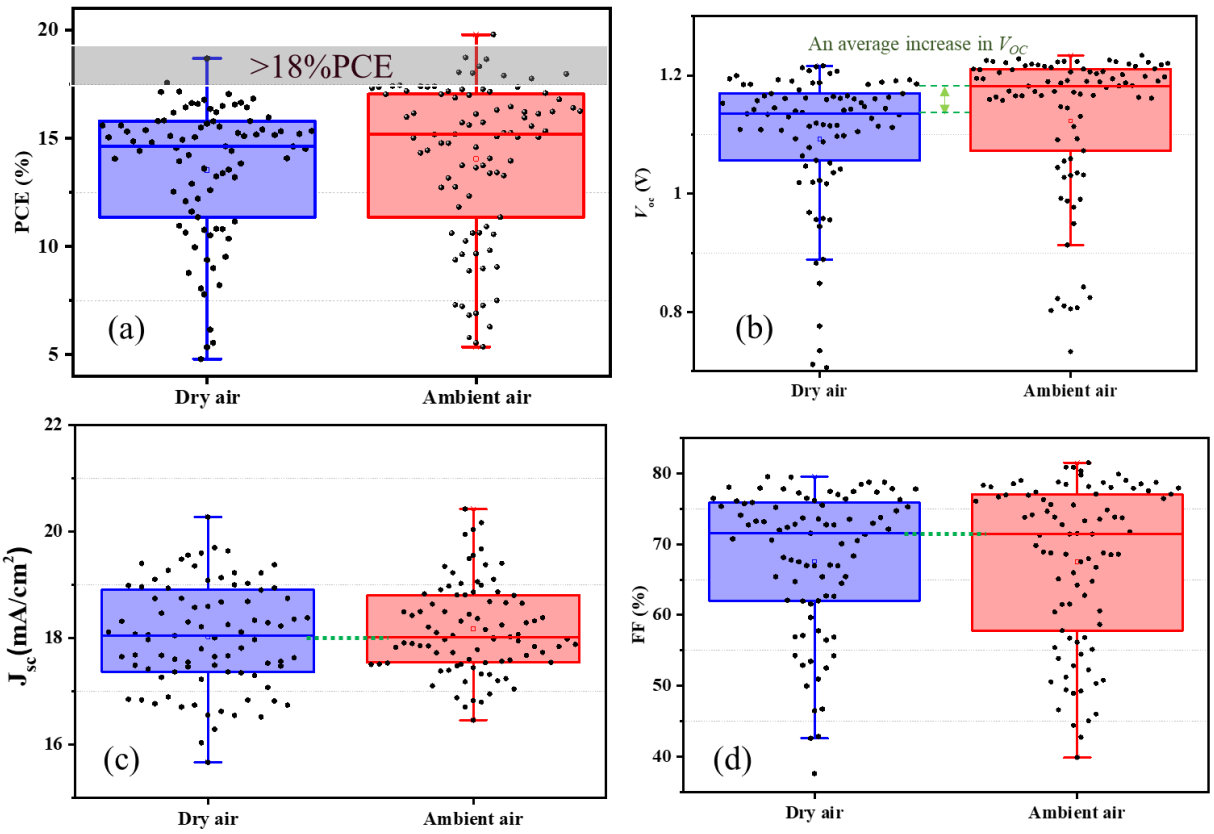

Figure 3.9 Box chart of 18 dry air and 18 ambient air annealed films based individual devices with a total over 90 pixels, a) PCE %, b) Open circuit voltage V_{OC}, c) Current density J_{SC}, and d) Fill factor *FF*.

Figure 3.10 shows the V_{OC} histogram for devices. It can be seen that there is a clear difference for V_{OC} with an average value of 1.14 Volts and 1.18 Volts for dry air and ambient air respectively, which shows that the device based on the ambient air annealed films outperform as compared to dry air annealed film-based devices.

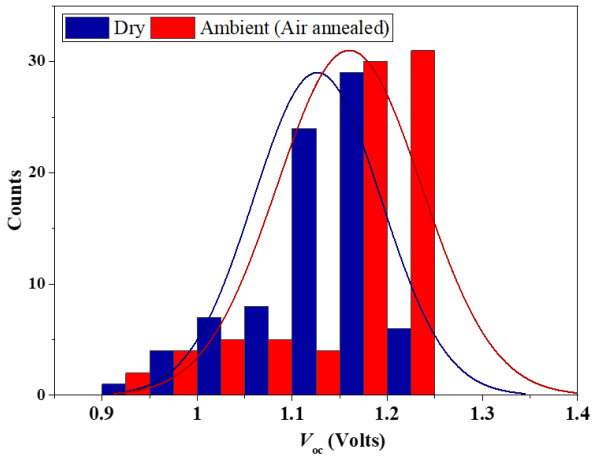

Figure 3.10 Histogram of V_{OC} for dry and ambient air-annealed $CsPbI_3$ film-based devices.

Finally, the long-term stability of both types of devices was measured for 1500 hours. Over all four devices for each condition were measured simultaneously. **Figure 3.10** shows the normalized PCE over time for 13,13 pixels data for dry and ambient air annealed samples device. Both devices show almost similar stability with burn-in in the initial few hours and then similar T_{S80}.

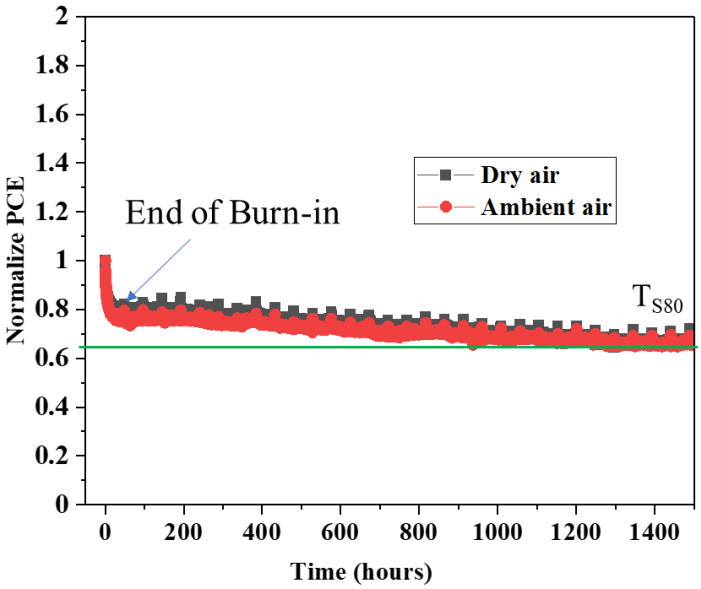

Figure 3.10. Long-term stability measurements for 1500 hours for dry and ambient air-annealed $CsPbI_3$ film-based devices.

3.8 Conclusion

A detailed comparative study was conducted for the $CsPbI_3$ annealing step in a dry air box and in ambient air. It shows that there is no difference in the morphology and quality of the film.HAXPES study reveals that there is no new bond formation that happens on the $CsPbI_3$ surface rather it shows a surface band bending during ambient air annealing. The tr-SPV measurements reveal better charge extraction for ambient air annealed $CsPbI_3$ samples and HTM layer interface. Moreover, it also shows that less defects in ambient air-annealed perovskite film. The findings suggest that ambient-air annealing-induced band bending at the $CsPbI_3$/HTM interface improves charge carrier extraction and dynamics. The perovskite solar cell based on ambient air-annealed $CsPbI_3$ results in a PCE of 19.8%. This overall study opens the horizons for new annealing strategies focusing on inorganic perovskite solar cells in the air.

(Z. Iqbal, Q.Wang, and Prof. Antonio Abate perceived the idea. Z.I. made all the samples and solar cell devices in this work. R. Felix, E.Hüssam supported this work with HAXPES measurements at the HIKE endstation and helped in analyzing the data with Prof.Marcus Bär

and R. Wilks. A. Musiienko supported this project by measuring trSPV and KP, and theoretical simulations. J. Thiesbrummel helped in measuring steady-state photoluminescence for the samples. E Partida did help in this project by TRPL measurements for the samples while M. Stolterfoht has helped in analyzing the data. Q.Wang has been the daily supervisor of this project and she helped and trained for device fabrications and *JV* measurements at HySprint Lab. Hans Köble supported this project with MPP tracking measurements at HZB)

References

1. X. Zhao, T. Liu, Q. C. Burlingame, T. Liu, R. Holley, G. Cheng, *et al*., "Accelerated aging of all-inorganic, interface-stabilized perovskite solar cells.", *Science*, 2022, **377** (6603), 307-310.
2. H.Yao, J.Zhao, Z. Li, Z. Ci, and Z.Jin "Research and progress of black metastable phase $CsPbI_3$ solar cells", *Materials Chemistry Frontiers*, 2021, **5**, 1221-1235.
3. W. Ahmad, J. Khan, G.Niu, J.Tang "Inorganic $CsPbI_3$ Perovskite-Based Solar Cells: A Choice for a Tandem Device" *Solar. RRL* 2017,**1**, 1700048.
4. W. Xiang, S. (F.) Liu, Wolfgang Tress. "A review on the stability of inorganic metal halide perovskites: challenges and opportunities for stable solar cells", *Energy & Environmental Sciences,* 2021, **14**, 2090-2113.
5. J.A. Steele, H. Jin, I.Dovgaliuk ,R.F. Berger ,T. Braeckevelt , H.Yuan , C.Martin , E.Solano, K.Lejaeghere,S. M. J. Rogge, C.Notebaert, W.Vandezande, K. P. F. Janssen, B. Goderis, E. Debroye, Y. Wang, Y. Dong, D. Ma, M.Saidaminov, H. Tan, Z. Lu, V.Dyadkin, D. Chernyshov, V.V. Speybroeck, E. H. Sargent, J. Hofkens, M. B. J. Roeffaers. "Thermal unequilibrium of strained black $CsPbI_3$ thin films" *Science*., 2019, **365**, 6454 679-684.
6. A. Swarnkar, A. R. Marshall, E. M. Sanehira, B. D. Chernomordik, D.T. Moore, J. A. Christians,T.Chakrabarti, J. M. Luther " Quantum dot–induced phase stabilization of α-CsPbI3 perovskite for high-efficiency photovoltaics" *Science*, 2016, **354**, 6308, 92-95.
7. Y. Wang, M. I. Dar, L.K. Ono, T. Zhang1, M. Kan1, Y. Li, L. Zhang, X. Wang1, Y. Yang, X.Gao, Y. Qi, M.Grätzel, Y. Zhao. "Thermodynamically stabilized *ß*-CsPbI3–based perovskite solar cells with efficiencies >18%", *Science* 2019, **365**, 591–595.
8. Y. Wang, X. Liu, T. Zhang, X. Wang, M. Kan, J. Shi und Y. Zhao. "The Role of Dimethylammonium Iodide in $CsPbI_3$ Perovskite Fabrication: Additive or Dopant?", *Angewandte Chemie International Edition*, 2019, **131**, 16844 – 16849.
9. H. Meng, Z. Shao, L. Wang, Z. Li, R. Liu, Y. Fan, G. Cui, S. Pang. "Chemical Composition and Phase Evolution in DMAI-Derived Inorganic Perovskite Solar Cells" *ACS Energy Letter*, 2020, **5**(1), 263–270.

10. W. Ke, I. Spanopoulos, C.C. Stoumpos , M. G. Kanatzidis. “Myths and reality of HPbI 3 in halide perovskite solar cells”, *Nature Communications*, 2018, **9**, 4785.
11. H. Bian, H.Wang, Z. Li, F. Zhou, Y. Xu, H. Zhang, Q.Wang, L. Ding, S.(F.) Liu, Z. Jin. “Unveiling the Effects of Hydrolysis-Derived DMAI/DMAPbIx Intermediate Compound on the Performance of $CsPbI_3$ Solar Cells.”, *Advance Science*, 2020, **7**, 1902868.
12. A. R. Marshall, H. C. Sansom, M.M. McCarthy, J. H. Warby, O.J. Ashton, B. Wenger, H. J. Snaith “Dimethylammonium: An A-Site Cation for Modifying CsPbI3” *Solar RRL*, 2021, **5**, 2000599.
13. S.Chang Liu, Z. Li, Y. Yang, X. Wang, Y.X. Chen, D.-J. Xue, J. -S. Hu. “Investigation of Oxygen Passivation for High-Performance All-Inorganic Perovskite Solar Cells”, *Journal of the American Chemical Society*, 2019, **141**(45), 18075–18082.
14. G. Wu, R. Liang, M. Ge, *et al*., “Surface Passivation Using 2D Perovskites toward Efficient and Stable Perovskite Solar Cells.”, *Advanced Materials*, 2022, **34**, 2105635.
15. H. Kim, S.-U. Lee, D. Y. Lee, et al., “Optimal Interfacial Engineering with Different Length of Alkylammonium Halide for Efficient and Stable Perovskite Solar Cells.”, *Advanced Energy Materials*, 2019, **9**, 1902740.
16. Y. Tian, M. Peter, E. Unger, M. Abdellah, K. Zheng, T. Pullerits, *et al*., “Mechanistic insights into perovskite photoluminescence enhancement: light curing with oxygen can boost yield thousandfold.” *Physical Chemistry Chemical Physics*, 2015,**17**(38),24978-24987.
17. A. D. Wright, R. L. Milot, G. E. Eperon, H. J. Snaith, M. B. Johnston, L. M. Herz, “Band-Tail Recombination in Hybrid Lead Iodide Perovskite”, *Advanced Functional Materials*, 2017, **27**, 1700860.
18. M. Ledinsky, T. Schönfeldová, J. Holovský, E. Aydin, Z. Hájková, L. Landová, N. Neyková, A. Fejfar, S. D. Wolf, “Temperature Dependence of the Urbach Energy in Lead Iodide Perovskites”, *The Journal of Physical Chemistry Letters*, 2019, **10**(6), 1368–1373.
19. D. Wippler, R. G. Wilks, B. E. Pieters, S. J. Van Albada, D. Gerlach, J. r. Hüpkes, *et al*., “Pronounced surface band bending of thin-film silicon revealed by modeling core levels probed with hard x-rays.”, *ACS Applied Materials & Interfaces*, 2016,**8**(27),17685-17693.
20. D. Wippler, R. G. Wilks, B. E. Pieters, S. J. Van Albada, D. Gerlach, J. r. Hüpkes, *et al*., “Pronounced surface band bending of thin-film silicon revealed by modeling core levels probed with hard x-rays.”, *ACS Applied Materials & Interfaces*, 2016, **8**(27),17685-17693

21. O. Romanyuk, A. Paszuk, I. Bartoš, R. G. Wilks, M. Nandy, J. Bombsch, et al "Band bending at heterovalent interfaces: Hard X-ray photoelectron spectroscopy of GaP/Si(001) heterostructures.", *Applied Surface Science*, 2021,**565**,150514
22. O. Romanyuk, O. Supplie, A. Paszuk, J. P. Stoeckmann, R. G. Wilks, J. Bombsch, et al. Hard X-ray photoelectron spectroscopy study of core level shifts at buried GaP/Si(001) interfaces.", *Surface and Interface Analysis*, 2020, **52**(12),933-938
23. O. Romanyuk, A. Paszuk, I. Gordeev, R. G. Wilks, S. Ueda, C. Hartmann, et al. "Combining advanced photoelectron spectroscopy approaches to analyse deeply buried GaP(As)/Si(100) interfaces: Interfacial chemical states and complete band energy diagrams.", *Applied Surface Science*, 2022, **605**, 154630.
24. M. Stolterfoht, P. Caprioglio, C. M. Wolff, J. A. Márquez, J. Nordmann, S. Zhang, *et al*., "The impact of energy alignment and interfacial recombination on the internal and external open-circuit voltage of perovskite solar cells." *Energy & Environmental Science*, 2019, **12** (9), 2778-2788.
25. P. Caprioglio, J. A. Smith, R. D. J. Oliver, A. Dasgupta, S. Choudhary, M. D. Farrar, *et al*., "Open-circuit and short-circuit loss management in wide-gap perovskite p-i-n solar cells." *Nature Communications*, 2023, **14**(1), 932
26. T. Dittrich and S. Fengler, "Surface Photovoltage Analysis of Photoactive Materials", World Scientific (Europe), 2020.
27. S. Fengler, H. Kriegel, M. Schieda, *et al.*, "Charge Transfer in c-Si(n++)/TiO2 (ALD) at the Amorphous/Anatase Transition: A Transient Surface Photovoltage Spectroscopy Study.", *ACS Applied Materials & Interfaces*, 2020, **12**, 3140−3149.
28. I. Levine, A. Al Ashouri, A. Musiienko, *et al.*, "Charge transfer rates and electron trapping at buried interfaces of perovskite solar cell", *Joule*, 2021, **5**, 2915–2933
29. Z. Hawash, L, K. Ono, S. R. Raga, M. V. Lee, Y. Qi, "Air-Exposure Induced Dopant Redistribution and Energy Level Shifts in Spin-Coated Spiro-MeOTAD Films" *Chemistry of Materials*, 2015, **27**, 562−569.
30. A. Abate, T. Leijtens, S. Pathak,a J.Teuscher, R Avolio, M. E. Errico,J Kirkpatrik, J. M. Ball,P. Docampo, I. McPherson, H.J. Snaith, " Lithium salts as ''redox active'' p-type dopants for organic semiconductors and their impact in solid-state dye-sensitized solar cells" *Physical Chemistry Chemical Physics*, 2013,**15**, 2572.

Chapter 4

Interface Design for Better Charge Extraction and Energy Level Alignment at the Interface

This chapter is based on the peer review article "**Interface Modification for Energy Level Alignment and Charge Extraction in $CsPbI_3$ Perovskite Solar Cells**."
DOI :10.1021/acsenergylett. 3c01522.

4.1 Highlights of the work

Perovskite solar cells (PSCs) are considered the most promising candidates for their ease of fabrication. However, the interfaces need to be designed to approach the theoretical limit for these types of materials as the main energy losses come from the interfaces as mentioned in **Chapter 1 Section1.10**. Normally, the passivation strategy is used to improve the stability and efficiency of the devices. Here, it is introduced an interface that is designed by employing a passivation layer and a dipole molecule. This dipole molecule helps to optimize the energy level alignment, better charge extraction, and increase stability. This work will open new strategies for interface designs for perovskite solar cells. As an added, it was measured the overall energy production of the modified devices. Thus, a paradigm shift in the performance parameters to compare devices among labs.

4.2 Statement of the Challenges

- Inorganic perovskite solar cells have greater open circuit voltage deficit (V_{loss}) than hybrid organic-inorganic perovskite solar cells. The higher loss primarily originates from the interfaces due to their energy misalignment. Here, an interface is introduced with an improved V_{OC} due to better energy alignment at the interface.
- Photoluminescence methods have limitations in differentiating the role of interlayer in terms of charge carrier extraction layer or defect passivation. Both charge extraction and defect states can contribute to quenching. Here, a method, based on the transient surface photovoltage technique (trSPV) and charge transport simulations is introduced that helps to differentiate between charge extraction and passivation role.

4.3 Introduction

In $CsPbI_3$-based perovskite solar cells, photoactive phase stability at the working temperature and crystallization growth are the foremost associated challenges with device fabrication. [1,2]

Recently, organic additives, *e.g*.hydrogen lead iodide "$HPbI_3$" and dimethyl ammonium iodide DMAI-assisted film growth [3,4], and molten salt-based strategies have been adopted to address these challenges. To date, over 21% efficiency has been reported for $CsPbI_3$ with V_{OC} of over 1.2V, [5] but inorganic perovskite solar cells have large open circuit voltage deficit as compared to organic-inorganic halide perovskite solar cells. [5,6] Currently, inorganic perovskite film passivation methods have been very persuasive in increasing open-circuit voltage values. [7-9] However, less energy level alignment between the inorganic perovskite layer and the charge selective contacts suggests interfacial engineering to resolve open circuit voltage deficit. [10-12]

Surface band bending is the strategy to mitigate the energy offset at the interfaces. Inorganic perovskite has a flat band surface and introducing a surface band bending has been proven to be favorable for charge extraction. [13] L.Canil *et al*.,[14] introduced the method to tune the energy levels alignment by the molecular treatment on the perovskite surface. They have systematically studied the Fermi level tuning of triple-cation perovskite with ($Cs_{0.05}[MA_{0.15}FA_{0.85}PbI_{0.85}Br_{0.15}]_{0.95}$) composition by depositing dipole molecules on the surface. In another example, M. Nazeeruddin *et al* reported surface band bending on a perovskite surface, they deposited perhydropoly(silazane) on top of triple-cation perovskite film [15] and found that this surface band bending led to an efficient hole extraction and consequently a higher efficiency and stability. S. Wang *et al.* introduced *n*-type surface band bending. They treated the flat $CsPbI_3$ surface with propylamine hydrochloride molecule that causes surface band bending. [16] This surface band bending incited better charge extraction and they have achieved 20.17% state-of-the-art efficiency for inverted $CsPbI_3$-based solar cells. These recent reports suggest that surface band bending is an effective method to modulate the interface for better energy level alignment and efficient charge extraction at the interfaces.

Soek II *et al*. introduced a method for $CsPbI_3$ film growth in which they controlled the intermediate stage by MACl dripping and then employed *n*-octyl ammonium iodide (OAI) for the defect-passivation of $CsPbI_3$. They have reported 20.3% state-of-the-art efficiency with 1.19 V_{OC}. [17]. Passivating the surface defects of the perovskite is considered one of the most effective strategies to enhance stability. [18,19] Normally, *n*-octyl ammonium iodide (OAI) like long-chain alkylammonium halides were the most common molecules used for perovskite surface passivation. [20,21] I have taken this already reported work on $CsPbI_3$ as our control sample. However, in this work, it is revealed that OAI treatment leads to a downward band bending at the surface, which makes a more *n*-type perovskite film. To optimize the energy

alignment, it was introduced the dipole molecule trioctylphosphine oxide (TOPO) to induce a perovskite upward surface band bending without changing the concentration of surface defects on a well-passivated perovskite film. These improved interface samples are referred to as "with TOPO" (w/TOPO). TOPO treatment on the control film in *n-i-p* PSCs improved the charge selectivity six-fold, causing a decrease in energy offset and optimizing the energy level alignment, significantly impacting the stability of state-of-the-art inorganic PSCs.

The role of the TOPO molecule was challenging to differentiate by the photoluminescence techniques. Both charge extraction and defects can contribute to quenching. Here a method based on time-resolved surface photovoltage (tr-SPV) [22] and charge transport simulation was developed to resolve both carrier extraction and defect passivation. Generally, the higher efficiency and stability were mainly attributed to the suppression of non-radiative recombination induced by surface defects. [23,24] This method allows us to associate the improved stability of $CsPbI_3$ perovskite solar cells directly with the superior charge selectivity (of TOPO) since I separated the role of defect-passivation from upward surface band bending by adopting TOPO as a surface dipole on top of OAI for creating upward surface band bending. I also validate the impact of the interfacial energy level alignment and the consequently improved charge extraction on the stability of PSCs.

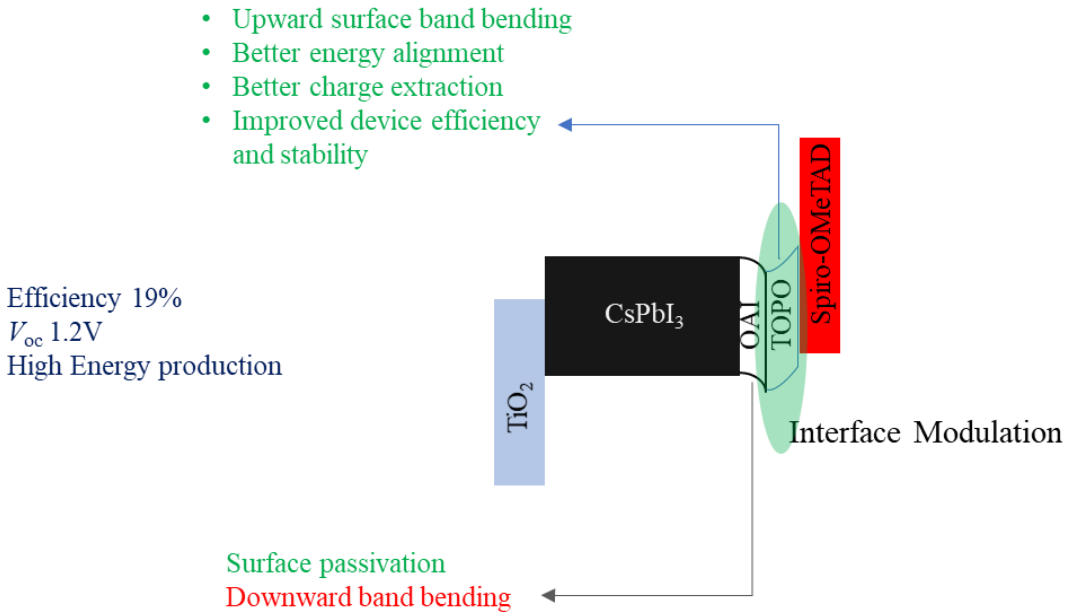

Figure 4.1 Table of content (ToC) for Chapter 4. The interface engineering by the dipole molecule.

4.4 Result and Discussion

4.4.1 $CsPbI_3$ film characterizations

Experimental details for perovskite film preparation and device fabrication are mentioned in **Appendix Section A.3.1-2**.

To ensure the inorganic nature of the $CsPbI_3$ layer and the quality of the film. Initially, a series of characterization tools were used. These include UV-Vis absorption spectroscopy, XRD, XPS, scanning electron microscopy (SEM), and atomic force microscopy (AFM).

I. XRD: The crystal phase structure of our bare perovskite films *via* XRD. As shown in **Fig. A4.1a**, the sample presents dominating diffraction peaks at 14.35° and 28.86°, corresponding to the (100) and (220) facets of β-$CsPbI_3$ crystallites. [(3)] The diffraction peak of $DMAPbI_3$ at 2theta of around 12°, as reported in reference [(4)] was not observed here, indicating that the DMA^+ cation decomposed during the annealing step.

II. XPS: XPS measurements were conducted to examine further if any trace amount of organic moieties were left from DMAI or MACl in the pristine $CsPbI_3$ perovskite. **Fig. A4.1b** shows no signals for N 1s peak at the surface (< 10 nm) of $CsPbI_3$ thin films.

Together with the XRD data that revealed the absence of $DMAPbI_3$ in the bulk and surface of $CsPbI_3$ thin films, it proved the chemical nature of $CsPbI_3$ inorganic perovskite.

The TOPO treatment effect on perovskite film was investigated by UV-Vis absorption spectroscopy, scanning electron microscopy, and atomic force microscopy (AFM). The TOPO treatment barely changes absorption spectra, film thickness, and roughness as detailed in the **Appendix section**.

III. UV-Vis: An optical bandgap of around 1.70 eV is observed from the Tauc plot as shown in **Fig A4.2 b.** That is in line with the literature values. [(4)]

IV. SEM: There is no difference in the grain size and film thickness of $CsPbI_3$ before and after TOPO treatment. **Fig. A4.3** shows an average grain size of around 300 nm with the extrapolated grain size histogram. Yet, the surface morphology changed slightly due to the coverage of the TOPO layer deposited at high concentrations (particularly 20 mM).

V. AFM: The film roughness was characterized by atomic force microscopy (AFM), with the topography images presented in **Fig. A4.4**. It shows a slight increase in film roughness, which is likely caused by the slight changes in surface morphology during the dripping process of solutions for the additional layers.

These techniques confirm that this method can deposit pure, pinhole-free, thick, and smooth $CsPbI_3$ film.

4.4.2 Surface Passivation

The steady-state photoluminescence (st-PL) for neat perovskite films was conducted as shown in (**Fig 4.2a)**. TOPO-treated samples at varying concentrations of 5 mM, 10 mM, 15 mM, and 20 mM exhibited a similar photoluminescence quantum yield (PLQY) and thus a similar quasi-Fermi level splitting (QFLS) (**Fig. A4.5**). This indicates that TOPO treatment has barely any contribution to defect passivation. Time-resolved photoluminescence (TRPL) spectra given in **Fig. 4.2b** were fitted with the biexponential equation **(Equation 2.17/A4.1)** as discussed in the **Appendix**. The fitted lifetime, t_2, referring to the non-radiative recombination, showed that all samples have a very similar value of around 3.5 µs. Thus, it further supports the steady-state PL data that TOPO treatment does not contribute noticeably to defect passivation.

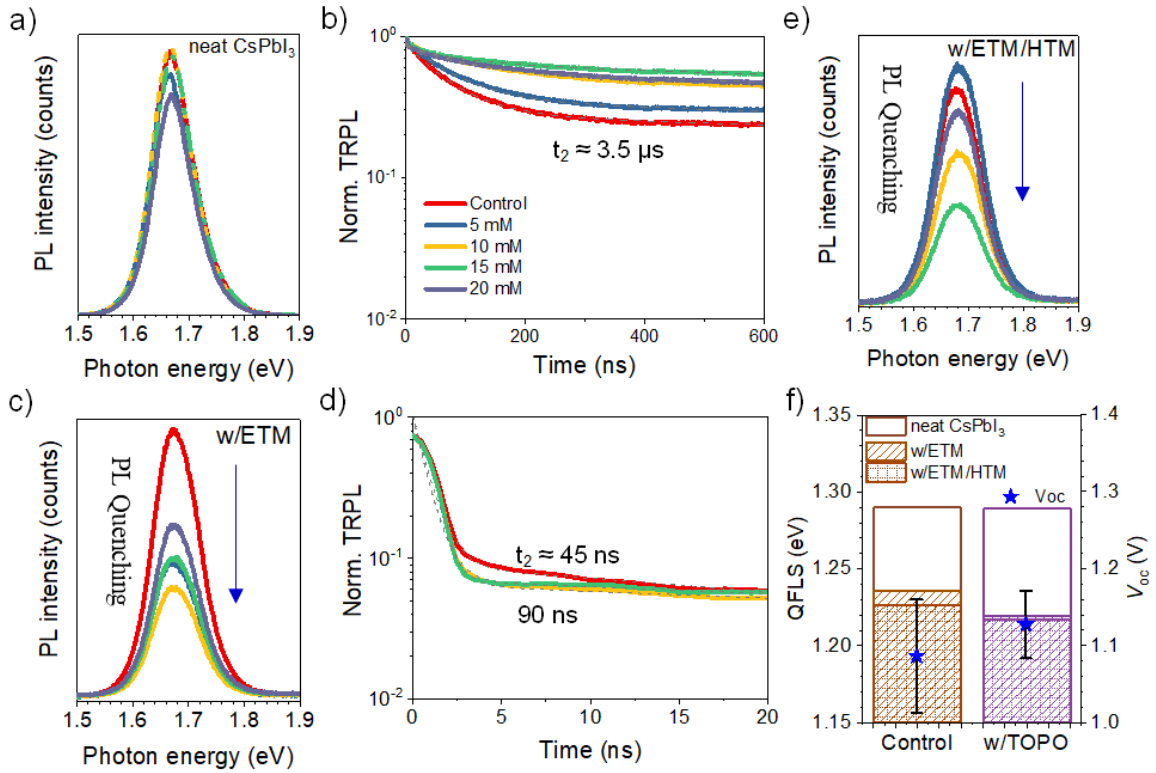

Fig. 4.2 | Surface Passivation a) Steady-state and b) time-resolved photoluminescence of neat perovskite films for control (red line), 5 mM (steal blue line), 10 mM (yellow line), 15 mM (green line) and 20 mM (lavender line) TOPO treated samples. c) Steady-state and d) time-resolved photoluminescence of perovskite films with ETM for control (red line), 5 mM (steal blue line), 10 mM (yellow line), 15 mM (green line) and 20 mM (lavender line) TOPO treated samples. e) Steady-state photoluminescence of perovskite films with ETM and HTM for control (red line), 5 mM (steal blue line), 10 mM (yellow line), 15 mM (green line), and

20 mM (lavender line) TOPO treated samples. f) QFLS for neat perovskite (hollow bars), with ETM (bars with stripes), and with ETM and HTM (bars with dashed lines) for control and 10 mM TOPO treated samples.

Perovskite films deposited on top of the electron transport layer (ETL) were characterized with PL as well (**Fig. 4.2c**). Faster quenching is observed for all TOPO-treated samples. TRPL in **Fig. 4.2d** shows that TOPO-treated samples have a t_2 longer than that of the control, indicating that the fast quenching is unlikely originating from trap states but rather from faster charge extraction at the interface of perovskite and ETM. **Fig. 4.2e** presents the steady-state PL of samples with both ETM and HTM. For 10 mM and 15 mM TOPO-treated samples, stronger quenching is observed. The QFLS for control and 10 mM TOPO-treated samples are summarized in **Fig. 4.2f**. It shows that a smaller difference between QFLS and V_{oc} (averaged from over 40 solar cells) is seen in TOPO-treated samples.

It can be concluded from the neat film analysis that TOPO does not contribute to defect passivation. However, PL analysis of the ETL and HTL layers shows quenching. This PL quenching could be due to charge extraction or defect passivation. (The detailed discussion is added in **Appendix A4.3**) As mentioned at the start the PL technique is a limitation to differentiate the origin of the quenching. This point will be further discussed in Charge Extraction section **4.4.5**.

4.4.3 XPS study

To know the interaction of $CsPbI_3$ with the OAI molecule and TOPO molecule, a detailed X-ray photoelectron spectroscopy (XPS) study was conducted. XPS results (**Fig.4.3**) revealed that the OAI treatment shifted the Pb 4f and I 3d spectra towards higher binding energy by 250 meV and 200 meV, respectively. This is in line with the previous report and is likely due to the stronger coordination of the Pb-I bond with the introduction of a long-chain cation. [(4)] The change of work function position within the band gap can be determined from the shifts of occupied electronic states (valence and core levels). Analysis of core levels provides direct information on the change of the chemical states, but the valence bands are overlapped with contributions from perovskite and top layers which render the analysis difficult. As a result, it was estimated the work function change within the band gap, from the core level electrons binding energy shift of I 3d (as it has a lower kinetic energy of the photoelectrons as compared to that of Pb 4f, which probes the magnitude of surface band bending more precisely), that leads to a downward band bending at the surface by 200 meV.

With further TOPO treatment, Pb 4f and I 3d peaks are shifted to lower binding energy by 80 meV and 100 meV respectively. Thus, it indicates a lower downward band bending at the surface by 100 meV. It suggests here the core level binding energy shift in Pb 4f and I 3d comes from the electron-donating nature of TOPO [25]: the ligand may donate electrons to positively charged ions, such as Pb^{2+} or iodine vacancies [26] on the perovskite surface, thereby leading to a weaker coordination of Pb-I bond. In addition, TOPO was reported to form a dipole layer at the surface of perovskite that points outwards and reduces the work function (in other words, shifts the vacuum level to lower energy).[14, 26]

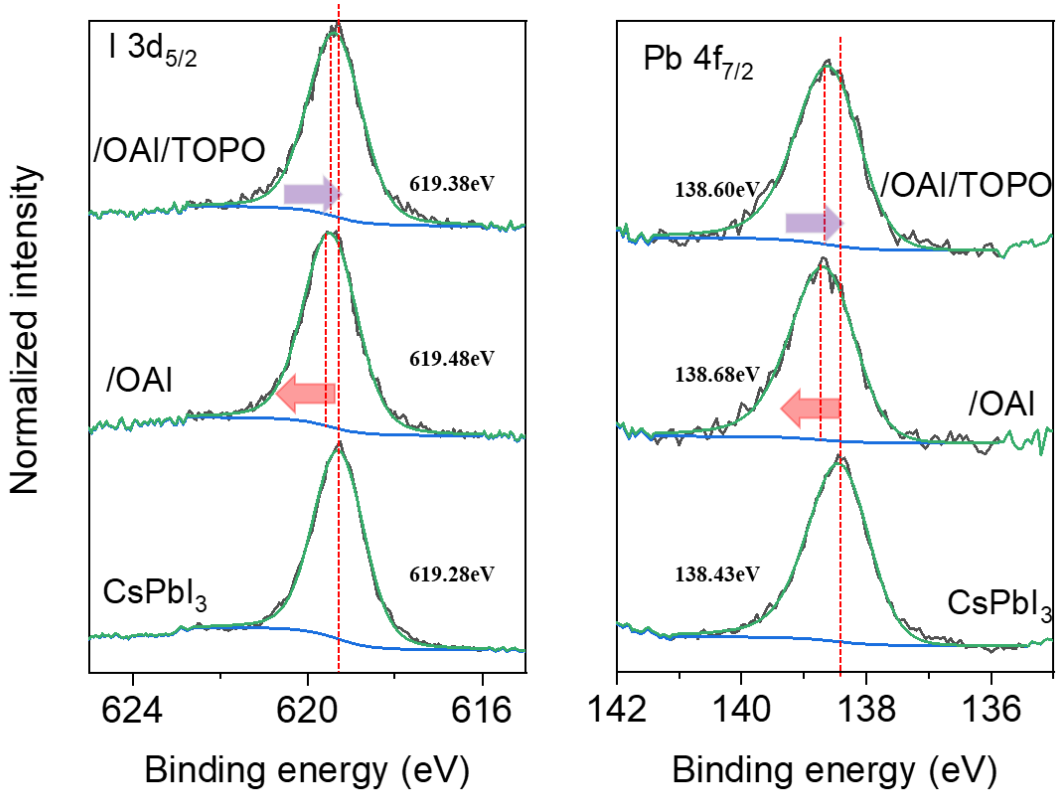

Fig.4.3 XPS Spectrum of (left panel) Pb $4f_{7/2}$ and (right panel) I $3d_{5/2}$ core-shell spectra of bare $CsPbI_3$, control sample and w/TOPO. Solid lines in green are fitted curves and red dashed lines show the peak position with values in eV on the corners.

The core level binding energy shift in Pb 4f and I 3d also implies the direct contact between TOPO and perovskite film in our work. It is reasonable as we do not expect to have a compact thin layer of OAI on top of perovskite film that will lead to the formation of an insulating layer. Rather OAI is expected to incorporate into the perovskite crystal structure and form a 2-dimensional structure on the surface. [21] It is suggested that OAI treatment has passivated most of the under-coordinated Pb2+ at the perovskite surface, and TOPO donates electrons more

likely to the interfacial iodine vacancies as they are found to be benign. [26] This would explain what is observed in PL analysis in **Fig. 4.2a** that, TOPO does not contribute noticeably to defects passivation. From the XPS in **Fig.A4.7**, we detected signals for P 2s and O 1s peaks originating from TOPO molecules for TOPO-treated samples.

XPS analysis suggests work function (WF) change due to electronic interaction at the surface. It further confirmed the shift in WF in the samples using the Kelvin probe. **Fig. 4.4 a** shows the average WF of these samples given with an error bar. It is observed that bare $CsPbI_3$ film has an average WF of 4.35 eV, reduced to 4.18 eV for control samples, and further reduced to 3.9 eV after TOPO treatment. The energetic level scheme is presented in **Fig. 4.4 b**, with values summarized in **Table A4.2**. The decrease in WF agrees well with the UPS measurements, which will be discussed in the next section.

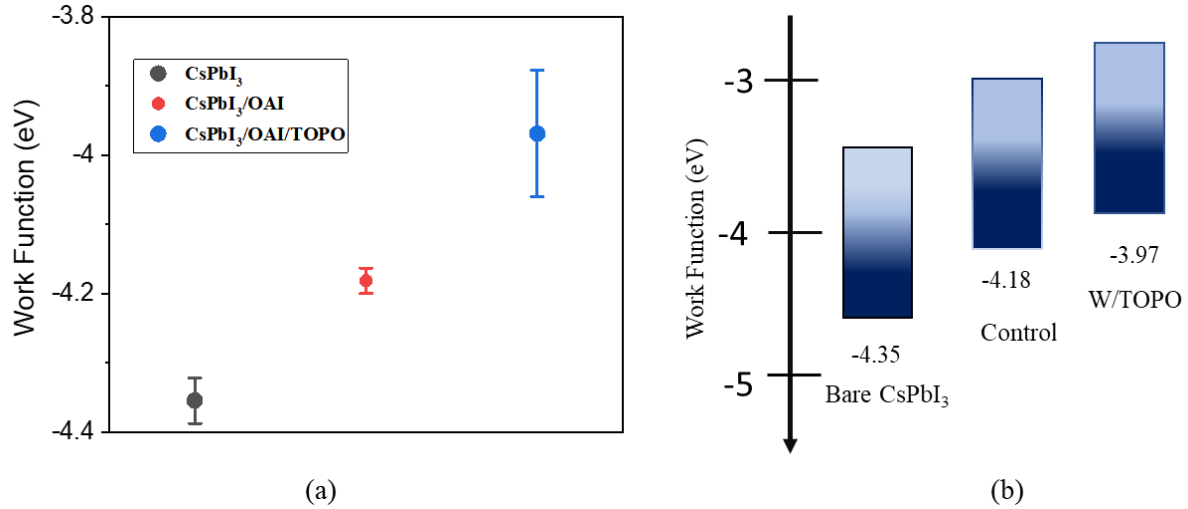

Fig. 4.4. a) Work function (Φ) of bare $CsPbI_3$ (black sphere), control $CsPbI_3$ (red sphere), and w/TOPO (blue sphere) with error bars (standard deviation, in the unit of eV), measured by Kelvin probe technique. b) energy level diagram of these samples, taking the average value plotted in.

4.4.4 Interfacial Energy Level Alignment

The XPS and KP measurements demonstrated a chemical interaction of the valence core levels of $CsPbI_3$ with OAI and TOPO, which causes a band bending and change in work function. Further, to study the energy levels profile and energy levels alignment at the interfaces, a detailed Ultraviolet photoelectron spectroscopy (UPS) measurement was conducted for bare $CsPbI_3$, OAI passivated $CsPbI_3$ (control $CsPbI_3$) and OAI passivated and TOPO treated $CsPbI_3$ (w/TOPO). **Fig. 4.5a** shows the secondary electron cut-off spectra of the samples, from which the work function (WF) can be obtained using this equation: $WF = h\upsilon - E_{cut-off}$, where $h\upsilon$

is the photoelectron energy of He (I) light, and $E_{cut\text{-}off}$ is the secondary electron cut-off. **Fig. 4.5b** shows the valence band (VB) spectra of these samples on a linear intensity scale of the photoelectrons. However, the VB onset of perovskites is extrapolated on a logarithmic intensity scale **(Fig. A4.8)** to accurately infer the band edge position for perovskites. [27,28]. **Fig. 4.5c** shows the energetic levels of bare $CsPbI_3$, control $CsPbI_3$ and w/TOPO. The following relation calculates the conduction band minimum (CBM),

$$CBM = VBM - E_g \qquad 4.1$$

The optical bandgap (E_g) was obtained from the Tauc plot for control and TOPO-treated samples given in **Fig. A4.2b**. The values of WF, VBM (valence band maximum), and CBM are summarised in **Table A4.3**. We observed a decrease in WF in both OAI and TOPO-treated samples. This trend confirms the Kelvin probe measurement. (**Fig. 4.4, Table A4.2**).

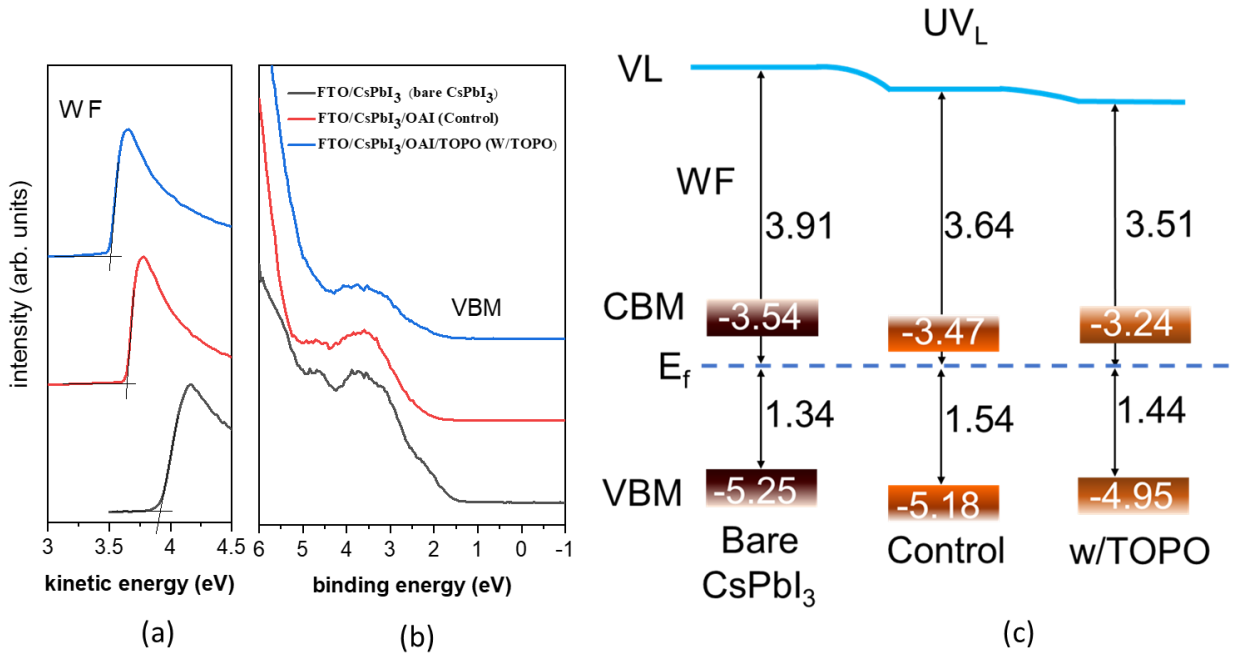

Fig. 4.5 Energy levels profile. a) Ultraviolet photoelectron spectroscopy (UPS) spectra of bare $CsPbI_3$, control $CsPbI_3$, and with TOPO treatment: secondary electron cut-off (SECO) (b) valence spectra. Energetic level scheme of c) bare $CsPbI_3$, control $CsPbI_3$ and w/TOPO.

Additionally, as revealed by XPS analysis, OAI treatment introduced a downward band bending of approximately 200 meV at the surface, resulting in a more *n*-type perovskite film which is in line with a recent report. [29] The addition of a TOPO layer, on the other hand, reversed the surface band bending into an upward one by around 100 meV, as shown in **Fig. 4.5c.**

To study the energy levels alignment at the interface with the adjacent hole transport material (HTM), *i.e.* Spiro-OMeTAD in this work. The HTM layer was deposited on the control sample and then on the TOPO-treated sample. It was observed that the ground state interfacial energy levels exhibit dramatic changes in both samples, which is believed to be caused by charge carrier rearrangement at the interface of perovskite and HTM, as observed in the previous studies. [30,31] It is also noted that the abrupt increase in vacuum level at the interface is almost identical to both samples by around 870 meV. To approach the interfacial energy level alignment under device operating conditions, the UPS measurement under the additional white light with light intensity equivalent to 1 sun (dashed line in **Fig. 4.6a, b**). The energy levels of the spiro-OMeTAD layer are found to exhibit dramatic downward shifts by 0.66 eV and 0.62 eV for the control and TOPO-treated samples, respectively. Such shifts, as recently observed in perovskite/organic semiconductor interfaces, [30,31] are caused by charge carrier accumulation at the interface under illumination, which leads to a realignment of the energy levels at the perovskite/spiro-OMeTAD interface. With spiro-OMeTAD HOMO shifting towards the perovskite VBM. It is noted that the measured energy levels from photoemission always refer to the Fermi level of the conductive FTO substrate. Given the unchanged perovskite energy levels upon white light illumination, the large energy offset between perovskite VBM and spiro-OMeTAD HOMO is then significantly reduced to 210 meV for control and to 260 meV for TOPO-treated samples.

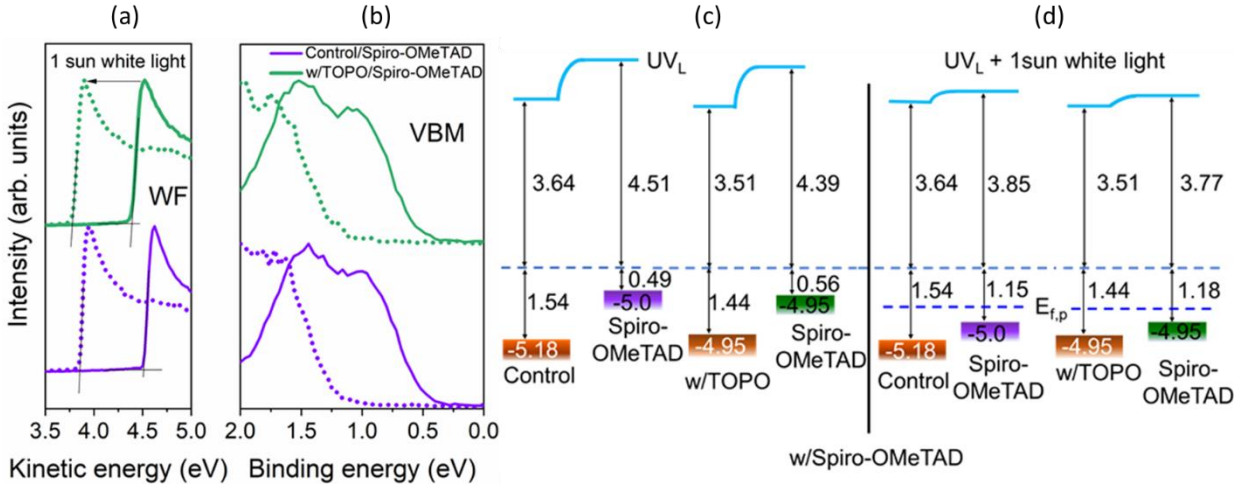

Fig. 4.6 Interfacial Energy level alignment. (a) UPS spectra of control/spiro-OMeTAD, and w/TOPO/spiro-OMeTAD: SECO (a) and valence spectra (b). Dashed lines are UPS spectra measured in the white light with 1 sun equivalent intensity. Energy band diagram of (c) control/spiro-OMeTAD and w/TOPO/spiro-OMeTAD in the dark, and d) under 1 sun white light illumination. All samples were deposited on top of FTO/TiO_2. UV_L refers to the low UV flux attenuated by the monochromator.

So far, the two roles of the TOPO layer have been revealed. One is its function as a dipole pointing towards the perovskite film leading to a decrease in WF compared to the control sample, confirmed from both UPS (~130 meV) and Kelvin probe measurement (~ 210 meV). The influence of tuned WF on device stability was studied in one recent work [29] It was reported that a lower WF, *i.e.* a less negative vacuum level, reduces the halide migration activation energy and thus leads to more pronounced hysteresis and less device stability. [29] This is not what is observed in this work. However, a decrease in WF for TOPO-treated samples was detected. The other role of TOPO is the chemical bonding with surface ions in perovskite that leads to an upward surface band bending of 100 meV. This change in interfacial energy level alignment is in our great interest. In the following, there will be discussed its effect on charge exaction and charge selectivity and, most importantly, on device stability.

4.4.5 Charge Extraction Dynamics

The UPS measurements provide evidence that TOPO-treated samples have low energy offset with the HTM, *i.e.*, energy levels are more aligned than control samples. To further investigate how it boosts charge carrier extraction, the samples were characterized using transient surface photovoltage spectroscopy (tr-SPV). The tr-SPV signals are directly proportional to the separated charges, as given by **Equation 2.23**. Therefore, transient SPV provides important insights into charge extraction and recombination dynamics. [32,33]

Transient SPV was measured for several different samples, *i.e.* control perovskite films, TOPO-treated perovskite films, control perovskite films with spiro-OMeTAD, TOPO-treated perovskite films with spiro-OMeTAD (all deposited on glass/TiO_2). The samples were also measured on glass. (**Fig. A4.9**). It shows that $CsPbI_3$ films deposited on glass have shallow and deep trap states (with activation energy up to 0.8 eV), while the TiO_2 substrate helps to remove these trap states and results in a clean and sharp SPV contour plots at a wide spectral range from 1.8 to 3.0 eV.

Fig. 4.7a-c exhibit the penetration depth of three different photon energies used in tr-SPV characterization. The penetration depth is calculated from the absorption coefficient of perovskite films (**Fig. A4.2. d**) as the top HTM has an absorption onset of approximately 2.92 eV [34]. It shows that red light (1.8 eV) excitation can penetrate close to the middle of the film. At the green light (2.2 eV) excitation, it penetrates approximately 74 nm deep into the film. At the blue light (2.6 eV), it penetrates within 10 nm next to the interface. **Fig. 4.7d-f** presents the tr-SPV results of samples measured under these three photon energies at fluences of 0.010

μJ/cm^2, 0.029 μJ/cm^2, and 0.040 μJ/cm^2, respectively, corresponding to the carrier concentration of 1.4×10^{15} cm^{-3} close to 1 sun operation conditions. Such a measurement was also conducted at 0.1 sun and 10 suns equivalent (**Fig. A4.10**), as discussed in **Appendix.** These measurements show that the overall trend is the same in all used light intensities. Thus, the larger photon energies (*i.e.* 2.2 eV and 2.6 eV) generated charge carriers closer to the HTM. This includes free carrier nonuniformities in the perovskite film, demands longer charge diffusion distance, and results in lower SPV amplitude in the same samples. However, we observed the same trend for the measurement conducted at three photon energies and three light intensities TOPO-treated samples have higher SPV amplitude than the control samples.

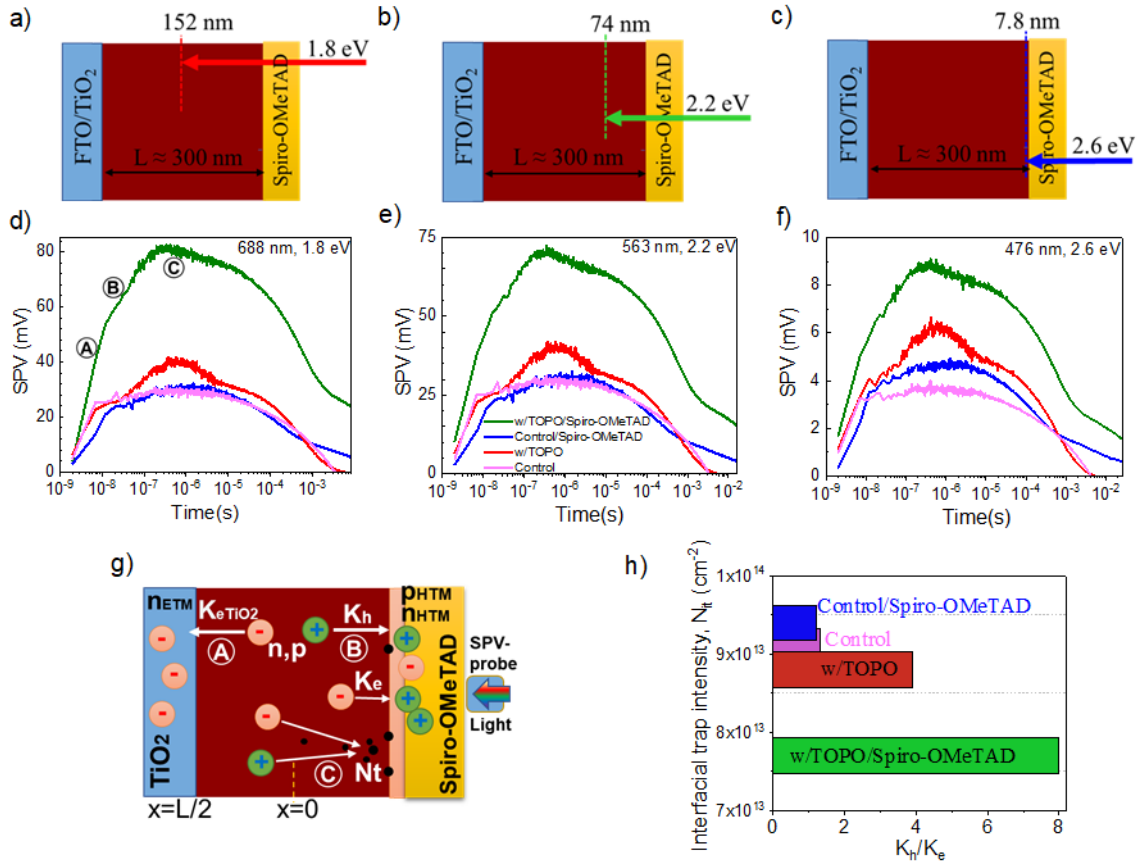

Fig. 4.7 Charge extraction. Scheme of light penetration depth into the samples for a) red light, b) green light, and c) blue light.Transient SPV of control, w/TOPO, control/Spiro-OMeTAD, w/TOPO/Spiro-OMeTAD measured at excitation source of d) 688 nm (1.8 eV), e) 563 nm (2.2 eV), and f) 476 nm (2.6 eV) at fluence of 0.010 μJ/cm^2, 0.029 μJ/cm^2, and 0.040 μJ/cm^2, respectively, equivalent to 1sun light intensity. g) charge extraction and recombination model describing charge carrier h) Fitted transient SPV data transport to ETL and HTM layers at two electrodes.

Generally, the SPV signal for efficient HTM (or ETM) appears as a fast exponential rise with a large amplitude. The recombination and non-efficient charge selectivity slow the rise and reduce the SPV amplitude. A significant boost of hole extraction in the TOPO-treated sample has been observed in the presence of adjacent HTM, approximately two times higher in the SPV amplitude and much faster signal rise than that of control samples in all studied laser photon energies. In contrast, the SPV amplitude is almost the same for control samples, with and without spiro-OMeTAD HTM. The rise in SPV amplitude in the control sample with HTM starts to be noticed under blue light illumination. In other words, for control samples, holes can be properly extracted only in the vicinity of HTM. Furthermore, TOPO-treated samples even without HTM, showed a higher SPV amplitude than the control and with HTM. This behaviour of TOPO-treated devices implies the positive effects of TOPO treatment on free electron extraction, hole extraction, and charge recombination.

To explain in detail, charge extraction dynamics, a 1D simulation of charge was applied. Here, mainly the processes that occurred during the 1 ns-10 µs timescale (four orders of magnitudes) were focused. As these are associated with carrier extraction and recombination. The initial charges are generated in the perovskite layer by the light and can be extracted to ETM and HTM with extraction rate constants K_{eETM} and $K_{h,}$ respectively, **Fig. 4.7g**. To describe charge selectivity properties at HTM, there are introduced electron injection rate constant K_e responsible for electron injection to HTM (for example, due to poor selectivity). The non-radiative and radiative charge recombinations are characterized by defect concentration N_T and band-to-band recombination C_b. To simplify the fitting procedure, the constants from the literature [35,36] were adopted (see **Table A4.4**). More details on the model can be found in **Chapter 2 Method Section 2.7.1**. The results of the fit and main fitting parameters are summarised in **Fig. A.4.11** (black curves) and **Table A4.5**.

According to the model results, the fast initial rise (region (A) in **Fig. A.4.11** is formed due to rapid electron extraction to TiO_2 with the rate constant (K_{eETM}) of 1.8×10^7 s^{-1}. The electron extraction rate constant only slightly decreased to 1.3×10^7 s^{-1} in other devices, signaling that other processes are responsible for dramatic carried dynamics changes in time regions (B) and (C). The difference in K_{eETM} can originate from a slightly faster electron extraction at the interface of TiO_2 and $CsPbI_3$ due to enhanced energy offset at the CBM level as characterized by the UPS measurement. [35]

It was found that TOPO treatment significantly boosts the free hole extraction rate (K_h) and selectivity properties of HTM. The value of K_h increased nearly twice in TOPO-treated samples with spiro-OMeTAD (8×10^6 s^{-1}) compared with the control sample (4.4×10^6 s^{-1}). The improved holes extraction near the TOPO surface is also observed in TOPO-treated perovskite films (3.9×10^6 s^{-1}) compared to the control sample (1.5×10^6 s^{-1}). In addition to improved hole extraction, TOPO significantly boosts the selectivity properties of HTL, which can be characterized by K_h/K_e ratio where K_e is electron injection in HTM **(Table A4.5**). **Fig. 4.7 h** shows that TOPO treatment increased the K_h/K_e ratio from the value of 1.3 in control to the value of 3.9 for perovskite films. Further, this value increased up to 8 in the presence of spiro-OMeTAD, meanwhile, control samples without TOPO treatment had a rather low value of 1.2. Finally, it is observed that slight passivation of non-radiative recombination in TOPO-treated samples with spiro-OMeTAD (interfacial trap density of 7.7×10^{13} cm^{-3}) in comparison with control samples with spiro-OMeTAD (9.4×10^{13} cm^{-3}). This aligns with what was observed in the PL measurement, as presented in **Fig. 4.2a**.

The overall picture of the charge dynamics suggested by tr-SPV with simulation demonstrates a significant role of TOPO in the improvement of hole extraction. The TOPO layer stimulates free hole extraction in HTM and repels electrons from the TOPO surface. The selectivity of neat HTM can result in noticeable suppression of charge recombination near the HTM surface and in HTM itself. The TOPO also provides chemical passivation of traps (18% decrease in trap concentration). We can believe that the suppressed recombination is mainly contributed by the enhanced hole selectivity due to the formation of upward surface band bending at the interface between $CsPbI_3$ and spiro-OMeTAD. The enhanced hole selectivity originates from better energetic alignment caused by upward surface band bending and dipole activity, which also contributes to recombination suppression.

4.4.6 Device Performance

To examine the effect of surface band bending-induced energy alignment and charge extraction on the photovoltaic performance, $CsPbI_3$ perovskite-based devices were fabricated with TiO_2 as the ETM and spiro-OMeTAD as the HTM, respectively. **Fig. 4.8a** illustrates the *J-V* curves for the champion devices in the reverse and forward scans. The photovoltaic parameters are summarized in **Table A4.6**. Box charts of V_{oc}, $J_{sc,}$ and *FF* of over 40 solar cells are given in **Fig. A4.12.** It shows that there is a clear improvement in V_{OC} and *FF* by TOPO treatment and, consequently an improvement in PCE. The TOPO treatment achieved the champion device

with 19% PCE and V_{OC} of over 1.2. **Fig. 8e** shows the EQE spectra of the champion devices with their *J-V* curve given in **Fig.8a**. It shows that all our devices exhibit an EQE of over 90% in broad wavelengths ranging from 400 nm to 580 nm.

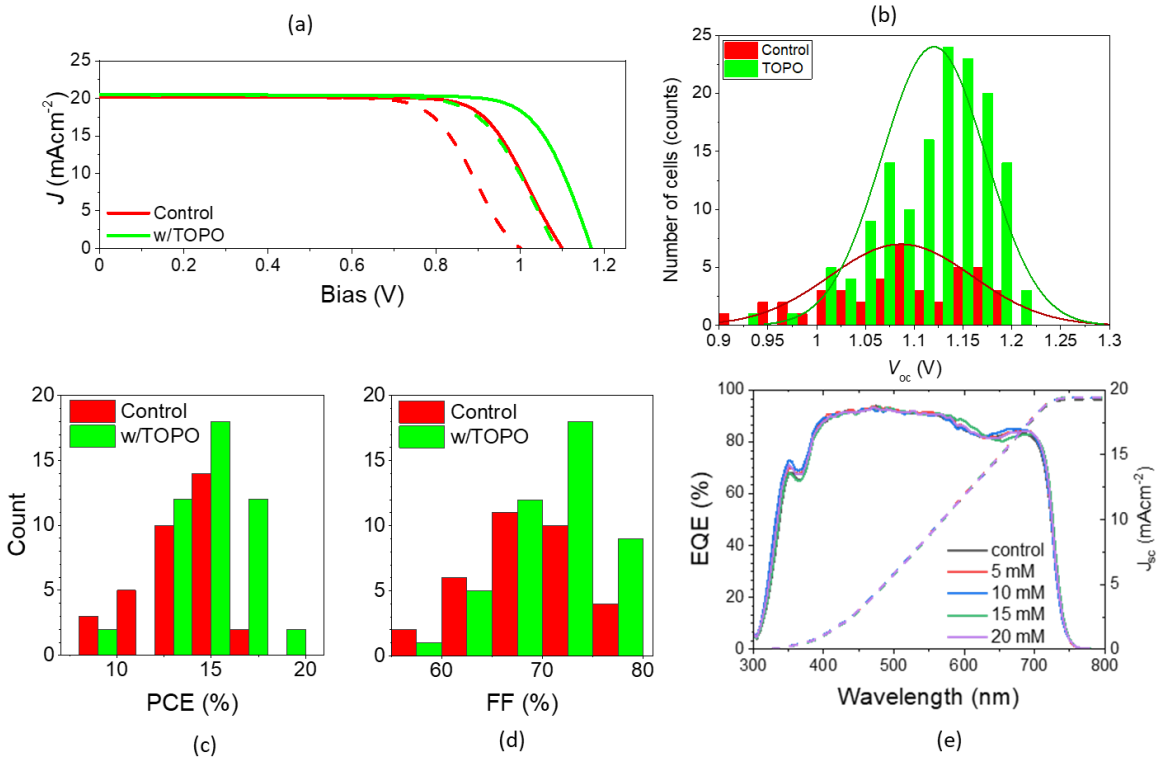

Fig 4.8. **Device Performance** a) *J-V* curve of the champion devices for $CsPbI_3$ with and without TOPO treatment, measured at 1 Sun AM1.5G at room temperature inside the nitrogen-filled glovebox at the scan rate of 200 mV/s for both forward (dash line) and reverse (solid line) scans.Device performance histograms(b) V_{oc} (c) PCE (d)*FF* for more than 40 devices e) EQE spectra of champion devices with the integrated J_{sc} from EQE spectra overplotted on the right y-axis.

4.4.7 Device Stability

Device stability was measured in a custom-built MPPT (maximum power point tracking) ageing system [37] according to ISOS-LC-1l [38], by alternating 12 hours of illumination under one sun and 12 hours of dark for 27 cycles separated in two runs with a break of 72 hours. The stability test was conducted in nitrogen and at an ambient temperature of 25 °C, including the 72-hour break in the dark phase for all measured samples. More details of the long-term stability test can be found in the **Appendix**. The UV component of the solar spectrum was filtered to prevent degradation caused by TiO_2 oxygen desorption. [39,40]. In parallel, the constant illumination ageing testing lasted up to 700 hours. **Figure 4.9a** shows that both types of devices undergo burn-in initially and then get stabilized. Compared to control, TOPO-treated

devices endure the efficiency for a long time. **Figure 4.9b** shows a normalized PCE for the representative devices. It shows that in the first run, both devices showed a similar trend, but in the second run, TOPO-treated devices showed less degradation than the control.

Figure 4.9c shows the energy produced per cycle calculated using **Equation 4.3.** Analysis based on four individual solar cells each. Each substrate carries six pixels, of which we selected the one that presented the best efficiency and stability. The ageing was conducted with four substrates (samples) for each type of solar cell (24 pixels per condition). We refer to this selection method as the "best PCE+stability filter" in the literature. In the figure, those champion pixels are shown.

$$\text{Energy produced } \Delta J = Power \times time \tag{4.2}$$

$$\Delta J = \int_0^{12} Pdt \tag{4.3}$$

$\Delta J_{1\rightarrow 27}$ Control devices

$\Delta J_{1\rightarrow 27}$ w/TOPO devices

$$J_{total\ (Control)} = Sum(\Delta J_1 + \Delta J_2 + \Delta J_3 \ldots\ldots\ldots\ldots\ldots\ldots\ldots + \Delta J_{27}) \tag{4.4}$$

$$J_{total\ (W/TOPO)} = Sum(\Delta J_1 + \Delta J_2 + \Delta J_3 \ldots\ldots\ldots\ldots\ldots\ldots\ldots + \Delta J_{27}) \tag{4.5}$$

In the first run (*i.e.* 14 cycles in 342 hours), we observe a similar degradation trend for both samples, while a much slower degradation process is observed in TOPO-treated samples in the second run (*i.e.* 15^{th} - 27^{th} cycles in 322 hours). The total energy produced in the 27 cycles was calculated by using **Equation 4.3-4.5**. **Fig. 4.9d** shows the overall energy generated by the solar cells is averaged. **Fig. 4.9d** shows that TOPO-treated solar cells can generate 16.8% more energy than the control, with the surplus energy mainly generated after 342 hours (33.3% over the control). It should be noted that control samples have a larger deviation than TOPO-treated ones.

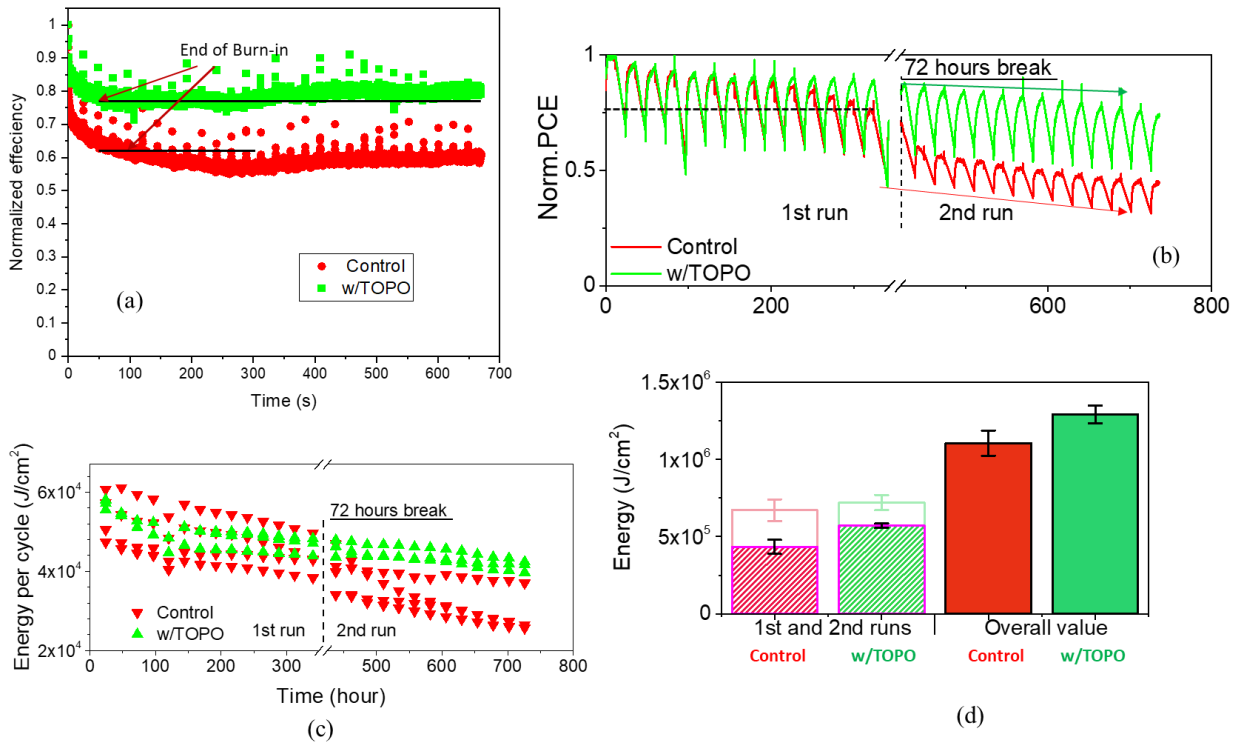

Fig 4.9 Device Stability a) MPP tracking for control and TOPO-treated samples for 700 hours. (b) Cyclic MPP tracking, Normalized PCE per cycle, with each cycle composed of 12 hours light-on and 12 hours of light-off, c) absolute energy per cycle of four individual solar cells d) Calculated energy output in the first and second runs and the overall value.

Why TOPO-treated Devices show more Stability; An explanation

I. The ion migration on the interfaces leads to chemical reactions and renders the efficiency and stability of the devices. The chemical reaction between spiro-OMeTAD$^+$ and migrating I^- reduced the HTM conductivity. [41,42] In this work, it can be speculated that TOPO treatment makes an energy barrier for the iodine ion to move across the interface, and the HTM conductivity remains preserved.

II. TOPO helps to make iodine vacancies less mobile by chemical bonding with iodine vacancies at the interface. Iodine vacancies at the interface are found to be benign, but illumination can promote the diffusion of iodine vacancies to the bulk which makes them detrimental for creating new non-radiative recombination centers [43]. This causes severe loss in V_{oc} in control samples but is effectively suppressed in TOPO samples.

III. The upward band bending by the TOPO treatment leads to better separation between electrons and holes at the interface, which causes less charge accumulation near the interface and thus less interfacial recombination as supported by tr-SPV data in **Fig. 4.6**. In return, it contributes to better stability in devices.[44] The synergy of the above

effects of TOPO provides better device stability and performance in TOPO-treated samples.

4.5 Conclusion

It is demonstrated that the TOPO molecule causes surface upward band bending on the well-passivated $CsPbI_3$ film and changes the WF. This decrease in WF, by the dipole molecule, changes the interfacial energy levels and reduces the energy offset between perovskite VBM levels and spiro-OMeTAD HOMO levels, which is measured by UPS measurements. Further, this alignment induces a change in charge transfer kinetics on the interface, as revealed by the trSPV study. Consequently, we have achieved a V_{oc} of over 1.2V with improved stability and 19% efficiency. This work reveals that interfacial energy level alignment (particularly the consequent charge selectivity) plays a critical role in device stability besides defects passivation and WF tuning.

(Z. Iqbal, Q.Wang, and Prof.Antonio Abate conceptualized the research question. Z.I. did all the experiments in the HySprint Lab. He made all the samples and devices involved in this work. He further extended his collaboration for spectroscopic and optical measurements.F.Zu supported this project with XPS and UPS measurements Artem helped in this work by measuring tr-SPV, Kelvin probe, and theoretical simulation of charge transport. E.G. Partida. conducted PL and TRPL spectroscopy measurements Hans Köbler helped in this work by measuring the long-term stability of solar cells The author acknowledges Q.wang for her help in drawing some schematic figures for this chapter.)

References

1. J.A. Steele, H. Jin, I.Dovgaliuk ,R.F. Berger ,T.Braeckevelt, H.Yuan, C.Martin , E.Solano, K.Lejaeghere,S. M. J. Rogge, C.Notebaert, W.Vandezande, K. P. F. Janssen, B. Goderis, E. Debroye, Y. Wang, Y. Dong, D. Ma, M.Saidaminov, H. Tan, Z. Lu, V.Dyadkin, D. Chernyshov, V.V. Speybroeck, E. H. Sargent, J. Hofkens, M. B. J. Roeffaers. “Thermal unequilibrium of strained black CsPbI3 thin films.”, *Science*., 2019, **365**, 6454 679-684.
2. A.Swarnkar,A.R. Marshall,E.M. Sanehira,B.D. Chernomordik, D.T. Moore, J. A. Christians,T.Chakrabarti, J. M. Luther “ Quantum dot–induced phase stabilization of α-CsPbI3 perovskite for high-efficiency photovoltaics.”, *Science*, 2016, **354**, 6308, 92-95.

3. Y. Wang1, M. I. Dar, L.K. Ono, T. Zhang1, M. Kan1, Y. Li, L. Zhang, X.Wang1, Y.Yang, X.Gao, Y. Qi, M.Grätzel, Y. Zhao, "Thermodynamically stabilized ß-CsPbI3–based perovskite solar cells with efficiencies >18%.", *Science*, 2019, **365**, 591–595.
4. Y. Wang, X. Liu, T. Zhang, *et al.*, "The Role of Dimethylammonium Iodide in CsPbI3 Perovskite Fabrication: Additive or Dopant?", *Angewandte Chemie International Edition*, 2019, **131**, 16844 – 16849.
5. Y.Cui, J.Shi, F.Meng, B.Yu, S.Tan, S. He, C.Tan,Y. Li, H. Wu, Y.Luo, D. Li, Q.Meng, "A Versatile Molten-Salt Induction Strategy to Achieve Efficient CsPbI3 Perovskite Solar Cells with a High Open-Circuit Voltage >1.2 V.", *Advanced Materials*, 2022, **34**, 2205028.
6. M. Jeong, I. W. Choi, E. M. Go, Y. Cho, M. Kim, B. Lee, S. Jeong, Y. Jo, H. W. Choi, J. Lee, J.-H. Bae, S. K. Kwak, D. S. Kim, C. Yang, "Stable perovskite solar cells with efficiency exceeding 24.8% and 0.3-V voltage loss.", *Science*, 2020, **369**, 1615–1620.
7. X.Chang, J. Fang, Y. Fan, T. Luo, H. Su, Y. Zhang, J. Lu, L. Tsetseris, T. D. Anthopoulos, S . (Frank) Liu, K. ZhaoQ. "Printable CsPbI3 Perovskite Solar Cells with PCE of 19% via an Additive Strategy.", *Advanced Materials*, 2020, **32**, 2001243.
8. X. Gu, W. Xiang, Q. Tian, S.(Frank) Liu," Rational Surface-Defect Control via Designed Passivation for High-Efficiency Inorganic Perovskite Solar Cells.", *Angewandte Chemie*,2021, **133**, 23348 –23354.
9. J. Qiu, Q. Zhou, D . Jia, Y.Wang,S.Li, X.Zhang, "Robust molecular-dipole-induced surface functionalization of inorganic perovskites for efficient solar cells.", *Journal of Material Chemistry A*, 2022, **10**, 1821–1830.
10. X. Zhao, T. Liu, Q. C. Burlingame, T. Liu, R. Holley, G. Cheng, *et al*., "Accelerated aging of all-inorganic, interface-stabilized perovskite solar cells.", *Science*, 2022, **377** (6603), 307-310.
11. W. Xiang, S (F) Liu, W.Tress., " Interfaces and Interfacial layers in Inorganic Perovskite Solar Cells.", *Angewandte Chemie*, 2021, **133**, 26644– 26657.
12. M. Grischek, P. Caprioglio, J. Zhang, F. Pena-Camargo, K. Sveinbjörnsson, F. Zu, *et al*., "Efficiency Potential and Voltage Loss of Inorganic CsPbI2Br Perovskite Solar Cells.", *Solar RRL*, 2022, **6**(11), 2200690.
13. Q. Wang, F. Zu, P. Caprioglio, *et al.*, "Large Conduction Band Energy Offset Is Critical for High Fill Factors in Inorganic Perovskite Solar Cells", *ACS Energy Letter*., 2020, **5**, 7, 2343–2348.
14. L. Canil, T. Cramer, B. Fraboni, *et al*., "Tuning Halide Perovskite Energy Levels", *Energy & Environmental Science*, 2021,**14**, 1429-1438.
15. H. Kanda, N. Shibayama, A.J.Huckaba, *et al.*, "Band-bending induced passivation: high performance and stable perovskite solar cells using a perhydropoly(silazane) precursor.", *Energy & Environmental Science*, 2020, **13**, 1222.
16. S. Wang, M.-H. Li, Y. Zhang, Y. Jiang, L. Xu, F. Wang, *et al*., "Surface N-type Band Bending for Stable Inverted CsPbI3 Perovskite Solar Cells with over 20% Efficiency.", *Energy & Environmental Science*, 2023,**16**, 2572-2578
17. S. M. Yoon, H. Min, J. B. Kim, *et al.*, "Surface Engineering of Ambient-Air-Processed Cesium Lead Triiodide Layers for Efficient Solar Cells", *Joule*, 2021, **5**, 183-196.
18. Q. Jiang, Y. Zhao, X. Zhang, *et al.*, "Surface passivation of perovskite film for efficient solar cells.", *Nature Photonics.*, 2019, **13**, 460–466.

19. F. Li, X. Deng, F. Qi, *et al.*, "Regulating Surface Termination for Efficient Inverted Perovskite Solar Cells with Greater Than 23% Efficiency.", *Journal of American Chemical Society*, 2020, **142**(47), 20134–20142.
20. G. Wu, R. Liang, M. Ge, *et al.*, "Surface Passivation Using 2D Perovskites toward Efficient and Stable Perovskite Solar Cells.", *Advanced Materials*, 2022, **34**, 2105635.
21. H. Kim, S.-U. Lee, D. Y. Lee, *et al.*, "Optimal Interfacial Engineering with Different Length of Alkylammonium Halide for Efficient and Stable Perovskite Solar Cells", *Advanced Energy Materials.*, 2019, **9**, 1902740.
22. I. Levine, A. Al Ashouri, A. Musiienko, *et al.*, "Charge transfer rates and electron trapping at buried interfaces of perovskite solar cell", *Joule*, 2021, **5**, 2915–2933.
23. J. Wang, J. Zhang, Y. Zhou, *et al.*, "Highly efficient all-inorganic perovskite solar cells with suppressed non-radiative recombination by a Lewis base.", *Nature Communication*, 2020,**11**, 177.
24. S. Gharibzadeh, P. Fassl, I. M. Hossain, *et al.*, "Two birds with one stone: dual grain-boundary and interface passivation enables >22% efficient inverted methylammonium-free perovskite solar cells.", *Energy & Environmental Science*, 2021, **14**, 5875-5893.
25. R. A. Belisle, K. A. Bush, L. Bertoluzzi, *et al.*, "Impact of Surfaces on Photoinduced Halide Segregation in Mixed-Halide Perovskites.", *ACS Energy Letter.*, 2018, **3** (11), 2694-2700.
26. W. Lan-Ying, M. Wei, L. Chao, and M. Sheng, "Benign Interfacial Iodine Vacancies in Perovskite Solar Cells.", *The Journal of Physical Chemistry C*, 2017, **121**, 11, 5905–5913.
27. J. Endres, D. A. Egger, M. Kulbak, *et al.*, "Valence and Conduction Band Densities of States of Metal Halide Perovskites: A Combined Experimental–Theoretical Study.", *The Journal of Physical Chemistry Letters*, 2016, **7**, 14, 2722–2729.
28. F. Zu, P. Amsalem, D. A. Egger, *et al.*, "Constructing the Electronic Structure of $CH_3NH_3PbI_3$ and $CH_3NH_3PbBr_3$ Perovskite Thin Films from Single-Crystal Band Structure Measurements.", *The Journal of Physical Chemistry Letters*, 2019, **10**(3), 601–609.
29. S. Tan, T. Huang, I. Yavuz, R. Wang, T. W. Yoon, M. Xu, *et al*., "Stability-limiting heterointerfaces of perovskite photovoltaics." *Nature*, 2022, **605** (7909), 268-273.
30. F. Zu, J.H. Warby, M. Stolterfoht, *et al.*, "Photoinduced Energy-Level Realignment at Interfaces between Organic Semiconductors and Metal-Halide Perovskites", *Physical Review Letters*, 2021, **127**, 246401
31. F. Zu, M. Roß, L. Frohloff, *et al.*, "Illumination-driven energy level re-alignment at buried interfaces between organic charge transport layers and a lead halide perovskite", *Solar. RRL*, 2022, **6**(6), 2101065
32. T. Dittrich and S. Fengler, "Surface Photovoltage Analysis of Photoactive Materials", World Scientific (Europe), 2020,
33. S. Fengler, H. Kriegel, M. Schieda, *et al.*, "Charge Transfer in c-Si(n++)/TiO2 (ALD) at the Amorphous/Anatase Transition: A Transient Surface Photovoltage Spectroscopy Study.", *ACS Applied Materials & Interfaces*, 2020, **12**, 3140−3149.
34. Q. Wang, E. Mosconi, C. Wolff, *et al.*, "Rationalizing the Molecular Design of Hole-Selective Contacts to Improve Charge Extraction in Perovskite Solar Cells.", *Advanced Energy Materials*, 2019, **9**, 1900990.

35. F. P. Camargo, J. Thiesbrummel, H, Hempel, *et al.*, "Revealing the Doping Density in Perovskite Solar Cells and Its Impact on Device Performance.", *Applied Physics Reviews* 2022, **9**, 021409
36. A. Musiienko, D. R. Ceratti, J. Pipek, *et al.*, "Defects in Hybrid Perovskites: The Secret of Efficient Charge Transport", *Advanced Functional Materials.*, 2021, **31**, 2104467.
37. H. Köbler, S. Neubert, M. Jankovec, *et al*., "High-Throughput Aging System for Parallel Maximum Power Point Tracking of Perovskite Solar Cells", *Energy Technology*, 2022, 220234.
38. M.V. Khenkin, E.A. Katz, A. Abate, *et al.*, "Consensus statement for stability assessment and reporting for perovskite photovoltaics based on ISOS procedures", *Nature Energy*, 2020, **5**, 35–49.
39. A. Farooq, I. M. Hossain, S. Moghadamzadeh, *et al.*, "Spectral Dependence of Degradation under Ultraviolet Light in Perovskite Solar Cells", *ACS Applied Materials & Interfaces*, 2018, **10**, 21985−21990
40. Z. Wang, Z. Zhang, L. Xie, *et al.*, "Recent Advances and Perspectives of Photostability for Halide Perovskite Solar Cells", *Advanced Optical Materials*, 2022, **10**, 2101822.
41. J. Carrillo, A. Guerrero, S. Rahimnejad, *et al*., "Ionic Reactivity at Contacts and Aging of Methylammonium Lead Triiodide Perovskite Solar Cells", *Advanced Energy Materials*, 2016, **6**, 1502246.
42. B. Cristina, A. Laura Elena, S. Viorica, *et al*., "Iodine Migration and Degradation of Perovskite Solar Cells Enhanced by Metallic Electrodes", *The Journal of Physical Chemistry Letters*, 2016, **7**, 24, 5168-5175.
43. W. Jing and Y. Wan-Jian, "Revisiting the Iodine Vacancy Surface Defects to Rationalize Passivation Strategies in Perovskite Solar Cells", *The Journal of Physical Chemistry Letters*, 2022, **13**(29), 6694-6700.
44. Q. Wang, "Influence of a Cobalt Additive in spiro-OMeTAD on Charge Recombination and Carrier Density in Perovskite Solar Cells investigated using Impedance Spectroscopy", *Physical Chemistry Chemical Physics*, 2018, **20**, 10114-10120.

Chapter 5

Interface Design for P3HT Hole Transport Layer

5.1 Statement of the Challenge

P3HT poly(3-hexylthiophene) is used as a hole transport layer (HTM) in the *n-i-p* device structure as an alternative to spiro-OMeTAD. However, it has a low optical band gap and morphology issues that lead to electronic coupling at the interface, result in non-radiative recombination at the perovskite/HTM interface, and hinder solar cell performances. Introducing a wide band gap molecule on the perovskite/P3HT is the proposed strategy to cope with these problems.

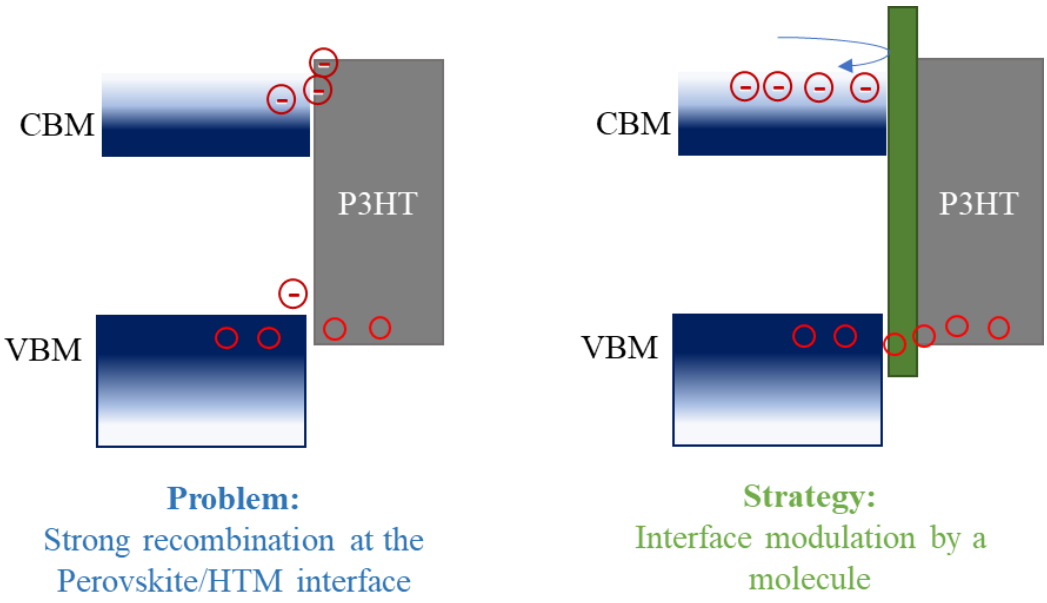

Figure 5.1. Table of contents for Chapter 5. This figure highlights the problem and the proposed strategy to resolve the interface problem.

5.2 Introduction

Perovskite solar cell (PSC) efficiency has crossed 82% of the SQ limit in single junction and more than 75% in tandem architecture. [1] However, the stability of perovskite solar cells is one of Achille's heels to find the marketplace. [2,3] Stability of the device is not only determined by the perovskite, but the other layers are also important for the best performance and stability. [4,5] Perovskite solar cell comprises two essential layers for charge extraction: the electron transport layer (HTM) and the hole transport layer (HTM). The list of the various ETLs and HTLs has been introduced in **Figure 1.4**. spiro-OMeTAD (2,2′,7,7′-tetrakis (*N, N-di-p-*

methoxyphenyl-amine)-9,9′ spirobifluorene is one of the widely used HTM in *n-i-p* device structures and is considered as standard for the efficient devices reported so far. [6] However, spiro-OMeTAD has several disadvantages for commercialization. Besides high cost, it is susceptible to high temperatures, needs time-consuming oxygen soaking, has film deposition issues, and needs dopants that may trigger the perovskite layer degradations. [7-10] Although several efforts have been made to make it workable by changing the doping methods (CO_2 bubbling) and dopants, etc. [11-17] The other physical properties of spiro-OMeTAD such as high-temperature sensitivity are still a challenge. P3HT is being used as an HTL as an alternative to spiro-OMeTAD. For practical purposes, it is comparatively low cost, easy to fabricate, and has potential optoelectronic properties. [18-20] Despite these advantages, there are some associated challenges with P3HT. It is a low band gap as compared to spiro-OMeTAD, *i.e.* ~2eV, and this band gap is very close to perovskite halides material's conduction band (CB) which results in non-radiative recombination at the interface and badly affects the open circuit voltage (V_{OC}). [21]

In **Chapters 3-4,** it is reported that V_{OC} over 1.2 V was achieved for $CsPbI_3$ with spiro-OMeTAD as an HTM. However, when the same material was used with P3HT, V_{OC} dropped to 0.5V for $CsPbI_3$, which clearly shows that the performance does not come to the perovskite layer only. There is a need to modify the interface according to HTM layers to extract the charges effectively. As a next step of the previous works (**Chapters 3 and 4**), the established method has been used for P3HT. The interface between perovskite and P3HT was modulated by a molecule *n*-hexyl trimethyl ammonium bromide (HTAB). This molecule passivates the $CsPbI_3$ surface and acts as a mediator between $CsPbI_3$ and P3HT. This molecule was already used by J.Soe *et al.* with P3HT. [22] They have reported over 22% PCE for triple cation perovskite halides. It is mentioned that the right choice of molecules plays a distinctive role in interface engineering. In **Chapters 3 and 4**, *n*-OAI was used as a passivating molecule. However, this molecule does not work for P3HT-based devices. This work does not provide insight or a detailed study of non-radiative recombination. However, the primary investigations provide a good starting point and an outlook on how the interface can be engineered for P3HT as HTM that may find practical applications in the future.

5.3 Methods

The devices were fabricated as mentioned in **Appendix A3.1**. However, the deposition of the HTAB molecule and P3HT are added here. A 1 mM solution of *n*-hexyl trimethylammonium

bromide (HTAB) solution was prepared in a solvent mixture containing *o*-dichlorobenzene and isopropanol in a 97:3 v/v io. The solution was spin-coated at 5000 rpm for 30 seconds on a perovskite layer, and then the film was annealed for 1 minute at 150°C. The HTM layer was also deposited by spin coating at 3000 rpm for 30 seconds, and its 5mg/ml solution was made in a solvent mixture of chlorobenzene and diphenyl ether in a 97:3 ratio.

5.4 Results and Discussion

The dense, uniform, and pinhole-free $CsPbI_3$ films were prepared as the method mentioned in **Appendix A3.1**. **Figure 5.1** shows SEM images of the bare $CsPbI_3$, OAI passivated, and HTAB passivated film. The SEM image shows that HTAB makes a layer on the top of $CsPbI_3$ film, unlikely OAI that settles in the grain boundaries. It can be inferred that the HTAB molecule acts entirely differently from OAI in layer formation. The exact orientation of the molecules is not studied here, but the chemical structure of the molecules suggests that it will make a 2D layer on the top of the $CsPbI_3$ surface like OAI. However, both differ in the number of long chains attached, which is responsible for the orientation on the surface.

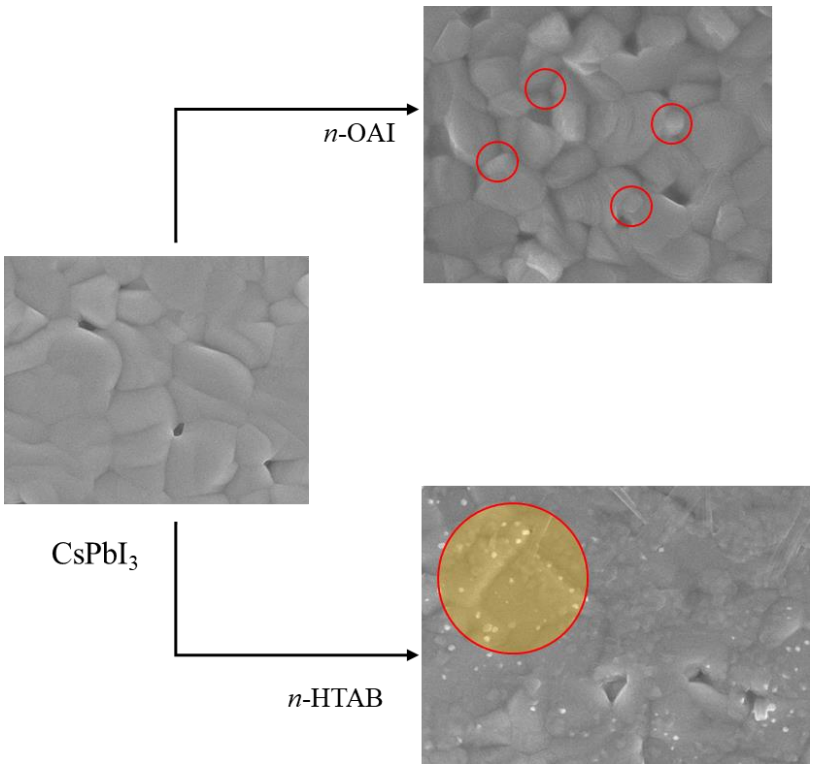

Figure 5.1: SEM image of bare $CsPbI_3$, OAI deposited $CsPbI_3$, and HTAB deposited $CsPbI_3$ films.

Figure 5.2 shows tr-SPV measurements for the samples bare $CsPbI_3$, P3HT on the top of $CsPbI_3$, $CsPbI_3$ passivated with HTAB with and without HTM. The red light laser pulse(with

energy 1.8eV) was used for excitation. It can penetrate close to the film's middle, as reported in **Chapter 4**.

In SPV, an exponential rise in signals with a large amplitude shows an efficient charge extraction at the interface. However, the non-radiative recombination or misalignments of the bands lead to slow down the rise and damping in amplitude. A significant boost of hole extraction in the HTAB-treated sample in the presence of adjacent HTM is observed, approximately three times higher in the SPV amplitude and much faster signal rise than that of the bare $CsPbI_3$ sample. In contrast, $CsPbI_3$ deposited P3HT and $CsPbI_3$ treated with HTAB show similar signals, meaning holes can be extracted from the HTAB-treated samples. The overall measurements show that HTAB-treated samples implied positive effects on charge extraction. Further, **Figures 5.3 b** and **c** show contour plots. These measurements were conducted on the glass as a substrate and show that HTAB passivates the subband gap defect.

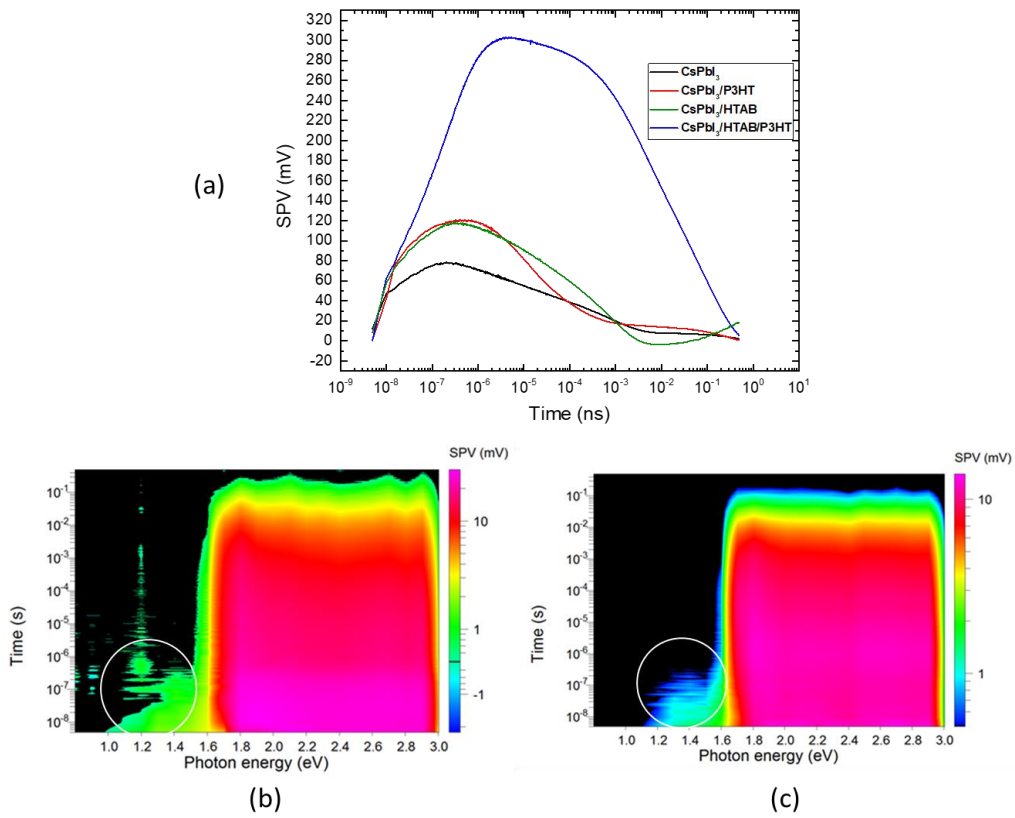

Figure 5.3 trSPV measurements at excitation source of 688 nm (1.8 eV) with the light intensity of 1 sun illumination (a) bare $CsPbI_3$, P3HT on the top of $CsPbI_3CsPbI_3$ passivated with HTAB with and without HTM on FTO/TiO_2 substrates. Contour plots of (b) bare $CsPbI_3$ (c) $CsPbI_3$/HTAB on glass

To know the effect of HTAB treatment on the interface, the devices were fabricated by using TiO_2 as ETL and P3HT as the HTL layer. The champion device without HTAB results in 12.1%

PCE, while with HTAB treatment, 14.2% PCE was achieved. There is an improvement in 60meV in V_{OC} for the champion device. Further, the stability of these devices was measured at 65°C. **Figure 5.4b** shows an exponential decay in the efficiency for both types of devices. However, HTAB devices succeed in retarding the exponential decay for a few hours.

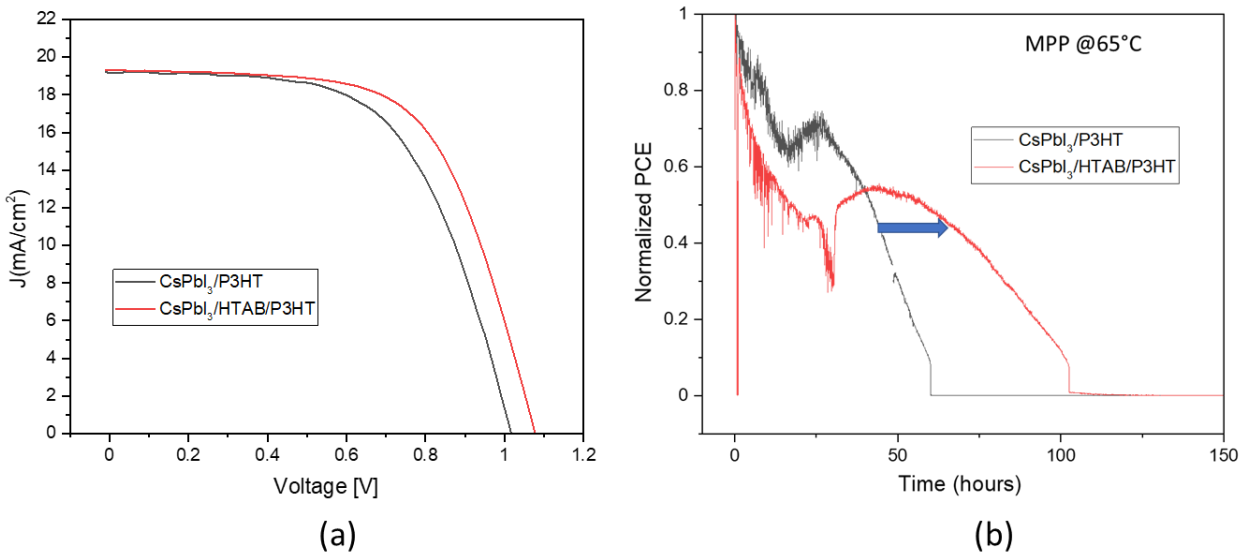

Figure 5.4 (a)*JV* measurement of the champion device with and without HTAB treatment. (b) MPP tracking for with and without HTAB treated device at 65°C.

5.4 Conclusion

P3HT can be used alternative to spiro-OMeTAD as HTL in *n-i-p* devices. However, it needs to improve the interfaces accordingly. HTAB makes a layer on $CsPbI_3$ film. The TrSPV measurements show that HTAB acts as a bridge for charge extraction and also passivates the defects in $CsPbI_3$.With HTAB-treated CsPBI3 fil, over 14 % efficiency was achieved for P3HT-based devices.

References

1. Best Research-Cell Efficiency Chart https://www.nrel.gov/pv/assets/pdfs/best-research-cell-efficiencies-rev220630 (accessed June15, 2023)
2. F. Lang, G. E. Eperon, K. Frohna, *et al.*, "Proton-Radiation Tolerant All-Perovskite Multijunction Solar Cells." *Advanced Energy Materials.*, 2021, **11**, 2102246.
3. M.V. Khenkin, E.A. Katz, A. Abate, *et al.*, "Consensus statement for stability assessment and reporting for perovskite photovoltaics based on ISOS procedures", *Nature Energy*, 2020, **5**, 35–49.
4. J. Jeong *et al.*, "Pseudo-halide anion engineering for α-FAPbI3 perovskite solar cells." *Nature*,2021,**592**, 381–385 (2021).
5. M. Jeong, I. W. Choi, E. M. Go, Y. Cho, M. Kim, B. Lee, *et al.*, "Stable perovskite solar cells with efficiency exceeding 24.8% and 0.3-V voltage loss.", *Science*, 2020, **369** (6511), 1615-1620

6. J. J. Yoo *et al*., "Efficient perovskite solar cells via improved carrier management.", *Nature,* 2021,**590**, 587–593.
7. Zhang, M. *et al*. "Stable and low-cost mesoscopic $CH_3NH_3PbI_2Br$ perovskite solar cells by using a thin poly(3-hexylthiophene) layer as a hole transporter." *Chemistry: A European Journal*, 2015**, 21**, 434–439
8. Rong, Y., Liu, L., Mei, A., Li, X. Han, H., "Beyond efficiency: the challenge of stability in mesoscopic perovskite solar cells." *Advanced Energy Materials,* 2015, **5,** 1501066.
9. Qin, T. *et al*. "Amorphous hole-transporting layer in slot-die coated perovskite solar cells." *Nano Energy,* 2017,**31**, 210–217.
10. S.Yong *et al*., "Challenges for Thermally Stable Spiro-MeOTAD toward the Market Entry of Highly Efficient Perovskite Solar Cells.", *ACS Applied Materials & Interfaces,* 2022,**14,** 30, 34220–34227.
11. Zhang *et al*., "Ion-modulated radical doping of spiro-OMeTAD for more efficient and stable perovskite solar cells.", Science, 2022,**377**, 495–501.
12. J. Kong *et al*., "CO2 doping of organic interlayers for perovskite solar cells.", *Nature*, 2021 **594**, 51–56.
13. B. Xu et al., "Ag-TFSI as p-Type Dopant for Efficient and Stable Solid-State Dye-Sensitized and Perovskite Solar Cells.", *ChemSusChem*, 2014, **7**, 3252–3256.
14. J.-Y. Seo *et al*., "Alkylammonium bis(trifluoromethyl sulfonyl)imide as a dopant in the hole-transporting layer for efficient and stable perovskite solar cells.", *Energy & Environmental Science*, 2018, **11,** 2985–2992.
15. E. Kasparavicius et al., "Oxidized Spiro-OMeTAD: Investigation of Stability in Contact with Various Perovskite Compositions.", *ACS Applied Materials & Interfaces,* 2021, **4**(12), 13696–13705.
16. A. Abate *et al*., "Protic Ionic Liquids as p-Dopant for Organic Hole Transporting Materials and Their Application in High-Efficiency Hybrid Solar Cells." *Journal of the American Chemical Society,* 2013,**135**, 13538–13548.
17. W. H. Nguyen, C. D. Bailie, E. L. Unger, M. D. McGehee, "Enhancing the Hole-Conductivity of Spiro-OMeTAD without Oxygen or Lithium Salts by Using Spiro(TFSI)2 in Perovskite and Dye-Sensitized Solar Cells.", *Journal of the American Chemical Society*,2014, **136**, 10996–11001.
18. Sirringhaus, H. *et al*. "Two-dimensional charge transport in self-organized, high-mobility conjugated polymers." *Nature*,1999, **401**, 685.
19. T.P.Osedach, T.L.Andrew,V.Bulovic, "Effect of synthetic accessibility on the commercial viability of organic photovoltaics." *Energy & Environmental Science,* 2013,**6**, 711–718.
20. Stolterfoht, M. *et al*. "The perovskite/transport layer interfaces dominate non-radiative recombination in efficient perovskite solar cells." arXiv preprint arXiv:1810.01333
21. E.H.Jung *et al.,* "Efficient, stable and scalable perovskite solar cells using poly(3-hexylthiophene)." Nature, 2019, **567**,511–515.
22. F. M,Rombach, S.A. Haque, T.J.Macdonald,. "Lessons learned from spiro-OMeTAD and PTAA in perovskite solar cells." *Energy & Environmental Science*,2021,**14**, 5161–5190.

*(*Zafar Iqbal has made all the samples and devices. Artem helped with trSPV measurements and Hans Köbler supported in MPP tracking measurements for the devices)

Chapter 6

Summary and Outlook

Energy is among the basic human needs in recent times. However, we are producing energy by burning fossil fuels which is causing a serious environmental issue for the planet's life. The alternative includes renewable energy sources in which energy is directly or indirectly driven by solar. It is estimated that solar energy has the potential to augment the energy requirement in the coming future. Up till now over 1TW energy is being produced by solar cells. However, it needs urgent initiatives to make use of solar energy to save life and the planet for the coming generations.

Perovskite solar cells (PSCs) have emerged as next-generation solar cells with excellent PCE and ease of fabrication. To date, researchers have succeeded in achieving 26%PCE from the solar cell in single junction and 33.7% in tandem architecture. However, there are many challenges for commercializing this technology on a larger scale. The major challenge is stability. Although, perovskite is a relatively stable material. However, the device stability does not depend on perovskite only. The overall device contains charge extraction layers, an absorbing layer, and electrodes. These charge extraction layers have a pivotal role in the device structure. The interaction of the absorbing layer surface and the charge extraction layers make interfaces. These interfaces are critical for device performance. The studies suggest that the main energy losses come at the interfaces. It further suggests that it needs to understand the interfaces deeply through the characterization tool and there is a need to design the interfaces for defect passivation, better charge transportation, and energy level alignment. **Chapter 1** narrates the recent work on the interfaces, their importance, their impact on the device physics, and the methods to improve the interfaces. **Section 1.6** states surface band bending phenomena in semiconductor material under the influence of electric potential. This feature of the semiconductor materials imprints the chemicals and optoelectronic properties of the interfaces developed by the semiconductor layers. However, surface band bending has been an intrinsic property of the semiconductor and recently molecular treatment (passivation) has successfully caused surface band bending in perovskite halides. This bending leads to a decrease in the energy offset at the interfaces and helps to optimize the energy level alignments. **Section 1.7** introduces the concept of energy level alignment at the interface and the efforts to date to achieve the energy level alignment at the interfaces. It also describes the easiest way to check the energy alignment, introduced by D. Neher *et al*. It states that equal values of QFLS and V_{OC}

propose energy level alignments at the interface. **Section 1.10** in **Chapter 1** states a discussion that how interfaces limit the SQ limit. There have been added statistical data evidence and mathematical equations to prove that state-of-the-art devices show less V_{OC} and *FF* that are limited by the interfaces largely. At the end of the chapter motivation toward this work is added and outlines are introduced.

Chapter 2 describes the sample preparation method and it also provides a tool kit for interface and device characterizations. The whole picture of energy alignment at the interface, charge extraction, defect passivation, and electronic levels can be envisioned by using PL, TRPL, KP, trSPV, and PES techniques. The stability of the device can be measured by employing MPP tracking methods. The right choice of technique can help to investigate the query. In **Chapter 4**, XPS and UPS have been used, while, in **Chapter 3**, HAXPES is used. Though, both of these techniques have the same basic working principle. However, HAXPES helps with buried interface studies with more penetration depth. trSPV is a versatile technique and helps in understanding charge extraction, trap concentration, and interface kinetics.

$CsPbI_3$ perovskite has a phase stability problem but it is the most stable material. To date, the most stable device reported was based on $CsPbI_3$ with 17% PCE and 33 years of outdoor operation. It suggests that there is a need to improve efficiency. As stated earlier, there is a need to investigate the interfaces. The $CsPbI_3$ layer is mainly deposited by auxiliary organic moieties that evaporate during annealing. However, the annealing medium varies from method to method. The most reported methods suggest dry air boxes and a few suggested ambient air annealing of perovskite films. To investigate the effect of annealing medium on film growth and electronic levels profile a detailed study was conducted with the help of PL, TRPL, KP,trSPV, and HAXPES**. Chapter 3** describes the comparison of two films annealed in dry air and ambient air. Initially, the quality of the film (thickness and grain size) was confirmed by SEM. It shows that ambient air does not have any adverse effect on the film growth and $CsPbI_3$ film can be annealed in air efficiently. The quality of the film was confirmed by the optical measurements. There was another question that needs to be investigated that air annealing lead to functionalizing the terminating surface of the perovskite with -OH or O_2 or oxygen bonding that passivates the defects and improves the efficiency? To study for $CsPbI_3$, HAXPES measurement was conducted due to its more penetration depth as compared to lab-based XPS. It confirms that there is no new bond formation on the surface of $CsPbI_3$ contrary to other perovskite compositions. However, a band bending is observed in ambient air-annealed $CsPbI_3$ samples. In HAXPES, both 6keV and 2keV excitation have been used that provide deep

analysis of the core and shallow energy levels. It has been revealed by this study that core and shallow energy levels of the ambient air annealed samples have low binding energy and are broadened. This indicates the band bending due to ambient air annealing. Further, QFLS were calculated from PL measurements for the ETL/Perovskite/HTL layer and compared with the best V_{OC} of the devices. It shows that there is less difference in QFLS and V_{oc} for ambient air-annealed film-based devices. Kelvin probe measurements show that ambient air annealed samples have a higher WF (*i.e.* close to HTM) and it needs less oxygen soaking time for HTL to get aligned for the charge extraction. **Section 3.7** in **Chapter 3** shows device performance in terms of efficiency and stability. The statistics show that there is an obvious difference in the device parameters and the devices fabricated by the ambient air annealed samples show higher PCE and V_{OC}.

Chapter 4 deals with two challenges. The first challenge comes from the V_{oc} deficit that is more pronounced in inorganic as compared to organic-inorganic perovskite halide solar cells. It suggests the interface design for better charge extraction and energy level alignment. To confront this challenge, state-of-the-art work with over 20% efficiency was taken as a control (reference). In this already-established work, they have employed an *n*-OAI molecule to passivate the $CsPbI_3$ surface. However, it was revealed in this dissertation that *n*-OAI is causing a downward band bending and making more *n*-type perovskite film. Further, it was revealed that it does not have an optimized energy alignment for charge extraction. To align the bands at the interface and better charge extraction, a dipole molecule TOPO was introduced at the interface on the *n*-OAI capped $CsPbI_3$.The TOPO has changed the interface dynamics largely.

Initially, the surface was analyzed by XPS. It shows that binding energy shifts for $CsPbI_3$ core levels that infer the band bending at the interface that is OAI treatment causes a downward band bending and TOPO treatment causes an upward surface band bending. This band bending was further studied by UPS measurements. It shows that TOPO treatment causes a surface upward band bending and it leads to a decrease in an energy offset between the hole transport layer and perovskite.

The effect of this band bending and energy alignment was further investigated by transient photovoltage (trSPV) measurements. This study reveals that thanks to optimized energy alignment at the interfaces there is a boost in charge extraction. Finally, it demonstrates an increase in device parameters and V_{OC}. This new interface design allowed us to achieve better stability and energy production that was calculated by cyclic MPP tracking measurements. The

significant increase over 1.2V suggests that interfaces need to be revisited for better energy alignment.

The second challenge was to define the role of TOPO. In PL spectroscopy, decay is associated with defect traps and charge extraction at the interface. The introduced method allows us to single out the role of TOPO as a passivating layer or charge extraction layer.

The most of the recent works on $CsPbI_3$, Spiro-OMeTAD is applied as a hole transport layer. However, spiro-OMeTAD is very vulnerable to high temperatures and it needs to change with some temperature-resistant layer (*i.e*. CuSCN, P3HT, *etc*.). Other than this spiro-OMeTAD is too expensive to commercialize perovskite solar cells. Although, poly (3-hexylthiophene (P3HT) is a good choice but due to the low band gap, it causes a chemical interaction at the perovskite/HTM interface that results in V_{OC} losses at the interfaces. In this work, a molecule a long-chain alkyl halide molecule, *n*-hexyl trimethyl ammonium bromide (HTAB) is introduced. This molecule acts as a bridge for chare extraction as revealed by trSPV and it passivates the defects in $CsPbI_3$ films. Finally, over 14% efficiency was achieved by using P3HT as an HTL.

Outlook

Perovskite solar cells (PSC) have reached a decent efficiency of 26% for inorganic-organic perovskite solar cells and over 21% for inorganic perovskite solar cells. However, the research community has failed to make it commercially available. Although, perovskite itself is a stable material that is easy to process and easy to fabricate it is not the only one that can promise stability. There is a need to work on the other layers to make them more and more compatible for higher PCE and stability. The study suggests the following research as an outlook for this work to make PSC commercially available.

- The study suggests that main power losses come at the interface. There is a need to optimize and design new interfaces for better energy level alignment and charge extraction.
- Surface band bending is a strategy to mitigate the energy offset of the interface. Until now, very few reports have explored surface band bending for $CsPbI_3$. Further work on surface band bending by applying various molecules can help to achieve better energy alignments.
- The dipole molecules have been very operative in tuning the energy levels. However, these molecules are also susceptible to high temperatures. Inorganic dipole molecules with functionalities *e.g.* silicates, phosphates, *etc.* need to be explored for surface treatment and energy level tuning.
- There is a need for inorganic hole transport layers that are easy to fabricate and less expensive. The transition metal-based oxides or SAM can be used for HTL.
- This work also suggests baseline architects for PSC that need further improvement. For example, for $CsPbI_3$ the most stable device that has been reported so far is CuSCN based. There is a further need to explore its interface to improve the efficiency and to make the CuSCN deposition methods more facile.
- **Chapter 5** suggests that P3HT has the potential to work as HTM with $CsPbI_3$.The right choice of molecules can improve this interface further to increase PCE. The molecules with less shallow valence bands and high conduction bands can be helpful for interface manipulations.
- The use of X-ray photoemission spectroscopy (PES) can be useful to explore the interfaces further. It further recommends the full package of IPES, XPS /(HAXPES), and UPS to analyze the interface properly.

Appendix

Measurements

I. UV-Vis Spectroscopy

Perkin Elmer LAMBDA 1050 UV/VIS spectrometer has been for the transmittance measurements of $CsPbI_3$ samples. Samples were encapsulated with a cover glass before taking out of a nitrogen-filled glovebox for the UV-Vis measurements.

II. Photoluminescence Spectroscopy (PL)

A 445 nm CW laser (Insaneware) has been used as the excitation source for the Photoluminescence measurements with an optical fiber connected to an integrating sphere where samples were loaded. Samples for the PL measurements were encapsulated with a cover glass before taking out of a nitrogen-filled glovebox. (More detail is added in appendix)

III. Time-resolved Photoluminescence measurements (trPL)

These measurements were performed with a TCSPC system (Berger & Lahr) after excitation with a mode-locked Ti: sapphire oscillator (Coherent Chameleon) that provides a pulse-picked and frequency-doubled output, with nominal pulse durations ~ 100fs and fluence of ~30nJ/cm² at a wavelength of 470nm.

IV. X-ray diffraction (XRD)

X-ray powder diffractometer Bruker D8 Advance in Bragg-Brentano geometry with Cu Kα as the target and LYNXEYE as the detector was used for the XRD measurement, at a voltage of 20 kV and current of 5 mA, The samples were scanned from 5° to 70° with step size of 0.01°.

V. Scanning Electron Microscopy

The SEM images of the perovskite film and the devices were recorded with the Hitachi S-4100 at an acceleration voltage of 5 kV.

VI. Kelvin probe

Kelvin probe measurements were performed with an apparatus containing vibrating gold mesh driven by a piezo-electric crystal (Kelvin probe S and CPD controller by Besocke Delta Phi). The samples were prepared in HySprint Lab in a nitrogen glove box and shifted to PVComB in a vacuum transfer box. These measurements were conducted in an inert atmosphere

VII. Transient surface photovoltage (tr-SPV) measurements

Charge extraction in the 5 ns up to 0.5 s time range was studied by non-contact SPV measurements exited by 5 ns above bandgap laser (1.8 eV). We used fluences of 0.072 μJ, corresponding to a carrier concentration of 3×10^{15} cm^{-3} close to 1 sun operation conditions. Detailed SPV setup description is given in the work[1]. Contour plots were recorded with a tunable laser in the range 0.6-3 eV using fluences of 72 μJ to ensure an excellent signal to noise ratio.

VIII. Ultraviolet photoelectron spectroscopy

Ultraviolet photoelectron spectroscopy (UPS) was conducted using a monochromated helium discharge lamp (HIS 13 FOCUS GmbH, photon energy of 21.22 eV) in an ultrahigh vacuum system (base pressure of 1×10^{-9} mbar). With a monochromator, the visible light was eliminated and UV flux was significantly reduced (attenuation by a factor of ca. 100 folds as compared to that of the standard helium lamp).

IX. X-ray photoelectron spectroscopy (XPS)

X-ray photoelectron spectroscopy (XPS) was performed using a standard Mg Kα radiation (1253.6 eV, anode power of 20 W) generated from a twin anode X-ray source. All spectra were recorded at room temperature and normal emission using a hemispherical electron analyzer (SPECSPhoibos 100). The illumination experiments were conducted using a white halogen lamp (Solux MR16 4700K, 50 W, daylight rendering) during UPS measurements with an intensity of ca. 100 mW/cm^2. The secondary electrons cutoff (SECO) spectra were conducted at a negative bias of 10 V.

X. HAXPES

HAXPES measurements were conducted at the HiKE endstation at the BESSY II KMC-1 beamline at Helmholtz-Zentrum Berlin (HZB)[(2,3)]. The endstation is equipped with a Scienta R4000 electron analyzer, allowing it to use of the excitation energy range (i.e., 2 – 10 keV) provided by the KMC-1 bending magnet beamline. Two different excitation energies are employed in this work, making use of other diffraction orders of the Si (111) crystal pair of the KMC-1 double crystal monochromator (i.e., 2 keV in 1st order and 6 keV in 3rd order); with these excitations, it is possible to probe the topmost and buried layers of approximately 12 and 30 nm, respectively [(4,5)]. The energy scale of the HAXPES measurements was calibrated using Au 4f reference spectra of a clean Au foil, setting the BE of the Au $4f_{7/2}$ line to 84.00 eV. Measurement protocols involving the use of a beam-attenuating Be filter (that effectively

reduces the 2 keV photon flux by 75% and the 6 keV photon flux by 10% of their unfiltered values) were implemented in this experiment, aiming at preventing/minimizing beam-induced damage to the sample. Moreover, we applied a segmented data acquisition approach to compare the evolution of core levels under X-ray radiation and move sample spots. The measured detail HAXPES spectra' curve fit analysis was conducted simultaneously with the Fityk software [6]. Voigt profile functions and linear backgrounds were used for these fits. Spin-orbit doublets were fit using two Voigt functions with intensity ratios set to obey the 2j+1 multiplicity rule. HAXPES-derived [Cs]:[Pb]:[I] composition ratio quantifications were carried out by correcting the peak intensities of the Cs $4d_{5/2}$, Pb $5d_{5/2}$ and I $4d_{5/2}$ HAXPES shallow core levels to account for differences in photoionization cross-section [7,8,9]. Due to the energetic proximity of these lines, the impact of differences in IMFP [4,5] and the transmission function of the electron analyzer [10] on the intensity of the core levels is negligible.

XI. J-V measurements

The light source was provided by an Oriel LCS-100 class ABB solar simulator (1Sun, AM1.5G, 100 $mWcm^{-2}$) installed inside a nitrogen-filled glovebox. Before the light J-V measurement, the light intensity was calibrated with a silicon reference cell (Fraunhofer ISE). A Keithley power meter (2400 SMU) was used for the bias application to solar cells for the J-V scans, programmed by LabView. The bias was applied to scan from 1.25 V to -0.1 V back and forth, with a scan rate of 200 mV/s and a step size of 0.02 V.

XII. EQE measurements

EQE spectra were recorded with the TracQ-Basic software, connected to the light source (Oriel Instruments QEPVSI-b system integrated with a Newport 300 W xenon arc lamp) with an optical fiber. The light source spectrum was calibrated with a Si reference cell with a known spectral response before the measurement. The monochromatic light was provided by a Newport Cornerstone 260 monochromator with a chopping frequency of 78 Hz.

XIII. Ageing of Solar Cells (long-term stability measurement)

Solar cells were aged in a custom-built High-throughput Ageing Setup.[11] A light-cycling experiment according to ISOS-LC-1I [12] was performed with cycles of 12 h illumination phase followed by 12 h dark phase. Special electronics were used to MPP-track all cells during the illumination phase. A perturb and observe algorithm [13] with a delay time of 1 s and a voltage step-width of 0.01 V was applied to track the MPP. PCE_{MPP} values were taken every 2 min for all cells automatically. During the dark phase, cells were fully shaded with an automatic shutter system and disconnected from the MPP trackers.

Additionally, JV-scans with a scan speed of 90 mV/s were performed on every cell after 11 h of the light phase of a cycle. During the dark phase, the shutter was shortly opened to perform JV-scans on selected pixels after 11.5 h of darkness.

Devices were always kept at 25 °C with the help of actively controlled Peltier-elements. Solar cells' active areas touched a heat pad for direct thermal coupling. Aging was performed under a continuous nitrogen flow in a closed box, no additional encapsulation was used. Sunlight with 1 sun intensity was provided by a metal-halide lamp using a H6 filter. A UV-blocking foil was used to block UV-light with wavelengths below 380 nm. The light intensity was actively controlled with the help of a silicon irradiation-sensor, calibrated using a KG3 silicon reference cell from Fraunhofer ISE.

XIV. Ageing of Solar Cells

Solar cells were aged in a custom-built High-throughput Ageing Setup [(11)]. Special electronics were used to MPP-track all cells individually. A perturb and observe algorithm [(13)] with a delay time of 800 ms, integration time of 200 ms and a voltage step-width of 0.01 V was applied to track the MPP. One complete track cycle (voltage step and 2 probe voltage steps) amounts to 3 s. PCE_{MPP} values were taken every 2 min for all cells automatically. Additionally, JV scans with a scan speed of 90 mV/s were performed on every cell every 48 h. Devices were kept at 25 °C at all times with actively controlled Peltier-elements and with active areas touching a heat pad for direct thermal coupling. The active area of devices under test was 0.18 cm^2. Ageing was performed under a continuous nitrogen flow in a closed box, no additional encapsulation was used. Sunlight with 1 sun intensity was provided by a metal-halide lamp using a H6 filter. Mitsui's UV-blocking foil „KFU15"was used to block UV-light with wavelengths below 380 nm. The light intensity was actively controlled with the help of a silicon irradiation-sensor, calibrated using a KG3 silicon reference cell from Fraunhofer ISE. The test is by the protocol ISOS-L-1I [(12)].

References

1. I. Levine, A. Al Ashouri, A. Musiienko, *et al.* "Charge transfer rates and electron trapping at buried interfaces of perovskite solar cell", *Joule*, 2021, **5**, 2915–2933.
2. M. Gorgoi, S. Svensson, F. Schäfers, G. Öhrwall, M. Mertin, P. Bressler, O. Karis, H. Siegbahn, A. Sandell, H. Rensmo, W. Doherty, C. Jung, W. Braun, W. Eberhardt., "The high kinetic energy photoelectron spectroscopy facility at BESSY progress and first results." *Nuclear Instruments and Methods in Physics Research Section A: Accelerators, Spectrometers, Detectors and Associated Equipment*, 2009,**601**,48-53.

3. F. Schaefers, M. Mertin, and M. Gorgoi., " KMC-1: A high resolution and high flux soft x-ray beamline at BESSY.", *Rev Sci Instrum*, 2007,**78**, 123102.
4. S.Tanuma, C. J. Powell, D. R. Penn., "Calculation of electron inelastic mean free paths(IMFPs) VII. Reliability of the TPP-2M IMFP predictive equation.", *Surf. Interface Anal*.2003,**35**,268 – 275.
5. S.Tougaard, QUASES-IMFP-TPP2M Program, Quases-Tougaard Inc., Odense, Denmark, 2002.
6. M.Wojdyr., "Fityk: a general-purpose peak fitting program.", *J. Appl. Crystallogr*.2010, 43, 1126.
7. M.B,Trzhaskovskaya,V.I.Nefedov, V.G. Yarzhemsky., "Photoelectron Angular Distribution Parameters for Elements Z=1 to Z054 in the photoelectron Energy range100-5000 eV.", At. Data Nucl. Data Tables,2001, 77, 97–159.
8. M.B,Trzhaskovskaya,V.I.Nefedov, V.G. Yarzhemsky., "Photoelectron Angular Distribution Parameters for Elements Z=1 to Z=54 in the photoelectron Energy range100-5000 eV.", *At. Data Nucl. Data Tables*,2002,**82**, 257–311.
9. M.B,Trzhaskovskaya,V.I.Nefedov, V.G. Yarzhemsky., "Photoelectron Angular Distribution Parameters for Elements Z=1 to Z=54 in the photoelectron Energy range100-5000 eV.", *At. Data Nucl. Data Tables*,2006,**92**, 245-304.
10. M.P. Seah., "A system for the intensity calibration of electron spectrometers.", *Journal of Electron Spectroscopy and Related Phenomena*,1995,**71**,191-204.
11. H. Köbler, S. Neubert, M. Jankovec, *et al.* "High-Throughput Aging System for Parallel Maximum Power Point Tracking of Perovskite Solar Cells", *Energy Technol.* 2022, 2200234, doi:10.1002/ente.202200234.
12. M.V. Khenkin, E.A. Katz, A. Abate, *et al.* "Consensus statement for stability assessment and reporting for perovskite photovoltaics based on ISOS procedures", *Nat. Energy*, 2020, **5**, 35–49.
13. L. Rakocevic, F. Ernst, N. T. Yimga, *et al.* "Reliable Performance Comparison of Perovskite Solar Cells Using Optimized Maximum Power Point Tracking", *Solar RRL*, 2019, **3**, 1800287.

Appendix A3

A3.1 Experimental section

A 3.1.1 Chemicals

CsI (99.999%, ABer), lead(II) iodide (PbI_2, 99.99%, TCI), dimethyl ammonium iodide (DMAI) (98%, Sigma-Aldrich), methyl ammonium chloride (MACl, Dyenamo), n-octylammonium iodide (OAI, GreatCell Solar), dimethylformamide (DMF, 99.8%, Sigma-Aldrich), dimethyl sulfoxide (DMSO, 99.9%, Sigma-Aldrich), iso-propanol (IPA, 99.5%, Sigma-Aldrich), toluene (99.8%, Sigma-Aldrich), chlorobenzene (99.8%, Sigma-Aldrich), tris(2-(1H-pyrazol-1-yl)-4-tert-butylpyridine)cobalt(III)tri[bis-(trifluoromethane)sulfonimide] (FK209, Dyenamo), bis(trifluoromethane)sulfonimide lithium salt (Li-TFSI, Sigma-Aldrich), ethanol (99.9%, Merck), Spiro-OMeTAD (Lumtec), titanium diisopropoxide bis(acetylacetonate) (TIAP, 75 wt % in isopropanol, Sigma-Aldrich), 4-tert-butylpyridine (tBP) (98%, Sigma-Aldrich), trioctylphosphine oxide (TOPO) (99%, Sigma-Aldrich).

All chemicals are used as received.

A3.1.2 FTO substrates cleaning

Patterned FTO substrates (TEC 15, Yingkou company, with dimensions 2.5 cm×2.5 cm) were numbered on the back side (glass side). These numbers were designated to every device. Substrates were cleaned with 2% Mucosal solution with a very fine brush to clean the FTO surface, then washed with distilled water to remove soap contents. Afterward, cleaned with acetone and isopropanol for 15 min by sonication. After drying with a nitrogen gun, the substrates were placed in a UV-ozone cleaner for 15 minutes right before the titanium oxide layer deposition.

A3.1.3 Solution preparation

- 2% Mucasol solution was made by mixing 20 mL mucasol in 1000 ml distilled water.
- TiO_2 solution was prepared by adding 150 µL TIAP into 15 mL of ethanol.
- 1.0 M PbI_2 solution was prepared by dissolving 1.17 g of PbI_2 solution in 2.422 ml DMF solvent. The mixture was stirred at 80 °C for 2 hours to get PbI_2 solution.
- To get 0.60 M $CsPbI_3$ solution, 1.987 ml PbI_2 solution was added in 0.4370 g CsI salt and stirred for 10 min until it completely dissolved.
- To make 1:1:1 (atomic ratio) CsI: PbI_2: DMAI solution, 2.542 ml above $CsPbI_3$ solution was added in DMAI and stirred for 10 min until a clear, yellowish perovskite solution was formed.

- 45 mM MACl solution was made by dissolving 57.7 mg MACl salt in 19 mL IPA and was stirred for two hours until it completely dissolved.
- OAI solution was prepared by dissolving 3 mg of OAI in 1mL IPA and stirring for 1 hour.
- 20 mM TOPO solution was made by dissolving 15 mg TOPO in 1.940 ml toluene and other concentrations were made by using the dilution formula that is $M_1V_1 = M_2V_2$. (Only for Chapter 4)
- A 36 mM solution of Spiro-OMeTAD was prepared by dissolving 200 mg Spiro-OMeTAD in 2.2 ml chlorobenzene with 87.78 µL tBP, 51.11 µl LiTFSI with stock solution of 520 mg/ml in acetonitrile, and 22.22 µl FK209 with stock solution of 375 mg/ml in acetonitrile.

A 4.2 Device Fabrication

TiO_2 compact layer

TiO_2 compact layer was deposited by spray pyrolysis with oxygen as the carrier gas. 16 substrates were placed on a hot plate installed inside a fume hood. One edge of each substrate is covered by around 5 mm using a cover glass to keep the conductive FTO side exposed for low contact resistance. Then the substrates were heated up to 450 °C and were kept at this temperature for 15 min before and 30 min after the spray of the precursor solution. The whole solution was transferred into a spray nozzle and sprayed at roughly 20 cm away from the substrates with an inclination angle of 45 degrees, with at least 20 s of delay between each spraying cycle. Afterward, substrates were left for cooling down to room temperature and then put in an ozone chamber for 15 minutes before perovskite film deposition.

Deposition of control perovskite films

After the ozone treatment, substrates were transferred into a glove box filled with nitrogen (O_2 <0.1 ppm, H_2O <0.1 ppm). The substrates were placed on a hot plate at 70 °C for 5 min before perovskite deposition. 80-100 µl perovskite solution was added and spin-coated quickly at 3000 rpm for 30 seconds. Then 350 µl MACl solution was dropped on the top and spin-coated for another 35 seconds. The wet films were then annealed in a dry air box with relative humidity (RH) of ~ 1% for 1 min at 210 °C. Afterward, substrates were transferred back to a nitrogen-filled glove box, where 100 µl OAI solution was dropped on the top and spin-coated at 5000 rpm for 30 seconds, followed by annealing at 100 °C for 5 min.

Perovskite films with TOPO treatment (Only for Chapter 4)

After the control perovskite films cooled down to room temperature, 200 µl TOPO solution at varied concentrations was deposited by spin coating at 5000 rpm for 30 seconds. No annealing is needed for this step.

Hole Transport Layer (HTM) deposition

100 µl Spiro-OMeTAD solution was deposited by spin coating at 3500 rpm for 30 seconds. No annealing is needed for this step.Afterward, all the samples were transferred into a dry air box (RH ~ 0.1%) for oxygen soaking.

Deposition of metal contact

Gold was evaporated using a thermal evaporator under a vacuum of approximately $1*10^{-6}$ pa. The deposition rate was programmed at 0.02 Å/s for the first 1 nm, 0.1-0.2 Å/s for the following 5 nm, and then 0.5 Å/s until 20 nm and then 1Å/s for the rest of the deposition. Overall, it takes around 25 min for the deposition of 100 nm of gold. The active area of the device was 0.18 cm^2 defined by the shallow mask.

Measurements

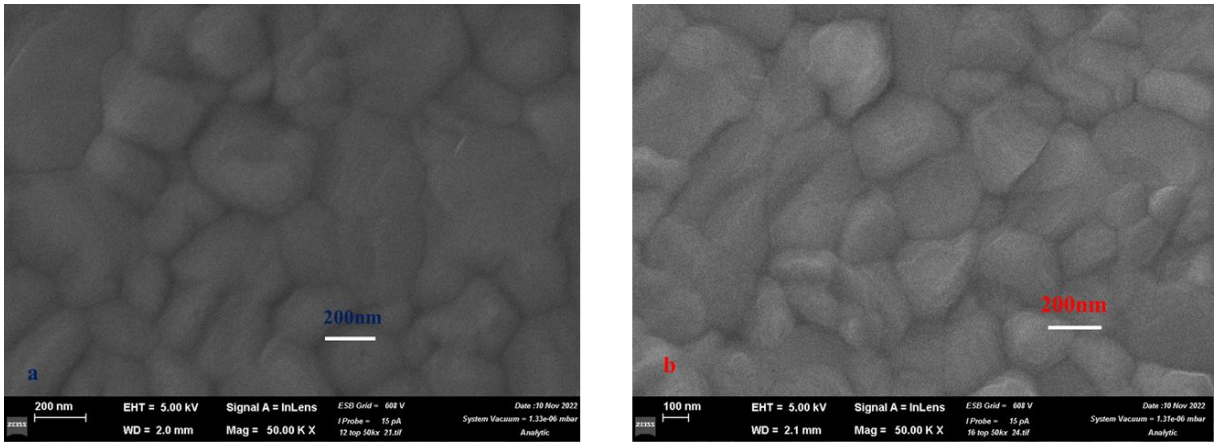

Figure A3.1 Top view SEM image of (a) Dry air annealed (b) Ambient air annealed films spin coated on compact TiO_2 layer and FTO substrates**.**

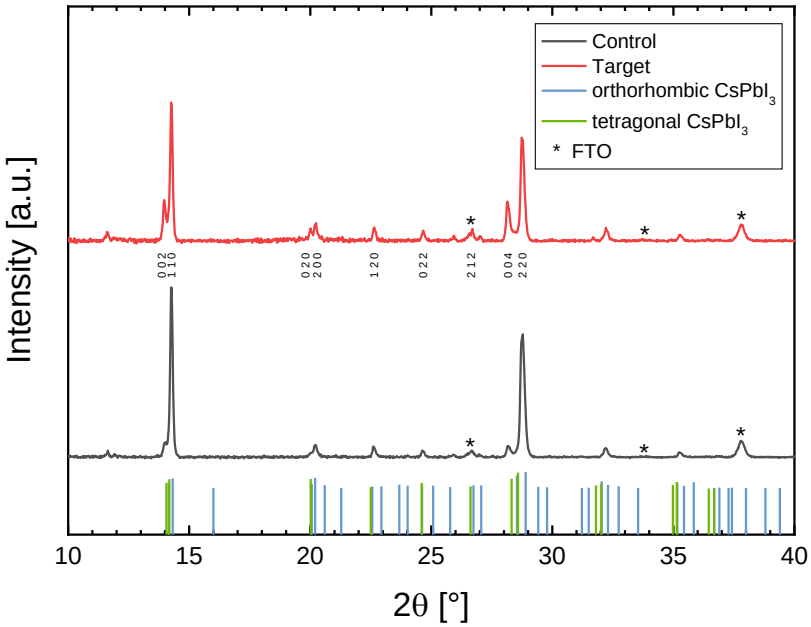

Figure A3.2 XRD data of the dry air and ambient air annealed films. These films were deposited on FTO substrates. The reflection peaks show that there is no yellow phase and both films exist in orthorhombic (γ) and tetragonal phase (β).

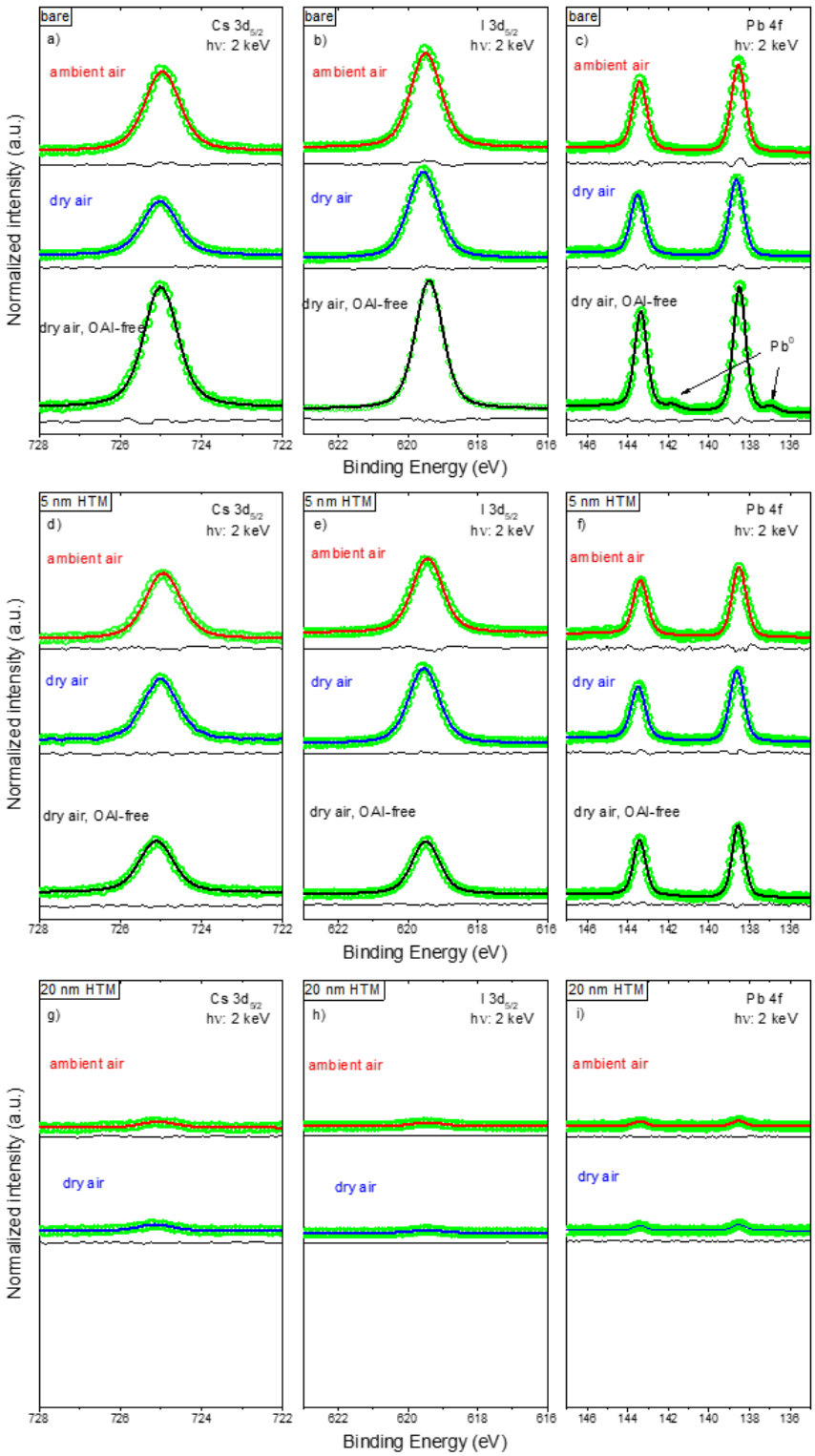

Figure A3.3 HAXPES detail spectra of the Cs $3d_{5/2}$ (a, d, g), I $3d_{5/2}$ (b, e, h) and Pb 4f (c, f, i) photoemission lines for the variously treated $CsPbI_3$ films (*i.e.*, OAI-free, dry air annealed and ambient air annealed) with 0 nm (*i.e.*, bare), 5 nm and 20 nm films of Spiro-OMeTAD, respectively. The spectra were measured using 2 keV excitation and normalized to background intensity, with vertical offsets added for clarity. Curve fit results are included

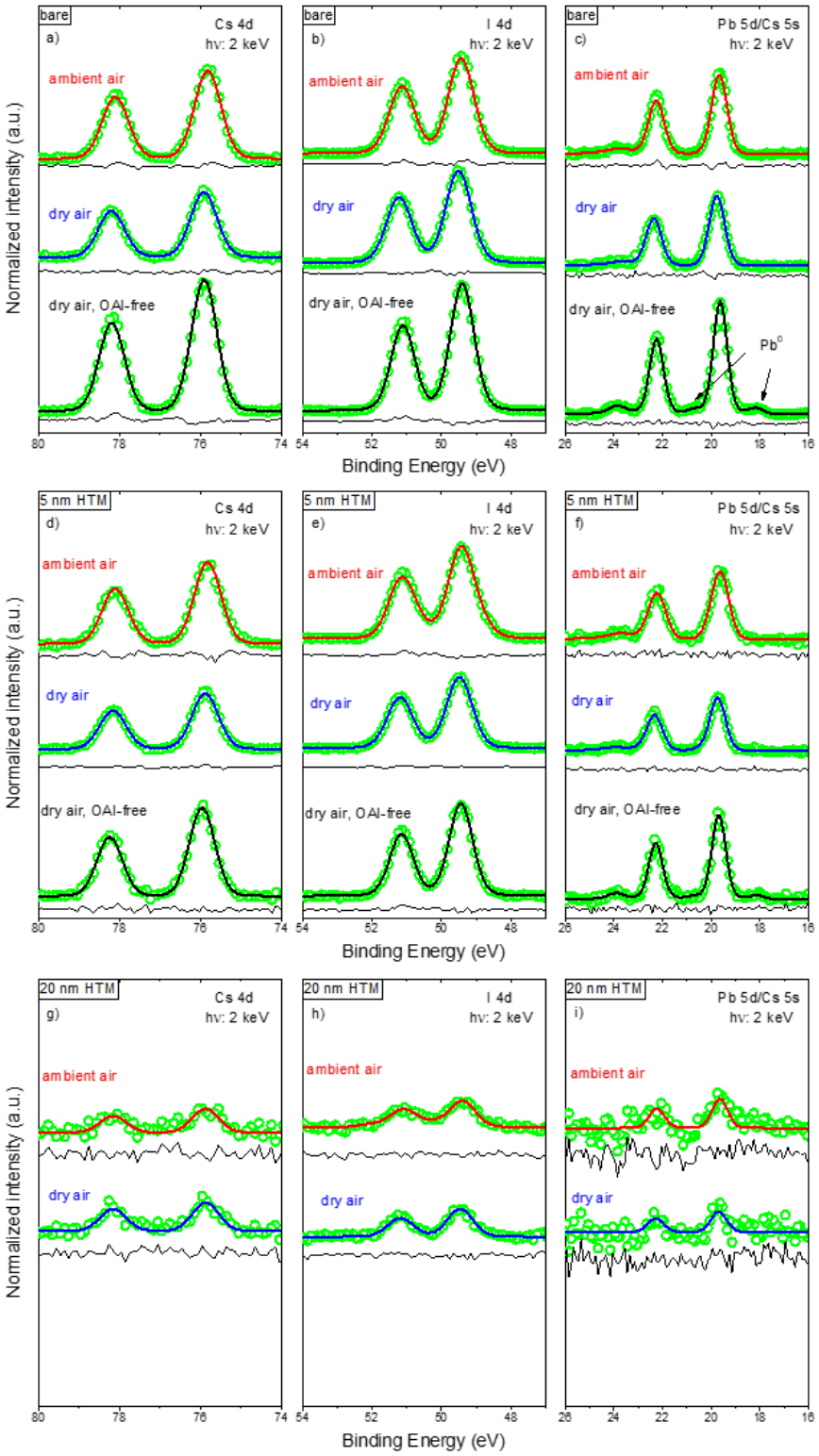

Figure A3.4 HAXPES detail spectra of the Cs 4d (a, d, g), I 4d (b, e, h) and overlapping Pb 5d/Cs 5s (c, f, i) photoemission lines for the variously treated $CsPbI_3$ films (*i.e.*, OAI-free, dry air annealed and ambient air annealed) with 0 nm (*i.e.*, bare), 5 nm and 20 nm films of Spiro-OMeTAD, respectively. The spectra were measured using 2 keV excitation and normalized to background intensity, with vertical offsets added for clarity. Curve fit results are included.

.

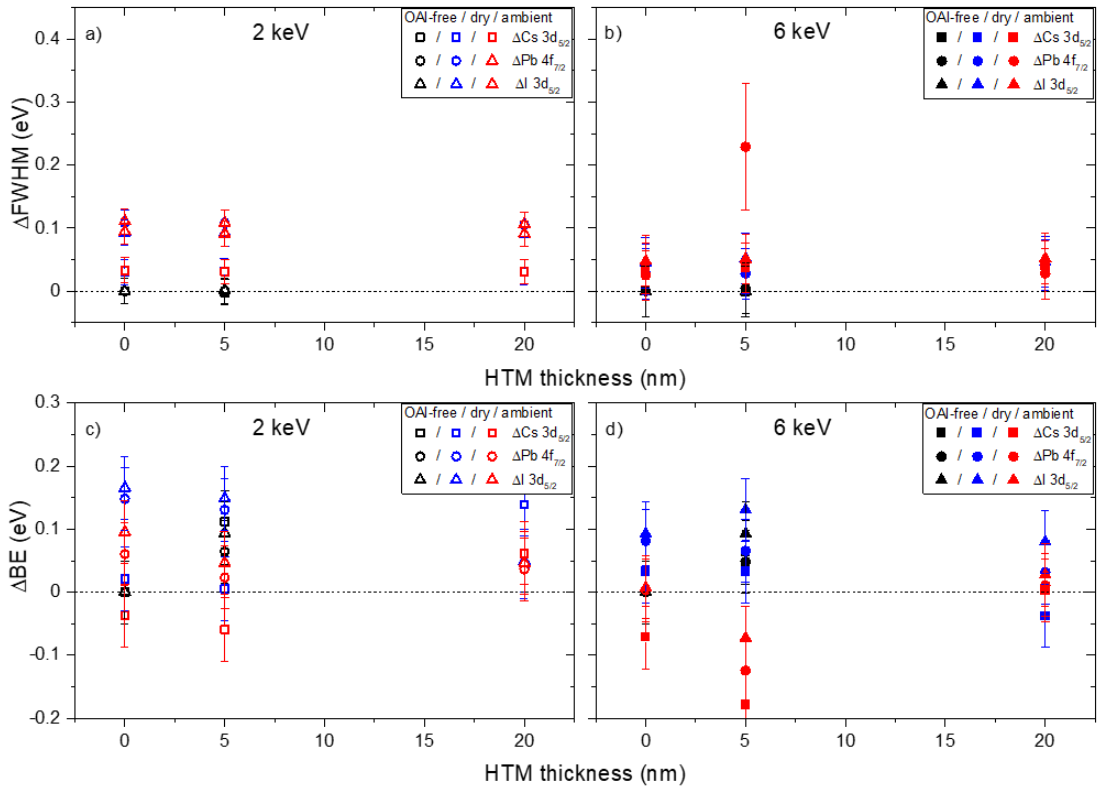

Figure A3.5 Changes in full-width-half-maximum (FHWM) values of the HAXPES Cs $3d_{5/2}$, I $3d_{5/2}$ and Pb $4f_{7/2}$ peaks, measured with a) 2 keV and b) 6 keV excitations, of the investigated samples (shown in Figs. S7 and S8), compared to peak FHWM values of the bare, OAI-free $CsPbI_3$ sample. Changes in BE values of the HAXPES Cs $3d_{5/2}$, I $3d_{5/2}$, and Pb $4f_{7/2}$ peaks, measured with excitation energies of c) 2 keV and d) 6 keV, compared to the corresponding peak BE values of the bare, OAI-free $CsPbI_3$ sample.

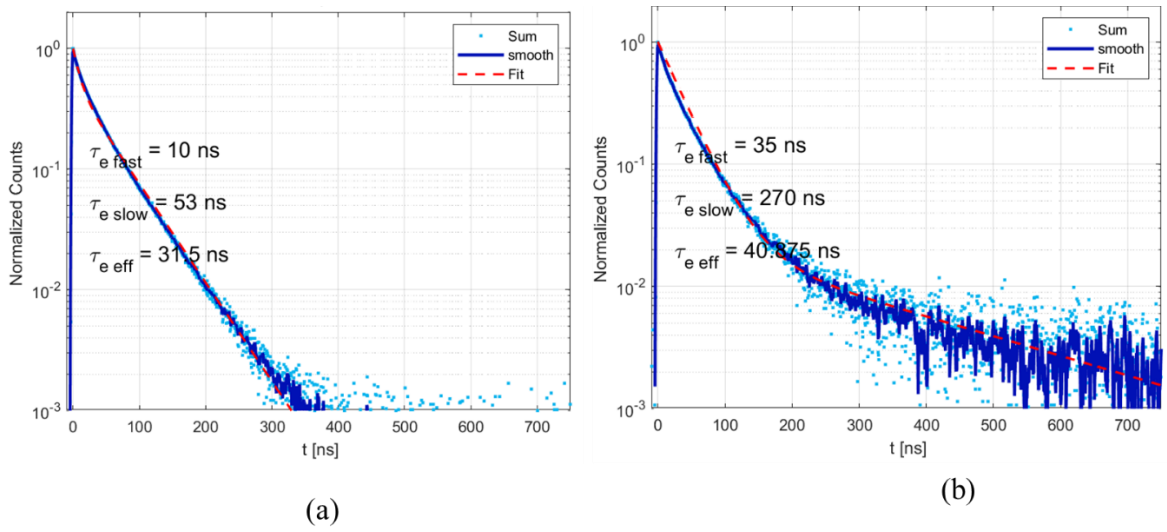

Figure A 3.6 Time resolved Photoluminescence Spectroscopy (trPL) for (a) dry air annealed sample and (b) ambient air annealed sample. The data was fitted with biexponential decay equation **(Eq2.17).** Sample stack (Glass/TiO_2/perovskite/OAI)

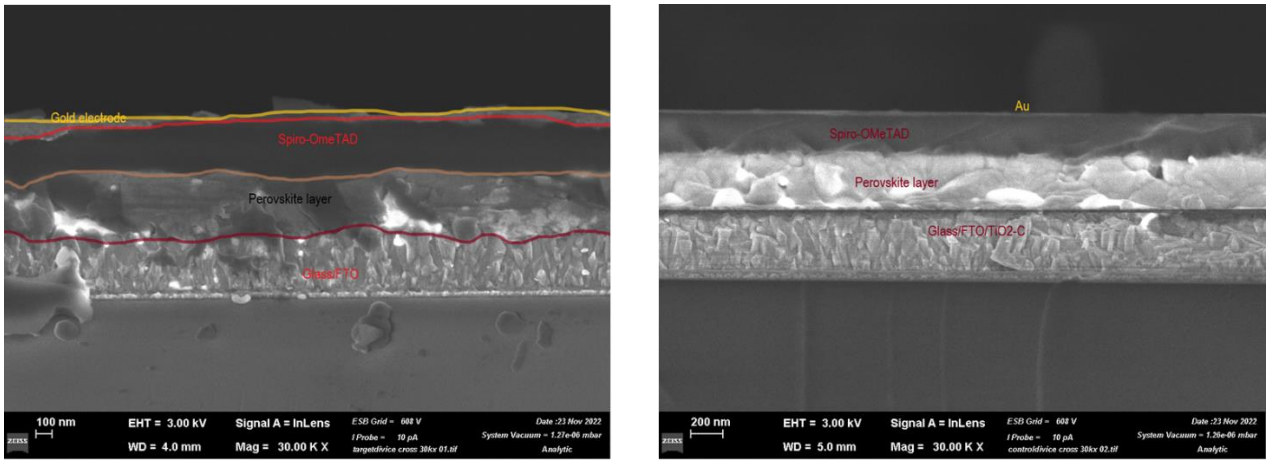

(a) (b)

Figure A3.7 Cross sectional SEM of (a)dry (b) ambient air annealed films based device, taken at 3000 resolution.

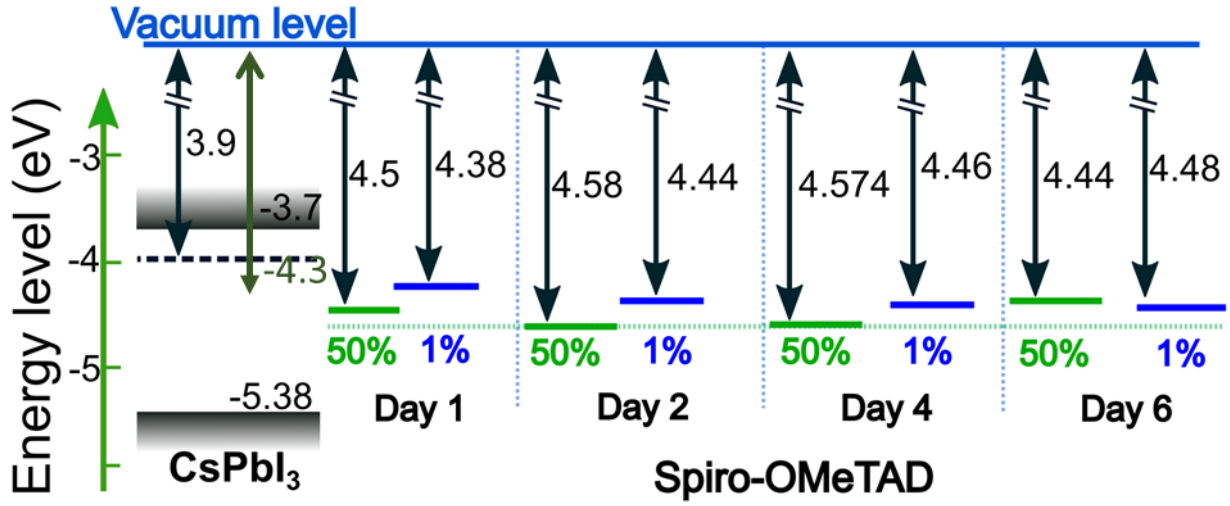

Figure A3.8 Work function of the dry air (1%RH) and ambient air (50%RH) over TiO_2 (ETL) and with HTL measured after 12, 24hours,48 hours,72 hours O_2 soaking. The Kelvin probe data show that with O2 soaking (doping) there are changes with work function and air annealed (target) samples have better energy alignment with Spriro-OMeTAD as compared to control samples.

Table 3.1: Fitted parameters of trPL data

Sample	τ_1(ns)	τ_2 (ns)	τ_{eff} (ns)
Glass/TiO2/$CsPbI_3$: OAI (dry air)	10	53	31.5
Glass/TiO2/$CsPbI_3$: OAI (Ambient air)	35	270	40.9
Glass/TiO2/$CsPbI_3$: OAI/Spiro-OMeTAD((dry air)	7	250	31.3
Glass/TiO2/$CsPbI_3$: OAI /Spiro-OMeTAD (Ambient air)	13	270	46.4

Table A3.2 Main fitting constants of simulation. N_{St} – concentration of surface defects inducing non-radiative recombination of carriers, K_h – hole injection rate, STD is the average standard deviation of the fit from the experimental SPV signal.

Interface	K_h, s^{-1}	N_{St}, cm^{-3}	*STD*, %
Dry air annealed	2.4×10^6	5.6×10^{11}	16
Ambient Air annealed	6.1×10^6	3.7×10^{14}	7

Chemicals Structures

1. *n*-OAI

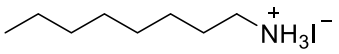

n-Octylammonium iodide

2. MACl

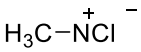

chloro(methyl)amide

3. TOPO (trioctylphophine oxide)

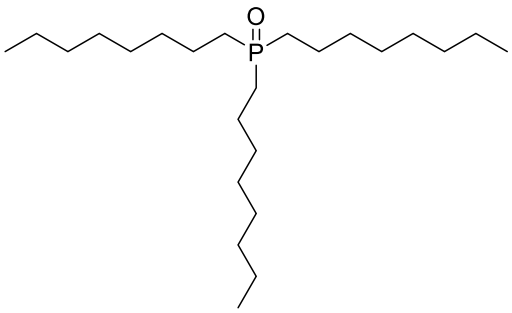

trioctylphosphine oxide

4. spiro-OMeTAD

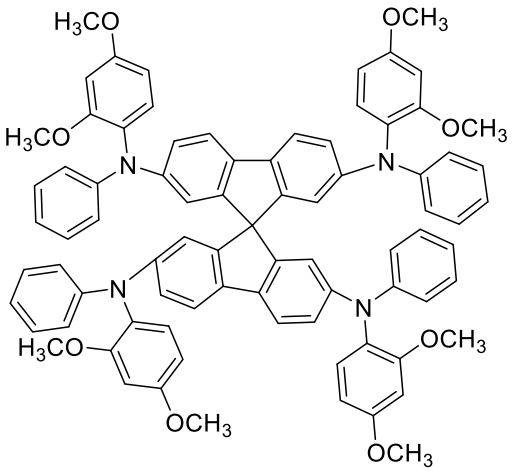

$N^2,N^{2'},N^7,N^{7'}$-tetrakis(2,4-dimethoxyphenyl)-$N^2,N^{2'},N^7,N^{7'}$-tetraphenyl-9,9'-spirobi[fluorene]-2,2',7,7'-tetraamine

5. Lithium bis(fluorosulfonyl) imide.

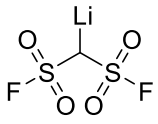

(bis(fluorosulfonyl)methyl)lithium

6. FK-209(It is a coblat complex),C42H45CoF18O12N12S6

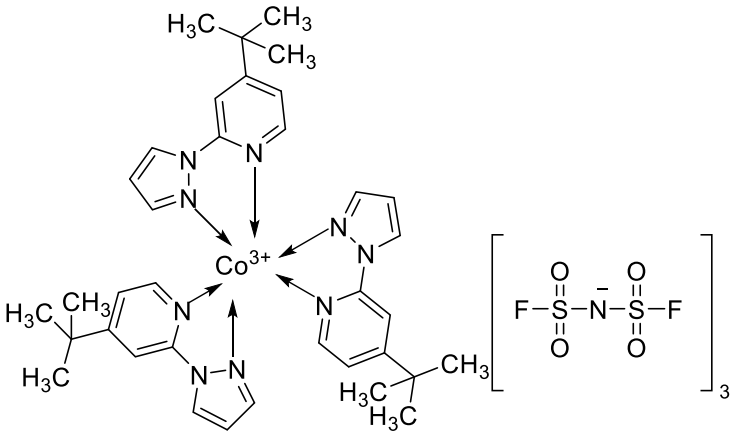

FK-209(It is a coblat complex),C42H45CoF18O12N12S6

7. 3 - 4-tert-Butylpyridine.

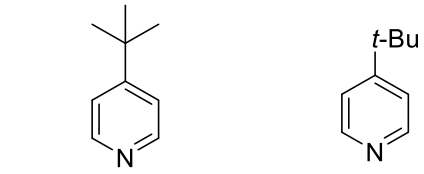

4-(*tert*-butyl)pyridine

8. P3HT (a polymer molecule)

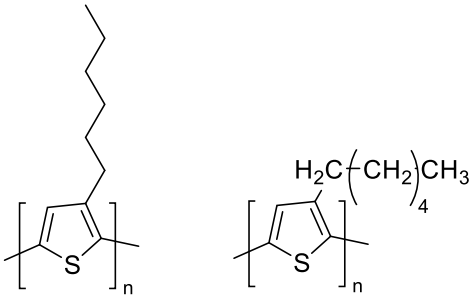

9. HTAB

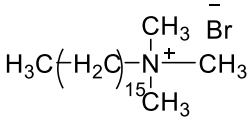

10. Chlorobenzene

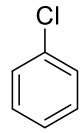

chlorobenzene

11. Diphenyl ether

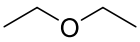

ethoxyethane

12. o-dichlorobenzene.

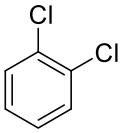

1,2-dichlorobenzene

13. Toulene

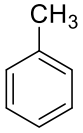

toluene

14. Acetonitrile

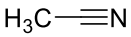

acetonitrile

15. IPA

propan-2-ol

(Green = solid molecules, blue=solvents)

Appendix A 4

A4.1 Measurements

Inorganic nature of $CsPbI_3$

The sample presents dominating diffraction peaks at 14.35° and 28.86°, which corresponded to the (100) and (220) facets of β-$CsPbI_3$ (*Pbnm* space group) crystallites[1]. The two broad peaks at 9.73° and 21.57° are likely to be (100) and (111) facets of β-$CsPbI_3$ (yellow phase) with amorphous features[2,3]. This could be caused by the slow penetration of moisture into the dome filled with nitrogen during the XRD data measurement. The diffraction peak of $DMAPbI_3$ at 2theta of around 12° as reported in reference [4,5] was not observed here, indicating that DMA^+ cation mostly vanished after the annealing.

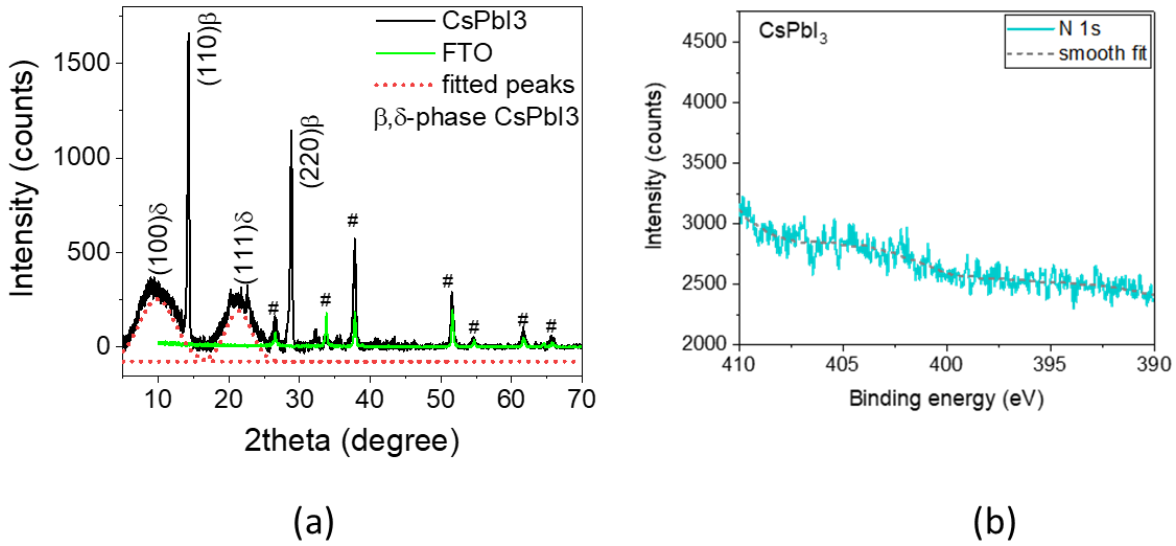

Fig. A4.1. **a)** XRD spectra of $CsPbI_3$ film deposited on TiO_2-covered FTO. **b)**. XPS of N 1s core-shell spectrum of as-obtained $CsPbI_3$ sample after annealing in a dry air box.

Optical bandgap of $CsPbI_3$

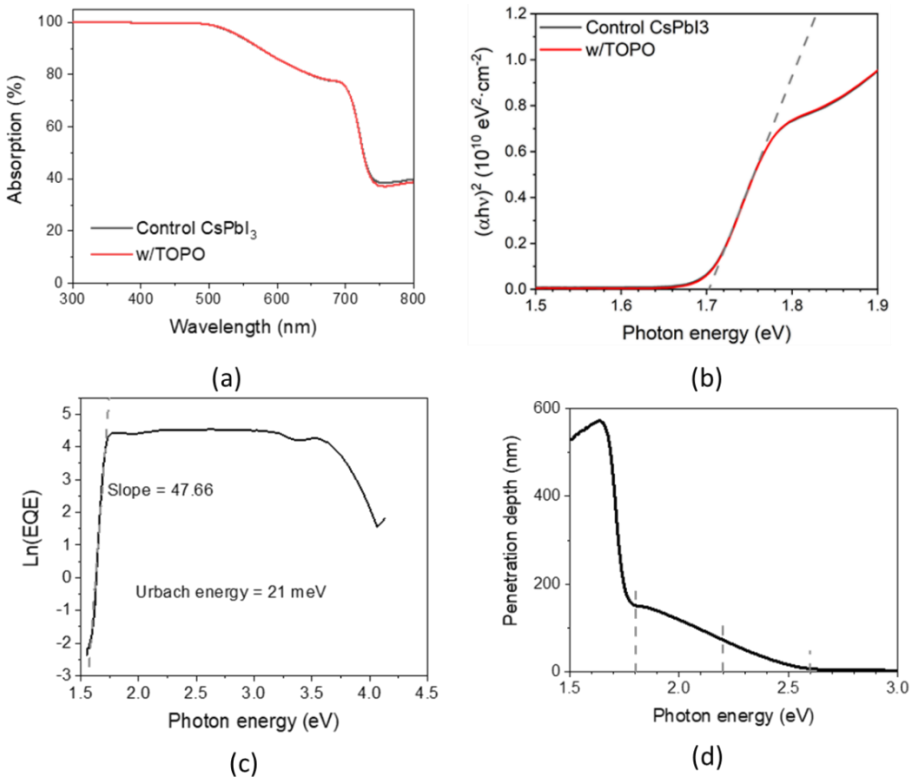

Fig. A4.2. a) Absorption spectra and b) Tauc plot of control and TOPO treated $CsPbI_3$ perovskite films. c) Urbach energy of $CsPbI_3$ perovskite calculated from EQE. d) Penetration depth of light into $CsPbI_3$ perovskite films.

SEM Images

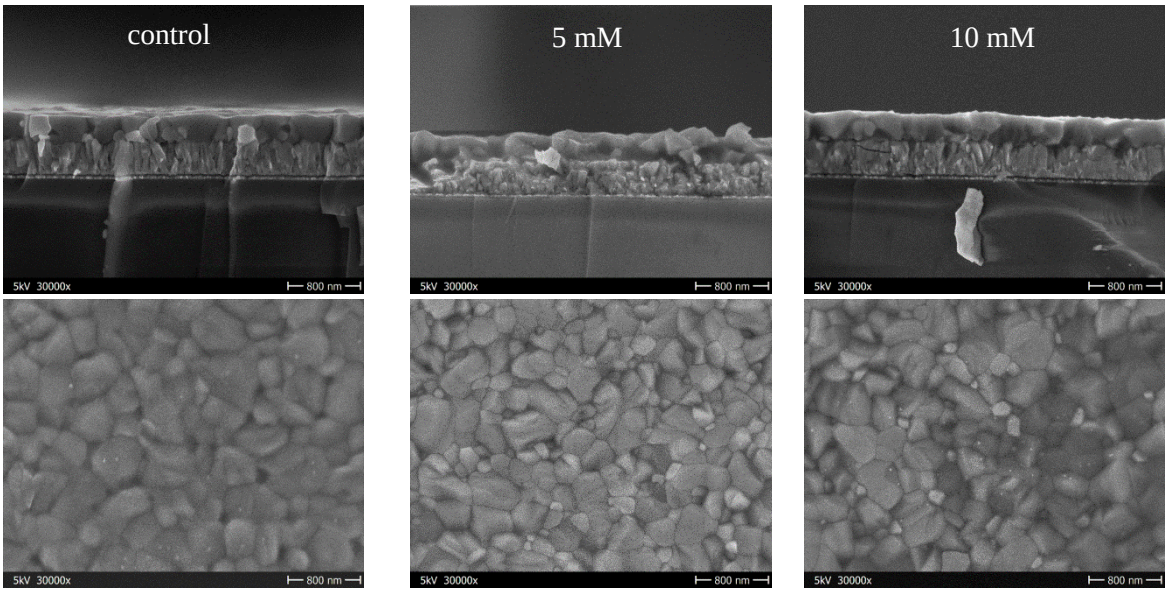

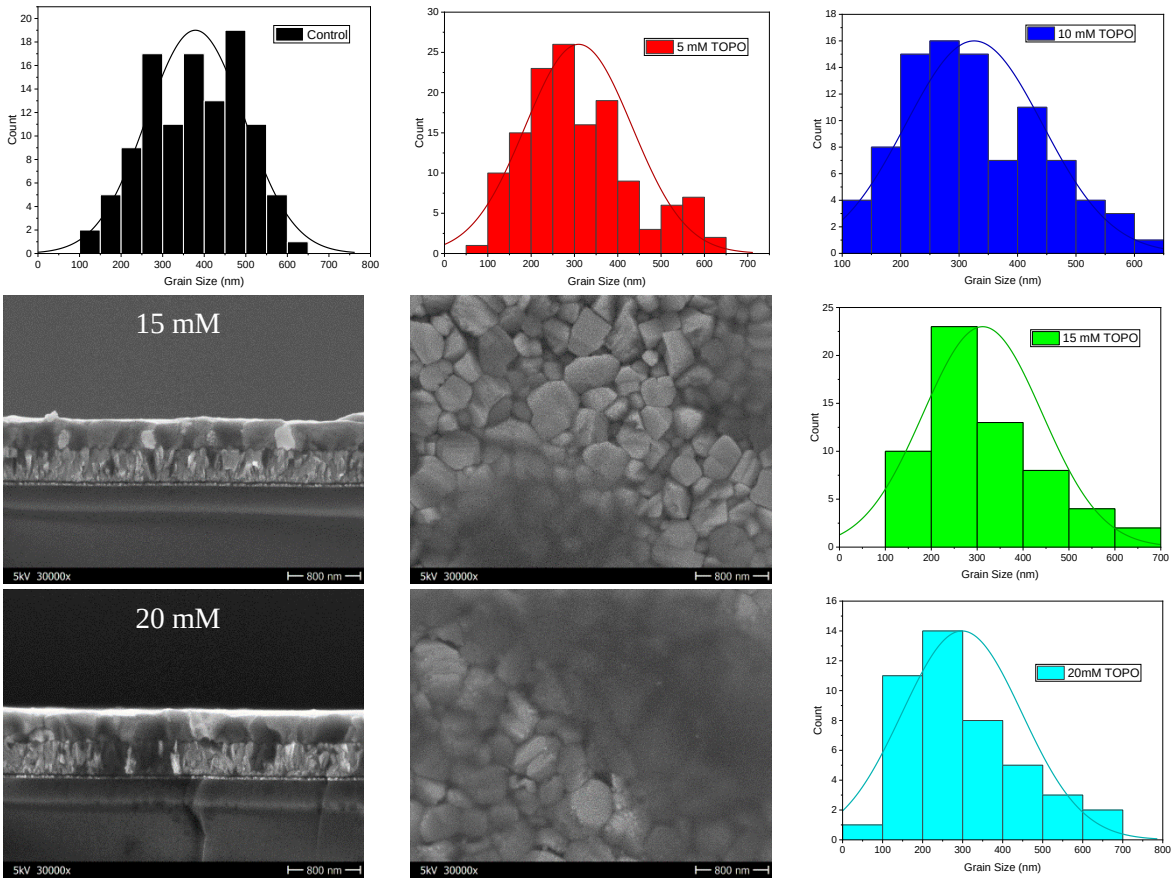

Fig. A.4.3. SEM images (cross-section and surface morphology) of $CsPbI_3$ samples with and without TOPO treatment.

AFM (Film roughness)

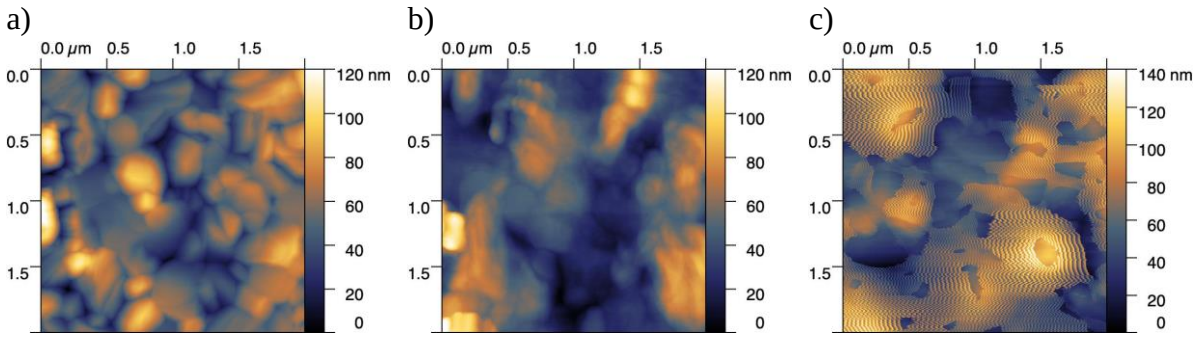

RMS = (16.6 ± 3.4) nm	RMS = (20.1 ± 4.3) nm	RMS = (24.3 ± 5.2) nm
Max. Height: 128.6 nm	Max. Height: 128.8 nm	Max. Height: 146.7 nm

Fig. A4.4. Topography images of a) bare CsPbI3, b) control CsPbI3 and c) w/TOPO, characterized by AFM.

Note: The "lined" features in TOPO-treated samples (c) are likely to be caused by the effect of dipole force on the cantilever during the measurement.

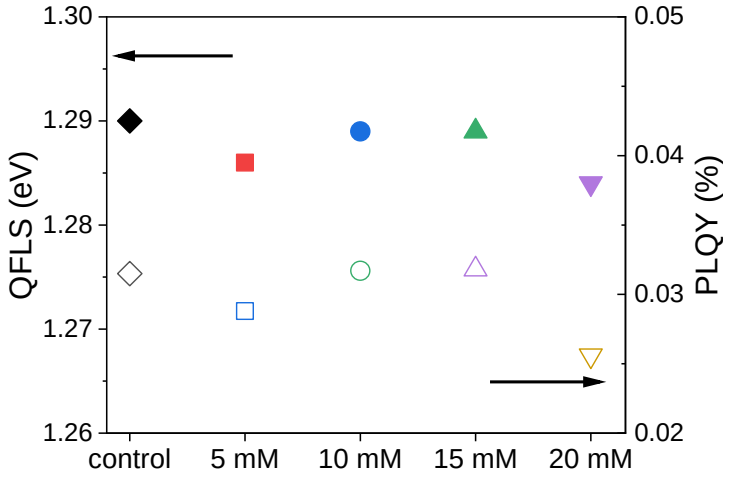

Fig. A 4.5. PL quantum yield (PLQY) and quasi-fermi level splitting (QFLS) of control and TOPO-treated samples.

For TOPO-treated samples at varying concentrations of 5 mM, 10 mM, 15 mM and 20 mM, they exhibited a similar photoluminescence quantum yield (PLQY) and thus a similar quasi-Fermi level splitting (QFLS)

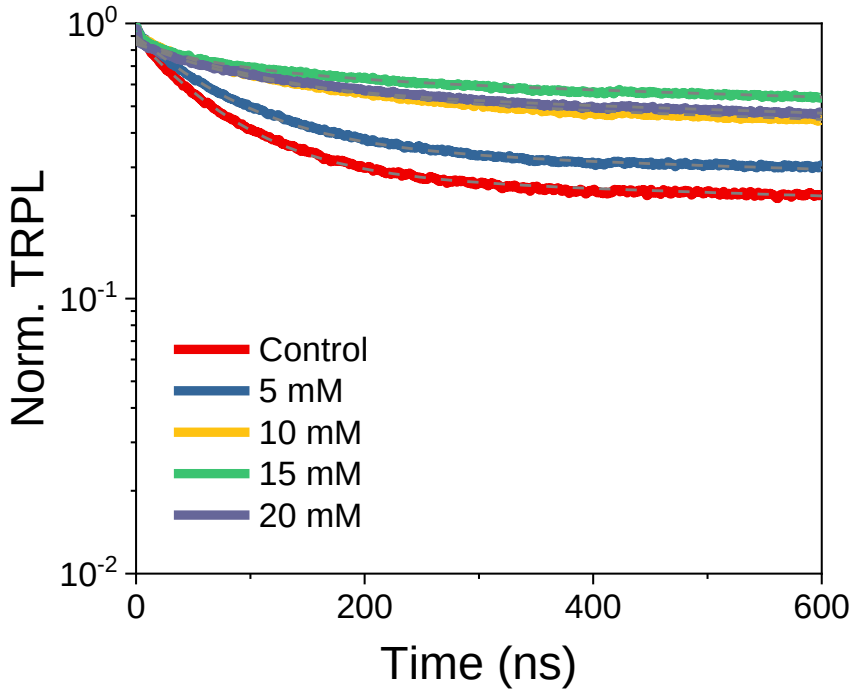

Fig. A.4.6. TrPL fitted with a bi-exponential equation.

The TRPL data were fitted with a bi-exponential equation given in the following:

$$y = A_1 * \exp\left(\frac{-x}{\tau_1}\right) + A_2 * \exp\left(\frac{-x}{\tau_2}\right) \qquad \text{(Eq. A 4.1)}$$

Table A4.1. Fitted parameters of TRPL spectra in **Fig. 4.1 b,d**

Neat perovskite film	A_1	A_2	t_1 (ns)	t_2 (ns)
Control	0.6	0.28	68	3500
5 mM TOPO treatment	0.55	035	77	3500
10 mM TOPO treatment	0.34	0.53	110	3500
15 mM TOPO treatment	0.2	0.64	92	3500
20 mM TOPO treatment	0.29	0.56	90	3500
w/ ETM	0.96	0.09	0.8	45
10 mM TOPO treatment	0.95	0.07	0.75	90
15 mM TOPO treatment	0.95	0.07	0.75	90

Comparing the τ_1 extracted from Fig. **4.2b** and **4.2d**, the value is dropped by approximately one order of magnitude, indicating the τ_1 related decay happened much faster in the samples with ETM. Meanwhile, the weight (A_1) of the first exponential decay over the whole PL decay curve increased in **Fig. 4.2**, indicating the τ_1 related decay contributes to a large portion of the PL decay. We believe the difference comes from the presence of an electron contact layer in samples presented in **Fig. 4.2 d**. For neat perovskite films without ETM or HTM, the PL decay comes from either the trap-related monomolecular recombination or the electron-hole-related bimolecular recombination. In our trPL data, the τ_1 reflects the decay due to the electron-hole-related bimolecular recombination while the τ_2 reports the decay coming from the trap-related monomolecular recombination. The long monomolecular lifetime of up to 3.5 μs extracted from our work agrees with the literature. [6,7]

With the ETM adjacent layer, the photo-generated electrons and holes in the perovskite film can experience bimolecular recombination and trap-inducted monomolecular recombination, and additionally, electrons be extracted at the interface. Each of the three paths will lead to a decay in the PL signal. It is likely that for perovskite with ETM, τ_1 relates to the electron extraction reduced PL decay because we did not observe such a fast decay in neat perovskite films. τ_2 might connect to trap-related monomolecular recombination or electron-hole bimolecular recombination. If it reflected the decay due to monomolecular recombination, then the value is reduced by nearly two orders of magnitude compared to the neat perovskite samples. This would mean a large increase in trap densities because of the introduction of the ETM adjacent layer. However, the contour plots of the transient SPV in **Fig.A4.9** reflects no formation of trap states below the bandgap of $CsPbI_3$ perovskite deposited on TiO_2-ETM. Thus, we believe that τ_2 is not likely related to trap-related monomolecular recombination. Here we assign it to the decay process caused by electron-hole bimolecular recombination. The value falls in the similar range of the τ_1 in neat perovskite samples.

XPS spectra of P 2s and O 1s.

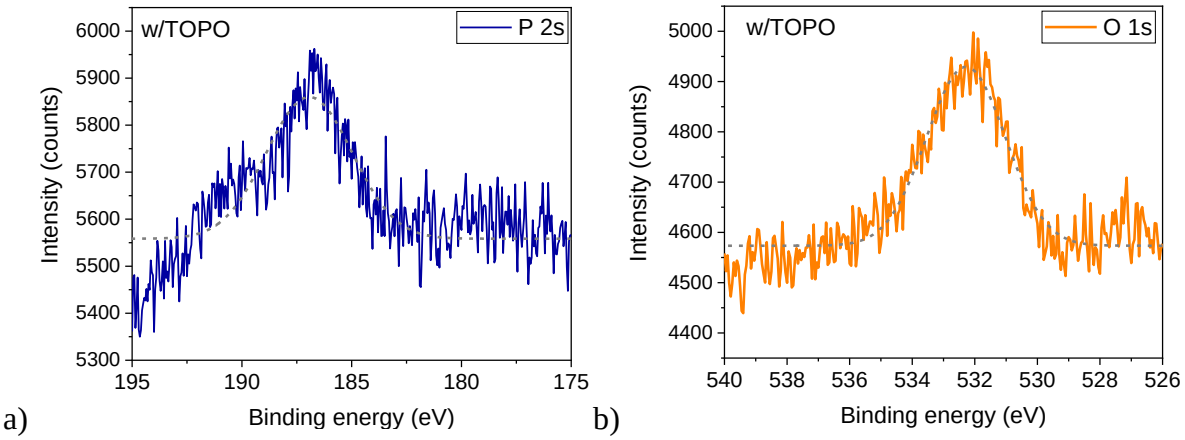

Fig. A4.7 XPS of a) P 2s and b) O 1s core-shell spectra of $CsPbI_3$ sample with TOPO treatment (dash lines are the Gaussian fitting of each peak).

Table A4.2. Work function (Φ) of the following samples was measured by Kelvin probe.

Samples stack	WF Point1 (eV)	WF Point2 (eV)	WF Point3 (eV)	WF Average (eV)	Standard deviation (eV)
Bare CsPbI3	-4.333	-4.401	-4.330	-4.355	0.033
Control CsPbI3	-4.205	-4.178	-4.161	-4.183	0.018
w/TOPO	-4.098	-3.916	-3.893	-3.969	0.092

Table A4.3. Work function (Φ), ΔE and VBM of the following samples extracted from UPS measurement.

Samples stack	Φ (eV)	ΔE (eV)	VBM (eV)	*CBM (eV)
bare $CsPbI_3$	-3.91	1.34	-5.25	-3.54
control $CsPbI_3$	-3.64	1.54	-5.18	-3.47
w/TOPO	-3.51	1.44	-4.95	-3.24
control/Spiro-OMeTAD-dark	-4.51	0.49	-5.00	-2.08
w/TOPO/Spiro-OMeTAD-dark	-4.39	0.56	-4.95	-2.03
control/Spiro-OMeTAD-light	-3.85	1.15	-5	-2.08
w/TOPO/Spiro-OMeTAD-light	-3.77	1.18	-4.95	-2.03

*Notes: CBM was calculated from the VBM-Eg (optical bandgap, calculated from Tauc plot given in Fig. S7 for CsPbI3 (*i.e.* 171 eV). The optical bandgap of spiro-OMeTAD of 2.92 eV was taken from our previous publication. [8]

The difference in absolute values of WF between the Kelvin probe and UPS characterization could be caused by the slight sample variation or the different measurement environments of the two techniques. The slightly lower values of WF probed by UPS can also be explained by the illumination of samples by the Ultra-violate light during the measurement, which increased sample conductivity and occupied free states.

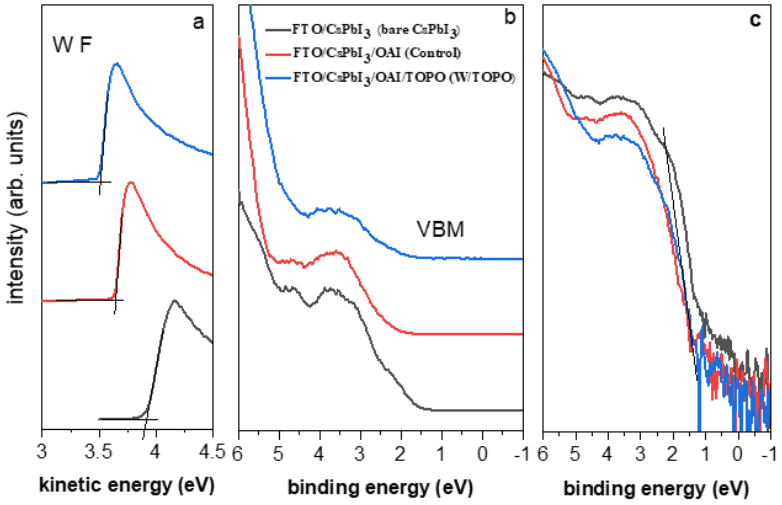

Fig. A4.8. Secondary electron cut-off (a), valence spectra (b), and zoomed valence spectra on logarithmic intensity scale (c) of bare $CsPbI_3$, control $CsPbI_3$, and w/TOPO.

Influence of substrates characterized by tr-SPV

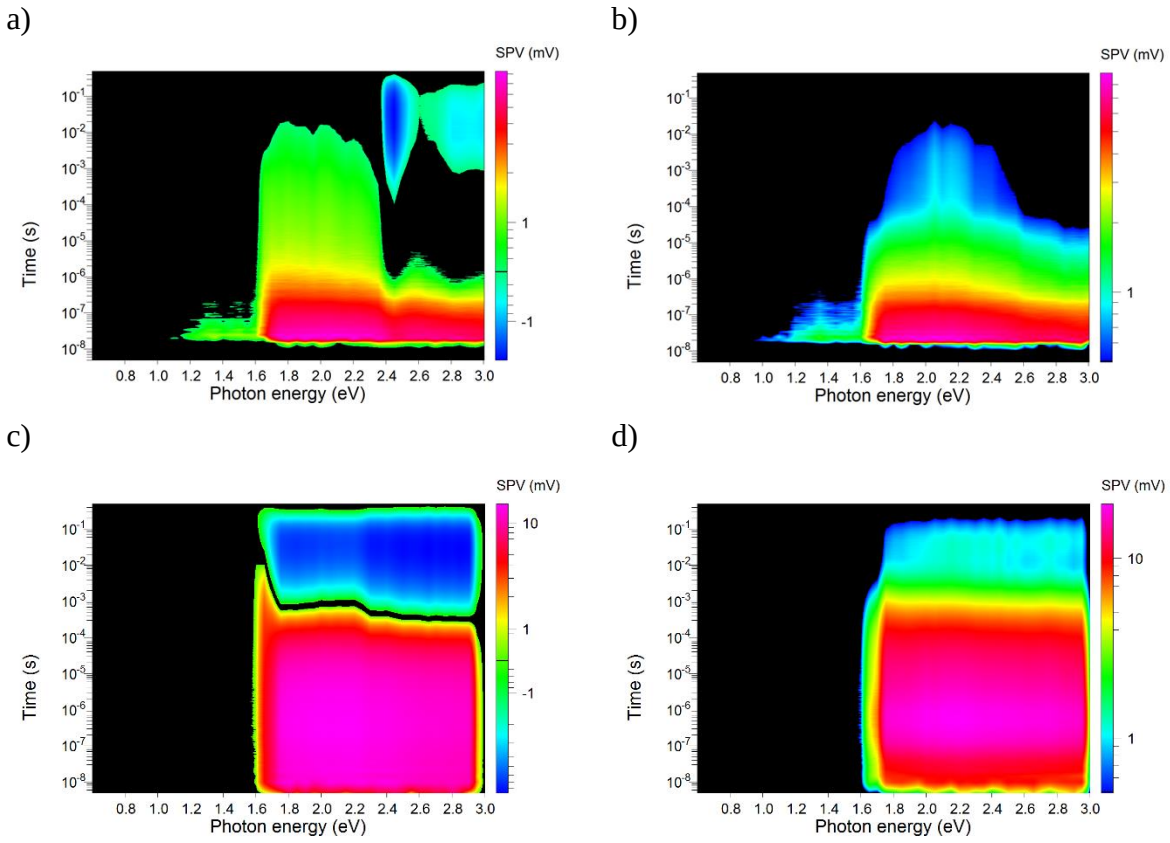

Fig. A4.9. Contour plots of the transient SPV illuminated by different light energies of a) glass/$CsPbI_3$/OAI (Control), b) glass/$CsPbI_3$/OAI/TOPO, c) glass/TiO_2/$CsPbI_3$/OAI(Control), d) glass/TiO_2/$CsPbI_3$/OAI/TOPO.

Transient SPV at 0.1 sun and 10 suns

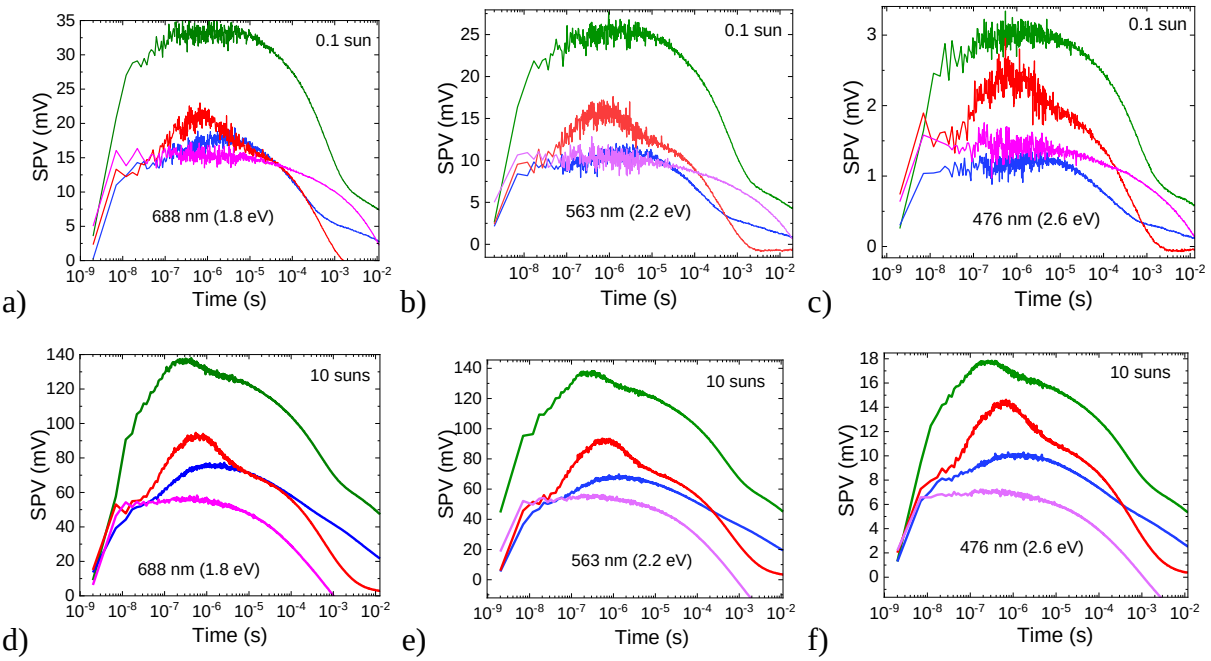

Fig. A.4.10. Transient SPV of control (black line), w/TOPO (red line), control with Spiro-OMeTAD (blue line), w/TOPO/Spiro-OMeTAD (green line) at a) 1.8 eV, 0.1 sun, b) 2.2 eV, 0.1 sun, c) 2.6 eV, 0.1 sun, d) 1.8 eV, 10 suns, e) 2.2 eV, 10 suns, and f) 2.6 eV, 10 suns.

Table A 4.4 Additional Constants for Simulations

Where N, P, C_b, σ_e, σ_h, v_e, and v_h are photo-induced electron concentration, photo-induced hole concentration, radiative recombination constant, electron capture-cross section of trap, hole capture cross-section of trap, the thermal velocity of electron and hole, respectively. ε_{per}, ε_{ETM} and ε_{HTM} are dielectric constants. τ_{HTM} and τ_{ETM} are lifetimes in HTM and ETM. The concentration of free carriers (N, P) was calculated according to the fluence of 0.010 μJ/cm^2. Constants C_b, v_e, v_h, and $\boldsymbol{\varepsilon_{per}}$, were adapted from the previous study[9]. Dielectric constants ε_{ETM} and ε_{HTM} were adapted from literature[10,11]. Constants τ_{HTM}, τ_{ETM}, K_{eETL}, σ_e, and σ_h are fitted directly and are in agreement with previous reports[9, 13, 14].

N (P), cm^{-3}	C_b, cm^{3}s^{-1}	K_{eETL}, 10^7 s^{-1}	σ_e, cm^2	σ_h, cm^2	v_e, cms^{-1}
1.1×10^{15}	5×10^{-10}	1.2-1.8	10^{-13}	4×10^{-14}	3×10^{7}
v_h, cm s^{-1}	ε_{per}	ε_{ETM}	ε_{HTM}	τ_{HTM} s	τ_{ETM} s
3×10^{7}	18	3	3	$2\text{-}5\times10^{-5}$	$2\text{-}4\times10^{-4}$

Transient SPV fitting results

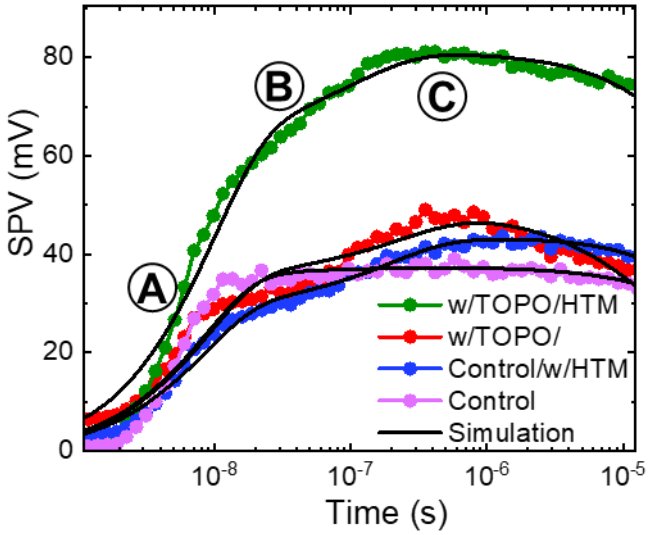

Fig. A.4.11. Transient SPV of control sample (black line), w/TOPO (red line), control with Spiro-OMeTAD (blue line), w/TOPO/Spiro-OMeTAD (green line). Fitted results are given in black lines.

Table A4.5 Main fitting constants of simulation. $N_{non\text{-}rad}$ – concentration of non-radiative recombination defects (both surface or bulk), K_h – hole injection rate, K_e – electron injection rate, K_{hb} – hole reinjection rate, and K_{eb} – electron reinjection rate. *STD* is the average standard deviation of the fit from the experimental SPV signal.

Interface	K_h, s^{-1}	K_e, s^{-1}	K_h/K_e	$N_{non\text{-}rad}$, cm^{-3}	*STD*, %
w/TOPO/Spiro-OMeTAD	8×10^6	10^6	8	7.7×10^{13}	11.6
control/ Spiro-OMeTAD	4.4×10^6	3.6×10^6	1.2	9.4×10^{13}	6
w/TOPO	3.9×10^6	10^6	3.9	8.8×10^{13}	15.2
Control	1.5×10^6	1.1×10^6	1.3	9.1×10^{13}	8

Table A4.6. Photovoltaic parameters summary for champion devices of $CsPbI_3$ perovskite.

	J_{sc} (mAcm^{-2})	V_{oc} (mV)	*FF* (%)	PCE (%)	
Control	20.2	1100	74.7	16.6	re
	20.2	1000	70.5	14.3	fw
5 mM TOPO	20.3	1135	76.3	17.6	re
	20.3	1064	74.2	16.0	fw
10 mM TOPO	20.5	1169	78.0	18.7	re
	20.5	1085	73.1	16.2	fw
15 mM TOPO	20.2	1121	76.6	17.3	re
	20.2	1038	74.4	15.6	fw
20 mM TOPO	20.4	1147	76.9	18.0	re
	20.4	1058	74.3	16.0	fw

Notes: "re" and "fw" indicate the reverse scan (bias sweeps from V_{oc} to J_{sc}) and forward scan (bias sweeps from J_{sc} to V_{oc}.), respectively.

Statistic *J-V* data

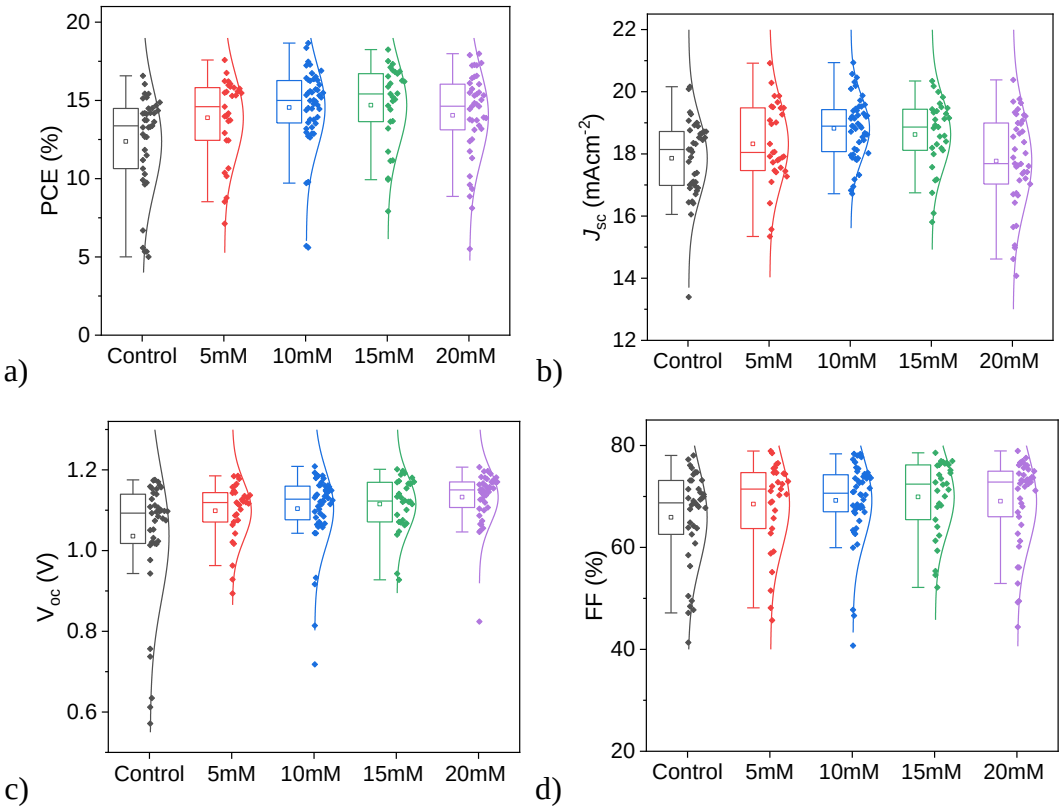

Fig. A.4.12. Box charts of a) PCE, b) J_{sc}, c) V_{oc} and d) FF of more than 40 solar cells ("shunted/dead" solar cells data are removed and not included).

The data shows that there is an improvement in PCE and other parameters for TOPO treated samples.

References

1. Y. Wang1, M. I. Dar, L.K. Ono, T. Zhang1, M. Kan1, Y. Li, L. Zhang, X.Wang1, Y.Yang, X.Gao, Y. Qi, M.Grätzel, Y. Zhao, "Thermodynamically stabilized ß-CsPbI3–based perovskite solar cells with efficiencies >18%", *Science*, 2019, **365**, 591–595.
2. N. K. Cho, H. J. Na, J. Yoo, *et al*. "Long-term stability in γ-CsPbI3 perovskite via an ultraviolet-curable polymer network", *Commun. Mater.*, 2021 2, 30.
3. J. A. Steele, H. Jin, I. Dovgaliuk, *et al.* "Thermal unequilibrium of strained black CsPbI3 thin films", *Science*, 2019, 365, 6454 679-684.
4. A. Marronnier, G. Roma, S. B. Richard, *et al.* "Anharmonicity and Disorder in the Black Phases of Cesium Lead Iodide Used for Stable Inorganic Perovskite Solar Cell", *ACS Nano*, 2018, 12, 4, 3477–3486.
5. Y. Wang, X. Liu, T. Zhang, *et al.* "The Role of Dimethylammonium Iodide in CsPbI3 Perovskite Fabrication: Additive or Dopant?", *Angew. Chem.*, 2019, 131, 16844–16849.
6. E. V. Péan, S. Dimitrov, C. S. De Castro, *et al*., "Interpreting time-resolved photoluminescence of perovskite materials", *Phys. Chem. Chem. Phys.*, 2020, 22, 28345-28358
7. C. Stavrakas, A. A. Zhumekenov, R. Brenes, *et al*., "Probing buried recombination pathways in perovskite structures using 3D photoluminescence tomography", *Energy Environ. Sci.*, 2018, 11, 2846-2852
8. Q. Wang, E. Mosconi, C. Wolff, *et al.* "Rationalizing the Molecular Design of Hole-Selective Contacts to Improve Charge Extraction in Perovskite Solar Cells", *Adv. Energy Mater.*, 2019, 9, 1900990.
9. I. Levine, A. Al Ashouri, A. Musiienko, *et al.* "Charge transfer rates and electron trapping at buried interfaces of perovskite solar cell", *Joule*, 2021, **5**, 2915–2933.
10. Y. C. Lin, L. Y. Chen, & F. C. Chiu, "Lossy Mode Resonance-Based Glucose Sensor with High-κ Dielectric Film", *Cryst*., 2019, 9, 450.
11. F. Anwar, R. Mahbub, S. S. Satter, *et al*., "Effect of Different HTM Layers and Electrical Parameters on ZnO Nanorod-Based Lead-Free Perovskite Solar Cell for High-Efficiency Performance", *Int. J. Photoenergy*, 2017, doi: 10.1155/2017/9846310.
12. A. Musiienko, D. R. Ceratti, J. Pipek, *et al.*, "Defects in Hybrid Perovskites: The Secret of Efficient Charge Transport", *Adv. Funct. Mater.*, 2021, 31, 2104467.
13. A. Musiienko, J. Pipek, P. Praus, *et al*., "Deciphering the effect of traps on the electronic charge transport properties of methylammonium lead tribromide perovskites", *Sci. Adv.*, 2020, 6, doi: 10.1126/sciadv.abb6393.

Declaration of Originality

I (Mr.Zafar Iqbal) declare that this dissertation is from my original Ph.D. projects, except the parts which give rightful references to other people's works or are reproduced with permission. The scientific help and support to accomplish the experiments have been acknowledged. This work has not been submitted to any other university by me. It is also declared that no artificial intelligence (AI) based tool has been used for writing this manuscript.

Berlin. Germany

July 2023

Acknowledgment

Here, I list all the individuals whose contributions were instrumental in the completion of my Ph.D. dissertation and research.

I express my gratitude to my Ph.D. supervisor, Prof. Antonio Abate, for his invaluable help, guidance, and unwavering support throughout my work. His positive approach, encouragement for collaboration, and ability to think outside the box motivated me, making my ideas more practical in the lab. I am also thankful for his training in science communication and his tremendous mental support.

My appreciation extends to my supervisor at the University of Potsdam, Prof. Andreas Taubert, for his consistent support, guidance, prompt responses to my inquiries, and assistance in crafting my thesis. I have benefited greatly from his expertise in Chemistry and his experience in administration.

I would like to highlight the contributions of Dr. Qiong Wang to my work. Our joint efforts on $CsPbI_3$ in the HySPRINT lab required considerable time to yield better results initially. Dr. Wang consistently aided me with experiments, data analysis, and writing. I extend my thanks to senior colleagues Silver Hamill, Jorge Pascal, and Meng Li for their guidance.

I am grateful to the Deutscher Akademischer Austauschdienst (DAAD) for funding my Ph.D. and providing financial support. Special thanks go to Frau Dagmar Beerwerth, my program focal person, for her continuous support and care, even during the challenges posed by the Corona days.

Acknowledgment is due to collaborators: Prof. Dieter Neher's group at the University of Potsdam, Prof. Norbert Koch’s group at Humboldt University, and Marcus Bär's group at HZB for their contributions to optical and spectroscopic measurements.

I also appreciate the contributions of my senior colleague Artem Musiienko for measurements, simulations, and discussions, and Florian Ruske for aiding in thesis writing and supporting my Ph.D.

My gratitude extends to all colleagues and group members, including Marion Flatken, Laura Canil, Hans Köbler, Chiara Frasca, Shengnen Zuo, Thomas Gries, Valerio Stacchini, Yanyan Duan, Zahra Loghmannia, Izaz Ali, Paola Alippi, Mehmoud Aldamasy, Rebab, Yuqian Yang, Madineh, and Titan Noor, for their assistance, enjoyable moments, discussions, and support during my Ph.D.

As Morten Meldal, Nobel Laureate in Chemistry 2022, said, "Great discoveries are not made behind the office desk; they are made in the laboratory." However, true respect is reserved for those who maintain the labs' functionality and sustain an environmentally friendly atmosphere. I extend my gratitude to lab managers Prof. Steve Albrecht and his group, Prof. Eva Unger and her group, and lab technicians Moni, Hagen, Carola Ferber, Carola Klimm, Johannes, Andreas von Kozierowski, and Thomas Lußky. I am also very thankful to our helpful secretaries Antonia Tallarek and Marion Krusche.

Special mention goes to my teachers who educated me in my early years and university, enabling me to achieve my goals. Additionally, I am thankful to my friends for their ongoing support and best wishes for my work.

Lastly, I want to acknowledge my family members for their care and support. I express gratitude to my mother for her dedication to my education and upbringing, which paved the way for my Ph.D. My wife deserves special thanks for her support during my Ph.D., and both she and my son, Mujtaba, deserve additional appreciation for enduring the challenges caused by my late work hours.